

# Tissue database of autofluorescence response to improve intra-operative diagnosis of primitive brain tumors

Thèse de doctorat de l'Université Paris-Saclay  
préparée à l'Université Paris-Sud

École doctorale n°564 Physique en Île-de-France  
Spécialité de doctorat: Physique

Thèse présentée et soutenue à Orsay, le 26 Septembre, par

**Fanny Poulon**

Composition du Jury :

**Mme. Fabienne Mérola**

Directrice de recherche, Université Paris Sud (LCP-UMR 8000)

Président

**M. Jürgen Popp**

Professeur, Université de Jena

Rapporteur

**M. Huikai Xie**

Professeur, Université de Floride

Rapporteur

**M. Frederic Jamme**

Scientifique de ligne, Synchrotron SOLEIL (Ligne DISCO)

Examineur

**Mme. Eva Compérat**

Professeure (PU-PH), Université Paris Sorbone-Hôpital Tenon

Examineur

**Mme. Darine Abi Haidar**

Maitre de conférence, Université Paris Diderot (IMNC-UMR 8065)

Directeur de thèse





# Contents

<b>French Summary</b>	<b>1</b>
<b>Acknowledgements</b>	<b>7</b>
<b>1 Introduction</b>	<b>9</b>
1.1 Central nervous system cancer . . . . .	10
1.1.1 Preamble . . . . .	10
1.1.2 Gliomas . . . . .	11
1.1.3 Meningioma . . . . .	12
1.1.4 Metastasis . . . . .	13
1.2 How to diagnose brain tumor . . . . .	13
1.2.1 Imaging techniques . . . . .	13
1.2.2 Biopsy . . . . .	18
1.2.3 Histology . . . . .	19
1.3 How to treat brain tumor . . . . .	22
1.3.1 First choice of treatment for brain tumors . . . . .	22
1.3.2 Other standard treatment . . . . .	24
1.4 Current technologies of assisted resection with intra-operative imaging . . . . .	24
1.4.1 ioMRI . . . . .	25
1.4.2 ioUS . . . . .	25
1.5 New contrast in intra-operative imaging: the fluorescence . . . . .	26
1.5.1 Exogenous fluorescence . . . . .	26
1.5.2 Endogeneous fluorescence . . . . .	27
1.5.3 Methods of measurements based on fluorescence signal . . . . .	31
1.6 Optical developments in optical endomicroscopy . . . . .	35
1.6.1 Optical coherence tomography . . . . .	35
1.6.2 Wide-field endomicroscopy . . . . .	36
1.6.3 Confocal endomicroscopy . . . . .	36
1.6.4 Multi-photon endomicroscopy . . . . .	40
1.6.5 State of the art in multi-photon endomicroscopy . . . . .	43
1.7 Thesis project . . . . .	47
1.7.1 Context . . . . .	47
1.7.2 Actors and partners . . . . .	48
1.7.3 Design of the project . . . . .	49

<b>2</b>	<b>Could quantitative bimodal optical measurements under visible excitation discriminate fixed brain tissue nature ?</b>	<b>51</b>
2.1	Context of the study . . . . .	51
2.2	Paper: Optical properties, spectral, and lifetime measurements of central nervous system tumors in humans . . . . .	55
2.2.1	Introduction . . . . .	56
2.2.2	Materiel and methods . . . . .	57
2.2.3	Results . . . . .	59
2.2.4	Discussion . . . . .	63
<b>3</b>	<b>Could spectral and lifetime measurements, under visible excitation discriminate freshly extracted brain tissue nature ? Were fluorescent measurements established on fixed tissue suitable enough to build an optical database ?</b>	<b>67</b>
3.1	Context of the study . . . . .	67
3.2	Paper: Multimodal optical analysis discriminates freshly extracted human sample of gliomas, metastases and meningiomas from their appropriate controls . . . . .	72
3.2.1	Introduction . . . . .	73
3.2.2	Materiel and methods . . . . .	74
3.2.3	Results . . . . .	76
3.2.4	Discussion . . . . .	81
<b>4</b>	<b>Could mono and bi-photon excitation discriminate label-free fluorescence emission of meningioma tumor grade ?</b>	<b>85</b>
4.1	Context of the study . . . . .	85
4.2	Paper: Multimodal optical analysis of meningioma and comparison with histopathology . . . . .	88
4.2.1	Introduction . . . . .	89
4.2.2	Material and methods . . . . .	90
4.2.3	Results . . . . .	92
4.2.4	Discussion . . . . .	95
<b>5</b>	<b>Could two-photon imaging match the performance of H&amp;E standard in discriminating primary and secondary brain tumor ? Could multimodal quantitative detection improve brain tumor diagnosis ?</b>	<b>101</b>
5.1	Context of the study . . . . .	101
5.2	Paper : Real-time Brain Tumor imaging with endogenous fluorophores: a diagnosis proof-of-concept study on fresh human samples . . . . .	105
5.2.1	Introduction . . . . .	106
5.2.2	Materiel and methods . . . . .	107
5.2.3	Results . . . . .	110
5.2.4	Discussion . . . . .	117
<b>6</b>	<b>Could multimodal and multiscale optical analysis from DUV to NIR, be a reliable tool for diagnosis of primary and secondary tumor ?</b>	<b>121</b>
6.1	Context of the study . . . . .	121
6.2	Paper: Multimodal analysis of central nervous system tumor tissue endogenous fluorescence with multiscale excitation . . . . .	126
6.2.1	Introduction . . . . .	127

6.2.2	Matériel and methods . . . . .	128
6.2.3	Results . . . . .	133
6.2.4	Discussion . . . . .	137
<b>7</b>	<b>Discussion and Conclusion</b>	<b>141</b>
7.1	Autofluorescence as a diagnosis tool . . . . .	141
7.1.1	Qualitative analysis of label-free fluorescence images compared to gold standard H&E-stained . . . . .	141
7.1.2	Quantitative measurements based on autofluorescence emission . . . . .	143
7.1.3	From multimodal detection to automated algorithms . . . . .	147
7.2	Optical development towards an intra-operative endomicroscope . . . . .	149
7.2.1	First bi-modal non linear endomicroscope . . . . .	149
7.2.2	Position and improvement of our set-up compared to two-photon endomicroscopy state of the art . . . . .	152
7.3	Towards other problematics : the bladder cancer . . . . .	153
7.4	Conclusion . . . . .	156
<b>A</b>	<b>Paper : Characterization of fiber ultrashort pulse delivery for nonlinear endomicroscopy</b>	<b>183</b>
<b>B</b>	<b>Paper : Spectral and fluorescence lifetime endoscopic system using a double-clad photonic crystal fiber</b>	<b>193</b>
<b>C</b>	<b>Paper : Two-photon optical imaging, spectral and fluorescence lifetime analysis to discriminate urothelial carcinoma grades</b>	<b>199</b>

# French Summary

Ce manuscrit de thèse intitulé *Base de données sur le signal d'autofluorescence des tissus pour améliorer le diagnostic per-opératoire des tumeurs cérébrales*, traite d'aspects importants liés à l'utilisation d'approches d'imagerie spectroscopique pour le diagnostic de tumeur cérébrale en per-opératoire. Une telle étude a été motivée par la place prise par le cancer dans la société.

En 2011, Le ministère français de la santé et l'institut national du cancer(INCa) ont réalisé une étude sur la perception de cette maladie. Les résultats ont montré que dans l'esprit des gens le cancer avait toujours une connotation fortement négative. La plus part considérant que c'est la maladie la plus mortelle, bien loin devant le SIDA. Alors qu'en réalité l'étude montre également, que si un homme sur deux et une femme sur trois déclarent un cancer dans leur vie, le taux de survie est aujourd'hui supérieur à 50% [1].

Néanmoins le cancer traîne toujours cette forte connotation négative, due à certaines formes très agressives présentant encore une forte et rapide mortalité, laissant place à de nombreux défis oncologiques. Les tumeurs cérébrales font parties des cancers présentant toujours un fort taux de mortalité et donc défis dans le processus de traitement. Les tumeurs cérébrales ne sont pas les plus fréquentes, 17<sup>ème</sup> cancer seulement en terme d'incidence. Toutefois dans certains groupes d'âge, il s'agit de l'une des formes les plus meurtrières. Une étude réalisée en 2016 a montré qu'il s'agissait de la première cause de décès liés au cancer chez les 0 à 14 ans et la troisième chez les 15 à 39 ans [8, 9].

Comme le montrent ces statistiques, le diagnostic et le traitement des tumeurs cérébrales sont des sujets brûlants dans le monde de l'oncologie. Le principal défi étant l'amélioration du taux de survie à long terme des patients. Ceci est particulièrement un challenge en neuro-oncologie dû à la nature majoritairement infiltrante des tumeurs, résultant en processus complexe pour atteindre un diagnostic fiable. Aujourd'hui, le standard pour établir un diagnostic définitif sur la nature d'un tissu cérébral est l'examen histologique, c'est-à-dire l'analyse microscopique *ex vivo* d'échantillons de tissu extraits lors de la chirurgie et ensuite chimiquement traités (fixation, coloration). Pour un diagnostic per-opératoire, rapide et fiable de nouvelles méthodes et approches sont nécessaires de manière urgente, tel que de nouvelles techniques d'imagerie ou de mesures en temps réel. C'est exactement le rôle que pourrait jouer la microscopie optique à détection multimodale, en mettant l'accent sur l'imagerie d'autofluorescence, ainsi que les routines d'analyses automatisées pour l'analyse per-opératoire des tumeurs cérébrales présentées dans cette thèse.

Pendant ces trois années de doctorat j'ai mené des recherches au sein du laboratoire français IMNC (Imagerie et modélisation en neurobiologie et cancer) dans le groupe de Darine Abi Haidar. Cette équipe de recherche travaille avec un hôpital français (Le Centre Hospitalier Sainte-Anne, Paris, France) afin d'apporter de nouvelles solutions techniques pour améliorer la précision et qualité des résections chirurgicales des tumeurs cérébrales, le but étant de prolonger l'espérance de vie des

patients. Pour répondre à cette problématique, l'équipe a démarré, en collaboration avec l'hôpital, un projet visant à développer un nouvel outil révolutionnaire, afin d'intégrer l'endomicroscopie non linéaire au bloc opératoire. Une base de données sur la réponse optique des tissus a également été construite, pour être utilisée avec l'endomicroscope afin de guider le chirurgien lors de la résection des tumeurs et d'obtenir les meilleurs résultats possibles.

Ma thèse s'est inscrit dans ce projet large et interdisciplinaire, avec un focus particulier sur la construction de la base de données multimodale et multi-échelle de la réponse optique des tissus cérébraux. Ce manuscrit s'articule autour de cinq publications majeures écrites et publiées pendant mon doctorat, une large introduction sur le contexte clinique et technique à l'origine de ce projet est d'abord présentée, puis les cinq articles sont articulés afin de répondre à cinq grandes questions soulevées pendant ma thèse autour du diagnostic optique des tumeurs cérébrales. Le manuscrit ce conclut par une discussion sur les résultats obtenus et les futures orientations et perspectives du projet.

Le chapitre d'introduction est divisé en 7 sous-chapitres, commençant par un résumé des différentes formes de tumeurs cérébrales et de leur physiopathologie. Pour mieux comprendre les défis se rapportant aux tumeurs cérébrales, il est important de connaître les différents types de tumeurs malignes pouvant provenir des cellules du cerveau et leur classification. La classification des tumeurs cérébrales est basée sur leur cellule d'origine et leur agressivité. Deux groupes principaux peuvent être dégagés: les tumeurs primaires et secondaires. Une tumeur primitive provient des cellules et des tissus du cerveau et ne se propage généralement pas vers d'autres organes. Ce type de tumeur peut être soit bénigne, se développant lentement avec une limite distincte présentant un danger seulement si elle comprime une fonction vitale, ou alors maligne, se développant rapidement avec des limites irrégulières et avec la capacité d'infiltrer les zones environnantes [10]. Environ la moitié des tumeurs cérébrales primitives se développent à partir de cellules gliales et sont classées dans la catégorie des gliomes, avec un grade allant de I à IV dépendant de leur agressivité [10]. Elles peuvent également provenir des cellules nerveuses (tumeurs de Schwannome), de l'hypophyse (adénomes de l'hypophyse), du cervelet (tumeurs médulloblastomateuses, les plus courantes chez les enfants), des cellules germinales et également de la membrane entourant le cerveau, la méninge, ce qui entraîne l'apparition de tumeurs appelées méningiomes [10, 11]. Les tumeurs secondaires, appelées métastases, proviennent de cellules ayant migré d'une tumeur primaire dans un autre organe - poumon, sein, peau, rein et côlon sont les origines les plus courantes des métastases cérébraux [10].

Au cours de cette thèse, les gliomes (principalement les glioblastomes de grade IV), méningiomes et métastases ont été étudiés. Trois catégories pouvant présenter un caractère infiltrant, particulièrement les tumeurs gliales, rendant le diagnostic et traitement chirurgical très compliqué. Même si le panel de tumeurs cérébrales est large, elles subissent toutes le même protocole de diagnostic et traitement. Tout d'abord le patient doit passer par une phase de diagnostic, où en cas de suspicion de tumeur au cerveau, une combinaison de techniques d'imagerie sera prescrite pour réaliser un diagnostic préliminaire. Pour évaluer la présence ou non d'une tumeur, un scanner de tomographie axiale (CT-Scan) et une imagerie par résonance magnétique (IRM) sont prescrits. Ensuite, si l'oncologue et les chirurgiens ont besoin d'informations plus précises et plus fonctionnelles pour commencer à planifier le traitement, ils demanderont une imagerie plus avancée (IRM fonctionnelle (IRMf), tomographie par émission de positrons (TEP)). Dans le cas d'une masse détectée, ce ne sera que la première étape vers un diagnostic final. Pour avoir toutes les informations sur la nature et le l'agressivité de la tumeur, une analyse histologique sur prélèvements après une biopsie, doit être réalisée. Ceci amenant à un rapport pathologique définitif, qui sera alors analysé par une équipe composée d'un oncologue, d'un radio-oncologue et d'un neurochirurgien afin d'élaborer le

plan de traitement. Les décisions de traitement sont individualisées et basées sur le type de tumeur, la localisation, la malignité et le patient (âge, condition physique). Toutefois la méthode privilégiée et appliquée en premier lieu est la résection chirurgicale, celle-ci peut être ensuite suivi de radiothérapie et chimiothérapie. Parfois, un seul type de traitement peut être nécessaire, mais la plupart du temps, une combinaison de ceux-ci est recommandé. Dans ce processus de traitement l'étape la plus compliquée et qui est à l'origine du faible taux de survie des patients, est la qualité de la résection chirurgicale. Si les tumeurs sont fortement infiltrantes, il n'existe à ce jour aucun moyen per-opératoire pour identifier les zones infiltrées en marge de la tumeur solide. La seule méthode pour s'assurer de la qualité de la résection est de faire l'analyse histologique des berges, cependant ces analyses sont réalisées *ex-vivo* et donc coûteuses en temps et moyens.

Pour améliorer la qualité de la résection plusieurs approches ont été considérées, tout d'abord chirurgicale, avec la chirurgie électro-stimulée et éveillée. Une méthode qui permet d'élargir au maximum la résection tout en préservant les fonctions vitales du patient pour lui assurer une qualité de vie post-opératoire. Ces techniques ont montré une amélioration du taux de survie et de la qualité de vie du patient, toutefois la résection est toujours réalisée sans connaître la réelle nature du tissu réséqué, certaines régions enlevées peuvent être complètement saines et certaines cellules tumorales oubliées dans les régions hautement fonctionnelles. Les chirurgies sont allongées, et par conséquent coûteuses à l'hôpital et aux patients.

Une autre approche pour améliorer la résection des tumeurs cérébrales et se rapprocher d'une résection totale, fût d'améliorer les techniques d'imagerie per-opératoire. La première direction prise pour obtenir des évaluations per-opératoires en temps réel consista à introduire les techniques d'imagerie préopératoires actuelles, telles que l'IRM ou l'échographie, dans la salle d'opération. Malheureusement même si ces techniques offrent plus d'assurance au chirurgien dans ces choix, elles manquent toujours en résolution à l'échelle cellulaire et ne peuvent identifier l'infiltration. Ceci laisse place à une recherche interdisciplinaire, pour apporter la possibilité au chirurgien de discriminer en temps-réel les berges tumorales. Une direction importante prise pour répondre à ce défi médicale est l'utilisation de la fluorescence, et les différentes façons de l'imager.

En premier lieu la fluorescence exogène a été explorée, des marqueurs des types cellulaires, des protéines ou des gènes, sont introduits chez le patient, excités et leur signal émis collecté par l'endoscope. Les fluorophores les plus testés et répandus pour la résection des tumeurs cérébrales sont la fluorescéine de sodium, le vert d'indocyanine(ICG) et l'acide 5-aminoluvulinique(5-ALA). Toutefois le développement des marqueurs exogènes a été ralenti dû au long et difficile processus d'approbation par les comités médicaux et la difficulté à trouver des marqueurs spécifiques de la tumeur à l'échelle cellulaire. Ces limitations et la disponibilité des technologies d'imagerie à haute résolution ont poussé les physiciens à envisager un autre moyen de contraste: l'autofluorescence. Dans tous les tissus, on peut trouver des molécules dans les cellules qui, lorsqu'elles sont excitées à une longueur d'onde appropriée, deviennent fluorescentes. Ces fluorophores endogènes sont liés aux propriétés morpho-fonctionnelles de la cellule et du tissu. Tous les changements intervenus au cours de processus physiologiques et pathologiques ont une incidence sur la distribution des fluorophores et donc sur leurs caractéristiques d'émission. Il en résulte un outil puissant pour surveiller directement l'état morphologique et physiologique d'un tissu et ou d'une région de cellules.

Le signal de fluorescence peut être caractérisé par trois paramètres quantifiables: 1) le spectre de fluorescence, intensité de la fluorescence en fonction de la longueur d'onde, 2) le rendement quantique, efficacité du processus d'émission et 3) la durée de vie de la fluorescence, temps moyen pendant lequel un fluorophore reste dans son état excité. Les technologies de détection ont été développées pour tirer avantage de ces paramètres et donner des indicateurs quantitatifs aux ré-

gions observées. De plus, d'autres transitions peuvent être excitées et permettent également une détection quantitative. Ils sont classés dans la spectroscopie Raman. Afin d'améliorer l'information donné au chirurgien, les nouvelles techniques de microscopie hautement résolues ont été développées. Afin d'essayer de produire des images à l'échelle cellulaire et de quantifier les différents paramètres de l'autofluorescence. Les différentes techniques modernes de microscopie, plein champ, confocale et multiphoton, ont vu l'intérêt s'accroître afin d'obtenir des outils miniaturisés pour s'adapter à l'environnement chirurgical et être utilisé de façon per-opératoire. Les technologies les plus récentes suscitant l'intérêt afin d'assurer la différenciation en temps réel des cellules tumorales sont la spectroscopie Raman et la microscopie multiphotonique. Ces techniques en sont encore au stade de la validation de la conception et n'ont pas encore été appliquées dans des essais cliniques de phase III et ne sont toujours pas dans les protocoles de routine. L'un des principaux éléments techniques manquants dans le développement à ce jour est l'absence de détection multimodale, ainsi qu'une base de données de haute qualité sur le tissu étudié. Par conséquent, la technologie actuelle ne parvient pas à conférer une discrimination suffisamment fiable aux normes cliniques. Cela laisse de la place pour le développement d'une technologie précise et fiable d'assistance à la chirurgie des tumeurs cérébrales, car le tissu cérébral en particulier manque d'une base de données optique sur sa réponse en autofluorescence. L'équipe de recherche du Dr Darine Abi Haidar a choisi de travailler sur cette question clinique en apportant son expertise technique. Ce groupe de recherche possède une expérience en optique et en microscopie, plus précisément en techniques non linéaires. Grâce aux collaborations de l'équipe, une large gamme d'échantillons de biopsie fut disponible au près du centre hospitalier Saint-Anne(CHSA), ainsi que trois plates-formes d'imagerie. Un endoscope visible placé au département de neuropathologie du CHSA pouvant mesurer la réponse spectrale à un photon et la durée de vie de la fluorescence. La plate-forme PIMPA (plate-forme d'imagerie du petit animal) consistant en un microscope à deux photons avec quatre modalités de détection (imagerie par fluorescence, SHG, spectroscopie et FLIM). Sur la ligne DISCO du synchrotron SOLEIL, de la microscopie à excitation dans l'UV profond possible dans deux configurations : microscopie plein-champ et spectroscopie.

Dans ces conditions de larges campagnes de mesure sur la réponse d'autofluorescence des tissus cérébraux ont put être menées pendant ma thèse, afin de répondre à cinq grandes questions:

Des mesures optiques bimodales quantitatives sous excitation visible pourraient-elles discriminer la nature du tissu cérébral fixé ?

Les mesures spectrales et de durée de vie, sous excitation visible, ont-elles permis de discriminer la nature du tissu cérébral fraîchement extrait ? Les mesures de fluorescence sur tissu fixé aurait-elle pu être suffisante pour constituer une base de données optique?

L'excitation mono et bi-photonique pourrait-elle discriminer l'autofluorescence des grades de ménin-giomes ?

L'imagerie à deux photons pourrait-elle fournir des informations équivalentes au standard H&E pour discriminer les tumeurs cérébrales primaires et secondaires ? La détection quantitative multi-modale pourrait-elle améliorer le diagnostic des tumeurs cérébrales?

Comment une étude optique multi-échelle et multimodale pourrait-elle améliorer la précision et

la fiabilité de la discrimination des tumeurs primaires et secondaires? Ces questions trouveront une réponse dans les études publiées dans cinq articles écrits lors de mon doctorat et présentés dans la suite de ce manuscrit.

Afin de répondre à la première question : Des mesures optiques bimodales quantitatives sous excitation visible pourraient-elles discriminer la nature du tissu cérébral fixé ?, le chapitre 2 présente une étude publiée dans Scientific Reports rapportant comment les coefficients optiques, l'émission d'autofluorescence et les données de durée de vie peuvent mettre en évidence la structure du tissu cérébral. Cette première étude analyse quantitativement la fluorescence endogène en dérivant plusieurs indices optiques, à partir des résultats tirés d'un endoscope à détection bi-modale et excitation dans le visible. Cette étude a été menée sur des coupes de tissus fixés et inclus 28 patients. Les résultats ont montré la capacité de discriminer à partir d'indicateurs optiques les tissus tumoraux des tissus sains. Cependant, pour appliquer ces paramètres optiques en per-opératoire, ils doivent également être confirmés sur du tissu cérébral frais.

Ainsi, le chapitre 3 décrit la caractérisation de tissus cérébraux fraîchement extraits après la chirurgie sur 54 patients. Les tissus ont été analysés par microscopie à un ou deux photons détectant l'autofluorescence avec une détection multimodale (imagerie de durée de vie par fluorescence, de fluorescence à deux photons et de génération de seconde harmoniques (SHG), ainsi que des mesures spectroscopiques). Le but de cette étude également publiée dans Scientific Reports est de répondre à la question : "Les mesures spectrales et de durée de vie, sous excitation visible, permettent-elles de discriminer la nature du tissu cérébral fraîchement extrait? Les mesures de fluorescence établies sur du tissu fixé eut-elle été suffisantes pour constituer une base de données optique?" Ces analyses *in vivo* ont montré la capacité de détection quantitative bimodale sur la fluorescence endogène à discriminer la nature des tissus. Cependant, cette configuration ne présente pas de modalité d'imagerie et donc la possibilité de comparaison avec le standard histologique, la coloration H&E. Pour pouvoir fournir des informations comparables, la modalité d'imagerie doit combiner des informations nucléaires et extracellulaires, la microscopie non linéaire est un excellent candidat car elle produit deux signaux complémentaires : la SHG et la fluorescence par excitation à deux-photons (TPEF). Les images TPEF-SHG ont permis d'identifier les structures typiques du standard histologique, montrant que cette technique optique pourrait être équivalente à la coloration H&E avec le grand avantage d'être plus rapide et d'être exempte de produits chimiques. L'excitation à deux-photons permet aussi de réaliser des mesures quantitatives de spectroscopie et de temps de vie. Ces résultats préliminaires sur une excitation à deux photons ont montré le potentiel de discrimination qualitative et quantitative en ajoutant une troisième dimension spatiale par rapport à la configuration de configuration visible.

Les résultats prometteurs trouvés sur cette petite cohorte de tissus de tumeurs cérébrales ont ouvert la possibilité de les utiliser pour des problèmes neuropathologiques avec une précision comparable à celle de l'analyse histologique. Le chapitre 4 présente une étude publiée dans Journal of Biophotonics afin de répondre à une autre question importante en neurochirurgie, à savoir si les tumeurs de méningiome peuvent être classées selon leur grade utilisant la réponse d'autofluorescence excitée à un ou deux photons. Cette étude portant sur neuf échantillons de méningiome humain a montré le potentiel de la méthode pour différencier le grade de ces tumeurs, une question importante à traiter lors d'une intervention chirurgicale car le grade détermine le pronostic du patient. Les résultats majeurs sont: 1) des images fusionnées de TPEF et de SHG comparables au standard histologique H&E; 2) La réponse spectrale à un et deux photons produisant une intensité plus élevée pour le grade II que pour le grade I; 3) la durée de vie de fluorescence résultant en une valeur plus courte pour le grade II que pour le grade I; et 4) l'intensité de la fluorescence corrélée à un indicateur



de prolifération histologique, Ki-67. Avec cette étude, la microscopie à deux photons a montré son potentiel pour aider à répondre à une question clinique relativement précise. Ces résultats nous rapprochent de l'objectif plus large qui consiste à distinguer toute tumeur cérébrale d'un tissu sain.

L'étape suivante a consisté à concevoir une étude visant à trouver des critères optiques permettant de distinguer les tumeurs primaires et secondaires des tissus sains, en utilisant une configuration au microscope à deux photons et des échantillons de tumeurs fraîchement extraites. Les résultats de cette campagne sont présentés dans le chapitre 5, publié dans Scientific Report. Dans cette étude un système de notation quantitative basé sur une analyse minutieuse des données d'imagerie non linéaires a été développé pour obtenir une discrimination fiable des natures tissulaires. Ce travail a été réalisé sur 25 patients. Pour exploiter au mieux les données de cette étude, trois indicateurs quantitatifs ont été extraits: métabolique (rapport d'oxydoréduction), structurel (intensité du SHG) et conformationnel (mesures de la durée de vie), afin de créer un système de notation en 3D. Dans cette représentation 3D, chaque type de tissu occupait une région spécifique de l'espace, soulignant la possibilité d'une discrimination automatisée utilisant l'analyse de la fluorescence endogène. Les types discriminés ainsi sont les tumeurs primaires des tumeurs secondaires. Cependant, on a également appris à quel point une analyse statistique pouvait être sensible et qu'il existait une grande variabilité d'un type de tissu à l'autre. Ces observations ont conduit à prendre conscience de la nécessité d'aller plus loin dans l'analyse des données et de trouver d'autres molécules pouvant aider à confirmer le diagnostic. Pour obtenir plus de données pour l'analyse, pourquoi ne pas examiner une plage d'excitation plus large, de l'UV profond au proche infrarouge?

C'est cette réflexion qui conduit à l'étude du chapitre 6, publié dans Frontiers. Une étude qui est basée sur une cohorte de patients statistiquement pertinente, présentant un algorithme discriminatif quantitatif basé sur des données d'autofluorescence linéaires et non linéaires allant de l'UV au proche infrarouge, et couvrant un large éventail de fluorophores endogènes.

L'algorithme trouvé ici basé sur des approches multimodales et multi-gammes a permis une discrimination fiable entre les tissus contrôles, les tumeurs primaires et secondaires. Les résultats, notamment ceux basés sur l'algorithme multimodal, présentent un taux de faux négatifs inférieur à 5%, ouvrant la voie à l'automatisation du diagnostic. Ceci est renforcé par le développement d'algorithme non basé sur des notions de fit, tel que le clustering, pouvant être la première étape d'algorithmes de classification automatisés.

Ces résultats ouvre la porte vers un diagnostic effectué par une intelligence artificielle et non par un opérateur humain. Dans les chapitres 2 à 6, une vaste base de données sur l'évaluation des tumeurs primaires et secondaires par rapport à des tissus contrôles a été construite et a abouti au développement d'un algorithme discriminant pouvant être automatisé dans un endomicroscopie. Ces résultats soutiennent le développement d'un endomicroscope à deux photons pour fournir au chirurgien une réponse en temps réel au cours de l'opération. La thèse se termine par une discussion des résultats expérimentaux obtenus, ainsi qu'une ouverture sur l'utilisation des méthodes pour discriminer d'autres types de cancer, comme les tumeurs de la vessie, et la présentation des perspectives du projet, tel que de futures études *in vivo*.

# Acknowledgements

Working on this thesis project has been a real professional and personal journey. I think it has been one of my biggest learning and growing experience in all my academics. Still like every journey, it cannot be achieved alone. And countless people were there to guide, help or just even support me.

The first person I would like to acknowledge and thank is my thesis director, Darine Abi Haidar. From the first day I came to you for my master internship, you took a chance on me, when it was not an evidence. Since then you trusted me and support me to be a PhD student on this project. I had the chance to witness your passion towards science and be inspired by your work ethic and commitment. You lead me to this amazing results after three years, simply thank you. And of course conferences are always better with you.

I would also like to thanks all the person that have been working on this project at the Saint-Anne hospital, giving to me and this project, the possibility to work so close of the clinic. I would to specially thanks professor Devaux and Varlet for their medical input throughout my thesis.

As one very wise person said during my years of PhD : "your are a PhD student, you can still do this". Yes, I could embark on the experience of the night shifts at the synchrotron SOLEIL. This has been the most humbling part of my PhD and one of the most rewarding. All of this was possible, thanks to Frederic Jamme and Matthieu Refregiers. Working with you, open for me a door on another aspect of physics, with different backgrounds and experiences, and gave me the opportunity to learn more.

The success of the project, gave us the opportunity to expand our applications and work on the bladder with Professeur Eva Comp  rat and Dr benjamin Prad  re. Working in collaboration with you has been a very rewarding experience, thank you for all the knowledge your share with me and medical input you brought to this project.

All the work of my thesis will of course not have been possible without team work, and all the amazing people that came along our team through these four years. Marc and Ali who where there at the beginning, through my first steps in the project. Ali, nothing will have been the same without you as a post-doc through my first two years and half, we learned, worked, stressed, screamed and made silly optic tutorial videos together. Hussein, you started with us as an intern and joined me on the ride of the PhD adventure, making it fun to work until the last day, cheering me on, listening to all my craziness and anxiety. And of course learning me how to do hummus (well I still have a long road until making it good like yours). All the interns that came along, and brought their piece and knowledge to this giant puzzle, a very special thanks to the group of them here during my last year, Audrey, Elise, Emile and Elliot, you made all the work easier, better, more challenging and even funnier.

Of course this adventure will not have been the same, if it was not for the atmosphere and

people at the IMNC laboratory. Marjorie for opening my eye to the biological world and helping me with all my samples. Mathilde, who have been my work godmother at the lab and checked on me when needed. All the people having lunch in "salle de vie", for all the stories and moments shared. The 128, my office roomies, from the original cast to the last five musketeer. It was more than an office, like a second home, even without the "pouf" but one day maybe. To my favorite work roommate of all, Carlotta, I would not have survive these last two years without your input, our lunches, the magic of coffee break that you brought into my life, the hugs, you listening to all my crazy moods, the discovery of bouldering and our friendship. I can now say, "Ciao", "che fai ?" and "come va?", certainly the biggest achievement of my PhD.

During these three years, I could balance the craziness of the science, with my sport family. Thank you to all my teammates for always giving me a happy place to escape to. And also to the other people around, my second moms and dads, for being so caring and have support me beyond sport on this PhD ride, until cheering me on at my defense and mading it an amazing day. Thank you to my partner in crime, my rock and the only person that embrace all my crazy ideas, Blandine, none of these last years would have been the same without you. You kept me sane and in the craziest of time you made sure I stayed that way with your checked up calls or always calling crap on my crazy moods.

Also a special thanks to the friends that always have been a constant support and always make life outside the office fun and memorable. My best friends since childhood, Angela, Claire, Sarah and Mathilde. My original sport family, Laura, Marie, Marine, Delphine and Sherley, the best "Ginette" I know. My friends from the other "hard" time of my student life, prep school, Hasna, Justine, Pauline and David.

The last but not least thank you goes to my family, and more espacially my parents. Mom and Dad, you always have supported me in all my choices and made it so much easier to arrive there, all these achievements are as much mine than yours. Thank you so much for being these amazing parents.

# Chapter 1

## Introduction

In 2011, the French Ministry of Health and The National Institute of Cancer (INCa) did a study on the perception of cancer in the French society. The image stuck in people's heads was strongly negative. Most people considered it as the most deadly disease, far ahead of AIDS. However the study also showed that even if one in two men and one in three women have cancer some time in their lives, the survival rate in reality is higher than 50% [1].

Nevertheless this disease still frightens society because some of its forms are strongly and rapidly deadly resulting in major ongoing medical challenges. Using only current medical resources to unlock all the mysteries surrounding cancer doesn't seem enough. Medical research turns to other domain of science such as chemistry and physics to perform interdisciplinary research in order to improve diagnosis and treatment in the remaining deadly forms of cancer. It is in the context of this fast growing field of interdisciplinary research, that the work of my thesis takes place. I have conducted my research for the last three years, in the French IMNC laboratory (Imaging and Modelisation in Neurobiology and Cancer) in Darine Abi Haidar's group. This research team has been working with a French hospital (Le Centre Hospitalier Saint-Anne, Paris, France) to answer the problem of how to improve surgical accuracy during tumor resection to extend patient life expectancy. To answer that question the team started, in collaboration with the Saint-Anne Hospital (Paris, France), a project to develop a revolutionary new tool to address several modern scientific challenges by bringing nonlinear endomicroscopy to the surgical operating room. A database on tissue optical response was also built and used with the endomicroscope in order to guide the surgeon during resection of tumor and to achieve the best possible results.

I will orient this thesis around the scientific articles that have been produced during the three years of my project. The manuscript will be constructed as follows: there will be a long introduction putting my work in context. Then the different questions and answers arising during this thesis will be illustrated in the scientific articles. Finally I will discuss the results obtained and show the future directions and perspectives of the project. In this introduction I will first explain the terminology and biology of cancer with a focus on brain tumor. Secondly, the state of the art on the current methods of diagnosis and treatments of brain tumors will be presented. Thirdly, I will show the direction that the field of optical research is taking to help surgeons tackle the issue of cellular contrast during surgery. Finally I will show how my project takes place in this environment and what I was able to bring to the field.

## 1.1 Central nervous system cancer

### 1.1.1 Preamble

Cancer is a disease, that was first described in the ancient times by the Greek Hippocrates. He compared the tumors to a crab, to give it the first names of "karkinos" and "karkinoma" (meaning crabs) [2]. For a long time, cancer has been an incurable disease. Nowadays, however, one patient in two survives cancer. This has been possible thanks to strong advances in prevention and diagnosis in the last century [1]. Yet the word cancer still retains a powerful symbolic charge, associated with particularly dark imagery. Even though undeniable progress has been made in management, reducing the risk of death, and consequently demystifying the disease. Our lifestyle maintains cancer as a recurrent disease, and some forms of it remain highly deadly [3].

Cancer shouldn't be a singular noun because it refers to a very varied panel of diseases that concur only in their way of emerging. Cancer is used as a generic name to regroup a large number of diseases in any part of the body, defined by the fast reproduction of abnormal cells that can migrate and spread to other organs [4]. It is initiated by a lesion in the DNA that results in a transformed cell able to indefinitely divide itself and avoid programmed cellular death [5]. This process creates a mass of cancerous cells in the organ of origin called a malignant tumor or a malignant neoplasm. Non-malignant or benign tumors (or neoplasms) can exist and are not as dangerous as cancer (figure 1.1). At some point in their growth cancerous cells can develop the capacity to migrate to other organs through blood or lymphatic vessels, and there to redevelop secondary tumoral masses called metastases [5].

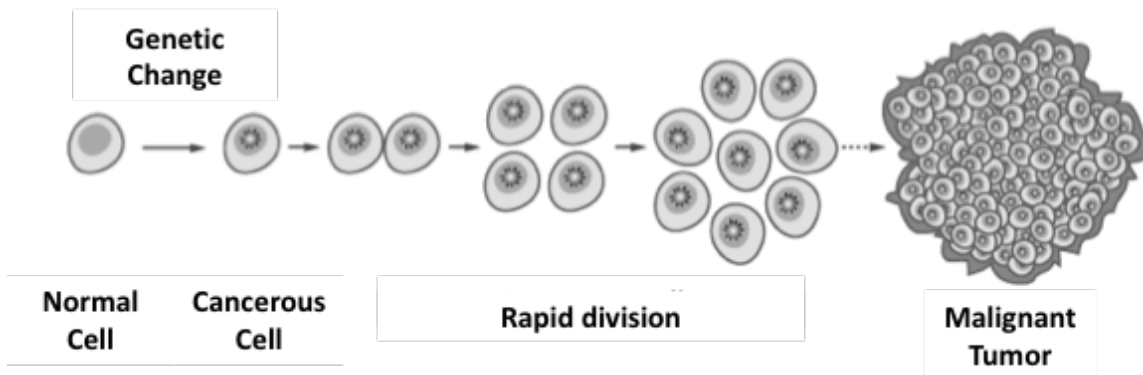


Figure 1.1 – From the cancerous cell to a malignant tumor [6].

The mortality following a cancer depends on the types (organ of origin) and the population group (children, young adults, adults, elderly). It is the second leading cause of death in the world, with 8.8 million deaths in 2015, and the number of new cases is set to rise by about 70% in the next twenty years [7].

In this work, the focus will be on a specific group of cancers, issuing from the brain and central nervous system (CNS). Looking at the statistics on the whole population, brain and CNS cancers are 17<sup>th</sup> in terms of new cases expected in 2018 and 10th in the number of expected deaths [8]. However, in certain age groups, it is one of the most common and deadly forms of cancer. A study

## CHAPTER 1. INTRODUCTION

in 2016 showed that it was the first and most common in cancer-related deaths in the 0 to 14 age category and the third in the 15-39 age group [8, 9].

As these statistics show, diagnosis and treatment of brain and CNS cancer are a hot topic in the world of oncology, with the constant research to improve patients long-term survival rate. To better understand these tumors and the challenges related to them, it is important to know the different types of malignant ones that can arise from brain cells and how they are classified.

Classification of tumors is based on their origin and aggressiveness. Inside the brain two main groups can be found : primary and secondary tumors. A primary tumor takes its origin from brain cells and tissues and usually does not spread to other organs. This kind of tumor can be benign, so it can grow slowly with distinct boundary and can be dangerous only if it compresses any vital functions, or malignant, so it grows quickly with irregular boundaries and with the capacity to infiltrate surrounding areas [10]. The primary tumors can be divided in subgroups according to the types of cells and tissues from which they originate. About half of all primary brain tumors grow from glial cells and are classified as glioma, with a grade from I to IV depending on aggressiveness [10]. They can also arise from nerves (Schwannoma tumors), pituitary gland (Pituitary adenomas), cerebellum (medulloblastoma tumors, the most common in children), germ cells and from the membranes that surround the brain, which result in meningioma tumors [10, 11]. Secondary tumors, called metastasis, come from cells that have migrated from a primary tumor in another organ - lung, breast, skin, renal and colon are the most common origins of metastasis [10]. Subgroups in secondary tumors metastasis are classified by their organ of origin [11]. In this work glioma (mainly grade IV glioblastoma), meningioma and metastasis have been studied; their different location are show in figure 1.2 shows the different locations. Each of them will be detailed in the following sections.

### 1.1.2 Gliomas

Gliomas are the most common intra-axial primary tumor. These tumors, affecting glial cells, consist of a central mass surrounded with single invasive cells decreasing in number toward the periphery of the main lesion. The diffuse nature of these tumors were discovered when the standard surgical procedure of resection failed to eradicate them [12].

They are classified according their aggressiveness from grade I to IV by the World Health Organization (WHO). Grade I gliomas are usually astrocytomas occurring in young people. The most common grade II gliomas consist of diffuse astrocytoma and oligodendrogliomas. Diffuse astrocytomas, mostly arise in young adults and are slow-growing, infiltrating neoplasms. This tumor always infiltrates the brain parenchyma, making complete surgical removal practically impossible. Diffuse gliomas transform most of the time into grade III or IV tumors. The timing of the transformation into such an aggressive tumor will define the patient outcome [13]. Oligodendrogliomas are infiltrated glial neuroplasms commonly arising from the frontal lobe. They represent 6% of glial tumors [14]. The architecture of oligodendroglial tumors is a highly cellular lesion with closely packed, relatively small cells, that often infiltrate far away from the central lesion with prominent secondary structure formation [15]. Grade III gliomas consist of anaplastic astrocytomas and anaplastic oligodendrogliomas. This higher grade of astrocytoma or oligodendroglioma present atypical features and increased mitotic activity. One quarter are new tumors and three quarters are the consequence of lower grade tumor transforming into higher grade [16]. Grade IV gliomas are glioblastomas (GBM). GBM represents 82% of malignant gliomas. These tumors are highly aggressive and are

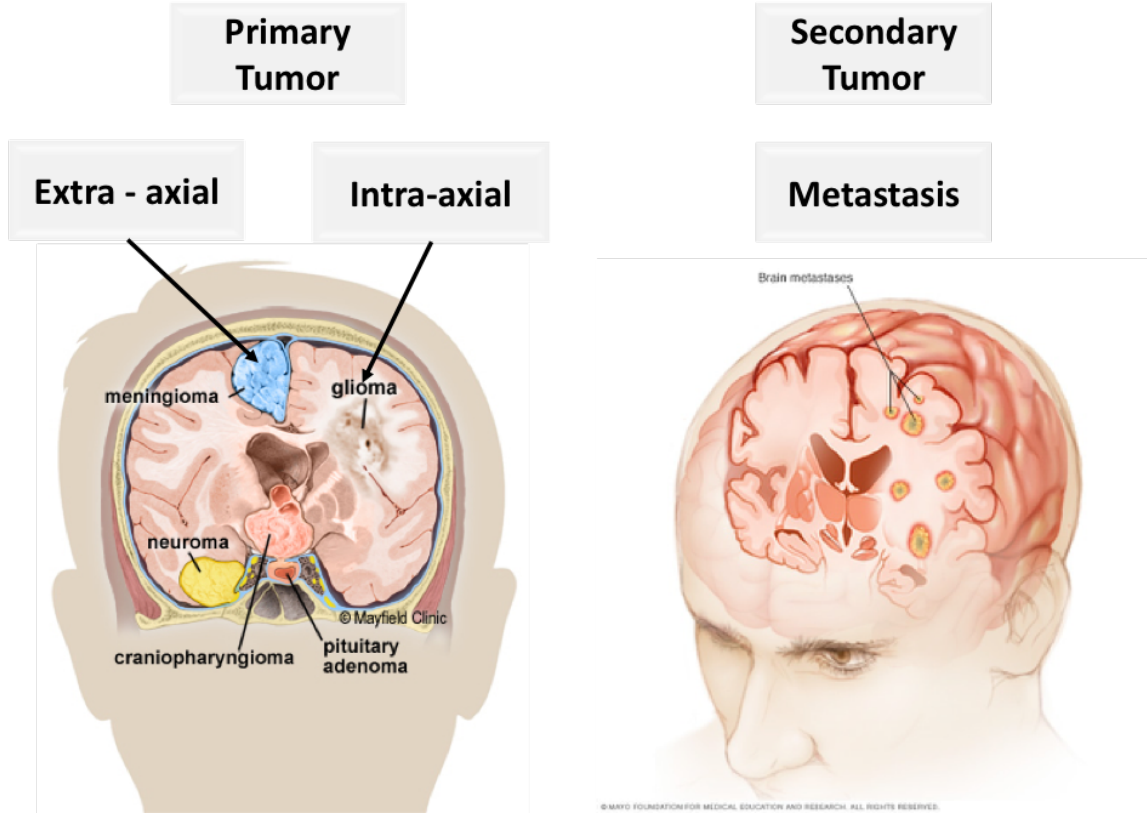


Figure 1.2 – The different types of brain tumor that were studied in this work [10, 11]

characterized by architectural features such as high cellularity and mitotic activity, vascular proliferation, and necrosis. These tumors are highly invasive, infiltrating the brain parenchyma. However, they do not metastasize [17]. Recurrence is almost inevitable with glioblastoma, arising within two centimeters of the original tumor site. About 10 percent are accompanied by additional non-contiguous lesions [18]. In the last twenty-five years, multiple modalities of treatment have been tried experimentally and are now standardized for this type of tumor. The treatments are cytoreductive surgery, radiation therapy, and chemotherapy [19, 20].

### 1.1.3 Meningioma

Meningiomas are the most common extra-axial tumor. Meningiomas are tumors affecting meninges, arising from arachnoid cells with a progressive enlargement compressing adjacent structures and leading to clinical symptoms (epileptic seizures, neurological deficits, increased intracranial pressure). These tumors are classified in three grades by the WHO, from Grade I to the most malignant Grade III which has a five-year survival rate of 44% [21]. The main treatment for these tumors is surgical resection which can cure or allow long-term control of the cancer. The capacity

## CHAPTER 1. INTRODUCTION

of completing a total resection on meningioma depends on the extent, and the localization of tumor infiltration in the dura, bone and vascular sinuses. Residual left in any of these adjacent compartments lead to high risks of tumor recurrence even for benign meningiomas [22].

### 1.1.4 Metastasis

Secondary tumors are the most predominant. For example in the US, two hundred thousand cases of brain metastases occur each year, which is 10 times higher than the number of patients diagnosed with primary brain tumors [23]. Brain metastasis results in high morbidity and poor prognosis, even after diagnosis and the classical choice of treatment: surgical resection, radiotherapy (stereotactic radio-surgery or whole brain radiotherapy), chemotherapy and immunotherapy. Metastases are formed through the following mechanisms: cells dissociate from the bulk tumor to invade neighboring tissue, then will invade new or pre-existing blood vessels, traveling through vessels to other parts of the body and then extravating from the vessels to invade tissues growing into micro-metastases and macro-metastases, namely secondary tumors [24]. The pattern in which the metastases migrate into the brain can be very dependent on the origin of the primary tumor (lung cancer, melanoma). To achieve invasion of the brain they degrade the extra-cellular matrix [23, 25].

## 1.2 How to diagnose brain tumor

### 1.2.1 Imaging techniques

The first step toward any medical treatment solution is to detect and diagnose the disease. In the case of brain tumor the symptoms that will draw the patient to the doctor office are headaches that worsen in the morning, seizures, stumbling, dizziness, speech problems, weakness on a body side, nausea and vomiting [11, 26]. The doctor will first obtain the patient's personal and family medical history and perform a complete physical and neurological exam (memory, cranial nerve function, muscle strength, coordination, reflexes, and response to pain). He can also order more tumor specific test if he suspects a type of tumor with the described symptoms, such as audiometry (detects hearing loss due to tumors near the cochlear nerve), endocrine evaluation (detect abnormal levels caused by pituitary tumors) or lumbar puncture (examine cerebrospinal fluid for tumor cells, proteins, infection, and blood). From the results of all these primary exams if a brain tumor is suspected, the next step toward a definite diagnosis is the use of imaging techniques [26].

An imaging diagnosis can confirm the absence of tumor, but in the case of a detected mass it will only be the first step to a final diagnosis. A confirmed diagnosis will be given after tissue sampling and histological analysis. Still with the imaging techniques available nowadays you can collect much information on the tumors, and start planning the course of action to treat it. Imaging in the last few decades has accelerated and improved the capacity to detect many diseases. It has become in many cases the preferred first step on the road to diagnosis and treatment, due to its greatest advantage - non-invasiveness [27–29]. Table 1.1 resumes the different techniques used nowadays. All these imaging techniques are not competing with each other but work together in a common aim. If a brain tumor is suspected, to perform a high level preliminary diagnosis a combination of imaging techniques will be prescribed. To assess the presence or not of tumor, Computed Axial Tomography



## 1.2. HOW TO DIAGNOSE BRAIN TUMOR

Scan (CT-Scan) and Magnetic Resonance Imaging (MRI) are prescribed. Then if the oncologist and surgeons need more precise and functional information to start planning the treatment course of action, they will ask for more functional imaging (advanced magnetic resonance, functional MRI (fMRI) and Positron Emission Tomography (PET)).

### 1.2.1.1 CT-scan

CT-scan is a computerized x-ray that can show a combination of soft tissue, bone, and blood vessels. It was invented in 1972 by British engineer Godfrey Hounsfield and South Africa-born physicist Allan Cormack [38]. CT-scan was first designed only to image the head and explore the brain. The first CT-scan scans were very slow, and the patient had to be completely still for a long time. An acquisition could take hours. However the possibility of getting a 3D morphological representation of any body part spurred fast development of the technology [39]. CT-scan technology has made great improvements in speed, patient comfort, and resolution. Faster scanning helps to eliminate artifacts from patient motion such as breathing or peristalsis. Nowadays multi-slice CT-scan systems can collect up to 4 slices of data in about 350ms and reconstruct a 512 x 512-matrix image from millions of data points in less than a second, making the CT-scan scan the most widely available technology, and the first exam prescribed if an intra-cranial mass lesion is suspected [40]. It gives an initial work-up before using other technologies such as MRI. CT-scan is the gold standard to diagnose the presence of acute intracranial hemorrhage, calcifications, and osseous anatomy. However CT-scan still has limitations compared to MRI. It suffers from a lower contrast capability on soft tissue, fossa and spine regions, and the use of ionizing radiation. These limitations make the MRI the real gold standard for pre-surgical planning, post-operative assessment, pre-radiotherapy planning, and post-treatment assessment. Consequently MRI is the second imaging always prescribed along with the CT-scan of a suspicion of brain tumor [41].

### 1.2.1.2 MRI

MRI is the other major breakthrough of the last century in medical imaging. The fundamental principle was discovered in 1946 by Felix Bloch and Edward Purcell, who were awarded the Nobel Prize in 1952. Up until the 1970s MRI was being used for chemical and physical analysis. The first image on tissue was performed in 1971 by Raymond Damadian, who showed that nuclear magnetic relaxation times of tissues and tumors were different, motivating scientists to use MRI to study disease [42]. From that point on, MRI has experienced fast development for implementation in hospitals worldwide, becoming a standard in diagnosis. As with CT-scan, the MRI was first developed for neurology. It accelerated the knowledge of brain anatomy and the nervous system, becoming the standard to give images of the central nervous system. It could distinguish white matter, gray matter and cerebrospinal fluid.

MRI's multi-planar capability, superior contrast resolution, and flexible protocols have allowed it to play an important role in assessing tumor location and extent. It provides good soft tissue contrast, producing different types of contrast by varying excitation and repetition times. MRI has the capacity to give different contrasts in the image with the use of different acquisition protocols. Each of the protocols provide different and complementary information, contributing to the power of contrast in the technology. The most common protocols are : spin-echo T1-weighted image (T1WI), proton density-weighted image (PDWI), T2- weighted image (T2WI), and T1WI after the administration of paramagnetic agent. Tumors appears hypointense on T1WI and hyperintense on T2WI, and can show intermediate hyperintensity on PDWI. Contrast can be facilitated by contrast

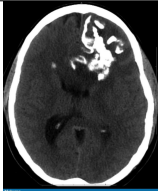
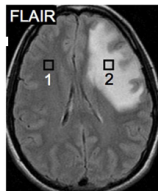
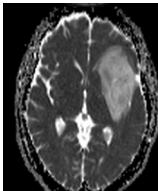
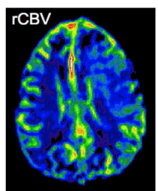
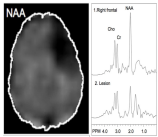
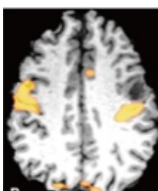
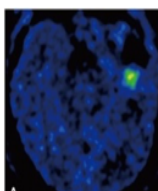
Technique	Image	Highlights	Limitations	Spatial Resolution
CT		Mass effect, herniation, hydrocephalus, hemorrhage, calcifications	Low contrast capability on soft tissue, fossa and spine regions use of ionizing radiation	0,5 to 1,5 mm [30]
MRI		Localizing the tumor and surrounding structures with a high-resolution image, diagnosis of extra- and intra-axial tumors	Difficult to differentiate brain neoplasms from non-neoplastic mass lesion lack of functional information	1 to 3 mm [30]
MR diffusion		Reduced in highly cellular portions of tumor. Establishing spatial relationships between tumor border and white matter	Problem can arise with the simplification in tensor calculation. Long scanning time so a system sensitive to physical motion.	0,8 to 1,2 mm [31]
MR perfusion		Tumor/tissue vascularity	User dependent on : the account for contrast leakage effects, define a region of interest, quantify the resulting parametric information	around 1 mm [32]
MR spectroscopy		Obtaining biochemical and metabolic information about the tumor, determining tumor type and grade by assessing the cellular contents	highly operator dependent, choose interest region avoiding areas of necrosis, hemorrhage, calcification and/or tumoral cysts	0,6cm <sup>3</sup> per voxel [33]
fMRI		Pre-operative functional mapping, research into treatment effects	phenomenon of neurovascular uncoupling : cortex adjacent to the tumor can show a false variation	2 to 4 mm [30]
PET		Metabolic assessment of Tumor aggressiveness. Shows highly metabolic area in tumor	Exposure to radioactive rays 10 to 20 min acquisition time : sensitive to patient movements	2 to 5 mm [30]

Table 1.1 – Different imaging techniques to diagnose brain tumors[34–37]

## 1.2. HOW TO DIAGNOSE BRAIN TUMOR

agents. The most commonly used in MRI for brain tumor is gadolinium (Gd). In brain tumors with the possible disruption of the blood-brain barrier, Gd can accumulate in the extracellular space of the tumor specific to it. This effect results in an enhanced contrast of the tumor in T1W1 compared to the surrounding normal brain tissue [19, 43].

MRI with or without contrast agents gives anatomical information on brain tissue. However it is still difficult based only on this imaging technique to always differentiate brain neoplasms from non-neoplastic lesions, or to easily distinguish low grade from high grade tumors. Indeed this assessment is based on the contrast intensity. However higher grade does not always induce contrast enhancement [34, 41]. To have a more complete initial work-up on the tumor, new more advanced MRI techniques have been developed to give physiological information (metabolic and molecular state of brain tissue) as well.

### 1.2.1.3 MR diffusion

Two diffusion imaging techniques can be derived from magnetic resonance imaging. These are the MR diffusion-weighted imaging (DWI) and diffusion tensor imaging (DTI). DWI is sensitive to water molecule motion in tissues, and from it the apparent diffusion coefficient (ADC) can be calculated. The ADC maps can show relatively low values in certain brain tumors, and mostly in high cellular tumors such as CNS lymphoma, and high grade glioma. DTI images water diffusion with more directional information than DWI. It generates maps of the fractional anisotropy and the mean diffusivity. This technique has been shown to differentiate between high grade and low grade glioma, and distinguish glioblastoma from metastases. Tumors margins can also be detected with more precision than in conventional MRI [34, 41]. These methods present certain limitations. The map obtained in DTI imaging comes from tensor calculations, in which simplifications are done along the way that could overlook some macroscopic effects and adjust them to microscopic features. Moreover this method presents long acquisition time making it hard to suppress the physical movement of brain while imaging [44].

### 1.2.1.4 MR perfusion

MR perfusion is a technique that give complementary information about the blood flow in brain tumors and the surrounding tissue. Two approaches have been developed, with and without the use of an exogeneous contrast agent. The method consist of either intravenously injecting a contrast agent and monitoring the loss of signal during its propagation through tissue, or taking direct advantage of the magnetically labeled blood itself as an endogenous tracer to quantify cerebral blood flow [45]. Brain tumors have the characteristic of showing neoangiogenesis (greater density of vessels per volume unit) which will affect these parameters. The disadvantages of this techniques are some highly user-dependent steps in the process: the accounting for contrast leakage, the definition of a region of interest, and the method of quantifying the resulting parametric information [34, 41].

### 1.2.1.5 MR spectroscopy

MR spectroscopy is an advanced MR based technique that relies on the phenomena of chemical shift and spin-spin coupling. This technique highlights certain metabolites in the volume of interest. The main metabolites that give information in brain tumors are N-acetylaspartate (marks neuronal integrity), choline (marks cellular membrane turnover), creatine (marks bioenergy storage), and also lipids and lactate (marks necrosis and hypoxia). These indicators will change in the presence of

## CHAPTER 1. INTRODUCTION

malignant brain tumor, where, for example an increase of choline and a decrease of N-acetylaspartate can be observed. The drawbacks of the technique are high operator dependence and the need to avoid necrosis, hemorrhage, or calcification areas while choosing the region of interest for the measurement [34, 41].

### 1.2.1.6 fMRI

fMRI uses the relative changes in blood oxygen level dependence to translate brain activity. It is based on the principle that neuronal activation within grey matter utilizes oxygen supplied in the form of oxygenated blood to a greater degree than areas of grey matter at rest or in a state of inhibition. In diagnosis of brain tumor it is used to pre-operatively map the brain area responsible for locomotion and language nearby the lesion [34, 41]. One drawback to be attentive to is the phenomenon of neurovascular uncoupling. In normal brain the regulation of cerebral blood flow is an interaction between neurons, glia and vascular cells. fMRI measurements are based on the fact that this interaction is still viable in presence of tumor. However some tumors can lack this interaction, phenomenon of neurovascular uncoupling, resulting in regions of cortex adjacent to the tumor that can show a false variation in fMRI parameters [46, 47].

### 1.2.1.7 PET

The standard for functional information is PET which uses a radioactive substance to quantify the metabolic activity of cells. A small amount of radioactive tracer is injected into a peripheral vein and the emitted radioactivity is detected. Tracers are labelled commonly with isotopes such as oxygen-15, fluorine-18, carbon-11, or nitrogen-13. The radiolabel 18-fluorodeoxyglucose (FDG) accumulates on glucose analogue allowing the measurement of the glucose consumption rate. Malignant tumors metabolize glucose at a faster rate than benign tumors, making the technology of use in the clinical discrimination of tumoral tissue by tracing their metabolic activity. A scan usually takes from 10-40 minutes [48].

The technology behind a PET is far from new and was actually discovered before CT-scan and MRI in 1950s. However, for a long time it stayed as a strictly research tool and only emerged as a clinical tool in the 1990s-2000s. The reason is that PET requires the use of a tracer, and the road to finding one both suitable for the target clinical application, and then approved by the hospital's committee was long. PET was able to take off when the tracer FDG was approved for its use in oncology. PET has since been combined with the other technologies of CT-scan and MRI, giving complementary information in an attempt to improve the power of discrimination of imaging techniques. However it remains a very new and hybrid technology that has to prove the real extent of its potential. A pitfall of PET scan is the relatively long acquisition time 10 to 20 minutes acquisition for a whole brain, making it very sensitive to patient movements or intracranial movements that will blur the resulting image [49].

CT-scan is a cheap, fast and good technique, so it is the first to be prescribed in the course of diagnosis. However contrast on MRI gives higher resolution and is more suited to evaluate brain tumors. It is the gold standard for this reason and has to be included in the initial workup. The goal of this initial assessment is to identify the lesions in order to determine if surgery can be avoided. Classical MRI giving only anatomical information can be insufficient to distinguish neoplastic from non-neoplastic tumor, and low grade from high grade. It is in these cases that advanced MRI

## 1.2. HOW TO DIAGNOSE BRAIN TUMOR

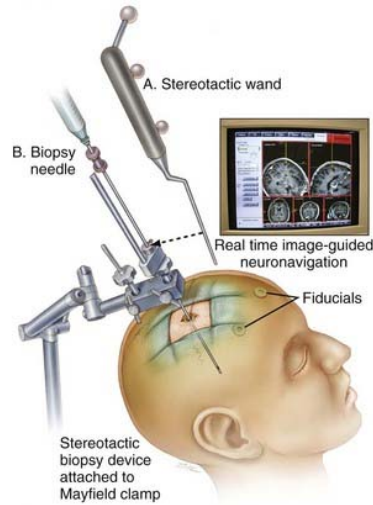


Figure 1.3 – Frameless stereotactic biopsy system that relies on neuronavigation systems for lesion targeting [52].

(diffusion, perfusion, spectroscopy and functional) can be done to get more information, identify the type of lesion, and make a more suitable decision on the next course of action. If surgery is chosen, fMRI will often be used to map the highly functional area surrounding the tumor.

### 1.2.2 Biopsy

Even though all of these techniques have witnessed growing developments in the last few decades allowing the detection of tumors at earlier stages, none of them are able to give a conclusive and high reliable diagnosis on the degree of malignancy and on the precise type of tumor in glial subgroups. The result is a continuing need for tissue samples for histopathological analysis [50]. This last step in diagnosis of brain tumor is called a biopsy, and remains the gold standard for assessment of tumor presence and malignancy. It consists of the surgical extraction of tissue samples to perform in depth *ex vivo* analysis by an experienced neuropathologist. The traditional biopsy method has been through a craniotomy, open skull surgery, but this procedure appeared in some cases to not be required or indicated, leading to the development of less invasive methods such as the stereotactic biopsy (SB). Stereotactic neurosurgery appeared in 1908, and involves a physical 3D-frame first developed by Horsley and Clarke. The goal is to perform a minimally invasive procedure using an electrode guide based on the 3D cartesian coordinate system [51].

It was first used in intracranial targeting for psychiatric and functional disorders, and saw reduced use through the end of 1960s. The development of CT-scan and advanced imaging techniques revived stereotactic neurosurgery with numerous new applications. This breakthrough was made possible with the publication, in 1979 by Russell A. Brown, of a new device called the N-localizer that enables the guidance of stereotactic surgery with imaging obtained on other devices, such as CT-scan, MRI or PET. The device is built with rods that form a capital "N" shape to relate the spatial information of a tomographic scan to spatial information in the physical world [53]. Stereotactic surgery is now widely used for delivery of radiation, surgical targeting of electrodes, and

## CHAPTER 1. INTRODUCTION

resection to treat tumors, epilepsy, vascular malformations, and pain syndromes [51]. Classical SB without assistance had a rate of conclusive diagnosis up to 68% to 98%. It is presented as a safe, efficient and valuable procedure, but it still can have fatal complications, with a morbidity rate up to 0,9 to 15%, and a mortality rate of 0 to 4.2% [54]. To improve SB, the imaging technologies previously described were used pre-biopsy to build a map to guide the procedure. Moreover the classical frame has been abandoned in most cases for scalp fiducials, which provide a physically less crowded system of external markers (fiducials) used to create reference points for surgery. This current method is referred to as a frameless stereotactic neuro-navigation system and is presented in figure 1.3. The protocol for the frameless neuronavigated biopsy is the following : 1) Head secured and fiducials are registered into the computerized navigation system. 2) A small incision is marked out and an opening in the skull (the size of a quarter) is made and the dura is opened. 3) A stereotactic biopsy needle, with a diameter around 2mm [55], is introduced into the target guided by the neuronavigation system to obtain biopsy samples [56]. Multi-planar neuro-navigated SB has given a 98-99% of conclusive diagnosis, a 0.7-0.9% of hemorrhage related morbidity, and no mortality [54, 57].

### 1.2.3 Histology

Once the sample has been extracted using one of these techniques, it needs to go through different processes (histopathological analysis) to obtain a definite diagnosis by an experienced neuropathologist.

#### 1.2.3.1 Classical process

The most widespread process is to first perform a chemical fixation of the tissue, in order to preserve tissue from degradation, and to maintain the structure of the cell and of the sub-cellular components such as cell organelles (nucleus, endoplasmic reticulum, mitochondria). The most common fixative is formalin (10% neutral buffered formaldehyde in water). Then to highlight the tissue structure, a stain is applied with one or more pigments. The table 1.2 summarizes the available stains and their purpose.

The most commonly used stain is still the combination of hematoxylin with eosin (H&E staining). It was introduced more than a century ago, and has remained the standard stain for histologic examination of human tissues [59]. H&E is commonly used mainly because it is an inexpensive dye working well with a large number of fixatives and highlighting a large panel of cytoplasmic, nuclear, and extracellular matrix structures [60, 61]. The hematoxylin will stain the nuclei in blue and the eosin will stain the cytoplasm and extracellular connective tissue matrix in different shades of pink. Once stained, histological slices are examined under a microscope [58]. The histological method of diagnosis has to be done *ex vivo* and in a neuropathology laboratory. In this procedure the most time consuming step is the chemical fixation which requires between 16 to 24 hours and more when special fixatives are used. Once the analysis is complete the medically trained specialist, a neuropathologist, formulates a pathology report. This report, usually produced several days after excision of biopsy, is the basis for assessing tumor nature and is required to choose the treatment protocol [62]. The other major limitation is the indirect diagnosis, when it is used to locate the region that should be later resected, the brain shift can be different once the surgeon opens the skull again and the coordinates of regions to resect are not exactly the same anymore.

## 1.2. HOW TO DIAGNOSE BRAIN TUMOR

Stains	Common use	Highlight structures
Haematoxylin	General staining when paired with eosin	Nucleus, Cytoplasm, nucleic acids and endoplasmic reticulum
Eosin	General staining when paired with haematoxylin	Cytoplasm, red blood cells, collagen fibers, elastic fibers and reticular fibers
Toluidine blue	General staining	Classical features and mast cells granules
Masson's trichrome stain	Connective tissue	Classical features and cartilage and muscle fibers
Mallory's trichrome stain	Connective tissue	Classical features and Keratin, Cartilage, Bone matrix and Muscle fibers
Weigert's elastic stain	Elastic fibers	Nucleus and elastic fibers
Heidenhain's AZAN trichrome stain	Distinguishing cells from extracellular components	Classical fibers and muscle fibers, cartilage, bone matrix
Silver stain	Reticular fibers, nerve fibers, fungi and reticular	reticular fibers and nerve fibers
Wright's stain	Blood cells	Classical features and neutrophil granules, eosinophil granules, basophil granules, platelet granules
Orcein stain	Elastic fibers	Nucleus, red blood cells, elastic fibers and smooth muscle
Periodic acid-Schiff stain	Basement membrane, localizing carbohydrates	Nucleus, collagen fiber, and glycogen and other carbohydrates

Table 1.2 – The most common stain in histology [58].

## CHAPTER 1. INTRODUCTION

### 1.2.3.2 Peri-operative process

The classical lengthy process far from operating room reality has spurred the development of peri-operative assessments with shorter processing time. Two techniques can be identified: the frozen section and the cytologic smear. As shown previously the factor limiting intra-operative assessment in the classical procedure is the long fixative process. In frozen section protocol, extracted tissues are immersed in liquid nitrogen ( $N_2$ ) and isopentane on dry ice, resulting in a fixative state that can be then sliced using a cryostat and stained. This method of fixation is much faster, from 10 minutes to an hour maximum and requires less equipment, making it possible to use during surgical procedure to help determine the next step in surgery, such as perioperative determination margin resection clearness [62].

In cytologic smear preparation, developed to give intraoperative neuropathologic diagnosis, the extracted piece of tissue is placed between two slides and gently squashed to obtain a thin smear. Then it goes through fixation by being immersed for five minutes in 95% ethylalcohol and is stained with papanicolaou for a few minutes processing, and can also have hematoxylin and eosin staining [63–65]. Compared to frozen section, cytology smear preparation requires less tissue leaving more for the definitive *ex vivo* diagnosis. It also avoids freezing artifacts, is simpler and quicker, around 10 minutes overall, and gives higher details in nuclear, cytoplasmic and fibrillary processes features. Nowadays, the two techniques are used together to improved diagnosis. It agrees with the final, gold standard histological analysis in 95% of CNS cases [64].

### 1.2.3.3 Limitations of peri-operative process

Even if these techniques have been shown to be faster than the classical paraffin-embed sampling, they still do not offer real-time diagnosis. The turnaround time is around 20 minutes for frozen section [66] and 10 minutes for squash smear [67]. The frozen section technique is also a costly technique. It requires access to a frozen environment (cryostat, liquid nitrogen,...) and a pathologist available to perform evaluation at the same time as the surgery [68]. Moreover DiNardo et al. have shown that the accuracy drastically drops in the case of positive margins. The accuracy was of 71.3% in the evaluation of close or positive final margins compared to a 98.3% on solid tumor. This lack of accuracy compared to the cost of technique is evaluated with a cost-benefit ratio of 20:1 [69]. The smear preparation was preferred in CNS lesions not only to reduce the cost and to avoid frozen artifacts but also to enhance cellular morphology. However the technique has a lower accuracy than with frozen section [70], failing primarily in assessing glial tumor grading due to inadequate sampling and lack of histological features [65]. Moreover heterogeneity inside a tumor can result in a low malignancy assessment within overall very aggressive tumors. This error is due to biopsy being performed on a fraction of a tumor [65]. These peri-operative assessments will be sufficient in biopsy surgical procedures where the intra-operative consultation only aims to show the presence of "lesioned tissue". However, for tumor grading and histological typing of the tumor during resection surgery, where specific diagnosis is required, these techniques will lack the needed accuracy [64]. So challenges still remain for improving intra-operative diagnosis. Moreover, even if faster, these neuropathological techniques still require tissue extraction and staining with external agents, introducing a bias versus the *in vivo* tissue condition and fail to provide real-time analysis for the surgeon during resection surgery.



## 1.3. HOW TO TREAT BRAIN TUMOR

<i>Tumor</i>	<i>Treatment</i>
Astrocytoma, anaplastic	Surgery and radiation
Astrocytoma, high grade	Surgery and radiation, optional chemotherapy
Astrocytoma, noninfiltrating	Surgery, optional radiation
Brain stem glioma	Radiation
Craniopharyngioma	Surgery, optional radiation
Ependymoma	Surgery, optional radiation
Ependymoma, anaplastic	Surgery and radiation
Glioblastoma multiforme	Surgery, radiation, and chemotherapy
Medulloblastoma	Surgery, optional radiation
Meningioma	Surgery, optional radiation
Meningioma, malignant	Surgery and radiation
Mixed glioma	Surgery and radiation, optional chemotherapy
Oligodendroglioma	Surgery, optional radiation
Oligodendroglioma, anaplastic	Surgery and radiation, optional chemotherapy
Pineal parenchymal tumor	Surgery and radiation, optional chemotherapy
Primary CNS lymphoma	Radiation and chemotherapy

Figure 1.4 – The treatment of choice for each type of brain tumors [28].

## 1.3 How to treat brain tumor

### 1.3.0.1 General treatment choice

Now that images and pathology reports are available, a team consisting of an oncologist, a radiation oncologist, and a neurosurgeon can together make the plan of action for the treatment. Treatment decisions are individualized and based on tumor type, location, malignancy, and the patient (age, physical condition). Classical ways to treat brain tumors include surgery, radiotherapy and chemotherapy. Sometimes just one type of treatment can be required but most of the time a combination of it is needed. Clinical trials would also be proposed as an option for some high-grade tumors [26, 28]. Figure 1.4 shows the classical combination of treatments depending on the tumors type.

### 1.3.1 First choice of treatment for brain tumors

In order to surgically remove a brain tumor, the surgeon performs a craniotomy, an operation where he makes an opening in the skull. If the complete removal is not possible without sustaining brain damage, he will remove as much as possible to help relieve symptoms. Three procedures have flourished in the last few decades: maximum extent resection, electro-stimulated surgery, and awake surgery.

#### 1.3.1.1 Maximum extent of resection

A theoretical principle of neurosurgical oncology is that a maximum resection will reduce mass effect and tumor burden resulting in improved diagnosis and prolonged survival. However some brain tumors such as high-grade glioma are very infiltrative and their removal can be challenging. The recent preferred approach is to perform maximal surgical resection, but these tumors can be

## CHAPTER 1. INTRODUCTION

located in highly functional area (language, motor, memory, ...) and resection of these regions have to be avoided at all cost to preserve a certain quality of life for the patient. The principle of brain tumor resection consequently become to achieve a maximal resection while monitoring the oncological-functional balance to preserve brain functional area. Such surgeries are based on the evaluation of tumor margins with previous biopsies and imaging analysis, combined with mapping of surrounding functional areas using advanced MRI techniques. So far the best pre-operative combination of functional imaging to a successful maximal resection surgery, is fMRI and DTI imaging, showing increase survival and better motor function post-surgery [71].

One of the major drawbacks of basing the surgical plan on pre-operative analysis is the phenomena of brain shift during craniotomy. The human brain is plastic by nature, and can be very flexible and easily deform once an open surgery is started. This phenomenon, called "brain shift", has been documented in the last years [72]. Different factors happening during a surgery can play a role in this shift, such as the mechanical action of resection, gravity, evacuation and drainage of fluid, cystic components and others. The displacement of a cortical target region preoperatively can be from 0.8 to 14.2 mm once the dura is opened [73]. This highlights the strong limitations of actual neuro-navigation methods which are established on preoperative data.

### 1.3.1.2 Electrostimulated surgery

To solve this issue and to improve surgical outcomes, new surgical methods have been developed. The first successful approach was to use electro-stimulation during surgery in order to map the cortical and subcortical function during the resection and to adjust it in order to insure the conservation of important functions for the patient post-surgery. If used under general anesthesia electro-stimulation can allow mapping of the motor functions. Bipolar electrodes are placed on the surface brain for few seconds with a current in the range of 2 to 16 mA, and patient is watched for movement response. If a region of the brain show activity when a movement is stimulated, the surgeon will stop resecting this area to preserve the essential function. However language and cognitive function could not be identified during surgery with this method [74]. If this method show great advantages over pre-operative function mapping by solving the problem of brain shift, there are still some limitations. Electrostimulation can result in some false negatives. Because the patient is under anesthesia any motor stimulations are external, and not coming voluntarily from the patient as they would be normally. Further external stimulation excites the largest axons and neurons first, where in voluntary movement stimulation can start from smaller neurons. Consequently these small neurons will not be activated with the external stimuli and may be wrongfully resected [75]. Another limitation that often results in false positive is the propagation of the signal along axons. Even if it is an advantage by highlighting the connectivity in the brain, it can also show signal after stimulation in a region that could have been resected [75].

### 1.3.1.3 Awaken surgery

To have access to all vital functions related to brain activity, the process of awake surgery was developed. The process of such surgery is asleep-awake- asleep protocol, the patient is asleep for scalp opening and bone removal and then fully awake for speech function mapping. The distance of the resection margin from the nearest language site is critical to hope for post-operative intact language function. A 40% language deficit is expected if the resection comes within 10 mm of important language sites. However, for distances greater than 1 cm, no permanent deficit can

be expected [74]. A recent study of awake surgeries with electrostimulation for function mapping showed that in 107 patients with glioma of grade II to IV, surgeons were able in 80% of cases to have a resection superior to 90% [76]. Also 74% of patient were able to resume their employment activity. They determined that with this technique, maximal functional-based resection, an increase in both survival and quality of life was possible [76]. Even if this surgical technique showed an improvement in patient survival and quality of life, the resection is still performed "blind" in the infiltrated margins and performed maximally to be sure to reach the 90% rate of resection [77]. However some resected regions may have been completely healthy and some cells may have been left in the highly functional regions.

### 1.3.2 Other standard treatment

If complete removal is not possible without sustaining brain damage, the surgeon will remove as much as possible to help relieve symptoms. The rest of tumor left can be treated with the additional and complementary options of radiation therapy and chemotherapy. Radiation therapy, also called radiotherapy, uses high-powered rays to damage cancer cells and stop them from growing. It can be done by two different processes. External radiation coming from a large machine is generally given over five days during several weeks, depending on type and size of tumor and the patient's age [10]. The other method is internal radiation therapy (brachytherapy), where radioactive implants are put directly in the tumor after resection of the tumor. With this process the radiation is impacted the first few millimeters of tissue in the resection cavity, where residual infiltration could sustained [10]. This limits radiation to other parts of the body, however the patient has to stay in the hospital for several days while the radiation is most active. In most of cancer another method of treatment, to avoid recurrences, is chemotherapy. Chemotherapy, is a treatment based on the use of drugs to eradicate cancer cells. The drugs are usually given orally or by injection (in bloods or muscle), they aim to disrupt mitosis to result in the death of abnormal cells and shrink the tumor [10]. However for a long time it has been considered inefficient for brain tumor due to the selectivity of the blood-brain barrier (BBB). Indeed to regulate the uncontrolled diffusion of most molecules into the brain, this one is surrounded by the BBB. It prevents harmful toxins and bacteria contained in the blood stream from entering the brain, enabling access only to selected substances and molecules like water, some gases, and essential nutrients. If it stays intact through appearance of malignant tumors, what should be seen as a life-saving defense, is also in reality a difficulty for treatment by blocking many drugs and agents from reaching brain cells and tissues [20, 78]. Recently new drugs appeared, with small size or high lipid solubility, naturally able to pass through the BBB, allowing efficient brain tumor chemotherapy. However even if these improvement, this technic still has to prove real impact in brain tumor management, especially in high grade glioma [79].

## 1.4 Current technologies of assisted resection with intra-operative imaging

To answer the problem of brain shift on pre-operative mapping and the limitation of electro-stimulated surgeries, another approach had been to find ways to give contrast at the cellular scale for the surgeon during his surgery. For this, intra-operative imaging techniques have been developed and have started to make their appearance in the operating room. The first direction taken to get real- time intra-operative assessments was to bring the current pre-operative imaging techniques,

## CHAPTER 1. INTRODUCTION

such as MRI or Ultrasound into the operating room [80].

### 1.4.1 ioMRI

One of the more advanced intra-operative non-optical technologies is the intra-operative MRI (ioMRI) [81, 82]. The first attempts began in the 1990s with a collaboration between researchers and physicians from Brigham and Women's Hospital in Boston (Massachusetts, USA), and engineers from General Electric Medical Systems, resulted in a pioneer 0.5THz intra-operative MRI system. Since then few other systems have been invented. Siemens produced a 0.2THz open-configuration system that was implemented and used in several places (Los Angeles, Heidelberg,...). Philips developed a high field 1.5T MR scanner with a pit configuration that requires in and out displacement of the patient between surgical actions and imaging [81]. These systems give the surgeon anatomical and functional information, helping to make a more precise decision on tumor margin delineation. ioMRI has a high sensitivity on soft tissue discrimination and allows 3D visualization of the operative site. It also helps the surgeon to adapt his surgical trajectory to a safer and more efficient option by enhancing the contrast of intra-cranial lesions. Consequently, the extent of resection can be optimized and the risk of critical hemorrhage greatly reduced. The studies of the use of ioMRI in brain surgery have shown little improvement in the quality of gross total resection. Eljamel et al showed that patients undergoing high grade glioma resection had a gross total resection rate of 70% with the use of ioMRI. Although this rate was assessed to be an improvement compared to non-assisted surgery, it was lower than with intra-operative ultrasound and fluorescein guided surgery [83]. Coburger et al. showed that in low grade glioma resection ioMRI correlated significantly with the histo-pathological diagnosis ( $p < 0.006$ ), however no test was done on the impact on gross total resection [84]. Kubeen et al. tried to compare ioMRI to conventional neuro-navigation guided surgery and did not find significant advantage with respect to extent of resection, clinical performance, and survival using ioMRI [82]. ioMRI has not shown significant results in assisting brain tumor resection and presents important drawbacks. It is a costly and time-consuming procedure, requiring specialized non-magnetic tools and a long acquisition time that disrupts the surgical workflow [80, 85]. Moreover some residual neoplastic tissue cannot be identified by this imaging modality. There is not always a correlation of contrast enhancement with presence of neoplastic tissue. Even if an increase in contrast correlates with tumor, a lack of contrast does not always correlate with the absence of lesions [86].

### 1.4.2 ioUS

Another technique implemented in the operating room is the intra-operative ultrasound (ioUS). It is a real-time imaging technique and inexpensive compared to ioMRI. The imaging scan can be performed several times during the surgery without major disruption to the workflow [80]. This is based on the technique of ultrasound imaging that uses high frequency sound waves which are sent to the examined area and the return echo is registered. A computing process gives a live image of the observed region inside the body. The probe is made of acoustic transducers that generate pulses of sound. When these pulses find a material with a different density, a wave is reflected back to the probe and detected as an echo. The system measures the time the echo takes to return and calculates the depth of tissue that generated the echo. In medical imaging the frequency of the pulses is in the range of 1 to 18 MHz. In ioUS the transducer is in direct contact with the examined organs, giving the advantages of avoiding any signal degradation due to air, bone, blood

or overlying tissue [87]. Petridis et al showed that in low grade glioma it gave better results than other intra-operative neuro-navigation systems. On 34 patients with low grade glioma, 15 were treated using ioUS and in all cases the tumor was identified. Nineteen were treated with standard neuro-navigation, which failed 5 times to identify and locate the tumor [88]. These results showed that used before resection, ioUS gives a useful and promising contrast on identifying low grade glioma and delineating its margins. The shortcomings showed in this study and others before is that once the resection have been performed ioUS image quality at the resection border decreases significantly and remaining tumors can be confused with artifact, such as the "rim effect". Another major shortcoming of ioUS is that it requires an experienced and trained operator to correctly interpret the images, which makes it difficult to include in a surgical workflow [80, 89].

Despite all their technical and computing advances, ioMRI and ioUS still do not provide the accuracy and precision required to assist with extended resection. Ultrasound, MRI and CT imaging are still not able to discriminate tumor heterogeneity and can not give precision at the near-cellular scale [90].

## 1.5 New contrast in intra-operative imaging: the fluorescence

### 1.5.1 Exogenous fluorescence

A new contrast of imaging that has been emerging in the area of biology and physics in the last decades, is the fluorescence. The principle is an incident light exciting an electron to an orbital state that will relax, emitting a photon. The first type of fluorescence to be explored was exogenous fluorescence. Fluorescent markers were introduced into target cell types, proteins, genes, where they will then be excited and their emitted signal collected by the endoscope. The first step is to find a specific probe for the analyzed tissue and cells. Some fluorophores are now able to provide reliable results in intra-operative diagnosis, and the next difficult step is to win approval for clinical application from different European and American committees. The most tested and widespread fluorophores are fluorescein sodium, indocyanine green (ICG) and 5-aminoluvulinic acid (5-ALA). We are going to review their discovery, performance and limitations [91].

#### 1.5.1.1 Fluorescein

Fluorescein was the first marker to be clinically used by Moore et al in 1948 on glioma surgery. It accumulates in glioma tissue and give a homogenous yellow fluorescent signal that can be observed with naked eye. However fluorescein will accumulate everywhere there is blood and will become highly non-specific [92]. These brought large debate and dispute in the literature on the real capacity of fluorescein to be tumor specific. Even though it was the first tested fluorophore, fluorescein is not FDA (Food and Drugs Administration, United-States) approved even today, and can only be used in clinical research study.

#### 1.5.1.2 ICG

Another interesting marker is ICG. It has to be excited in the near infrared range and it emits fluorescence in the same range. NIR light is in the therapeutic window of tissue, resulting in less

## CHAPTER 1. INTRODUCTION

absorption and is safer with regard to tissue damage. ICG has shown great results in the techniques of ICG video angiography, and has been used in other surgical procedures, assessment of blood flow, vessel patency, and not only intestinal perfusion but also in gastrointestinal oncology [93–95]. ICG could be used to show blood flow in glial tumor surgeries. The first studies showed that used alone it failed to give enough fluorescence. The most promising results have been when ICG was conjugated to other molecules enhancing the signal such as 5-ALA [96]. Still one of the major drawback of this fluorophore is the necessity to display the image on a monitor and use specialized detectors and instruments due to excitation and collection in the infrared region [90].

### 1.5.1.3 5-ALA

Where fluorescein and ICG are passive agents, accumulating in tissue by diffusion processes, 5-ALA is a metabolic targeting agent. This means that a metabolic process activates a non-fluorescent component into a signal-generating form in targeted tissue. It is an intermediate metabolite, that after oral administration the patient will convert to protoporphyrin IX (PpIX) an endogenous fluorophore emitting in near infrared (620-710nm) [97]. 5-ALA was first introduced in glioma surgery by Stummer et al. in 1998 [98] on 9 patients. They reported the usefulness of 5-ALA-PpIX in 7 of them to detect and remove residual tumor tissue. Later on, with a phase-III study in Europe, Stummer et al. demonstrated that the use of 5-ALA contrast resulted in higher rates of gross total resection (65% vs. 36%) and, in patient older than 55 years, an improved 6-month progression-free survival (41% vs. 21.1%) [99]. In Europe 5-ALA has been approved by regulation committees and used more and more by surgeons to assist their resection surgeries. It has shown great results in high glioma, more especially in GBM.

Still it has its limitations, in low grade glioma. Due to the needed blood-brain-barrier disruption, the accumulation of fluorophore can decrease and consequently decrease contrast [90]. These first studies were made using a 405 nm excitation source, that induced considerable photobleaching. Kantelhardt et al conducted a study of the PpIX fluorescence in orthopic glioma model using a two-photon imaging set-up (DermaInspect, JenLab). They were able to get a higher structural definition of the tumor tissue, with the high resolution of the two-photon microscopy [100]. Discrimination of fluorescence from the cytoplasm of tumor cells from the 5-ALA induced PpIX fluorescence of normal brain parenchyma adjacent to tumor were possible [100]. 5-ALA more and more used in clinical setting and evaluated by the different national ethical committees for general approval, have consequently be questioned on the eventual secondary effects that patient will suffer. The impact of 5-ALA has recently raised different arguments. Bi and Law have published a review of the literature where they assert that transient allergic reactions, including generalized edema, and photosensitivity have been described after 5-ALA administration in several case series [22]. However in a letter Stummer has answered that it was a single case of mucosal edema and that in 500 patients closely monitored no issues of this nature have been encountered and that no other case has been reported to the European Risk Management plan [101]. Coming to a conclusion on the impact that could have 5-ALA on patient safety, is a hard task and is one of the reasons that this exogenous method will take time to be accepted and used on a larger scale. Consequently, other methods must continue to be explored to tackle the question of assisted resection surgery.

### 1.5.2 Endogeneous fluorescence

Exogenous markers development was slowed down by difficult regulatory approval processes and the hard task of finding tumor specific markers at a cellular scale. These limitations and the

availability of high resolution imaging technologies, pushed physicists to consider another mean of contrast - autofluorescence. This is a signal from native components of biological tissue. It has been seen for a long time as a noise in exogenous fluorescence optical detection, recently gaining interest as a direct mean of contrast for optical tumor diagnosis. In all tissues, we can find molecules in cells, that when excited at a suitable wavelength becomes fluorescent. This emitted fluorescence, an intrinsic property of cells, is called autofluorescence in contrast with previously described exogenous fluorescence. Endogenous fluorophores are link to the morpho-functional properties of cell and tissue. All changes during physiological and/or pathological processes impact the distribution of fluorophores and so their emission features. It results in a powerful tool to monitor directly the morphological and physiological state of a tissue and/or region of cells.

### 1.5.2.1 Fluorescent molecules in brain tissue

Autofluorescence originates primarily from mitochondria (molecules such as reduced nicotinamide adenine dinucleotide (NAD(P)H) and flavin adenine dinucleotide (FAD) coenzymes, porphyrins and lipopigments), lysosomes (lipofuscins in cells), extracellular matrix (structural proteins such as collagen and elastin) and various aromatic amino acids (such as tyrosin and tryptophan)[102–104]. Figure 1.6 shows the distribution of these fluorophores as a function of on their optimal excitation wavelength and their emission spectrum [105].

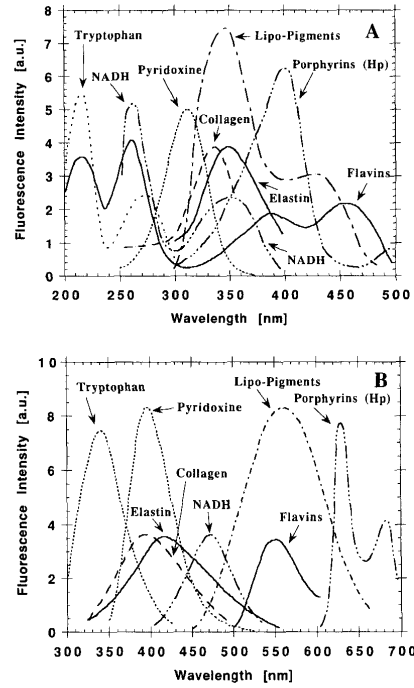


Figure 1.5 – Fluorescence excitation(A) and emission(B) spectra of various endogenous fluorophores [105].

NADH has a favored absorption wavelength at about 365 nm and emits fluorescence in the

## CHAPTER 1. INTRODUCTION

420-490 nm region. The fluorescent properties of NAD(P)H change with enzyme bidding and as a consequence a shift of the main emission peak can be observed. NADH is mainly involved in oxydoreduction reaction during energy production, which makes it a good metabolism indicator [106]. FAD has an absorption maximum at 445 nm and emits fluorescence around 525 nm. It is an oxidized form of the metabolic process of energy production in cells and as for NADH, the monitoring of its fluorescences give access to metabolic information [106]. Lipopigments, a product of lipid oxidation can be excited in the 340-440 nm range. The main peak of emitted fluorescence is at 600 nm with a broad width [106]. The signal is produced by granules that accumulates in cell cytoplasm and are associated with tumoral condition [107, 108]. This motivated the use of lipopigments as a diagnosis tool. Porphyrins, molecules involved in transport of oxygen, catalysis and pigmentation, emit fluorescence at 630 and 670 nm if excited in the visible range. Porphyrins have been observed as an indicator in necrotic tumors [109]. Some amino acids are also endogenous fluorescent molecules. They are best excited with wavelength under 280 nm, and three of them can emit fluorescence : tryptophan around 340 nm, tyrosin around 300 nm and phenylalanine around 280 nm. Their fluorescence response is influenced by structure, spatial conformation and microenvironment, making it an interesting tool to monitor tissue state [106]. Proteins themselves can also result in an autofluorescence signal, such as structural collagen proteins. The maximum absorption of collagen is around 340 nm with an emission peak at 400 nm. Collagen is one of the main component of the extracellular matrix (ECM) and presents different types, at least eleven. These proteins are able to produce fluorescence through formation of covalent cross-links [106]. During most cancers the ECM is altered through different mechanisms, which can result in increase of collagen or/and a more oriented alignment. Being able to quantify the amount of collagen could be a hallmark of tumoral nature. Also some types of collagen (I,II and V) have a very distinct triple helical structure, which make them, as shown before, a source for SHG signal and so an indicator of structural change in the ECM, such as fiber orientation [110].

Using this intrinsic contrast signal in multi-photon microscopy showed promising results, over linear microscopy, to give information at a cellular scale. Teams have worked on mouse models of gliomas to count cell density imaging two-photon autofluorescence of NADH and FAD [100]. Lepert et al. have applied multi-photon microscopy on *ex vivo* murine tumor and human brain tumor [111]. In murine tumor, the images of the autofluorescence response were compared to the gold standard H&E staining in histology. The demarcation between tumor and healthy tissue were identified in the multi-photon images with a cellular scale. The invasive tumor cells were identified at a single cell level and some sub-cellular structures too. They also explored some human *ex vivo* samples taken from macroscopic edge and solid tumor tissue after resection of a glioblastoma. In the margin, they showed single invasive cell as in murine tissue [111].

### 1.5.2.2 Metabolic activity

The metabolic activity of the brain is the sum of all the biochemical processes responsible for cerebral functions, like maintaining cell life and enabling their functions in the tissue. The brain is one of the most energy consuming organs, using 20 to 23% of the total body energy requirement [112]. When a cerebral stimulation occurs the metabolism activated requires higher adenosine triphosphate (ATP) production than typical basal state. Being able to measure this cerebral metabolic activity gives access to monitoring changes in brain activity and irregular physiological conditions such as hypoxia, hyperoxia and even acute ischemia [112, 113]. The two major pathways for brain metabolic activity are glycolysis and oxidative metabolism. These two process



are shown in figure 1.6. In these reactions co-factors NADH and FAD play role of electron donors and acceptors. NAD(P), an electron acceptor, has only its reduced form, NAD(P)H, that fluoresce. FAD a primary electron and proton acceptor has only its oxidized form, FAD, that fluoresce. Auto-fluorescence measurements of these co-enzymes consequently gives a way to monitor the energetic metabolism [103, 112, 114].

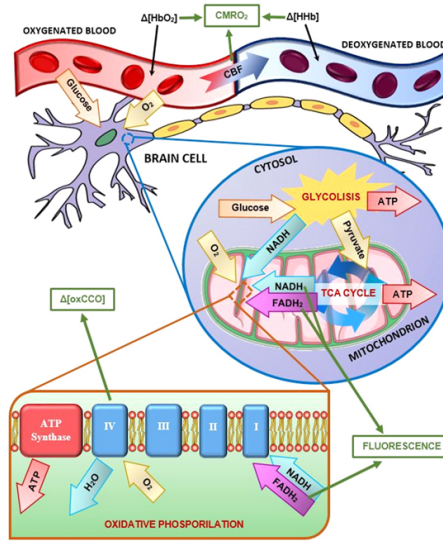


Figure 1.6 – Diagram of the major metabolic pathways in brain tissue [112].

A recent study has shown that measuring the fluorescence ratio of NADH over FAD could translate the different perturbations in the different metabolic process such as enhanced glycolysis and glutaminolysis, extrinsic and intrinsic mitochondrial uncoupling, and fatty acid oxidation and synthesis [115]. In cancerous tissue it was observed that the glycolysis pathway was favored. This phenomenon is called the Warburg effect [116]. An increased glucose consumption even in the presence of oxygen resulting in a change in the energy production and so a change in the ratio between NAD(P)H and FAD.

The method of the redox ratio were proved to be a tool to monitor such changes, different group have therefore proposed an experimental definition of this redox ratio as an indicator of malignancy of tissue. The definition of the redox ratio is not always consistent in the literature [117]. Skala et al. defined the redox ratio, as the ratio of the fluorescence intensity of FAD and NADH, measuring it in a dimethylbenzanthracene (DMBA)-treated hamster cheek pouch model of oral cancer [118]. The redox ratio was different from one type of cell to another in the epithelial layers however these results were not observed in precancerous tissue. Ranji et al. and Drezek et al. used another definition of the redox ratio [119, 120]. They presented it as the ratio of the fluorescence intensity of FAD and the sum of the fluorescence intensities of FAD and NADH. Ranji et al. observed apoptosis in myocardial cells and found a higher ratio in initiation of apoptosis [119]. Drezek et al. measured it in fresh section of normal and dysplastic cervical tissue [120]. A decreased redox ratio in dysplastic tissue sections was observed in one-third of the paired samples, which indicates increased metabolic activity. There are still very few studies reporting on the redox state in brain tumors versus normal brain tissue despite a growing use of fluorescence spectroscopy

## CHAPTER 1. INTRODUCTION

in brain cancer diagnosis. Chung et al. looked at in-vitro human brain tissue. A difference between normal and cancerous in term of intensity was found in both measured NAD(P)H and flavin fluorescence, however the computed redox ratio did not change from normal to cancerous [121]. Croce et al. investigated the autofluorescence properties of normal and neoplastic brain tissues on patients affected by glioblastoma. They used a ratio of fluorescence intensities at 520 (approximatively FAD emission peak) and 470nm (approximatively NAD(P)H emission peak) to monitor the change in the spectral shape with neoplastic growth. It gave a higher ratio in neoplastic tissue than in non-neoplastic tissue [103, 122].

### 1.5.3 Methods of measurements based on fluorescence signal

Fluorescence of molecules is the radiative transition from its first singlet state S1 to the ground singlet state S0. This transition is characterized by three parameters : 1) the fluorescence spectrum, fluorescence intensity as a function of wavelength, 2) the quantum yield, efficiency of the emission process and 3) the fluorescence lifetime, the average time during which a fluorophore remains in its excited state. Detecting technologies have been developed to take advantage of these parameters and give quantitative indicators on the observed regions. Moreover other transitions besides fluorescence can be excited and also result in quantitative detection. They are classified under the Raman spectroscopy. This section will described in details the quantitative methods used in this thesis to measure the fluorescence signal, the spectroscopy and fluorescence lifetime.

#### 1.5.3.1 Methods of spectroscopic measurements

Fluorescence spectroscopy (FS) is based on the measurement of fluorescence intensity which is the number of photons emitted at a specific wavelength. This measure is a function of the fluorophore concentration, the absorption, the scattering and the fluorophore quantum yield. This signal is a linear combination of the emitted fluorescence of each molecule in the tissue. This gives biochemical and morphological information based on the scattering and absorption dependence. Diffuse reflectance spectroscopy (DRS) excites tissue with a broad-band light source resulting in a series of absorption and scattering interactions producing a diffusely reflected light. The intensity of this reflected light will be measured by a detector defining the reflectance spectrum. With this technique the absorption and scattering coefficient of a tissue can be measured, translating the concentration of absorber into the size and density of cellular and subcellular structures [123]. The two methods are compared in the figure 1.7

A combination of the diffuse reflectance and intrinsic tissue fluorescence were used in a large study on primary and secondary brain tumors compared to control tissues. Algorithms were developed to find a discrimination criteria combining these two quantitative modalities. Lin et al. pursued their work with two-step algorithms [124]. Other groups have also started using intrinsic fluorescence and diffuse reflectance to find discrimination criteria in brain tumors [125]. However strong limitations lie in the fact that they use the complete spectral response over a large range of wavelengths and do not try to quantify biomarkers.

Method only based on the fluorescence spectroscopy were also developed [117, 126–128]. The spectral response over a large emitted wavelength range was analyzed. Either by developing fittings methods to get the area under emission peak [127, 128], or directly take the intensity value from the curve on specific emission band [117, 126]. These methods show statistical discrimination between normal and cancerous brain tissue in rat [117, 128] or human samples [127].

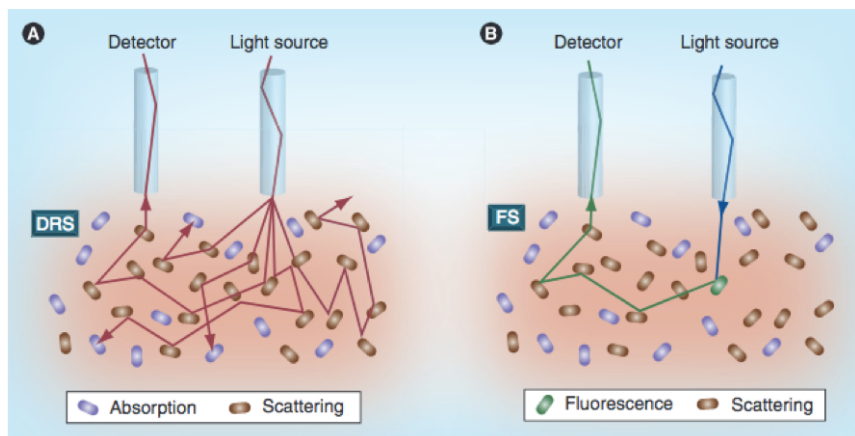


Figure 1.7 – Schematic overview of two optical spectroscopy methods. (A) Diffuse reflectance spectroscopy(DRS). (B) Fluorescence spectroscopy(FS) [123].

### 1.5.3.2 Methods of fluorescence lifetime measurements

When a molecule absorbs a photon, it can result in the photo-physical process of fluorescence. The time required by a population of  $N$  electronically excited molecules to be reduced by a factor of  $e$  in this process is called the fluorescence lifetime,  $\tau$ , which is on the order of nanoseconds [129]. Fluorescence lifetime is an intrinsic property of the fluorophore, independent of intensity-based parameters (intensity of excitation, detection gain, optical loss in setup, fluorophore concentration, microscope focusing, photobleaching). It is sensitive to environmental factors such as temperature, pH, oxygen and ion concentration, viscosity, molecular association (binding to other molecules, proteins) and polarity. These dependencies create the opportunity to use the fluorescence lifetime technique as a probe of the local microenvironment of the fluorophore [129–131].

#### 1.5.3.2.1 Detection technique

Fluorescence lifetime can be measured either in the time-domain or in the frequency domain. The major difference between these two methods is the type of excitation used. In the time domain short pulses of light with significant delay between the pulses are sent to the tissue. In the frequency domain a sinusoidally modulated light at a high frequency is used to excite the tissue [129]. The Figure 1.8 illustrates the detection methods for time-domain and frequency domain fluorescence lifetime techniques.

In the time domain, there are two major methods to detect and measure fluorescence lifetime. These are time-gated integration and time-correlated single photon counting (TCSPC).

In the time-gated method the excitation pulse is split in two in order to excite the samples and to trigger a gated CCD. The fluorescence emitted is detected and integrated during a certain time gate on the CCD, and gates with several delays are recorded to reconstruct the decay histogram [130]. This is not a photon counting method and can avoid the pile-up limitation. Consequently it can be used in configurations with higher photon fluxes and imaging rates. However it has so far never shown the same precision as the TCSPC method and is preferred in situations where speed

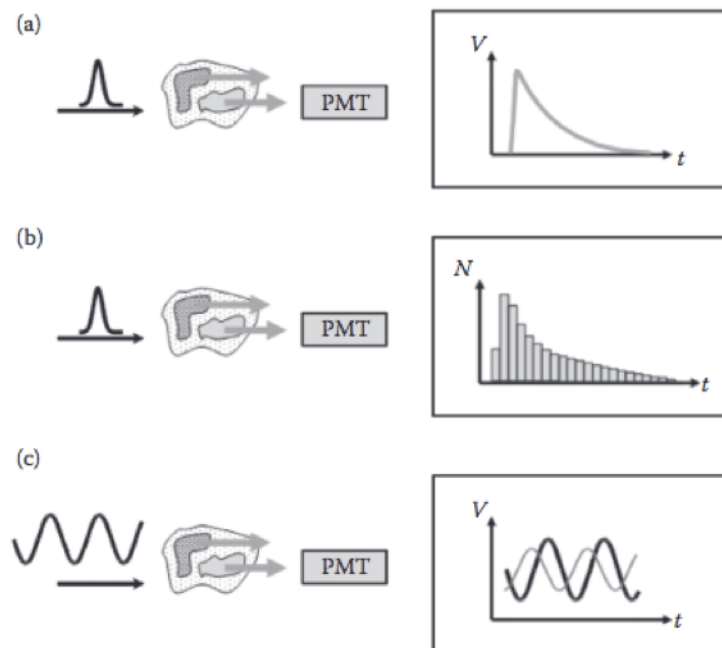


Figure 1.8 – Methods of single point lifetime measurements. (a) analog measurements of decay profile, time-gated method. (b) time-correlated single-photon counting (TCSPC). (c) frequency domain measurement of change in phase and modulation depth of fluorescence with respect to excitation signal [132].

prevails over resolution [132]. In the TCSPC method a voltage is recorded at each arrival of a photon and is related to the excitation pulse start, resulting in a time decay histogram by binning individual recordings in the same time frames. The main advantages of TCSPC are low sensitivity to shot noise, high photon economy, and high dynamic range. One drawback is the relatively low acquisition time, thus requiring low intensity. However in most recent electronic development this has been reduced and is less important than general limitations of fluorescence lifetime techniques such as photon pile-up [130, 132].

In the frequency-domain, a sinusoidally modulated excitation source will produce a fluorescence signal with the same periodicity but with a different modulation range and a delay in phase. The fluorescence lifetime is calculated from two parameters, relative modulation and phase delay). Data are acquired with photomultipliers or charge-coupled devices equipped with a gain modulator [130, 132].

The choice of either time or frequency domain to perform FLIM measurements will depend on the observed molecules. Frequency domain is more adequate to evaluate short-lifetime. The choice of FLIM instrumentation therefore depends on the particular. Time domain is more flexible and can access longer-lifetime molecules, which is better suited for tissue measurements where a broad range of molecules can be observed.

### 1.5.3.2.2 Analysis method

Time-domain and frequency approaches are mathematically the same. There is only a Fourier transform needed to convert data from one domain to another. Therefore the data analysis methods are the same for both [129]. The most popular analysis technique is curve fitting analysis, but other non-fitting methods have been developed. The collected data from fluorescence lifetime measurements can be analyzed with various methods. From the literature three major methods can be extracted: multi-exponential fitting, Laguerre polynomial fitting, and phasor plot analysis [130, 132].

Multi-exponential fitting is the most widespread technique, due to the relative simplicity of implementing it. Fluorescence lifetime measured in a region of interest in tissue is the convolution of the instrument response function (IRF) and the intrinsic fluorescence decay. The fluorescence lifetime of a unique molecule is an exponential decay. If you have a mixture of molecules, the response is a linear combination of the exponential decay of each of the molecules. Consequently in multi-exponential fitting two approaches can be applied: a deconvolution of the response by the measured IRF and several exponentials, or a tail fit where you fit only the second part of the decay after the IRF influence. The optimization of the fitting is usually done with an iterative least-squares method that minimizes residuals and chi-square goodness of fit ( $\chi^2$ ) [130].

A second method is the Laguerre polynomial fitting, the measured decays are individually fitted by a set of unique and discrete Laguerre functions in an orthogonal basis. The advantages of this technique over the polynomial fitting are the fact that no assumption is made on the decay form. The information on all pixels are processed simultaneously resulting in faster fitting and a unique best fit [130].

The third technique is the phasor plot analysis, which was first developed to analyze frequency-domain FLIM (Fluorescence Lifetime Imaging). In this method the modulation and the phase are transformed according to Eq 6.5 1 in order to be graphically represented as a phasor vector on the plot [130].

$$\begin{aligned}x &= M \cos \varphi \\ y &= M \sin \varphi\end{aligned}\tag{1.1}$$

Time-domain FLIM can also be analyzed by this method using pulsed frequency to go into the phasor space with modified equations [133]. The fluorescence lifetime information behind each pixel is represented in a 2D plot where analysis can be rapidly performed by identifying cluster of pixels. And a color can then be attributed at each cluster and projected in the 2D acquired image to obtain a pseudo-colored lifetime map. This type of analysis has the advantages on the other method to being free of "fitting", and offers a representation accessible to non-experts [130, 132].

### 1.5.3.2.3 Application of fluorescence lifetime to brain tumor imaging

Kanteldhard et al. performed a first study using two-photon imaging and FLIM measurements on mouse models and a few *ex vivo* samples of fresh brain tumor just after resection [134]. This study did not have enough samples to give statistical evaluation of the discrimination power (sensitivity and specificity). However they did show differences in lifetime in the different structures and found that the fluorescence lifetime of tumor-adjacent brain was consistently longer than that of normal

white matter [134].

More in-depth *ex vivo* studies were performed by Marcu et al., who showed on 23 samples (9 GBM, 9 cortex and 5 white matter) that the average lifetime was longer in tumor tissue than in normal white matter and cortex [131]. The study also showed, looking at 460nm emission wavelength, that GBM have a dominant form of bound NADH (average lifetime 1,3 ns) whereas normal tissue are dominated by the free form of NADH (average lifetime 1 ns) [131]. Butte et al performed a study on 17 patients (34 biopsy extracted) with primary brain tumor of different grades, and they showed that they could discriminate low grade from high grade glioma, and from normal cortex and white matter, with specificity and sensitivity in a range from 75 to 100% [135]. The first *in vivo* measurements were performed by Sun et al. who implemented FLIM detection in their fiber probe design for performing image-guided brain tumor surgery. They were able to perform a first exploratory clinical trial, on three patients undergoing craniotomy, evaluating the signal from 14 sites, and showed that GBM had a significantly more irregular excitation lifetime distribution as compared to normal cortex [136]. Butte et al. also reported *in vivo* measurements on glioma with two studies, they showed that low grade glioma had a shorter lifetime decay than normal tissue [137]. The high grade glioma could also be separated from low grade glioma and normal tissue, however with a lower sensitivity and specificity.

## 1.6 Optical developments in optical endomicroscopy

In order to answer limitations presented for ioMRI and ioUS, new miniaturized probes have been developed based on optical technics. Optical imaging is a field that has developed rapidly in the last few decades and has showed high resolution in bench-top configurations, if developments are able to brought these set-ups to clinical standard for intra-operative use, it will answer the lack of resolution and crowding of current techniques.

### 1.6.1 Optical coherence tomography

Optical coherence tomography (OCT), appeared in the 1990s. It is an optical imaging technique based on the interference of low-coherent light that detects singly backscattered light to reconstruct two and three dimensional images of tissue [138]. To get contrast OCT uses the scattering optical properties of tissue and get tomographic images with a micrometer spatial resolution at a few millimeters of depth [139, 140]. OCT has revolutionized the field of ophthalmology [141], gastroenterology [142] and cardiology [143], giving a 3D rendering of human tissue at a millimeter depth while being a non-invasive tool. More recently it started to be explored to image and diagnose cancerous tissue. In 2015 an *ex vivo* and an *in vivo* study were performed on brain gliomas (grade 2 and 4). They were able to discriminate *ex vivo* the grade with high sensitivity, and showed on a few *in vivo* patients that there were signal changes in infiltrated region, as histologically diagnosed [144].

If OCT probes showed promising results as a tool for optical biopsy, with the main advantages to give a large field of view and to be non-invasive, and a no-contact probe which integrates itself very well in the surgical field. This technique still suffers from some important drawbacks, the maximal resolution that can be obtained is 10 to 30 microns which is still higher than the cellular scale and have been proven to be insufficient in tumor margin identification [145]. Another disadvantages is that this technique use a slow scan system, in general 4mm requires 8 seconds, and during this time the respiratory and arterial cycle can induce movement of several millimeters that will result

## 1.6. OPTICAL DEVELOPMENTS IN OPTICAL ENDOMICROSCOPY

in distortion in the image or completely move out of the region of interest [139]. Added to that OCT scan cannot access any functional information about the tissue which reduces the quantity of collected information [146].

### 1.6.2 Wide-field endomicroscopy

The first and most common microscopy technique to have been used in endoscope is the wide-field microscopy. This technique refers to low power surgical microscopy, where the whole field of view (FOV) is seen at once (10-100 mm of FOV) and is acquired continuously with an eyepiece and/or a fast digital detector (CCD, charge coupled device, or CMOS, complementary metal oxide semiconductor). These systems have a magnifications of x5 to x40, and a spatial resolution from 10 to 100 microns, again much higher than the cellular level [90, 117]. The advantages of such techniques are, the capacity to view the full surgical field, to have a real-time assessment, an ease of use that does not interrupt the surgical workflow, all at a very low cost [140]. However strong limitations and drawbacks must be pointed out. One of the main drawbacks is ambiguity at the margins. The low resolution, higher than the cellular scale, results in the fluorescence intensity decay to even vanishing in regions where tumor cells density decline. However, on histological slice these regions show that there is still glioma cell infiltration [117]. Another limitation is the sensitivity to the variation in optical properties such as absorption and scattering of tissues that results in a subjective heterogeneous fluorescence [147]. The sensitivity in low grade tumor is also very low, with visible fluorescence not produced in 95% of cases [90, 117]. Moreover the geometry of excitation and collection causes much light loss compared to a point detection technique, and even today the state of the art shows no possibility to perform spectrally resolved data, giving access only to anatomical information [140].

### 1.6.3 Confocal endomicroscopy

#### 1.6.3.1 Principe of confocal microscopy

To address the limitations of wide-field imaging, the world of intra-operative imaging has looked at other microscopy techniques to bring into the operating room. One of the major breakthroughs in the modern area of microscopy was the invention of confocal microscopy, in 1957 by Marvin Minsky [148]. Its aim was to answer the current limitation of wide-field imaging. In wide-field, the whole sample is illuminated and the all fluorescence emitted is conjugated to a CDD to obtain a image. In the confocal configuration, in the detection path a pinhole is conjugated to the focal point to eliminate out-of-focus signal and performed a point-by-point detection. The image's optical resolution, particularly in the sample depth direction, is much better than the one in wide-field microscopy, due to the presence of the pinhole. This difference is shown in the figure 1.9.

However the point-by-point detection made it mandatory to have a scanning system to obtain images with the same field of you than wide-field imaging, resulting in a slower imaging system. The pinhole also reduces the quantity of fluorescence detected in each point, very sensitive detectors are consequently needed, making this technique also more costly than wide-field.

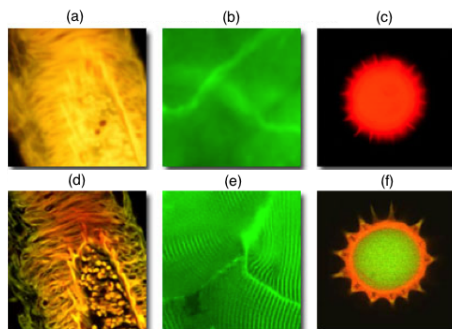


Figure 1.9 – Wide-field microscopy (a,b,c) against confocal microscopy(d,e,f) [149].

### 1.6.3.2 Adaptation towards a clinical use

Bench-top microscopy technology cannot be brought directly to the operating room due to spatial crowding, and the architecture of the excitation path making impossible to introduce object at a centimeter scale under, such as human brain. Miniaturization was required to see these technologies used intra-operatively. This was made possible with the development of three miniaturized technologies : optical fiber to guide the light to the sample, micro-optics, and a miniaturized scanning system to achieve centimeters scale tools that would also be easy for surgeons to handle.

**Optical fiber** The arrival of step-index fiber to serve as a light guide and allowing remote excitation light delivery was the first step to endomicroscopy. For confocal endomicroscopy, single-mode fiber (SMF) is well suited and easily available commercially. SMF fiber has a core refractive index usually 1 to 2% higher than the cladding index, with a numerical aperture equal to the sine of the half angle of the emitted light and a core diameter around 3 to 7 micrometers (for set-ups using a visible excitation) [150]. The SMF can be used in two configurations for confocal imaging. In one the single SMF serves for both excitation and collection, with a very small core size serving as the detection pinhole. In the second configuration (dual-axis imaging), two SMFs are placed apart from one another at an angle. One will excite and the other will collect the light. This configuration, compared to the first one, offers a longer optical working distance, no off-axis aberrations, and good axial resolution with economical objective lenses, at the cost, however, of harder alignment and less collection efficiency. Another type of fiber widely used on confocal endomicroscopy is the fiber bundle. The fiber bundle consists of hundreds of individual step-index fibers in a packed arrangement, with a diameter from hundreds of microns to a few millimeters. The advantage of such system is the possibility to use proximal conventional scanning systems. However one strong limitation is the low resolution due to image pixelation [150]. More recently few teams have been trying to use multimode fiber to perform confocal endomicroscopy and resolve some limitations of the other configurations. Multimode fibers can independently guide several spatial modes of light in cross-sectional diameter around  $100\text{ }\mu\text{m}$ , consequently allowing the transmission of multiple pixels image with diffraction-limited resolution. This solves the limitation of the SMF configuration that transmit only light with Bessel intensity profile and the limitation of the bundle configuration which has a low resolution due to the fiber spacing. However distortion through the multimode fiber propagation requires heavy computing processing to reconstruct the right image at the output



## 1.6. OPTICAL DEVELOPMENTS IN OPTICAL ENDOMICROSCOPY

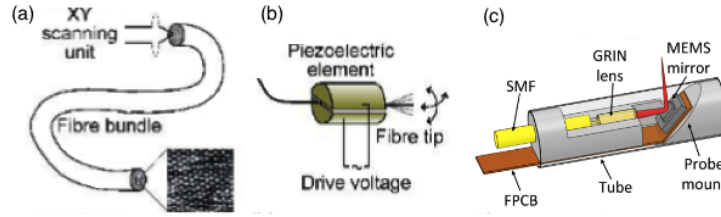


Figure 1.10 – Scanning mechanisms in miniaturized microscopy. (a) Proximal scanning of a fiber bundle [152]. (b) Mechanical resonance of fiber tip with piezoelectric actuators [152]. (c) a MEMS mirror [21].

[151]. This limitation is the reason that SMFs are still the most used method to perform confocal endomicroscopy.

**Scanning system** One of the most challenging parts of an endomicroscope configuration is the scanning system. Different architectures have emerged, divided into two big families: proximal scanning (placed between laser source and fiber probe) or distal scanning (placed at the tip of the fiber probe). Proximal scanning is classically used with fiber bundle probes and consists of a pair of galvanometric mirrors placed at the entrance of the bundle (Fig 1.6.a)[152]. A bundle of hundreds of fibers is scanned by the laser beam at the proximal end of the probe. Each fiber serves as a point source as well as a detection pinhole for imaging. The resonant galvanometer can go up to 15 frames/s [153].

Where a single fiber is used to excite tissue, distal scanning systems have been developed. Two technology have emerged: a piezoelectric placed at the distal end of the fiber, and a micro-electromechanical systems (MEMS) mirror placed after the distal tip of the fiber. For piezoelectric technology (Fig 1.6.b), when supplied with a signal closed to the resonance frequency of the fiber, a 2D scanning pattern is generated, which can be a lissajouls, or more often a spiral. The resolution of such a system is determined by the driving signal, but can achieve quite good performances. Some teams have shown imaging of organs with this scanning system [154]. The other distal technology for scanning is the use of a MEMS-mirror at the end of the fiber probe. It allows a fast X-Y scanning, and can be miniaturized at a very small scale (around 1mm). The linear scanning pattern makes it easier to reconstruct an image than with the different patterns accessible with the piezoelectric configuration. It was first used in OCT configurations, but now the endomicroscopy community is showing interest [155–157].

**Miniaturized optics** The third component for a successful confocal endomicroscopy system is the access to a miniature objective to focus the excitation light and to collect the emitted fluorescence. Recent advances in the development of micro-optics have largely contributed to the development of endomicroscope. The specification needed to achieve confocal endoscopy is a high-NA (numerical aperture) objective with a millimetric or sub-millimetric size and diameter.

Preferred are GRIN lenses (gradient index lenses) due to their small outer diameter, ranging from 350-1,000  $\mu\text{m}$ . Cylindrical GRIN lenses exhibit a refractive index that declines approximately quadratically with radius. They are usually used as a combination of two GRIN to form an objective. There is a first lens with a typical 0.4 to 0.6 NA, to reach a micrometer scale resolution and then

## CHAPTER 1. INTRODUCTION

a relay lens to reach deep tissue [150]. However GRIN lenses usually failed to reach a suitable correction of the chromatic aberration and curvature of field, often problematic in fluorescence confocal endoscopy [158].

Other lens designs have been studied to avoid these limitations. A solution is the use of custom-designed lens system [158]. Teams have developed systems combining five to six lenses [159–161]. The combination is composed of aspheric and achromatic lenses to work around the limitations found with the GRIN lens and reach an optimal collection efficiency for fluorescence imaging. However one difficulty to consider is the fabrication process for miniaturized aspherical or achromatic lenses that can be costly and technically difficult. To tackle that point systems of semi [161] or all plastic [160] lenses have been studied. The critical remaining point is the length of such an assembly that is still on the order of ten millimeters, which reduces the flexibility needed to reach certain organs compared to GRIN lens [158].

A last solution that is found in the literature is the use of vari-focal liquid lenses often combined with an aspheric lens to reach the high-NA required [162]. The ability to adjust the focal length avoids regions in tissue not clearly imaged due to tissue irregularity [163][164]. However there are still limitations to such systems. The axial resolution is only in the order of  $20\text{ }\mu\text{m}$  that can be a limitation for certain diagnoses based on structures with smaller size. The system can also be affected by pressure and temperature changes, parameters which can fluctuate in an operating room [164].

**Computing System** In order to reach a real-time assessment *in vivo* embedded computing systems had to be developed, combining advances in electronic and data analysis. To be able to process at a high rate the data recorded by the detector and to produce an image to the surgeon, FPGA (field programmable gate array) boards have been used. An FPGA is a reconfigurable logic circuit with logic elements allowing programming with flexibility on the number of inputs and outputs. An algorithm can be developed and loaded onto the FPGA chip and then combined to a display device as an output [165]. Different algorithms to reach a high quality image can be programmed in the board such as arithmetic, neighborhood and convolution operation filters. Teams have also added a daughter boards to serve as a Z-depth controller and to perform 3D imaging in real time [166].

### 1.6.3.3 Commercial system

The combination of these miniaturized technologies has allowed confocal microscopy to come into the operating room. Confocal endomicroscopy has been extensively tested in other medical applications such as Barrett’s oesophagus [167], urothelial bladder neoplasia [168] and cervical intraepithelial neoplasia [169]. These research projects have resulted in two commercial systems: the Optiscan FIVE 1 (Optiscan, Australia) and the Cellvizio (Mauna Kea Technologies, France). These techniques provide a better contrast than wide-field imaging by suppressing the out-of-focus background with the use of a pinhole in the optical path. It also allows in-depth imaging. With the Optiscan FIVE 1, 250 microns can be scanned, and with the Cellvizio up to 70 microns. Its first use in neurosurgery experiments was reported in 2010, with the use of *in vivo* confocal probe in a mouse tumor removal surgery [90, 170]. It appears in this study to be able to give real-time images close to histopathological standard without the long staining process [171]. The Cellvizio was used in a preliminary *in vivo* study on 9 patients with low and high grade glioma using two contrast agents used: 5-ALA or intravenous fluorescein. They reported differences between healthy and

## 1.6. OPTICAL DEVELOPMENTS IN OPTICAL ENDOMICROSCOPY

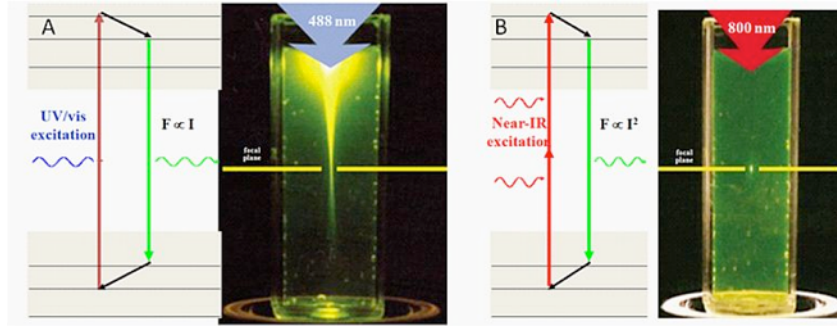


Figure 1.11 – Comparison between confocal(a) and multi-photon excitation(b) process [178].

pathological tissue, however they were not able to have enough specificity to differentiate low-grade from healthy [172]. Different studies were then performed with the Optiscan on human brain tumor using fluorescein as an exogenous marker [173]. Another study was performed with the Optiscan endoscope where ten patients with WHO Grades I and II gliomas underwent microsurgical resection with 5-ALA. Intra-operative confocal microscopy identified tumor fluorescence at a cellular level, where with macroscopic tumor fluorescence it was not evident [174].

### 1.6.3.4 Limitations

The preliminary studies with confocal endomicroscopy have showed promising results, however the medical community has not been easily convinced that it should become a standard in medical procedure. Important drawbacks : 1) the difficulty of interpreting the given image for non-specialist, such as surgeon, 2) the small field of view, 3) limited resolution at a scale higher than cellular structure, making it, for example, non-discriminant for low grade and infiltrated regions in glioma suspected regions, 4) access to only one contrast, resulting in difficulty in reliability and reproducibility of the results, and 5) limited penetration depth has also been an obstacle in fields like gastrointestinal surgery, where some important deeper layers could not be imaged. Newer techniques like two-photon endomicroscopy could remediate these current limitations [145, 175].

## 1.6.4 Multi-photon endomicroscopy

### 1.6.4.1 Confocal vs multi-photon

Linear microscopy has not succeeded in giving enough information to discriminate tumoral nature of tissue at a cellular scale. To address the limitations of confocal microscopy, the field has turned its attention to the new fast-growing technique of non-linear microscopy. This microscopy technique is based on the combination of several photons passing the energy gap and exciting the samples. Multi-photon excitation requires high spatial and temporal confinement resulting in no excitation of tissue outside of the focal points. This property, shown in the Figure 1.11, results in a 6 to 20 times better signal-to-noise ratio [176], allow less photo-bleaching compared to linear technology and higher optical sectioning giving a better imaging depth [177].

Another advantage of multi-photon microscopy is that NIR-near infrared excitation is in the therapeutic window, where the water and hemoglobin absorption of light is low, resulting in an

## CHAPTER 1. INTRODUCTION

increase of the possible imaging depth. In the literature it is reported that the maximum depth can be up to 1mm [179]. One of the major assets of multi-photon microscopy is an excitation wavelength (NIR range) far from the emission range (visible). There is no spectral overlap between the two, offering a better contrast due to less noise in the signal of interest.

These advantages of non-linear techniques such as two-photon imaging have been highlighted by Bao et al [180]. The same samples were observed in one-photon and two-photon imaging, and three parameters were compared: resolution, depth of imaging, and the risk of photo bleaching. In these three domains two-photon imaging showed an improvement over confocal technology. More structures were identifiable, two-photon could give an image 40 microns more in depth, and after 10 minutes of continuous scanning no change in intensity was observed, which is two times better than for one-photon excitation. Multi-photon also provides other contrasts than fluorescence such as harmonic generation, which will be discussed in the next-paragraph.

### 1.6.4.2 Second harmonic generation

Using two-photon excitation on tissue gives access to another imaging contrast besides emitted fluorescence. Incident photons can be scattered with a harmonic up-conversion process; It is coherent scattering, and the radiation patterns are highly sensitive to phase [181]. When two photons are combined, the process is called second-harmonic generation (SHG), producing emitted photons with twice the energy. Structures able to produce such signals have a specific molecular orientation, generally non-centro-symmetric molecular structures [182]. Some biological materials such as collagen [183], muscle myosin [184] and cellulose [185] present large non-centrosymmetric structures and are able to produce a SHG signal. SHG imaging is able to give information on molecular organization both at the micro and nano scale level. In a diseased state, such as cancer, where there is often alteration in the secondary, tertiary or quaternary structure of proteins, these changes will affect the level of SHG, making it a useful tool for diagnosis [182]. With the same excitation it is possible to observe the autofluorescence response of tissue and the SHG signal, resulting in two images modality with one set-up. Some molecules such as collagen can be found in different types of tissue in the human body and resulted either in a fluorescence signal or a SHG response. In ovarian cancer, an analysis method using the spatial structure and the intensity of SHG, has already been implemented. Indicators can be, for example, the ratio between elastin and collagen (SAAID, SHG to autofluorescence aging index of dermis) or the orientation of the collagen fibers at the tumor-stroma boundary (TACS, tumor-associated collagen signature). Nadiarykh et al. have shown that in ovarian cancer, compared to normal tissue malignant tissue had a denser and more ordered collagen [186]. Other groups also used the SHG signal in the detection of breast cancer. For example Conklin et al. have found that an increased presence of collagen fibers aligned perpendicularly to the tumor boundary (TACS-3) was associated with decreased survival [187].

### 1.6.4.3 Optical fiber

To achieve an endomicroscope architecture for multi-photon microscopy, new efforts are required in the development of optical fibers. Indeed, the ultrashort optical pulses (80 to 250 fs in duration) used for *in vivo* two-photon imaging generate a light-matter interaction while propagating in the glass fiber core of a SMF. This process will result in distortion of both the pulse shape and spectrum through a nonlinear process known as self-phase modulation (SPM), making it difficult to excite efficiently with the SMF used for linear imaging [150]. SMFs have a small numerical aperture and fiber core, so when used in a two-photon configuration the system aberrations are increased,

## 1.6. OPTICAL DEVELOPMENTS IN OPTICAL ENDOMICROSCOPY

resulting in fewer photons to form an image. A solution could have been the multimode fiber, but it cannot be focused to a spot size adequate to produce a nonlinear excitation, which requires high spatial confinement. A new type of fiber, photonic crystal fiber (PCF), which has appeared in the last decades has revolutionized the field. They had the properties able to overcome previous limitations. Traditional fiber is the association of two mediums with different refractive indexes guiding light with total internal reflection. PCF on the other hand uses a photonic crystal as a mechanical guide for light, surpassing the limits of traditional fiber.

Different architecture can be found and have been tested for non-linear ex-citation and imaging. They are shown in the Fig 1.12.

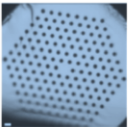
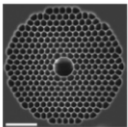
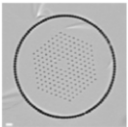
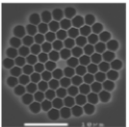
Features	LMA PCFS	Hollow-core PBFs	Double-clad PCFs	Highly nonlinear PCFs
Fibre Images				
Operation wavelength	Wide range	Near zero-dispersion wavelength	Wide range	Near zero-dispersion wavelength
Advantages	Reduced SPM effect for ultrashort pulse delivery. Endless single-mode over wide wavelength range.	Low loss; High power threshold for nonlinear effects; No prechirping for high energy pulse delivery.	Reduced SPM effect in the core; High NA in the inner cladding; Dual function for pulse delivery and collection.	Extremely high nonlinear coefficient; Ideal media to generate supercontinuum for multispectral imaging.
Limitations	Low NA for signal collection; Dispersion compensation is required.	Narrow operating wavelength window; Low NA for signal collection.	Dispersion compensation is required.	Broadened pulse durations; inefficient collection with small core.

Figure 1.12 – Different types of fiber used in multi-photon endomicroscopy [152]

One way to reduce SPM is to have a larger core size in the fiber. The advantages of PCFs over SMF for that, is that you can design a PCF that will have a larger mode area or even with an endless single-mode-operation. So the first group of fibers to be developed was the large-mode-area (LMA) PCF with large core size (up to 35 microns of diameter) and a single-mode guide for wavelengths where silica is transparent. This design strongly reduces the nonlinear effect for short pulse delivery, for 3nJ pulses at 800nm, you can deliver 140 fs pulses over 1.3m [188]. If these fibers have suitable characteristics for nonlinear excitation, the low NA make them more limited for an imaging setup.

Another design alternative is hollow core PCF. It offers high power for a good non-linear excitation and there is no need for a pre-compensation unit, but the collection of visible light cannot be performed by the same fiber due to a low NA. A point that could be a drawback in certain cases is that the hollow core fiber is designed to work a few tens of nanometers around the central wavelength, so it cannot be used in a tunable setup, and cannot collect the visible backward emitted light [189]. A design that could play this dual role of excitation and collection is the double clad crystal fiber (DCF). They possess a LMA core to reduce nonlinearity at the excitation and an inner cladding with a high NA and large diameter to propagate visible and near infrared light with a high efficiency that serves as a dual tool to excite and collect [190]. The drawback is the need for a pre-compensation unit to maintain a femtosecond pulse at the output. However, we will see in the next section that efficiency developments have been made to achieve that. Consequently, these fibers are the fiber of choice for recent developments of imaging non-linear endomicroscopes.

The latest popular design in PCFs is the highly non-linear PCFs, which exploit nonlinearity effects

## CHAPTER 1. INTRODUCTION

rather than avoiding them. Core sizes are very small, (around 1 micron) surrounded by microstructures, creating high nonlinearity. They are designed to have a zero-dispersion wavelength of choice, in visible and near infrared spectra [191]. This configuration generates a super-continuum with a bandwidth as large as sunlight however ten thousand times brighter, making it very efficient for multi-photon microscopy [192]. However, the drawbacks are the narrow window for excitation making not suited for tunable lasers and it cannot be used in a dual configuration of excitation-collection [152].

### 1.6.4.4 Pre-compensation unit

Two of the fiber designs presented in the previous section required pre-compensation in order to keep a very short pulse after long distances in the fibers. A first idea was to use pre-fiber with a negative dispersion that will compensate the dispersion from the second exciting fiber. However this solution implies never changing the excitation fiber length, nor changing the whole setup. The more fully developed solutions in the literature are passive pre-compensation units that can be adjusted to the characteristics of the second excitation fiber. Different solutions have been developed in the last decades, and are presented in the Table 1.3.

A first approach was to find system that compensate for second-order dispersion (SOD). Passive dispersive lines such as grating lines and prism lines were tried [193, 194]. With these methods pulses in the range of 100 fs could result at the output of the excited fiber for pulses of similar duration in a 1 or 2 meter fiber.

Still with these methods the third-order of dispersion (TOD) was not corrected resulting in pulses still suffering from temporally broadening through propagation. New combinations of passive systems were studied to compensate for SOD and TOD simultaneously, such as chirp mirrors before a prism line [194], or grism line (association of prism and gratings) [195]. These configurations resulted in pulses even shorter than at the input after several meters of propagation in the excitation fiber, making it a solution of choice for two-photon endomicroscopes [196–198].

Two-photon microscopy setups still require the same system elements as needed in confocal endomicroscopy and they can be translated fairly easily. The scanning systems are the same, the miniaturized objectives change in requirements (NA, focal length, wavelength of choice) but use the same technologies (GRIN, customized assembly), and the processing units are based on the same electronic technologies. Only the data process algorithms change.

### 1.6.5 State of the art in multi-photon endomicroscopy

Few research teams have already tackled the task of developing a miniaturized technology using two-photon excitation. The setups differ in the choice of excitation wavelength, modality of detection, fiber design, miniaturized objectives and scanning techniques. Their designs, advantages, and limitations will be discussed in this section and the first studies conducted with them will be presented.

The group of Laura Marcu at UC Davis University (California, USA) has been working for the past decade on the use of autofluorescence to improve medical diagnosis, for example, in tumor margin delineation [135]. They developed a probe system, compatible with peri-operative clinical use, based on the FLIM technique, as shown in Figure 1.13. The system uses as an excitation

# 1.6. OPTICAL DEVELOPMENTS IN OPTICAL ENDOMICROSCOPY

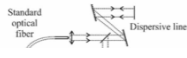
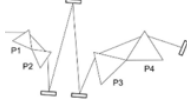
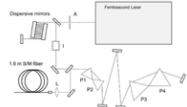
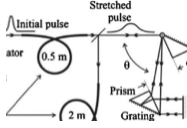
	Dispersive line	Prism line	Chirped mirrors + prism line	Grism line
<b>Set-up</b>				
<b>references</b>	[193]	[194]	[194]	[195]
<b>Architecture</b>	1m SMF + a pair of 1200 grooves/mm diffraction gratings	a 4 prisms line	one or two pairs of dispersive mirrors + a 4 prisms line	0.5m SMF + grisms line (2 prisms + gratings)
<b>Corrections</b>	SOD $+10.10^4 fs^2$ . Transmission around 35%	SOD corrected TOD $+62000 fs^3$ Transmission 31%	SOD and TOD corrected Transmission around 31%	SOD and TOD corrected $(-1, 28.10^5 fs^2, -8, 22.104 fs^3$ respectively)
<b>Fiber for light delivery</b>	fiber bundle (Fujikura, 30000 cores, $3.8 \mu m$ core spacing, $1.7 \mu mm$ core mode field radius, 0.35 N.A.)	0.6m LMA-PZ-800 (Crystal Fibre) Mode field diameter of $20 \mu mm$ NA=0.04 at 800 nm	1.6m LMA-PZ-800 (Crystal Fibre) Mode field diameter of $20 \mu mm$ NA=0.04 at 800 nm	2m SMF fiber with $3.5 \mu mm$ core
<b>Endoscope performances</b>	100 fs at 75 MHz at 830nm $\Rightarrow$ 250 fs after 1m	-	24 fs after 1.6m	150 fs at 76 MHz at 830nm : 45 fs after 2m

Table 1.3 – Different pre-compensation units in the literature

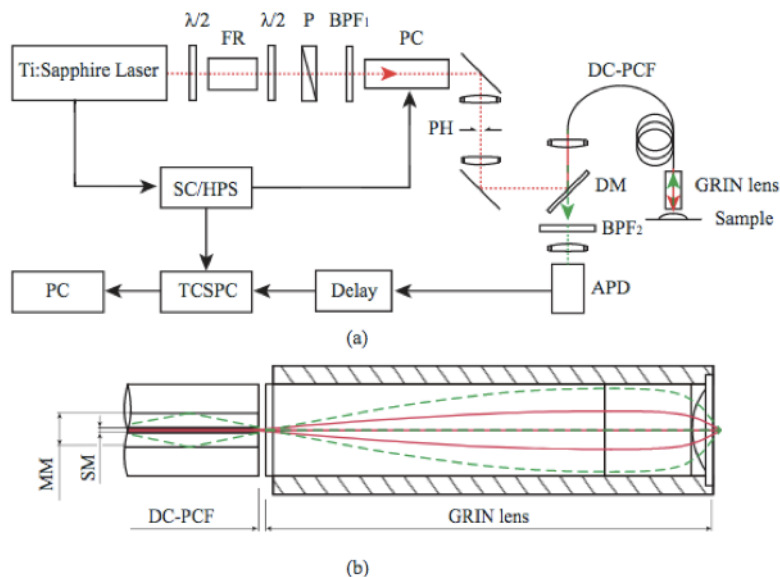


Figure 1.13 – Design of a fibered endomicroscope by the team of Laura Marcu at UC Davis University(USA) [199].

source a Ti:Sapphire laser (Chamelon, Coherent) with 690-1040 nm tuning range, 2.5 W, 140 fs pulse duration and 80 MHz repetition rate. The light is brought to the sample using a double clad photonic crystal fiber (DC-PCF) from Crystal Fibre (DC165 16, Crystal Fibre, Denmark) and a GRIN lens (GRIN, GT M0-080-018-810, GRINTECH GmbH, Germany) which serves as an objective at the end of the probe. Their setup doesn't use a pre-compensation unit before the excitation fiber, and the laser pulse is consequently temporally broadened during propagation from 140 fs to 1 ps in the focal plane [199]. However they were able to make measurements with this configuration using a 714 nm excitation wavelength, but will not be able to use it with a long excitation fiber (no more than 1 m). This point is a serious limitation for a clinical application, where the minimal fiber length must be around 5 m to fit into the surgical environment and workflow. This setup has been tested only on a few exogenous fluorescent molecules (Rhodamine, Coumarine) and *in vivo* muscle tissue, and was able to give a different lifetime value for each type of sample. However no large study on human tissue has been started with this set-up [199].

Towards the end of the 1990's the Medical Faculty of the Friedrich Schiller University (Jena, Germany) formed a company, JenLab, to commercialize CE-marked femtosecond laser based-technology for medical applications [200]. They initially worked on dermatology applications, with multi-photon microscope DermInspect, which has an imaging head at the head of a moving arm in order to be adaptable in a clinical setting or examining room [201, 202]. They then developed a technology more intended for *in vivo* optical biopsy. Called MPTflex, it was a commercial portable multi-photon tomograph, that performs FLIM measurements [134]. See figure 1.14. The optical setup of the MPTflex consists of a titanium:sapphire laser (pulse width of 100 fs, repetition frequency 80 MHz, in situ mean power 2-50 mW, wavelength range 710-920 nm) as an excitation



## 1.6. OPTICAL DEVELOPMENTS IN OPTICAL ENDOMICROSCOPY

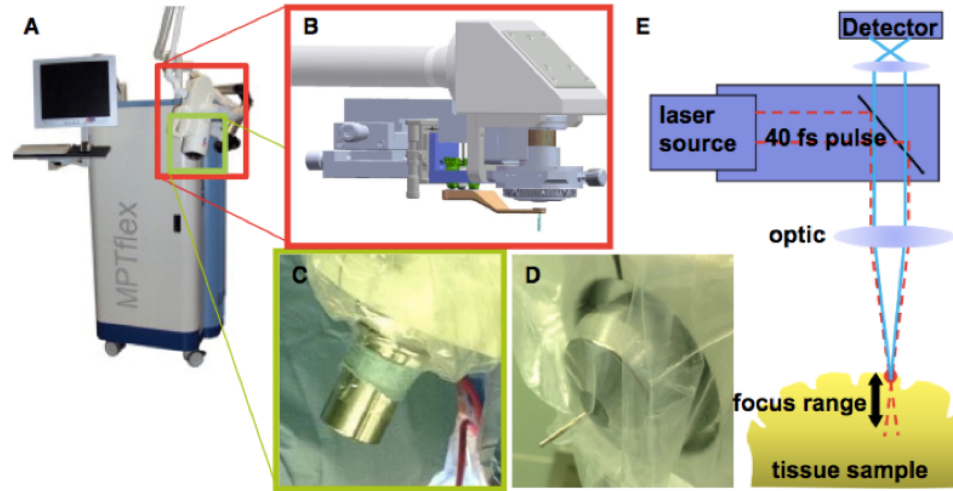


Figure 1.14 – Design of the MPTflex instrument (JenLab, Germany) [134].

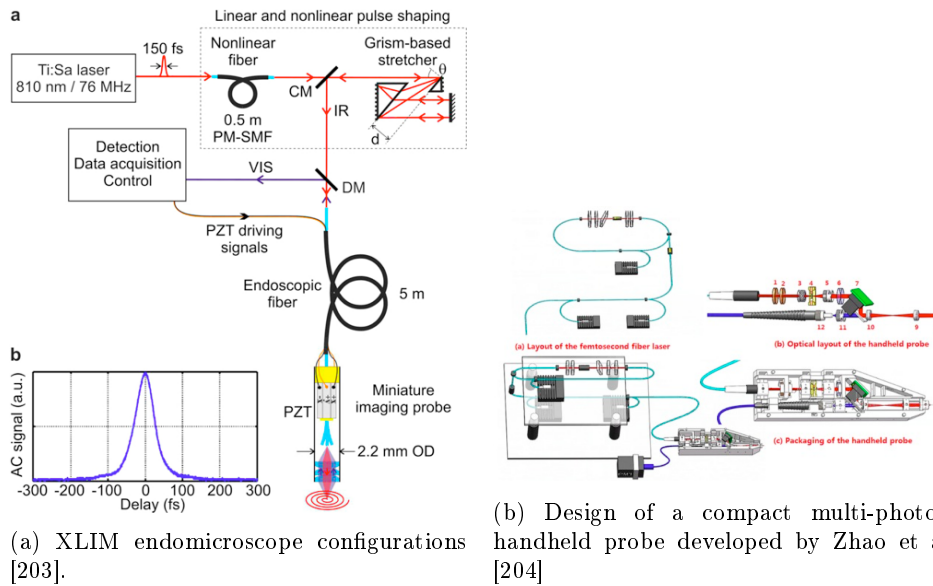
source [134]. It has an image acquisition time of 6 to 10 seconds per frame. Kanterldhart et al. used this tool to image human brain tumor. In their study the authors presented three stages of testing, from the murine tumor model, to the *ex vivo* human biopsy and finished with in-situ tests on patients with diverse human brain tumors (metastasis, meningioma, glioma) [134]. In *ex vivo* biopsy, multi-photon technology showed its capacity to highlight structure at a cellular scale concurring with the histology standard. *In vivo* only an exploratory campaign was performed to show the capacity to get a highly resolved image in the region that would be resected [134].

The team of Professeur Louradour, at the XLIM laboratory, the last years has been working on the development of a multi-photon endomicroscope. Ducourthial et al. recently published the technical specific of the technology with a few *ex vivo* and animal *in vivo* test [203].

The configuration of the endomicroscope is presented in Figure 1.15a. They used a Ti:Sapphire laser at a chosen wavelength of 810nm, a frequency rate of 76MHz and excitation pulse of 150 fs. A pre-compensation unit with a GRISM line was used to insure a 39 fs pulse at an average power of 20mW at the output of a five meter custom-made air-silica double-clad photonic crystal fiber (DC-PCF). A piezoelectric scanning system and a home-built achromatic triplet composed the head of the probe. TPEF (two-photon excited fluorescence)+SHG images were performed on a few rat and human *ex vivo* samples in order to demonstrate the ability to form an image. They also tried the setup *in vivo* on anesthetized mice, and looked at healthy and fibrotic kidney, highlighting the changes in the SHG signal. However, the architecture was not built for clinical use and doesn't provide quantitative information [203].

Recently an even more compact set-up has appeared for multi-photon endomicroscopy. The design is presented in Figure 1.15b. Zhao et al. have used a new very compact infrared femtosecond fiber laser (pulsewidth, 250 fs, output power, 180 mW, wavelength, 1580 nm). They combined it to a frequency doubling system to obtain an excitation wavelength suitable for two-photon excitation on endogenous fluorescence. This was followed by a MEMS scanning system and a focusing lens

## CHAPTER 1. INTRODUCTION



assembly and the all was packaged in a handheld probe [204]. At this point this system has never been used in any biomedical experiments, and is still a proof of concept technology. Even though the main advantage is the very compact system due to the use of a fibered laser, it can also be seen as the main drawback allowing only one wavelength. Consequently if one wants to change the excitation to target a new application, the whole system has to be changed.

## 1.7 Thesis project

### 1.7.1 Context

In this comprehensive, wide-ranging review of the literature, the medical challenges remaining in the treatment of brain tumors were presented. The different technical solutions tried in the last few decades were described and the needs still facing by surgeons explained. Technologies able to image or give information at a cellular scale have been adapted and designed for intra-operative clinical use. The latest technologies attracting interest and attention for being able to provide real-time differentiation of tumor cells are Raman spectroscopy [205] and multi-photon microscopy [134, 199, 204] based on the intrinsic fluorescence. These techniques are still at the proof of concept stage and have yet to be implemented in phase III clinical trials and in routine protocols. One of the major technical missing elements in the development to this point is the lack of multimodal detection, along with a high quality database on the studied tissue. Consequently current technology fails to give discrimination reliable enough for clinical standards. This leaves room for further development of a precise and reliable technology to assist brain tumor surgery, since brain tissue in particular lacks of an optical database on its autofluorescence response.

The research team of Dr Darine Abi Haidar at the IMNC laboratory have chosen to work on this clinical question bringing their technical expertise to the medical world. This research group has experience in optics and microscopy, more precisely in non-linear techniques. Drawing on the

strength of their expertise, they created a project with clinical partners, to bring to the operating room a new intra-operative technique. Looking at the various directions and approaches described in the literature, and based on their experience, they sought a technology capable of a high spatial resolution, miniaturized and adapted to the surgical operating room, with reliable and reproducible multimodal detection. The technical solution chosen by Dr. Abi Haidar's team is a two-photon endomicroscope with multimodal detection combining two imaging modalities (emitted fluorescence and second harmonic generation). In addition there are two quantitative modalities (spectroscopy and lifetime measurements) to monitor the autofluorescence of tissue.

It is in the context of this project that I was recruited to do my PhD. When I arrived, this dynamic research team had already reached several milestones in the development of such a tool. An intra-operative probe combining fluorescence and lifetime detection with a visible excitation, 375 and 405nm had been developed and tested on rat brain tissue [128]. The promising results obtained in these tests, brought this first set-up at the Sainte-Hospital close to the operating room to acquire data and suggested the development of a more advanced technology. They worked on the development of a two-photon endomicroscope, with a miniaturized probe to achieve the diameter of a surgeon's trocar, a tool with a 1.9 mm inner diameter. They worked on the development of a compensation unit based on the process of a GRISM line [195], and looked at the best fiber to achieve simultaneous excitation and collection in a two-photon microscope configuration [196]. They chose first to characterize various commercially available double clad fibers in order to determine if one could be suited to this application [196]. Then they looked at the resolution and collection efficiency that could be obtained combining these DCF with GRIN objectives [197]. These studies reached conclusions about an available architecture for a two-photon endomicroscope, however the best suited fiber did not yet exist. So they described the ideal fiber as a combination of some of the tested fibers, thus leading to the development of a custom made DC-PCF. These results showed the technical relevance and the possibility of two-photon endomicroscopy, however to bring a new technique to the operating room, its ability to answer the medical challenges has to be proved. In brain tumor has shown by the review of literature, there is only a few things done on two-photon imaging and quantitative detection of tissue fluorescence. In order to give sense to our technical development and to prove that medical practice could be revolutionized using optical endomicroscopy, a large project of establishing a database on the autofluorescence response of tissue was developed. This was the task of my PhD, working on brain biopsy samples, different optical excitations and methods of detection were tested to collect a large amount of data and developed reliable and reproducible algorithm to discriminate the nature of brain tissue. Several collaborations were developed to reach the most extensive and accurate database possible.

### 1.7.2 Actors and partners

I conducted my PhD at the IMNC laboratory a mixed unit of the CNRS (National Center of Scientific Research) and the French university (University of Paris Saclay and Paris Diderot). This lab contains several research teams all working on developing themes at the interdisciplinary boundaries of physics, biology and medicine, hosting talents from each field in the same environment. The three leading problems of the laboratory are: multimodal, pre-clinical and peri-clinical imaging (optical and isotopic), the modeling of tumoral processes and new approaches in radiotherapy. The lab contains a technical services and a biology team in addition to several research teams in the different themes. In this context, Dr. Darine Abi Haidar has formed a group developing non-linear endomicroscopy to improve, by optical methods, the quality of surgical procedure. With this project

## CHAPTER 1. INTRODUCTION

she was able to receive several funding from the CNRS, "plan Cancer", and create a flourishing environment for such a technological project. Consequently several collaborations were initiated.

For the technical development of the endoscope two collaborations were put in place. The team of Alexandre Kudlinsky of PhLAM (Physique des Lasers, Atomes et Molécules, Lille, France) lab. They work using a dedicated platform on the development of photonic crystal fibers (PCF) with properties adapted to the targeted application. A collaboration was put in place with them to develop a customized double clad photonic crystal fiber (DC-PCF) for the multi-photon endomicroscope answering the specifications defined through the characterization of commercial fibers [128]. The second collaborator for the technical development is the Sainte-Anne Hospital Center, (CHSA, Paris, France) specialized in psychiatry and neurology. This hospital is known to be one of the most active research centers. During the last century it has been the catalyzer of ground breaking techniques, such as the use of neuro-epileptic or stereotactic surgery. In the last few decades they developed a very strong department of neuro-oncology, able to diagnose and treat all types of tumor of the central nervous system (brain, meninges, nerve, ...). Developing a surgical tool without surgeons advice and guidance will lead nowhere. To envision a successful future endomicroscope, surgeons were questioned during various phases of design in order to build a tool adapted to their habits and workflow.

Sainte-Anne Hospital was also the main collaborator for the development of an optical database on brain tumor tissue. Their neurosurgery and neuropathology departments have been working closely with us to provide a large number of biopsy samples of different brain tumors and control tissues. They brought their knowledge on tissue diagnosis and analysis of histological staining to the project, and discrimination criteria were found in collaboration with them.

The second collaborator on the optical database was Synchrotron SOLEIL (Source Optimisée de Lumière d'Energie Intermédiaire du LURE) located in the city of Saint-Aubin in France. SOLEIL is a particle (electron) accelerator producing synchrotron radiation. The emitted light source has a brilliance ten thousand times brighter than sunlight, with a spectral range from infrared to hard X-rays. Further, it can be polarized and pulsed. We worked on the DISCO beamline (Dichroism, Imaging, mass Spectrometry for Chemistry and biology), that delivers deep ultra-violet (DUV) excitation and offers a detection station optimized at these wavelengths. Two setups are available at the DUV imaging center : A micro-spectrometer called POLYPHEME and a fast full field microscope with Z scanning and 3D reconstruction known as TELEMOS. This collaboration gave us access to a larger range of excitation to study the autofluorescence of tissue and have a better understanding of the studied response.

### 1.7.3 Design of the project

Due to these different collaborations and the previous work done by this research team, a large set of biopsy samples were accessible from the CHSA and three imaging platforms. First, at Sainte-Anne Hospital a visible endoscope in the neuropathology department could measure one-photon spectral and fluorescence lifetime response of tissue. Second at the IMNC, the PIMPA (plateforme d'imagerie du petit animal) platform consisted of a two-photon microscope with four modalities of detection (fluorescence imaging, SHG, spectroscopy and FLIM). And third, At SOLEIL, DUV microscopy was possible on two setups with imaging and spectroscopy detection. From this several problems could be considered and tackled :

Could quantitative bimodal optical measurements under visible excitation discriminate fixed brain tissue nature ?

Were spectral and lifetime measurements, under visible excitation, able to discriminate freshly extracted brain tissue nature? Were fluorescent measurements established on fixed tissue suitable enough to build an optical database ?

Could mono and bi-photon excitation discriminate label-free fluorescence emission of meningioma tumor grade?

Could two-photon imaging match the performances of H&E standard discrimination of primary and secondary brain tumor? Could multimodal quantitative detection improve brain tumor diagnosis ?

How could multi-range and multimodal optical study improve the precision and reliability of primary and secondary tumor discrimination ?

These questions will be answered through the articles written during my PhD project. In the last part I will discuss the place in the literature of such results, and to what extent we were able to shown a discriminative power on low density tumor cell regions. Finally, the future perspectives of such a project will be presented along with the new paths already being explored to improve such technology to furnish them to surgeons and hospitals.

## Chapter 2

# Could quantitative bimodal optical measurements under visible excitation discriminate fixed brain tissue nature ?

### 2.1 Context of the study

A bimodal endoscope under visible excitation able to acquire quantitative measurements was build and tested on rat by previous members of my research team [128]. It tracks the spectral response and the fluorescence lifetime of intrinsic molecules.

Fluorescence emission is very dependent on the absorption and the scattering of tissues and surrounding environment (hemoglobin, water). These two parameters can be known by calculating optical coefficients of absorption, scattering and anisotropy [206]. Different set-ups and methods of analysis have been tried in the literature. The knowledge of the optical properties of the tissue, obtained with different optical techniques can help to :

- Correct the spectral response of the different environmental absorbers, such as water, hemoglobin, fibers, melanin, ...
- Understand the variation of the emitted spectral intensity from one tissue to another.
- Differentiate tissue nature following scattering, depending on cells morphological structures, and absorption, depending on chromophores (blood, water, melanin, fat, yellow pigments) content.

Different studies from the literature attempt to characterize optical properties of health and tumoral human brain tissues. The major results are summarized in table 2.1.

These studies, performed on human brain tumor samples and healthy white or grey matter, have highlighted differences between healthy regions and tumors. In the majority of the studies the absorption of tumor tissues (glioma, GBM, meningioma) is higher than in healthy regions [207–

## 2.1. CONTEXT OF THE STUDY

Paper	Wavelength	Samples	Results
Eggert et al. 1987	200nm to 900nm	Frozen samples from 13 human cadavers White matter, grey matter, glioma, GBM and meningioma	No statistical differences between tumor types, White matters significantly different of all tumors for absorption and scattering,GBM and meningioma showed higher absorption than grey matter
Van der zee et al. 1993	500nm to 1000nm	2 post mortem neonatal brain samples, 2 postmortem adult brain samples	Comparison between white and grey matter $\mu_{agm} = 0.035mm^{-1}$ and $\mu_{awm} = 0.002mm^{-1}$ , $\mu_{sgm} = 62mm^{-1}$ and $\mu_{swm} = 47mm^{-1}$
Bevilacqua et al. 1999	674, 811, 849 and 956nm	2 patients with <i>in vivo</i> measurements during brain surgery	$\mu_{atumor}(0.09mm^{-1}) > \mu_{ahealthy}(0.03mm^{-1})$ , explained by higher vascularity in tumor. No significant differences in scattering
Yaroslavski et al. 2002	360nm to 11000nm	7 postmortem patients with healthy brain, 6 meningioma biopsy, 4 astrocytoma biopsy	Tumor tissue presented slightly higher scattering coefficients than normal grey brain $\mu_{sgm} \in [5, 10]mm^{-1}$ and $\mu_{st} \in [10, 20]mm^{-1}$ White matter compared to grey matter $\mu_{agm} \approx 0.002mm^{-1}$ and $\mu_{awm} \approx 0.01mm^{-1}$
Gebhart et al. 2006	400 to 1300nm	83 samples on 12 patients acquired during tumor resection open craniotomy	Significant differences with the scattering coefficient : white matter > tumor > grey matter. In absorption glioma are higher than grey matter after 700nm

Table 2.1 – Summary of literature on measurements of optical coefficient from brain tissue

210]. One group explained this difference by the presence of denser vascularity in tumor [208]. Hemoglobin being a strong absorber, the absorption coefficient will drop. Differences could also be found in the scattering. Two groups found a higher scattering in white matter than grey matter [209, 210], but one group found an opposite variation [211]. In two studies a higher scattering was found in tumor compared to grey matter [209, 210]. The literature contains collected data, on brain tumor tissue highlighting differences in the optical properties of tissues, and suggests the possibility of discriminating them based on intrinsic optical technique. Moreover it shows that the measurement of optical coefficients could be a diagnosis tool by itself.

A limitation noted in the literature is the lack of extensive study on large statistically significant cohort. Of the five articles three were based on fewer than 10 patients [208, 209, 211]. The other two contained 13 [207] and 12 patients (with 84 samples taken over the twelve patients)[210]. This lack of statistical significance combined with very different experimental conditions and deployed algorithms from one study to another results in values that are hardly comparable. Because the data values in the literature were very specific to the set-up configuration, tissue conservation, and method of analysis, it would have been biased to choose one as a standard.

In this first test of a bi-modal endoscope with visible excitation on human tissue, the question set to be answered was : can quantitative measurements of endogenous fluorescence signal discriminate brain tumor tissue type ? A study was designed, where spectral and lifetime endoscopic measurements were coupled to the measurement of optical parameters. Biopsies from twenty different patients were used to find quantitative discrimination between tumor types, and relate it to the intrinsic properties of tissue (absorption, scattering and anisotropy).

**Methods** A cohort of twenty-eight fixed in alcohol samples of brain tumor biopsy was analyzed at three different wavelengths, 375, 495 and 430nm, on two different set-ups. The samples were slices of 200 and 600 microns, from 10 healthy cortex, 10 metastasis, 4 diffuse glioma and 4 GBM. An integrating sphere set-up was used to determine the optical coefficients with a 430nm excitation diode laser. The second set-up was the bi-modal endoscope used in the previous rat study [128]. Spectral and lifetime measurements were done using 375 and 405 nm excitation.

**Results and discussion** A threshold value was found between control and tumor in both scattering and absorption coefficient. Looking at the scattering parameters, tissues with  $\mu_s < 26 \text{ mm}^{-1}$  were healthy and the ones with  $\mu_s > 29 \text{ mm}^{-1}$  were tumoral, in the interval where  $\mu_s \in [26, 29] \text{ mm}^{-1}$  no conclusion could be drawn on the tissue nature. For the absorption a threshold value around  $1 \text{ mm}^{-1}$  could be determined between control and three tumoral groups, glioblastoma, meningioma and metastasis. However the absorption coefficient of diffuse glioma wasn't significantly different from control. The metastasis could also be significantly discriminated from the other tumors using the absorption coefficients. These differences from tumor to healthy tissue could be explained by changes in tissues architecture and environment during tumor growth. In tumor, denser networks of collagen fibers form, which is a notable source of scattering. The meningioma is a tumor with particularly dense structures of collagen (psamome, enrollment of collagen fiber,...) and it resulted in the higher scattering coefficient. The increase in absorption was explained by the presence of denser vascularization in tumor, hemoglobin being a strong absorber of light. Metastasis, a tumor with formation of a highly dense vascular network resulted in the highest absorption coefficient significantly different from the other tissues. Even if it is difficult to truly compare values to the literature, the experimental conditions were very close to Yaroslavsky et al. and the values found were very similar to theirs [209]. These results highlighted that the intrinsic optical signal will



change from one tissue type to another as its optical coefficients are different, and could be a discriminative tool when monitored with quantitative measurements. However these differences in optical parameters also show that scattering and absorption could be an indicator for diagnosis, and that combining the results of both will give significant results from all types of tumor compared to control, even diffuse glioma.

The second part of the study was analysis of these biopsy samples using the bi-modal endoscope. The first response to be observed was the emitted spectral intensity and shape using 375 and 405nm excitation wavelengths. A higher emitted intensity in healthy tissue compared to all tumor types was found at both excitation wavelengths. This confirmed the conclusions made by looking at the optical properties. The variation of intensity from one tissue to another was in line with the observed change in absorption and scattering coefficients. An algorithm to fit the spectral response of the molecular contribution, allowed monitoring of a metabolic indicator, the redox ratio (NADH/FAD ratio), and the ratio between NADH and porphyrins, an indicator of various process such as transport of oxygen and catalysis [106]. The two indicators resulted in a significantly higher value in control than in tumoral tissue : at 375nm excitation for the redox ratio and a 405nm excitation for the NADH/Porphyrin ratio.

To confirm these results, a second parameters of fluorescence was evaluated, the fluorescence lifetime. The fluorescence lifetime is sensitive to different factors than is spectral response. It will be influenced by the molecular environment and conformation, whereas spectral response is more sensitive to the concentration of molecules. The lifetime of each molecules contributing to the fluorescence response was measured. A discrimination was found between control, glioblastoma and meningioma looking at the NADH lifetime at both 375 and 405 excitation. The porphyrin lifetime measured under 405nm excitation had a different value for each of the five groups of tissue while control tissue had the longer lifetime. As in the rat studies [128], porphyrin was revealed to be an important indicator of tissue nature, giving a discriminative response between each type of brain tissues, healthy or tumoral.

This first study on the quantitative analysis of the endogenous fluorescence, using a visible endoscope with bi-modal detection, showed promising results for discriminating brain tissues. These results were obtained on a significant cohort including twenty-eight patients. However this first study was done on fixed *ex vivo* samples and it has been shown in the literature that the optical parameters will certainly change in *in vivo* conditions [206]. Concentration of blood and water can be different and this will cause variation in optical response. All these observations lead my research project answering a second question : can we also quantitatively discriminate fresh biopsy with a bi-modal endoscope and how will the results differ from to *ex vivo* measurements ? This was the work of a second study that will be developed in the next chapter.


## 2.2 Paper: Optical properties, spectral, and lifetime measurements of central nervous system tumors in humans

www.nature.com/scientificreports

# SCIENTIFIC REPORTS

OPEN

## Optical properties, spectral, and lifetime measurements of central nervous system tumors in humans

F. Poulon<sup>1</sup>, H. Mehidine<sup>1</sup>, M. Juchaux<sup>1</sup>, P. Varlet<sup>2,3</sup>, B. Devaux<sup>4,5</sup>, J. Pallud<sup>3,4,5</sup> & D. Abi Haidar<sup>1,6</sup> 

Received: 26 July 2017

Accepted: 9 October 2017

Published online: 25 October 2017

A key challenge of central nervous system tumor surgery is to discriminate between brain regions infiltrated by tumor cells and surrounding healthy tissue. Although monitoring of autofluorescence could potentially be an efficient way to provide reliable information for these regions, we found little information on this subject, and thus we conducted studies of brain tissue optical properties. This particular study focuses on the different optical quantitative responses of human central nervous system tumors and their corresponding controls. Measurements were performed on different fixed human tumoral and healthy brain samples. Four groups of central nervous system tumors (glioblastoma, diffuse glioma, meningioma and metastasis) were discriminated from healthy brain and meninx control tissues. A threshold value was found for the scattering and absorption coefficient between tumoral and healthy groups. Emission Spectra of healthy tissue had a significant higher intensity than tumoral groups. The redox and optical index ratio were then calculated and these also showed significant discrimination. Two fluorescent molecules, NADH and porphyrins, showed distinct lifetime values among the different groups of samples. This study defines several optical indexes that can act as combined indicators to discriminate healthy from tumoral tissues.

The success of oncological surgery, the most widely used curative treatment for solid tumor whatever its histopathological type, is based on the accurate identification of the tumor's boundaries in order to achieve a complete tumor resection. For tumors of the central nervous system, the goals of oncological surgery are identical but their realization is made more difficult by their infiltrating character, especially the diffuse gliomas, within a highly eloquent organ. The main challenge of any neurosurgical oncological intervention is to define the limits of the resection while optimizing the onco-functional balance<sup>1</sup>. Resection is based on the limits of tumor infiltration, which should be removed, and on the identification of eloquent brain areas, which should be respected. The actual identification of the tumor infiltration at the cellular scale is not possible intraoperatively and requires the development of an efficient and reliable intraoperative imaging tool, based on an imaging database of the main tumors of the central nervous system (diffuse gliomas, metastases, meningiomas, and healthy tissues).

The development of an intraoperative probe/device should be accompanied by the construction of a large database of endogenous fluorescence response of tumor tissues. This intraoperative tool, in association with knowledge on collected optical response, will lead to an "optical biopsy" giving a real time result, and providing additional relevant morphological and physiological information during surgery, which may guide the surgical resection.

The optical properties of biological tissues have a major importance in several medical applications for diagnosis and therapy<sup>2</sup>. Knowing the optical properties of brain tissues results in quantitative information<sup>3</sup>, which allows the optimization of imaging techniques and the possibility of modeling the light path, the fluorescence distribution, the penetration depth and the possible interaction between fluorophores in the tissues. These parameters are related to the density and the distribution of sizes of the ultrastructure of a tissue, thus allowing the characterization of the tissues, particularly the differentiation of tumoral tissues from healthy ones—in other words, detection of the evolution of a pathology. Current knowledge of optical properties of healthy and tumoral brain

<sup>1</sup>IMNC Laboratory UMR 8165-CNRS/IN2P3, Paris-Saclay University, Orsay, 91405, France. <sup>2</sup>Neuropathology Department, Sainte-Anne Hospital, Paris, 75014, France. <sup>3</sup>IMA BRAIN, INSERMU894, Centre de Psychiatrie et de Neurosciences, Paris, France. <sup>4</sup>Neurosurgery Department, Sainte-Anne Hospital, 75014, Paris, France. <sup>5</sup>Paris Descartes University, Paris, France. <sup>6</sup>Université Paris Diderot, Sorbonne Paris Cité, F-75013, Paris, France. F. Poulon and H. Mehidine contributed equally to this work. Correspondence and requests for materials should be addressed to D.A. (email: [abihaidar@imnc.in2p3.fr](mailto:abihaidar@imnc.in2p3.fr))

### 2.2.1 Introduction

The success of oncological surgery, which the most widely used curative treatment for solid tumor whatever its histopathological type, is based on the accurate identification of the tumor's boundaries in order to achieve a complete tumor resection. For tumors of the central nervous system, the stakes of oncological surgery are identical but their realization is made more difficult by the infiltrating character of several tumors of the central nervous system, especially the diffuse gliomas, within a highly eloquent organ. The main challenges of any neurosurgical oncological intervention is defining the limits of the resection while optimizing the onco-functional balance<sup>1</sup>. Resection is based on the limits of tumor infiltration, which should be removed, and on the identification of eloquent brain areas, which should be respected. The actual identification of the tumor infiltration at the cellular scale is not possible intra-operatively and requires the development of an efficient and reliable intra-operative imaging tool, based on an imaging database of the main tumors of the central nervous system (diffuse gliomas, metastases, meningiomas, and healthy tissues). The development of an intra-operative probe/device should be accompanied by the construction of a large database of endogenous fluorescence response of tumor tissues. This intra-operative tool, associated with a knowledge on collected optical response, will lead to an "optical biopsy" giving a real time result, and providing additional relevant morphological and physiological information during surgery, which may guide the surgical resection.

The optical properties of biological tissues have a major importance in several medical applications for diagnosis and [208]. Knowing the optical properties of the brain tissues results in quantitative information[209], allowing the optimization of imaging techniques and the possibility to model the light path, the fluorescence distribution, the penetration depth and the possible interaction between fluorophores in the tissues. These parameters are related to the density and the distribution of sizes of the ultrastructure of a tissue, thus allowing the characterization of the tissues and in particular the differentiation of the tumoral tissues from healthy ones (detection of the evolution of a pathology). The knowledge of optical properties of human brain, healthy and tumor tissues is currently insufficient and do not exist for different tumoral variety [206, 212, 213]. There is a lack of data in the visible spectral range, especially for 405 nm excitation wavelength, which is optimal to excite different endogenous fluorophores such as nicotinamide adenine dinucleotide (NADH), flavins (FAD), lipopigments and porphyrins, but also a lack of results on human brain tissues[208, 209] where at the contrary we can find a large literature on rats, mice, pigs and kidney[214, 215]. Willing to answer the surgeon needs, this lack of guidance in the literature motivate our exploratory study on the optical coefficients, absorption, scattering and anisotropy. These optical parameters are required to apprehend correctly the signal from endogenous fluorescence of tissue, but to have a quantitative answer in real time of tissue nature. The most suited and growing technique is to follow the spectral response. Few research teams have already started to work on spectral emission of healthy or tumoral brain tissue [102], still none of them have really tackled a large type of brain tumors. Our previous study on the grade of malignancy of meningiomas in adults [216], gave us interesting results through the spectral response to discriminate tissues. Here, this will be applied to a larger cohort and will also be used to follow the metabolic changes. Indeed, we can find in the literature that some groups have started to calculate the ratio between the contribution of the molecules in the emission spectra to track the metabolic reaction [118, 217, 218]. Another quantitative response appear with the progress in nonlinear optics and the access to femtosecond pulsed laser, which is the measurement of the fluorescence lifetime[129, 137]. This measure is not influenced by the concentration, but by the conformational or environmental changes surrounding the fluorescent molecules. A study of the optical properties, the spectral response and

lifetime of the endogeneous fluorescence on brain tissue, will allow to have an understanding of the evolution of the hyperstructure, the metabolic process and environment going from a healthy region to a tumoral region. In this paper, we studied a wide cohort of brain tissues, including four tumor types and a control group (epileptic cortex). To span the wider range of tumor type, we chose primary (glioblastoma, meningioma and diffuse glioma) and secondary (metastasis) tumors of the central nervous system. Several optical properties were looked at, using integrating-sphere techniques and employing an inverse Monte Carlo technique. The absorption, scattering and anisotropy coefficients were measured using 405 and 430 nm excitation wavelengths. Moreover, spectral and lifetime fluorescence measurements were acquired on these tissues using 405 nm and 375 nm excitation wavelength. The 405 nm excitation wavelength was used to excite and collect efficiently the fluorescence signal of five endogenous fluorophores : NADH, FAD, lipopigments, porphyrins and chlorins. The 375 nm excitation wavelength was used to excite efficiently the NADH and the FAD. The 405 and 430 nm excitation wavelengths were used in the integrating sphere technique to study the effect of the wavelength on the optical coefficients. Through the analysis of all these quantitative data, we were able to define several discriminatory indicators between control and tumor samples and also we were able to discriminate several tumor types and grades of malignancy.

## 2.2.2 Materiel and methods

### 2.2.2.1 Samples

An approval of the Sainte-Anne Hospital - University Paris Descartes Review Board (CPP Ile de France 3) was obtained for this study in collaboration with the Neurosurgery and the Neuropathology Departments of the Sainte-Anne Hospital (S.C.3227). All the following methods were performed in accordance with the relevant guidelines and regulations from this protocol and a informed consent was obtained from all participants and/or their legal guardians.

<b>Healthy</b>	<b>10</b>
<b>Metastasis</b>	<b>5</b>
Thyroid carcinoma	1
Colloid adenocarcinoma	2
Primary renal carcinoma	1
Cell lung carcinoma	1
<b>Diffuse Glioma</b>	<b>5</b>
<b>Glioblastoma</b>	<b>4</b>
<b>Meningioma</b>	<b>4</b>

Table 2.2 – Summary of the cohort used in the paper

A cohort of twenty height samples was used , the repartition is resumed in the Table 2.2. A group of ten healthy cortex samples was obtained from epileptic surgery and compared to four different groups of central nervous system tumor. The tumoral cohort contains four Isocitrate Deshydrogenase (IDH) wildtype glioblastomas, five IDH-mutated diffuse gliomas, five meningiomas and five carcinoma metastases originating from different part of the organism

Once received from the hospital, the samples were stored at -80°C. Few hours before cutting they were put at -20°C. Then, the tissues were cut at -18°C into 200  $\mu\text{m}$  and 600  $\mu\text{m}$  slices using a cryostat (CM 1950, Leica Microsystems). After, tissues were fixed with ethanol at 100° and

stored at 4°C until the experiment. The slices of 200  $\mu\text{m}$  were used in the integrating sphere set-up to measure the optical coefficients and the slice of 600  $\mu\text{m}$  were use in the endoscopic set-up for spectral and lifetime measurements.

### 2.2.2.2 Integrating sphere set-up

A standard set-up was used for the measurements of transmittance  $T(\lambda)$  and reflectance  $R(\lambda)$ . It consists of an integrating sphere (model : IS200-4 thorlabs) including four identical ports, each port has a 12.7 mm diameter, and a fifth port with a 3 mm diameter used to collect light from the sphere to a spectrometer (HR2000-Ocean optics) using an optical fiber (QP60-600 $\mu\text{m}$  diameter, Ocean optics). The excitation was achieved with two laser diodes, emitting at 430 nm (LDH-P-C-430B, Picoquant Germany) and 405 nm (LDH-P-C-405B, Picoquant Germany ) respectively with a maximal power of 5.1 mW and 1 mW respectively. To have a 1 mm laser beam diameter, a diaphragm was placed just after the laser diodes. For collimated transmittance measurements, the integrating sphere is not used, three diaphragms were aligned in front of the laser, and an absorbant filter (OD=2.3) is placed to reduce the laser intensity. In each sample, five regions of interest (ROI), selected in area of same visual appearances, for the transmittance, the reflectance and the collimated transmittance were measured. The average of these five measurements was used to determine the optical coefficients of the sample.

### 2.2.2.3 Spectral and lifetime measurements

Details of this setup were published elsewhere [198, 216] .The excitation is performed with two pulsed diode lasers from Picoquant, emitting at 405 nm (LDH-P-C-405B, FWHM 60 ps, Picoquant-Germany) and 375 nm (LDH-P-C-375B, FWHM 45ps, Picoquant-Germany). The diodes are controlled by a driver (PDL-808 "Sepia", PicoQuant GmbH, Berlin, Germany), the repetition frequency used for this study is 40 MHz. A single-core fiber with a 200  $\mu\text{m}$  diameter, is used to bring the excitation to the sample, the signal is then collected through a single-core optical fiber with a 365  $\mu\text{m}$  diamter. Then the collected signal goes through a long pass filter (SR420, Semrock) to cut the signal from laser reflection. For spectral measurement, a spectrometer (QEPro 6500, Ocean Optics, 1.5 nm spectral resolution over a 365-950 nm spectral range) was used. For lifetime measurements a filter wheel (FW102C, Thorlabs, Newton, USA) with five filters (Semrock, New York, USA, 450  $\pm$  10 nm, 520  $\pm$  10 nm, 550  $\pm$  30 nm, 620  $\pm$  10 nm and 680  $\pm$  10 nm) in front a photomultiplier link to TCSPC acquisition card (PMA 182 and Time Harp 200, Picoquant, Germany) was used.

### 2.2.2.4 Data analysis

#### 2.2.2.4.1 Optical properties

Reduced scattering ( $\mu_s'$ ), absorption ( $\mu_s$ ) and anisotropy coefficients (g) of the samples were obtained from measured values of the reflectance, transmittance and collimated transmittance using the Inverse Adding Doubling (IAD) algorithm developed by scott Prahl (<http://omlc.ogi.edu/software/iad/>) [219]. This algorithm solves iteratively the radiative transport equation until the numerical adjustment and the experimental values of reflectance, transmittance and collimated transmittance matches, it takes also the parameters of the sample, the laser beam and the integrating sphere used into account to find the optical coefficients desired Noting that  $\mu_s'$  is the reduced scattering coefficient, we will deduce the scattering coefficient  $\mu_s$  using the equation 2.1

$$\mu_s = \frac{\mu_s'}{1 - g} \quad (2.1)$$

According to the literature [206, 208], the refractive index of human brain tissues is between 1.33 and 1.53. We have considered that the refractive index is  $n = 1.4$  for all samples [208].

#### 2.2.2.4.2 Spectral analysis

At the excitation of 375 and 405nm five fluorophores are excited : NADH, FAD, lipopigments, porphyrins and chlorines. The measured spectra present the sum of the emission spectrum of these endogenous fluorophores. Spectral data are processed from a Matlab program developed previously by our team and already used in a previous publication[216], using this program we can determine the contribution of each molecule by adjusting the measured data to the equation 4.1.

$$S_{total}(\lambda) = \sum_i f_i S_i(\lambda) \quad (2.2)$$

$S_{total}(\lambda)$  : measured spectra  
 $i$  : the fluorophore  
 $S_i(\lambda)$  : emission spectra of fluorophores  $i$   
 $f_i$  : multiplying coefficient

NADH spectra is adjusted by a spectra obtained from a previous experiment done by our team on rats at 375 nm [128]. FAD spectra is adjusted by a spectra taken from the literature [220], The other spectras of Lipopigments, Porphyrins and Chlorins are given by Gaussian adjustment.

#### 2.2.2.4.3 Lifetime analysis

The measured fluorescence decay curves obtained are adjusted by a mono-exponential fit using FluoFit software (Picoquant,Germany), which allows us to extract the fluorescence lifetime of the curve. Two criteria are taken into account to validate the fit :  $\chi^2$  must be  $-1.2 < \chi^2 < 1.2$ , and the residuals must have a distribution around 0 in an interval of  $[-4, 4]$ .

#### 2.2.2.4.4 Staistical analysis

Optical coefficients(scattering and absorption) and fluorecence lifetime results were evaluated using a one-way analysis of variances (ANOVA). If the ANOVA was statistically significant, a post-hoc t-test was performed. A probability value (p)  $< 0.05$  was considered statistically significant.

### 2.2.3 Results

Figure 2.1 summarizes the scattering ( $\mu_s$ ) and absorption ( $\mu_a$ ) coefficient for different types of brain tissues at two different excitation wavelengths. Figure 2.1.a and .b show the scattering coefficient results for healthy (control) and tumoral (diffuse gliomas, metastasis, meningioma and

glioblastoma tissues). The tumoral tissues present a significantly ( $p < 0.001$ ) higher scattering coefficient Figure 2.1.c and .d represent the absorption coefficient of tumoral and control tissues. Metastasis, meningioma and glioblastoma are significantly ( $p < 0.001$ ) different from control tissues. Diffuse gliomas other than glioblastoma have an absorption coefficient not significantly different from those of control tissues ( $p = 0.09$ ).

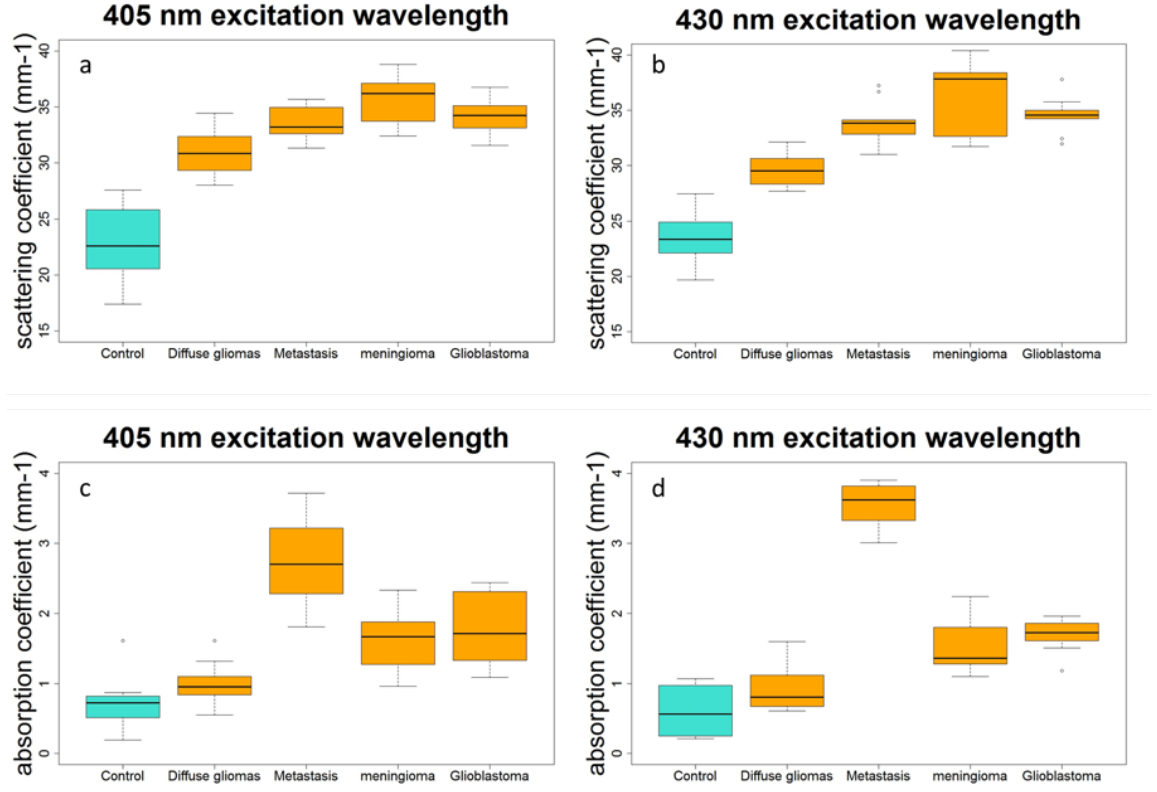


Figure 2.1 – Distribution of scattering coefficient values for tumoral and healthy control tissues excited with 405 nm(a) and 430 nm(b) , and of absorption coefficient using 405 nm(c) and 430 nm (d) excitation wavelengths.

The anisotropy coefficient could also be calculated for 405 and 430 nm excitation wavelength. The results for the different groups are plotted in figure 2.2. Three groups of tissues had already been examined in the literature and allowed us to compare our values, the meningioma with a  $g = 0.87$  [209] where we found 0.87 and 0.86 , the control tissue with a  $g = 0.86$  [209] where we found 0.85 and 0.865 and the diffuse gliomas with a  $g = 0.88$  [209] where we found 0.90 and 0.20. Our value were in line with the previous literature which validate our set-up and protocols. We also did measure two other types of tumor that were not tackled before, adding information to the existing literature. A trend can be extracted from the value, the tumoral tissues tend to have higher  $g$  value than the control tissues, nevertheless this is not statistically significant.

Having seen these differences in the fundamental optical properties of the tissue, we needed to

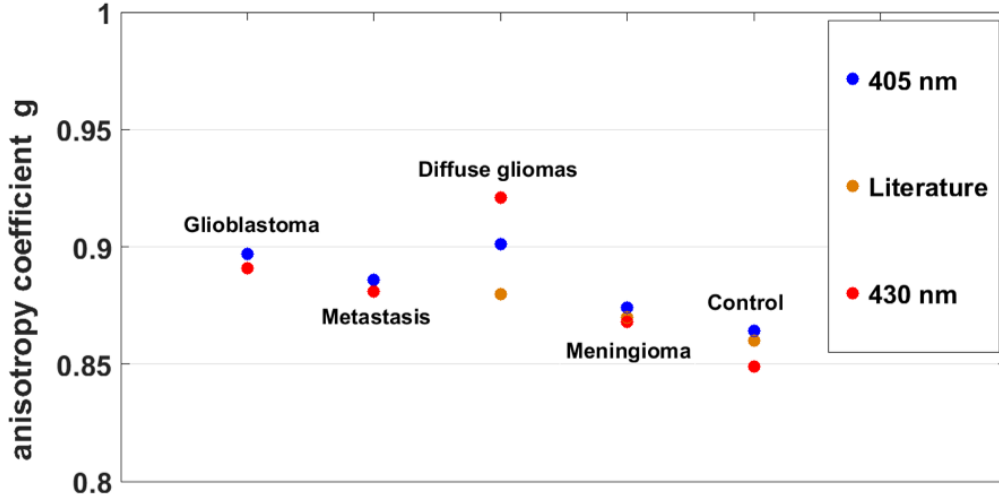


Figure 2.2 – Average of anisotropy coefficient  $g$ , under 405 and 430 nm wavelength excitation and compared to the  $g$  values found in literature.

look at other measurements of the endogenous fluorescence, that could be implemented more easily *in vivo* and could also give an insight on the metabolic state of the tissue. Through a first bi-modal device developed in our group [221], we did measure consequentially the spectral and fluorescence lifetime response from tissues. Figure 2.3 presents the emitted fluorescence of each type of tissue at the 375 and 405 nm excitation wavelengths. The shapes of the spectra change with 405 nm excitation wavelength. At this wavelength, we were able to excite five endogenous molecules. With 375 nm, we efficiently excite NADH and FAD only, thanks to their higher absorption cross section at this excitation wavelength. We can underline a difference in the fluorescence intensity between each type of tissue. The gap between control and tumoral tissues was significant and encouraging. At both wavelengths, the healthy tissue has significantly higher intensity than tumoral tissue. This is explained by the lower absorption and scattering coefficient in healthy tissue that results in more fluorescence emitted and collected by our set-up.

Every spectra is the sum of emission spectrum of five fluorophores : NADH, FAD, lipopigments, porphyrins and chlorins. In addition, by calculating the integral under the curve of the emission spectra of NADH, FAD and the porphyrins, using a Matlab program developed by our team[128], we obtained two different ratios under 405 nm and 375 nm excitation wavelength.

Under 375 nm excitation wavelength, we calculated the redox ratio [217] :

$$ROx = \frac{FAD - NADH}{FAD + NADH} \quad (2.3)$$

Under 405 nm excitation wavelength, we calculated the optical index ratio[222] :

$$OIR = \frac{NADH}{Porphyrins} \quad (2.4)$$



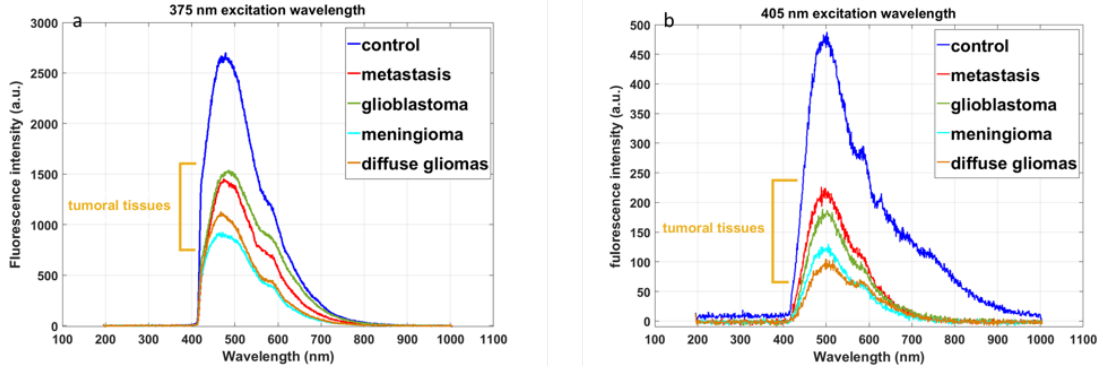


Figure 2.3 – Fluorescence spectra of all tissues excited with 405 nm wavelength (a) and 375nm (b).

At 375 nm, the calculated ratio has negative values because NADH is more present in brain tissues than FAD at the excitation wavelength [128, 223]. As shown in Figure 2.4.a, the healthy tissues have a higher ROx than tumor tissues ( $p < 0.001$ ), which is inline with the literature [217]. At 405nm, the Figure 2.4.b also shows a significant difference ( $p < 0.001$ ) tumoral and healthy tissues. Similar results were obtained on bladder tumor tissues [223].

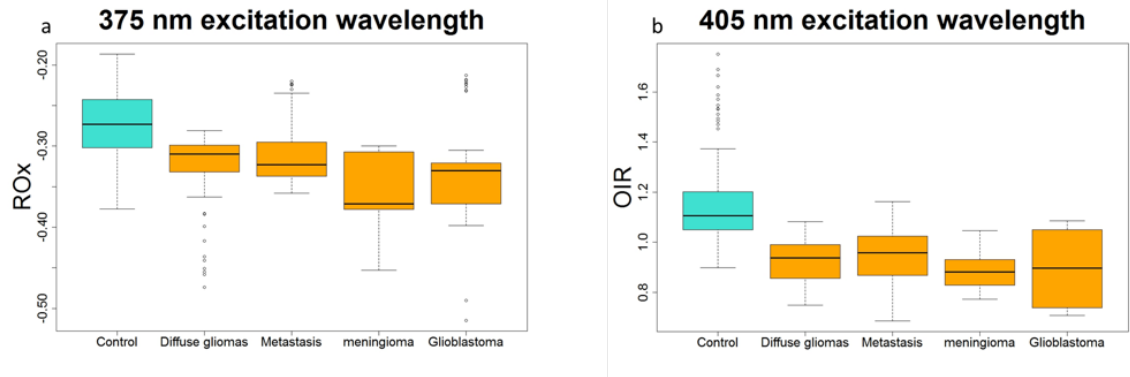


Figure 2.4 – (a) Variation of the ROx report of all tissues excited with 375 nm and (b) Variation of the NADH/ Porphyrins of all tissues excited with 405 nm.

To complete our study, we also collected data from a promising quantitative technique, the fluorescence lifetime. As previously done, we used two excitation wavelengths, 375nm and 405nm. We had a closer look at two molecules emitting endogenous fluorescence, this choice was motivated by our previous study on a cohort of fresh samples that highlights the changes in NADH and our study on brain rats that show a variation in porphyrins [128, 223].

In Figure 2.5.a and .b we see that at both excitation wavelengths, the NADH presents a difference in lifetime between glioblastoma, meningioma, and control samples. Nevertheless, at 405 nm excitation wavelength, control has a shorter lifetime than healthy tissue, where at 375nm the control has a longer lifetime. The meningioma is very well distinguished from the control tissue

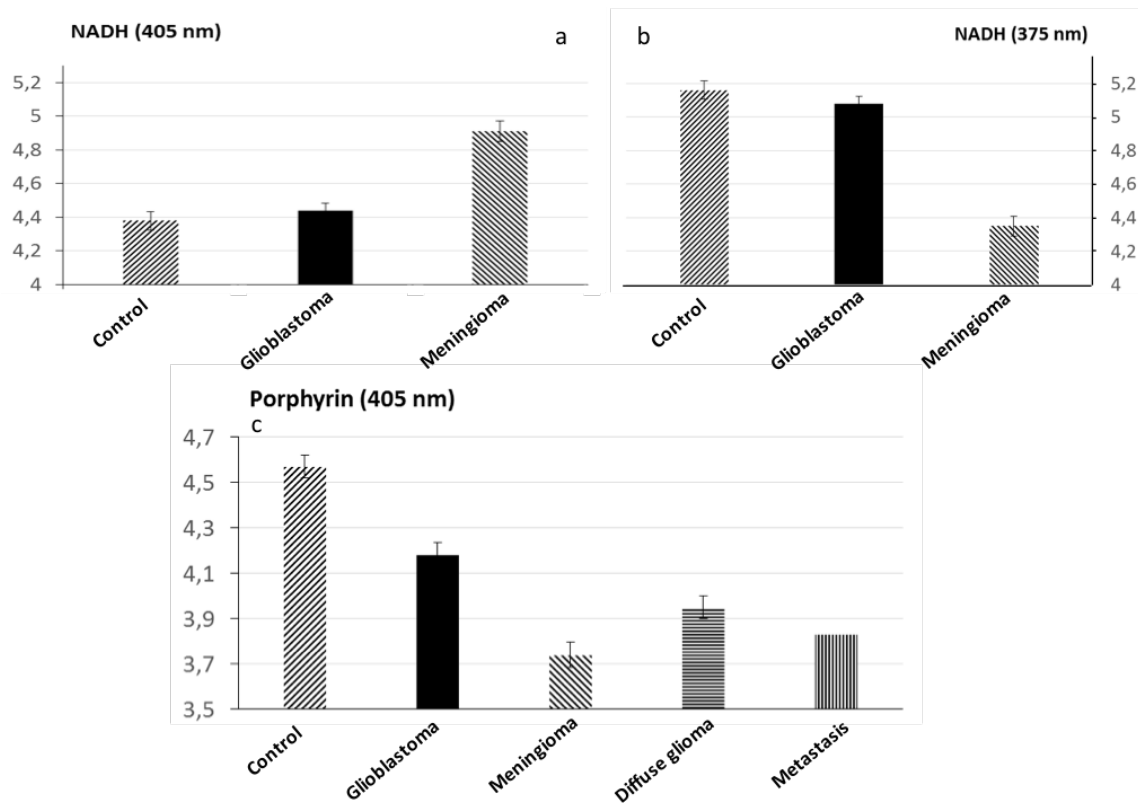


Figure 2.5 – Comparison of mean fluorescence lifetime in different types of tissues. Evolution of NADH lifetime at 375nm (a) and 405nm(b) in three types of tissues (control, glioblastoma, Meningioma). Evolution of porphyrins lifetime at 405nm between control, glioblastoma and meningioma (c), between diffuse gliomas and control (d) and between metastasis and control (c).

( $p=0.002$  at 405nm;  $p=0.004$  at 375nm ). In Figure 2.5.c the results for the porphyrin, well excited at 405nm are presented in all the tumoral tissues (Glioblastoma, Meningioma, Diffuse glioma and Metastasis) a significantly shorter lifetime than the control tissue, respectively with a p-value of  $p=0.05$ ,  $p=0.001$ ,  $p=0.02$  and  $p<0.001$ . The Figure 2.6 illustrates this difference between a tumoral tissue and a control looking at the histogram of fluorescence lifetime decay.

## 2.2.4 Discussion

In this study, an integrating sphere was used to measure the optical parameters of sample from healthy brain tissues and from tumor of the central nervous system of human patients. Different tumor tissues were selected, from primary or secondary tumors and with different grades of malignancy. We measured the optical properties with different excitation wavelengths. The results improved our understanding on the evolution of the absorption coefficient and scattering coefficient on different types of tissues. We could observe a trend from these results, the scattering coefficient

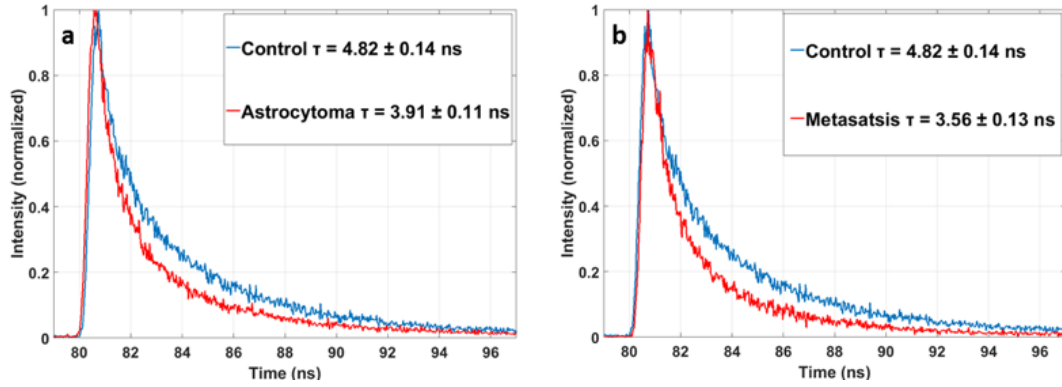


Figure 2.6 – Histogram of lifetime fluorescence decay of the porphyrin component with a 405nm excitation between astrocytoma and control (a) and between metastasis and control (b).

of healthy tissues is lower than those from the different tumor tissues. This difference can be explained by the fact that tumor tissues have more collagen fibers and a strongest vascularization than healthy ones, source of a stronger scattering. A threshold can be determined to discriminate between healthy and tumor, regarding this coefficient a tissue with  $\mu_s < 26$  is healthy and with a  $\mu_s > 29$  is tumoral, in the interval where  $\mu_s$  [26,29] no conclusion can be drawn on the tissue nature. The absorption coefficient also discriminate meningioma, glioblastoma and metastasis from healthy tissue, it can be explained by the stronger vascularization in tumoral tissue. In addition, the higher the grade of malignancy, the more the chromatin is condensed, so the absorption is higher (seen in the evolution  $\mu_a$  of from healthy, diffuse glioma to glioblastoma). The obtained values for the different coefficient were closed to the literature for the studied tissues in similar conditions or when applied on animals [209].

The spectral response confirmed the conclusions made on the optical properties. The evolution of spectra from a tissue to another one is in line with the observed change in absorption and scattering coefficient. These spectral measurements have been established in a "fibered" configuration to be as close as possible to clinical intra-operative configuration. These spectral results gave us another technique to look at the discriminating indicator found with the optical coefficients. Nevertheless, we exploited a bit further the spectral response by looking at the metabolic ratio in order to get a more robust indicator of tissue nature. In our previous work [128], we noticed that in rat brain tissues the porphyrin showed different responses in term of fluorescence lifetime depending on tissue nature. Observing the important presence of porphyrins in the human brain tissue spectral response, we wanted to exploit our knowledge on rat and look at the ratio between NADH and porphyrins to obtain more discriminatory informations. This ratio will link the metabolic and vascular aspect of tissues and consequently bring decisive information. To finalize the study and obtain more quantitative data, the fluorescence lifetime have also been measured with the intra-operative device configuration using 375nm and 405nm as excitation wavelength. Results are interesting and showed the sensibility "of the measure to the nature and state of conservation of tissues". If we compare these results on fixed tissues to the ones previously obtained on fresh tissues with same set-up [223], we can observe the variability of the results. For example for the NADH in cortex-control fixed tissue the mean lifetime is of 4.44 ns, whereas for the fresh tissue in our previous article the

mean lifetime is of 3.38 ns. We can also conclude, as in the rat studies, that porphyrin is a strong indicator of tissue nature, giving us a discriminatory response between tumoral and the healthy tissues and in between the tumors (glioblastoma, diffuse glioma, metastasis and meningioma), we went also further in this study showing that NADH had also a fluorescence lifetime different from one tissue to another, significantly discriminating meningioma from healthy tissue.

We intended to present an original study, based on the autofluorescence response of healthy and tumoral brain tissues observed with different modalities, either in a fiber configuration or in a integrating sphere set-up. All these techniques allowed to established a group of discriminating indicators between healthy and tumoral. To our knowledge, such a study on a substantial cohort of human samples have never been performed. To go further, we wish to expand our cohort to tumor margins, samples where the concentration in tumor cells is very low, in order to test the reliability of the indicators we demonstrated here.



## Chapter 3

Could spectral and lifetime measurements, under visible excitation discriminate freshly extracted brain tissue nature ? Were fluorescent measurements established on fixed tissue suitable enough to build an optical database ?

### 3.1 Context of the study

It was highlighted in the literature [206], that in the *in vivo* condition many elements will vary, such as blood, water and collagen content, impacting the light scattering and absorption. These elements are not as present in the *ex vivo* fixed condition, in which the fixative will stop the tissue in one state and hemoglobin will be altered [224]. Few teams have tried to evaluate the impact of the fixation with formaldehyde on tissue autofluorescence response [225–228]. They all pointed out that the intensity increase in fixed tissue compared to fresh analysis. This has been attributed to enzyme degradation, dehydration, along with changes in blood [227, 228]. Fillipidis et al. [225] and Xu et al. [227] showed that in monitoring over two to four days the spectral shape in human abdominal aortia and mouse skeletal muscle was not significantly affected by formaldehyde fixation. Majumder et al. [226] and Gabrecht et al. [228] looked at the impact of fixation when using spectral response to discriminate breast and bronchial tumor tissues from healthy ones. Majumder et al. showed that even if the spectral shape (the collagen contribution) and the intensity were impacted by the fixation process, the relative differences between cancerous and normal breast tissue were preserved and a discrimination could still be done [226]. Gabrecht et al. showed that neoplastic

### 3.1. CONTEXT OF THE STUDY

and normal tissue could be discriminated, however all the pre-neoplastic tissue had undifferentiated response after fixation, whereas they were able to be discriminated in fresh tissue [229]. These studies confirmed the hypothesis that optical parameters intensity will change in unfixed vs. fixed tissue, suggesting further focus on investigation of fresh tissue samples.

To study fresh biopsy material the bi-modal endoscope set-up was placed at a hospital, very close to the operating room. The tissue were brought to the set-up in less than two hours after the resection and could be analyzed close to intra-operative conditions.

To have more relevant results than on the fixed tissues study presented in chapter 2, in this work all the samples were compared to their appropriate control and the statistics was increased, fifty-four patients were included in the cohort. Three tumoral groups were analyzed : intra-axial primary glioma and secondary metastasis tumor that were compared to cortex control samples. Extra-axial tumor, meningioma were also studied and compare to healthy dura matter. This bi-modal endoscope didn't give access to an imaging modality that could allow comparison with histology gold standard H&E staining, consequently an exploratory study on 13 samples of this cohort was done using a two-photon excitation. The two-photon excitation using a bench-top microscope gave access to a merged image of the fluorescence emission and the SHG showing cellular and extracellular information. These spatial measurements were also combined to make quantitative assessments, in order to track at a molecular scale the changes in tissue. Five molecules that emit an autofluorescence signal were followed in this study : NADH, FADH, lipopigments, porphyrin and chlorine, giving information on metabolism and structure. Their responses were analyzed using a spectral detection and fluorescence lifetime imaging.

**Methods** Biopsy samples taken from fifty-four patients were analyzed in this study. They were originated from cortex-control (n=11), healthy dura matter (n=5), intra-axial glioma (n=16) and metastasis (n=14) tumors and extra-axial meningioma tumor (n=8). Two set-ups were used to measure the autofluorescence response of tissue. The whole cohort was first analyzed on the bi-modal endoscope used in chapter 2. This set-up performs spectral and fluorescence lifetime measurements using a 375 and a 405nm excitation. A portion of the samples (n=13) were used in an exploratory study on a two-photon set-up. A bench-top multi-photon microscope (TCS SP8 MP, Leica, Germany) coupled to Ti:Sapphire laser (Mai Tai Deepsee, Spectra-Physics, USA) with a tunable cavity from 690nm to 1040nm for two-photon excitation. For this study, two excitation wavelengths of 810 and 890nm were used. The set-up was used to perform fluorescence and SHG imaging, spectroscopy and fluorescence lifetime measurements.

**Results and discussion** Under visible excitation a decreased intensity in tumoral tissue compared to their respective controls was observed, for all excitation wavelengths and fitted molecules. This decrease has been attributed to two phenomena, the Warburg effect that decreases the amount of NADH in tumor cells [116] and also presence of structures such as necrosis (up to 87% of glioblastoma in the present series), tumor hyper-perfusion or neo-angiogenesis which are a high source of absorption [230]. Using 405 nm excitation wavelength, fluorescence lifetime measurements were significantly shorter in glioma group than in control group for NADH ( $p = 0.008$ ), FAD ( $p = 0.035$ ) and lipopigment ( $p = 0.035$ ). In metastasis we observed the same trend but the values were not all significantly different. At 375nm we could not extract a discrimination. Meningioma could be discriminated with a statistical significance from their control at both 405 and 375 nm excitation wavelengths. The lower NADH lifetime could be explained by changes in NADH bound/free ratio or in the distribution of NADH enzyme binding sites [231, 232].

	<b>Intensity (a.u.) control- cortex</b>	<b>RIId(%) Glioma- control</b>	<b>RIId(%) : metastasis- control</b>	<b>Lifetime(ns) control- cortex</b>
<b>Chapter 2</b> - fixed samples	455	55	53	4.44
<b>Chapter 3</b> - fresh samples	10	60	75	3.38

Table 3.1 – Comparison between fixed and fresh results on intensity and fluorescence lifetime of NADH emission at 470nm. RIId : Relative intensity decrease

To evaluate the impact of fixation on tissue, the results acquired on the visible bi-modal endomicroscope can be compared to the findings of the previous chapter. Table 3.1 compares the results of spectral and lifetime measurements of the NADH acquired on fixed and fresh samples for different tumor tissues. As in the literature [227], the intensity is higher in fixed tissue than in fresh ones. This is due to the impact of fixation on hemoglobin [224] and also some chemical process degrading enzymes and dehydrating the tissue. The increase in fixed tissue found in the literature were very variable. One study found a factor of 2.6 between 72 hours to 5 days [229], while another found a factor of 20 after 4 days [227]. In this chapter’s study the results were in the range of the second group results, a factor of 40. Knowing that the samples had been fixed for several days or weeks could explain the higher value. Also the probe to sample distance wasn’t precisely controlled from one experiment to another, which could also explain the higher value than in literature. Then, to understand if discrimination was still possible once fixed, the relative decrease in intensity between control and tumor were compared both in glioma and metastasis. For both tumors a difference higher than 50% was measured for fresh and fixed tumors. However the decrease was more significant in fresh tissue. These results translate to what was seen in the literature [229], that fixation diminishes the specificity, and consequently low grade tumors are hard to differentiate from healthy regions in fixed state. The lifetime results showed a decreased of 1 ns between fixed and fresh measurements which is non-negligible. However in the one reference found about fluorescence lifetime in fresh and fixed tissue, a significant change in the lifetime value and the amplitude factor was found [233]. Consequently it is difficult to draw conclusions about the reliability of the fluorescence lifetime response in fixed tissue. A more extensive study has been performed in our group in parallel of this work, on the impact of fixation on the spectral and fluorescence lifetime response. study should be performed to confirm or contradict the result that was found here. As in literature, a systematically longer fluorescence lifetime was found in fixed tissues compare to freshly extracted ones. However the relative difference between fluorescence lifetime of two tissue types did not appear to change from on condition to another. In conclusion using fresh tissue appears mandatory to have the best specificity for discrimination and exploit precise value of fluorescence lifetime. However to test the feasibility of a method, on different histological groups,



	<b>NADH/FAD</b>	<b>FAD/(NADH+FAD)</b>
Control	0.28	0.76
Glioma	0.31	0.75

Table 3.2 – Different redox ratio at 405nm excitation wavelength

fixed tissue will be sufficient.

In this paper, the different molecules contributing to the autofluorescence signal were studied separately looking at the spectral and temporal response. Significant discrimination was found for most of the molecules,  $p\text{-value} < 0.05$ . Being able to track molecules individually, such as NADH and FAD that are involved in metabolic processes opens doors to build metabolic indicators in order to precisely monitor tissue state. As shown in the introduction. Two formula of the ratio tried in the literature,  $FAD/(NADH+FAD)$  and  $NADH/FAD$ , were evaluated on the results of this chapter (table 3.2) to see if this method could be further developed in our analysis.

The  $NADH/FAD$  ratio gave a significant difference and could be a good quantitative indicator in further study to evaluate the metabolic state of tissue. The second ratio gave a less significant difference but still showed the same trend as in the literature.

These in vivo analyses showed the capacity of bi-modal quantitative detection on endogenous fluorescence to discriminate tissue nature. However this set-up lacked an imaging modality and the possibility of comparison to histology gold standard for diagnosis, the H&E stained images. The H&E are a combination of two stains, the nuclear information appears in purple-blue and cytoplasm and extracellular matrix are revealed in pink. The H&E stain, based on this dual information and the changes in contrast and textures, give access to vast intracellular information (mitochondria, filaments, mucous sites, lipides, vessels walls) and provides pieces of information on the functional status of the cells [60]. It makes H&E the standard for pathological diagnosis with a high accuracy. To be able to give comparable information, the new imaging modality must also combine nuclear and extracellular information. Non-linear microscopy is the best candidate because for example two-photon excitation produces two complementary signal : SHG from the light interaction with ECM fibered organization, and emission fluorescence highlighting cytoplasmic-nuclear information. The TPEF-SHG images of control-cortex and each tumoral groups were compared to their H&E equivalent stain. Typical structures of histology were identified in the fluorescence images. SHG signal highlighted lobules in metastasis, necrosis in glioma, and vessels in control. TPEF showed signal in cytoplasm cells, with lobular arrangement in meningioma, in dense areas of glioma cancerous cells, and in triangular neurons in control. These structures are standard elements used to make a diagnosis, showing that this optical technique could be an equivalent to H&E staining with the strong advantage of being faster and chemical free. Spectral measurements using the two-photon excitation resulted in similar spectral shape as the one-photon results, leading to the same quantitative molecular analysis as in the one-photon configuration. In the lifetime measurements different mean values were found for each tissue types, but the smallness of the group of samples did not allow a statistical comparison. These preliminary results on a two-photon excitation showed the potential of qualitative and quantitative discrimination using the addition of a third spatial dimension compared to the visible set-up configuration. To tackle more in depth clinical questions

### CHAPTER 3. COULD SPECTRAL AND LIFETIME...

with multimodal optical analysis of autofluorescence signal, the two-photon excitation would be preferred. The promising results found on this small cohort of brain tumor tissue, opened the possibility of using it on neuropathological challenges with a comparable precision to the histological analysis. To evaluate the capacity of the two-photon configuration, a study on tumor grading was then established to compare qualitative and quantitative optical analysis versus the H&E and immunohistochemistry analysis of neuropathologist. The results will be presented in the chapter 4.

### 3.2 Paper: Multimodal optical analysis discriminates freshly extracted human sample of gliomas, metastases and meningiomas from their appropriate controls

## SCIENTIFIC REPORTS

www.nature.com/scientificreports

OPEN

### Multimodal optical analysis discriminates freshly extracted human sample of gliomas, metastases and meningiomas from their appropriate controls

Marc Zanella<sup>1,2,3</sup>, Fanny Poulon<sup>1</sup>, Johan Pallud<sup>2,3</sup>, Pascale Varlet<sup>3,4</sup>, H. Hamzeh<sup>5</sup>, Georges Abi Lahoud<sup>2,3</sup>, Felipe Andreiulo<sup>3,4</sup>, Ali Ibrahim<sup>1</sup>, Mélanie Pages<sup>3,4</sup>, Fabrice Chretien<sup>3,4</sup>, Federico Di Rocco<sup>6</sup>, Edouard Dezamis<sup>2,3</sup>, François Nataf<sup>2,3</sup>, Baris Turak<sup>2,3</sup>, Bertrand Devaux<sup>2,3</sup> & Darine Abi Haidar<sup>1,7</sup>

Delineating tumor margins as accurately as possible is of primordial importance in surgical oncology: extent of resection is associated with survival but respect of healthy surrounding tissue is necessary for preserved quality of life. The real-time analysis of the endogenous fluorescence signal of brain tissues is a promising tool for defining margins of brain tumors. The present study aims to demonstrate the feasibility of multimodal optical analysis to discriminate fresh samples of gliomas, metastases and meningiomas from their appropriate controls. Tumor samples were studied on an optical fibered endoscope using spectral and fluorescence lifetime analysis and then on a multimodal set-up for acquiring spectral, one and two-photon fluorescence images, second harmonic generation signals and two-photon fluorescence lifetime datasets. The obtained data allowed us to differentiate healthy samples from tumor samples. These results confirmed the possible clinical relevance of this real-time multimodal optical analysis. This technique can be easily applied to neurosurgical procedures for a better delineation of surgical margins.

Surgical resection, whenever feasible, remains the first line of therapy to treat central nervous system tumors<sup>1,2</sup>. The extent of resection is a major prognostic factor, whatever the histopathological subtype<sup>3</sup>. Although maximal resection is required, preserving surrounding healthy brain areas is warranted to equilibrate the onco-functional balance: improving the outcomes through maximal tumor removal and preserving the postoperative quality of life. The identification of the tumor limits, in case of gliomas, metastases and meningiomas may be difficult intraoperatively. Intraoperative microscopy, intraoperative ultrasonography, or intraoperative MRI are insufficient to resolve tissue microstructure and discriminate between tumor induced tissue alterations and surgically induced changes, such as contusion, ischemia or edema<sup>4-6</sup>.

The most notable achievement concerning optical imaging for brain tumor margin delineation was realized by Stummer *et al.* with the use of external dye, 5-aminolevulinic acid (ALA)<sup>7</sup>. Clinical studies have shown an increased extent of resection and improved overall survival using ALA<sup>8,9</sup>, however, its sensitivity can be improved, especially in infiltrative areas<sup>10,11</sup>. Moreover, any dye has contraindications and side effects. Our group tries to overcome these limits by analyzing human tissue endogenous fluorescence. First attempts of label-free optical imaging were made during 1990s and active research is still currently underway in this field with no major clinical translation<sup>12-16</sup>. Meanwhile, nonlinear microscopy technique has emerged over the last 20 years<sup>17,18</sup>. It differs from classical confocal microscopy by its ability to use several endogenous contrasts, especially second harmonic

<sup>1</sup>IMNC Laboratory, UMR 8165-CNRS/IN2P3, Paris-Saclay university, 91405 Orsay, France. <sup>2</sup>Neurosurgery Department, Sainte-Anne Hospital, France. <sup>3</sup>Paris Descartes University, Paris, France. <sup>4</sup>Neuropathology Department, Sainte-Anne Hospital, France. <sup>5</sup>Center of Advanced European Studies and Research (caesar), 53175 Bonn, Germany. <sup>6</sup>Neurosurgery Department, Lyon Hospital, France. <sup>7</sup>Paris Diderot University, Sorbonne Paris Cité, F-75013, Paris, France. Correspondence and requests for materials should be addressed to D.A.H. (email: abihaidar@imnc.in2p3.fr)

SCIENTIFIC REPORTS | 7:41724 | DOI: 10.1038/srep41724

1

### 3.2.1 Introduction

Surgical resection, whenever feasible, remains the first line of therapy to treat central nervous system tumors [234, 235]. The extent of resection is a major prognostic factor, whatever the histopathological subtype [236]. Although maximal resection is required, preserving surrounding healthy brain areas is warranted to equilibrate the onco-functional balance: improving the outcomes through maximal tumor removal and preserving the postoperative quality of life. The identification of the tumor limits, in case of gliomas, metastases and meningiomas may be difficult intra-operatively. Intra-operative microscopy, intra-operative ultrasonography, or intra-operative MRI are insufficient to resolve tissue microstructure and discriminate between tumor induced tissue alterations and surgically induced changes, such as contusion, ischemia or edema [82, 237, 238]. The most notable achievement concerning optical imaging for brain tumor margin delineation was realized by Stummer et al. with the use of external dye,  $\delta$ -aminolevulinic acid (ALA) [98]. Clinical studies have shown an increased extent of resection and improved overall survival using ALA [99, 239], however, its sensitivity can be improved, especially in infiltrative areas [173, 240]. Moreover, any dye has contraindications and side effects. Our group tries to overcome these limits by analyzing human tissue endogenous fluorescence. First attempts of label-free optical imaging were made during 1990's and active research is still currently underway in this field with no major clinical translation [124, 125, 137, 241, 242]. Meanwhile, nonlinear microscopy technique has emerged over the last 20 years [150, 243]. It differs from classical confocal microscopy by its ability to use several endogeneous contrasts, especially second harmonic generation and two-photon fluorescence without introducing exogenous dye. The near infrared excitation source allows a deeper penetration and a lower level of photodamage compared with confocal microscopy, which helps to preserve tissue. Autofluorescence analysis is difficult primarily due to the low signal to noise ratio: the combination of multiple modalities could help distinguish tumor margins more precisely than techniques that offer a unique modality [144, 244, 245]. In this work we implement spectral and lifetime fluorescence in spatial imaging. This quantitative information provides additional information on the physicochemical environment and molecular interaction.

The present study investigated the ability of visible and nonlinear optical imaging techniques to discriminate between tumor and control healthy tissues. For this purpose, metastasis, glioma and meningioma samples were compared to their appropriate controls: healthy brain samples and dura mater samples, respectively. In this study, thin human samples, freshly extracted, are analyzed to be as close as possible to clinical conditions. We made qualitative and quantitative measurements on these different sample groups. This comparative study was made on two set-ups: endoscopic fibered set-up and multimodal microscope. With the optical fibered endoscope we acquired spectroscopic and lifetime measurements on freshly extracted human samples as a first step before *in vivo* clinical measurements. It allows excitation with two different visible wavelengths, 375 and 405 nm. These wavelengths are well known [128, 216] to excite different endogenous molecules, like reduced nicotinamide adenine dinucleotide (NADH), flavins (FAD), lipopigment, porphyrins. Our team is currently working on a new surgical tool that allows performing nonlinear optical analysis of endogenous fluorescence in real time during neurosurgical procedures. To further enhance the specificity and sensitivity of the optical analyses, four different contrasts will be studied: (1) one and two-photon spectral detection, (2) time domain measurement and two-photon Fluorescence Lifetime Imaging, (3) second harmonic generation imaging and (4) one and two-photon fluorescence imaging. The aim is to help neurosurgeons to realize maximal resection of brain tumors based on the endogenous contrast between the fluorescence of tumor tissue and healthy surrounding tissue.

As a first step before this fibered multimodal optical surgical tool, we have chosen to use a

multimodal bench top microscope. It allows us to (i) test the safety of multimodal excitation on fresh human samples, (ii) obtain the four different contrasts previously discussed, (iii) compared fluorescence images with gold standard histopathology and (iv) discriminate potential differences between the different samples (glioma, metastasis, meningioma, and healthy cortex).

### 3.2.2 Materiel and methods

#### 3.2.2.1 Samples

The inclusion criteria for this monocentric prospective collection of fresh samples were: (1) adult patients; (2) newly diagnosed central nervous system tumor at the Sainte-Anne Hospital (Paris, France); (3) available fresh samples to be analyzed on optical set-ups in addition to the routine histopathology protocols; (4) selection by a senior neuropathologist of representative and homogeneous samples (meningioma, glioma, metastasis, and control). The institutional review board of the Sainte-Anne Hospital center – University Paris Descartes approved the study protocol (number SC3227), all the following methods were performed in accordance with the relevant guidelines and regulations issue in this protocol. Moreover informed consents were obtained from all the samples coming from human subjects. Sample size varied from 32 mm<sup>3</sup> (4x4x2 mm) to 750 mm<sup>3</sup> (15x10x5 mm). They were maintained in normal saline solution to avoid desiccation, in a temperature-controlled dark room dedicated to optical imaging. They were cut with a scalpel to obtain a planar surface. The sample was studied first on a visible set-up then on a nonlinear multimodal set-up. The whole process took less than 120 min. The fresh samples were then fixed with 4% paraformaldehyde, embedded in paraffin and stained with Hematoxylin-Eosin then digitized using Digital Slide Scanner NanoZoomer 2.0 (Hamamatsu Photonics K.K, Hamamatsu, Japan). Detailed clinical data including age at diagnosis, past medical history and histopathological data including presence of mitosis, necrosis, neoangiogenesis and immunohistochemical analysis were recorded. We examined non-tumor brain parenchyma fresh samples as control samples for intraparenchymal tumor samples (glioma and metastasis) and dura mater samples for meningioma samples. The non-tumor brain parenchyma samples (n = 11, the so-called control group) provided from patients operated for a drug-resistant temporal epilepsy during the same period. Dura mater control samples (n = 5, the so-called meningioma control group) provided from dural boundaries far from meningioma resection. A senior neuropathologist performed a central review of definitive Hematoxylin-Eosin staining of the study's samples, without prior knowledge of the two-photon analysis status (performed or not). Detected tissue alteration were reported to the investigators.

#### 3.2.2.2 Optical endoscope architecture

Two pulsed diode lasers, one emitting at 405 nm and the other one at 375 nm, from PicoQuant (GmbH, Berlin, Germany) were used as laser sources. The diode 375, FWHM 45 ps and 405 nm, FWHM 60 ps were used. The same “Sepia” driver controlled the diodes. Repetition frequency can be set between 2.5 and 40 MHz. Repetition frequency used for this study is 40 MHz. Excitation and collection were acquired thanks to a bi-fibered configuration. The fibres used for tissue excitation and collection had a core diameter of 200  $\mu\text{m}$  and 365  $\mu\text{m}$ , respectively, with a numerical aperture of 0.22. The spatial resolution was of 500  $\mu\text{m}$ . A beam Splitter divided and sent the collected fluorescence into two detectors: 70% of the signal toward a computer controlled cooled spectrometer (Ocean optics QP600-1-UV-VIS) for spectroscopic analysis and 30% toward a Photomultiplier Tube a Photomultiplier Tube (PMT) (PMA-182 NM, PicoQuant GmbH, Berlin, Germany) for lifetime

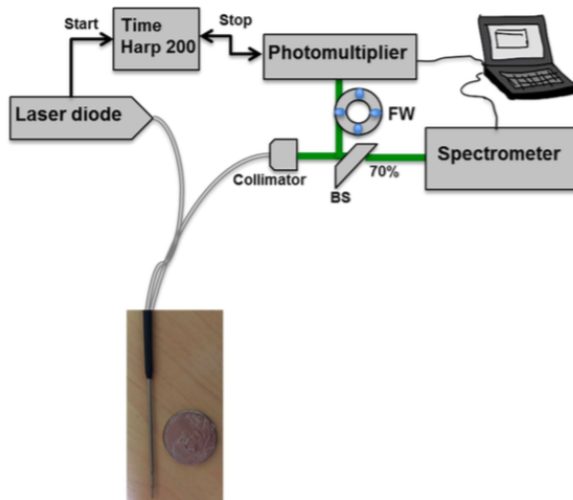


Figure 3.1 – Optical fibered endoscope setup. Spectral and lifetime measurements were acquired using this set up and under 405 and 375 nm excitation wavelength. Two fibered was used for excitation and fluorescence collection.

measurement. The synchronization output signal from the diode driver and the start signal from the PMT were connected to their respective channels on the data acquisition board Time-Correlated Single Photon Counting (TCSPC) (TimeHarp 200, PicoQuant GmbH, Berlin, Germany). A filter wheel was used to select the spectral emission band during lifetime measurement. Five filters were used when exciting with 405 nm ( $450 \pm 10$  nm,  $520 \pm 10$  nm,  $550 \pm 30$  nm,  $620 \pm 10$  nm and  $680 \pm 10$  nm). Using these filters we can respectively detect the emitted fluorescence from NADH, FAD, lipopigments, porphyrin I and porphyrin II. Two filters are used when exciting with 375 nm ( $450 \pm 10$  nm and  $520 \pm 10$  nm) for NADH and FAD (Fig. 3.1). Each lifetime measurement lasted 2 seconds. Data were adjusted by a mono-exponential fit via FluoFit software (PicoQuant, GmbH, Berlin, Germany) to recover the lifetimes from the measured fluorescence decays. Spectral acquisition was accomplished for several longitudinal lines of each sample thanks to a specific mechanical support mounted on a motorized microtranslator stage (Thorlabs, Newton, USA) [128] and it lasted 5 to 10 minutes per sample. The spectral measurements were processed using a homemade Matlab program, as previously described [128]. The same five fluorophores were considered: reduced Nicotinamide adenine dinucleotide (NADH), flavins (FAD), lipopigments, porphyrin I and porphyrin II. Data were adjusted by a mono-exponential fit via FluoFit software (PicoQuant, GmbH, Berlin, Germany) to recover the lifetimes from the measured fluorescence decays.

### 3.2.2.3 Microscopic multimodal setup: Confocal, two-photon and FLIM imaging of endogenous fluorescence

A Mai Tai DeepSee Ti:Sapphire laser source (Mai Tai DeepSee, Spectra-Physics, Santa Clara, USA) with automated dispersion compensation. The average power is around 2.4 W at 800 nm

excitation wavelength. It's tunable from 690 to 1040 nm. The repetition rate of the laser source was 80 MHz and the output pulse duration was around 70 fs. This laser is combined to a TCS SP8 MP confocal microscope from Leica Microsystems (Leica Microsystems, Wetzlar, Germany). This set up was used for confocal, two-photon and fluorescence lifetime (FLIM) imaging of samples. The presence of two additional filters (FF01-448/20-25 and FF01-520/35-25, Semrock, New York, USA) on the dichroic cube set the detection band for each path toward one of the two external hybrids. This optical set-up recorded four different optical signals on the Regions Of Interest (ROI): (1) one and two-photon Spectral analysis, (2) two-photon FLIM measurement, (3) second harmonic generation imaging and (4) Fluorescence imaging under one and two-photon excitation. Analyses were performed using the dedicated Leica software (Leica Microsystems, Wetzlar, Germany). Fluorescence and second harmonic generation images processing were made using the dedicated Leica software as well as Matlab and imageJ. For FLIM measurements, three positions at least per sample were analyzed using 810 and 890 nm excitation wavelengths. The data were collected and analyzed via the software Symphotime (PicoQuant, GmbH, Berlin, Germany). On each FLIM image, twelve ROI were selected on the different structures and fitted by a mono or bi-exponential decay to extract the fluorescence lifetime.

### 3.2.2.4 Statistical analyses

Fluorescence intensity and lifetime results were evaluated using a one-way analysis of variances (ANOVA). If the ANOVA was statistically significant, a post-hoc Wilcoxon test was performed. A probability value ( $p$ )  $< 0.05$  was considered statistically significant. All statistical analyses were performed using JMP software (version 11.0.0, SAS Institute Inc).

## 3.2.3 Results

### 3.2.3.1 samples

Clinical and histopathological characteristics are summarized in figure 3.2. Fifty-four samples (tumor and control samples) were analyzed. Thirty-eight fresh human tumor samples from 38 patients (21 men, 17 women, mean age at diagnosis  $58.3 \pm 12.1$  years) have been analyzed on the endoscopic fibered set-up and ten of these 38 samples (26%) have also been analyzed on the nonlinear microscopic set-up. This cohort was divided into two parts: intra-axial tumor part, subdivided in Glioma group ( $n = 16$ ) and Metastasis group ( $n = 14$ ), and extra-axial tumor part, Meningioma group ( $n = 8$ ). Each part was compared to appropriate controls: healthy cortex samples ( $n = 11$ ) for intra-axial tumor part, named Control Group and healthy dura mater samples ( $n = 5$ ) for extra-axial tumor part, named Meningioma Control Group.

No significant difference in tissue alteration was noticed between the samples analyzed with the optical endoscope only and the samples analyzed on both set-ups.

### 3.2.3.2 Fibered set-up results

#### 3.2.3.2.1 Spectral measurements of endogenous fluorescence

. As shown in Fig. 3.3, glioma group auto fluorescence is almost two times lower than control group autofluorescence. At 405 nm excitation wavelength and at 375 nm excitation wavelength, fluorescence intensity from glioma tissue was lower for all investigated endogenous molecules than the control group. This difference was significant for NADH ( $p = 0.018$ ), lipopigment ( $p = 0.038$ ),

Group	Glioma Group (n = 16)		Metastasis Group (n = 14)		Control Group (n = 11)		Meningioma Group (n = 8)		Meningioma Control Group (n = 5)	
Parameter	No.	%	No.	%	No.	%	No.	%	No.	%
<b>Clinical findings</b>										
Mean age at diagnosis, years	57.7	—	57.2	—	40.1	—	61.4	—	72.6	—
Range	26.2–77.4	—	39.8–74.4	—	23.9–61.9	—	53.2–72.4	—	58.6–92.3	—
<b>Gender</b>										
Male	11	69	6	43	5	45	2	25	1	33
Female	5	31	8	57	6	55	6	75	2	67
Previous treatment on Central Nervous system (Surgery and/or Radiotherapy and/or Chemotherapy)	2	13	0	0	0	0	2	25	0	0
<b>Two-photon Multimodal Imaging</b>										
Yes	4	25	3	21	3	27	3	38	0	0
No	12	75	11	79	8	63	5	62	5	100
<b>Histopathological Findings</b>										
<b>Necrosis</b>										
Yes	12	75	12	86	0	0	2	25	0	0
No	4	25	2	14	11	100	6	75	5	100
<b>Angiogenesis</b>										
Yes	13	81	1	7	0	0	1	13	0	0
No	3	19	13	93	11	100	7	87	5	100
Mean Proliferation rate (%)	21	—*	—*	—	—	—	5	—	—	—
Range	10–40	—	—	—	—	—	1–12	—	—	—

Figure 3.2 – Clinical and Histopathological Characteristics of our human samples series. \*Only one sample had a calculated proliferation rate.

and porphyrin I ( $p = 0.048$ ) whereas a trend existed concerning FAD ( $p = 0.054$ ), and porphyrin II ( $p = 0.126$ ) without reaching statistical significance. At 375 nm excitation wavelength, fluorescence emission from glioma tissue was also reduced for NADH ( $p = 0.007$ ) and FAD ( $p = 0.005$ ).

Metastasis group emitted significantly less autofluorescence than control group. At 405 nm and at 375 nm excitation wavelengths, fluorescence intensity was significantly reduced at all investigated emission wavelengths compared to control group. With 405 excitation wavelength, fluorescence emission of each molecules from glioma samples are lower than control: NADH ( $p > 0.001$ ), FAD ( $p = 0.002$ ), lipopigment ( $p = 0.006$ ), porphyrin I ( $p = 0.033$ ) and porphyrin II ( $p = 0.029$ ). At 375 nm excitation wavelength, fluorescence intensity was also reduced for NADH ( $p = 0.009$ ) and FAD ( $p = 0.012$ ).

Glioma and Metastasis groups did not exhibit significant differences. However, fluorescence intensity was reduced for NADH in Metastasis group compared to Glioma group with 375 nm and 405 nm excitation wavelengths without reaching statistical significance.

Meningioma group presented a 4-fold decrease in autofluorescence compared to meningioma control group (Fig. 3.4). At 405 nm excitation wavelength, fluorescence intensity was significantly reduced at four investigated endogenous molecules compared to meningioma control group: NADH, FAD, porphyrin I and porphyrin II ( $p = 0.028$ ,  $p = 0.028$ ,  $p = 0.019$ , and  $p = 0.019$ , respectively). At 375 nm emission wavelength, fluorescence intensity was reduced for both NADH and FAD ( $p = 0.019$ , and  $p = 0.028$ , respectively).

### 3.2.3.2.2 Lifetime measurements of endogenous fluorescence

. Lifetime values of glioma, metastasis, meningioma and respective control group using 375 and 405 nm excitation wavelength are resumed in figure 3.5.

Using 405 nm excitation wavelength, fluorescence lifetime measurements were significantly shorter in glioma group than in control group for NADH ( $p = 0.008$ ), FAD ( $p = 0.035$ ) and lipopigment ( $p = 0.035$ ). As shown in Fig. 3.6, no significant difference existed using 375 nm excitation wavelength.

Concerning metastasis group, the same trend as glioma group is observed as shown in Fig. 3.6.



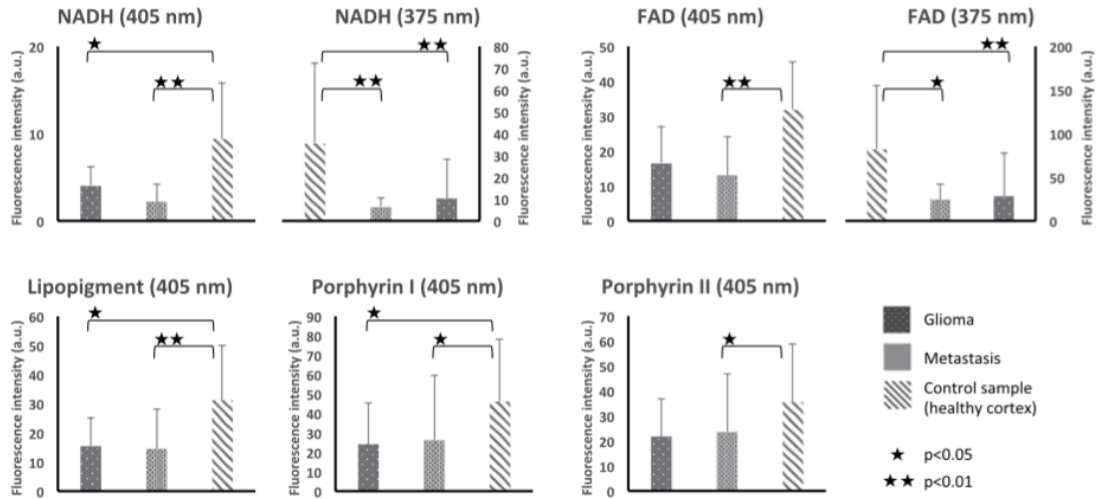


Figure 3.3 – Results of spectroscopic endogenous fluorescence measurements for intra-axial tumor part. Fluorescence intensity of NADH and FAD when exciting with 405 and 375 nm for Glioma, metastasis and control samples. Results for Lipopigment, porphyrin I and II are presented for 405 nm excitation wavelength. ★ ★ Under a bar denote statistically significant difference ( $p < 0.01$ ).

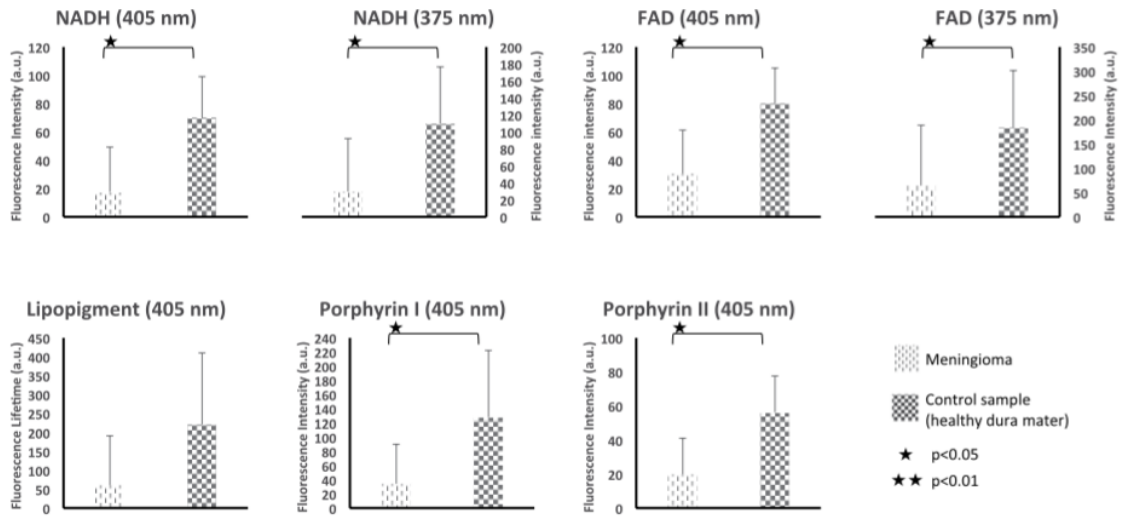


Figure 3.4 – Results of spectroscopic endogenous fluorescence measurements for extra-axial tumor part. Fluorescence lifetime of NADH and FAD when exciting with 405 and 375 nm from meningioma and control samples. Results for Lipopigment, porphyrin I and II are presented for 405 nm excitation wavelength.

	<b>Glioma Group</b>	<b>Metastasis Group</b>	<b>Control Group</b>	<b>Meningioma Group</b>	<b>Meningioma control Group</b>
<b>Lifetime values (ns)</b>	<b>(n = 16)</b>	<b>(n = 14)</b>	<b>(n = 11)</b>	<b>(n = 8)</b>	<b>(n = 5)</b>
<b>Parameter</b>	<b>Mean (SD)</b>	<b>Mean (SD)</b>	<b>Mean (SD)</b>	<b>Mean (SD)</b>	<b>Mean (SD)</b>
<b><math>\lambda_{exc} = 375 \text{ nm}</math></b>					
NADH	4.01 (1.29)	4.05 (1.02)	3.41 (0.80)	3.94 (0.58)	5.30 (0.30)
FAD	3.88 (1.18)	4.29 (0.81)	3.87 (0.56)	3.90 (0.69)	5.22 (0.27)
<b><math>\lambda_{exc} = 405 \text{ nm}</math></b>					
NADH	2.55 (0.61)	2.71 (0.51)	3.38 (0.62)	3.22 (0.73)	4.58 (0.98)
FAD	2.71 (0.64)	2.71 (0.53)	3.29 (0.55)	3.27 (0.67)	4.83 (0.87)
Lipopigment	3.80 (1.18)	3.66 (0.80)	5.21 (2.72)	3.86 (0.88)	9.58 (5.16)
Porphyrin I	2.57 (0.88)	3.00 (1.17)	2.92 (1.12)	2.60 (0.46)	4.00 (0.88)
Porphyrin II	2.41 (1.19)	2.53 (1.16)	2.96 (0.92)	1.91 (0.36)	3.25 (0.77)

Figure 3.5 – Fluorescence Lifetime measurements of our human samples series.

Fluorescence lifetime values were significantly shorter in metastasis group than in control group for NADH ( $p = 0.009$ ), FAD ( $p = 0.026$ ) and lipopigment ( $p = 0.040$ ). No significant difference existed at 375 nm excitation wavelength. With 405 and 375 nm excitation wavelengths, fluorescence lifetime values were significantly reduced in meningioma group compared to meningioma control group. Figure 3.7 present this tendency.

### 3.2.3.3 Results on multimodal microscopic imaging set-up

#### 3.2.3.3.1 Choice of the excitation wavelength

. A specific spectral study was accomplished to define the best excitation wavelength able to excite endogenous fluorescence as well as second harmonic generation signal. For this purpose we made an excitation-emission matrix, thanks to the tunable Ti:sapphire lasers (from 690 to 1040 nm). This study reveals that 810 nm was best suited to excite endogenous fluorescence, whereas 890 nm was the adequate wavelength to excite fluorescence as well as second harmonic generation signal and confirmed our previous results [216]. These two wavelengths was used as excitation wavelength for our study.

#### 3.2.3.3.2 Multimodal nonlinear analysis of endogenous fluorescence under nonlinear excitation

Figure 3.8 illustrates the results of this multimodal analysis of intra and extra- axial tumor analysis.

**A-Glioma group** . Using two-photon excitation, at 810 nm excitation wavelength, glioma samples showed a peak centered at 540 nm and a second peak at 660 nm. At 890 nm excitation

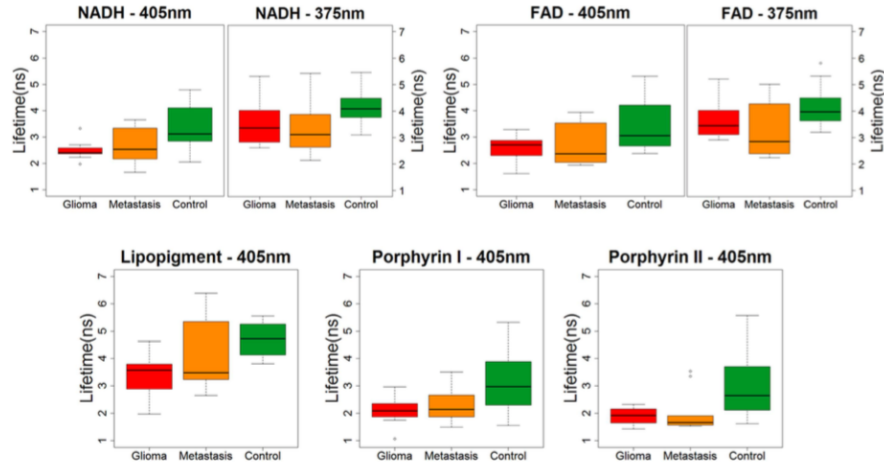


Figure 3.6 – Boxplot of endogenous fluorescence lifetime measurements for intra-axial tumor part. Lifetime variation of NADH and FAD when exciting with 405 and 375 nm from Glioma, metastasis and control samples. Results for Lipopigment, porphyrin I and II are presented for 405 nm excitation wavelength.

wavelength, besides the two described peaks, second harmonic generation signal was visible at 445 nm. At 810 nm excitation wavelength, FLIM study found out two components with lifetimes values of 2.40 ns and 0.40 ns, always longer than the values of control group.

**B-Metastasis group** . At 810 nm excitation wavelength, metastasis samples exhibited one peak centered at 540 nm. At 890 nm excitation wavelength, the same peak centered at 540 nm was observed as well as second harmonic generation signal was detected around 445 nm. At 810 nm excitation wavelength, FLIM study found out two components with lifetime's values of 2.57 ns and 0.50 ns, once again the values increased compared to control group.

**C-Control group** . At 810 nm excitation wavelength, control samples showed a peak centered at 520 nm. At 890 nm excitation wavelength, the same peak was observable. At 810 nm excitation wavelength, FLIM study showed two components with lifetimes values of 2.10 ns and 0.35 ns.

**D-Meningioma group** . At 810 nm excitation wavelength, meningioma samples emitted three peaks centered at 520 nm, 580 nm and 640 nm with a broad fluorescence emission. At 890 nm excitation wavelength, a peak at 445 nm was visible corresponding to second harmonic generation signal. At 810 nm excitation wavelength, FLIM study showed three components with lifetimes values of 2.30 ns, 1.8 ns and 0.40 ns.

Using one photon excitation, all tumors spectra were red shifted and presented lower fluorescence intensity than control samples. These statements were less visible with two-photon excitation. Spectrum shape and intensity were quite different for each tissue type. Extra-axial and intra-axial tumors strongly differentiate with a broader spectrum in extra-axial due to a higher contribution of porphyrins and chlorins, a difference is also noticeable in the three types of intra-axial tissues, glioma

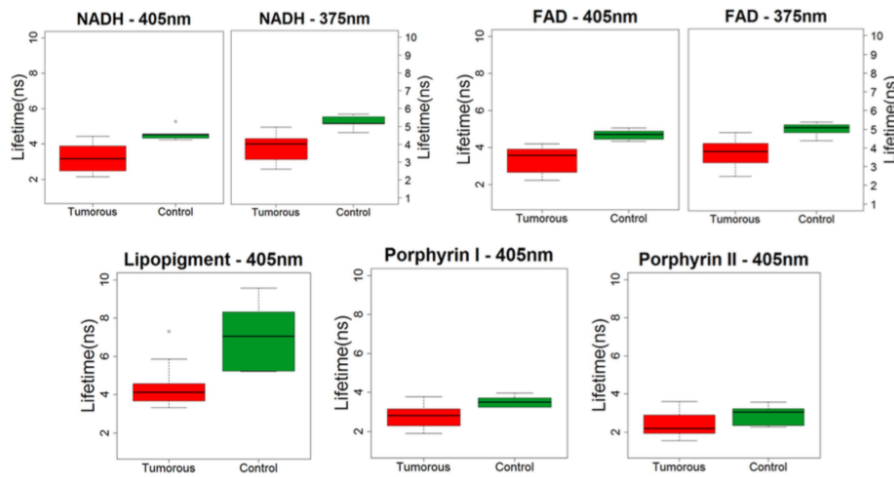


Figure 3.7 – Boxplot of Endogenous Fluorescence lifetime measurements for extra-axial tumor part. Lifetime variation of NADH and FAD when exciting with 405 and 375 nm from tumorous and control tissue. Results for Lipopigment, porphyrin I and II are presented for 405 nm excitation wavelength.

appears narrower in the principal peak, explained by a very low lipopigment signal, compared to metastasis and control tissue.

### 3.2.3.3.3 Comparison with gold standard histopathology

. Figure 3.8 represents illustrative cases and we observed variability in spectral acquisition from a sample to another. Two-photon images revealed the same structures as than gold standard H&E images. The second harmonic generation signal, in green, delimited lobules in metastasis and necrosis in glioma whereas it was absent from the control sample. It corresponded to the spectral acquisition made at 890 nm excitation wavelength. Autofluorescence signal, in red, underlined cell cytoplasm and, for instance, showed the lobular arrangement in the meningioma sample. Image from nonlinear set-up showing SHG signal in green corresponding to collagen fibers and two distinct zones of red fluorescence, one pale corresponding to necrosis and the second intense corresponding to glioma cells. Hematoxylin-Eosin staining showing necrosis and collagen fibers.

## 3.2.4 Discussion

We have, for the first time, carried out a multimodal optical analysis in a cohort of 58 fresh human brain tumors samples compared to their appropriate control samples. We showed that: (i) glioma, metastasis and meningioma emitted significantly lower fluorescence than their controls at 405 and 375 nm excitation wavelengths; (ii) at 405 nm excitation wavelength, lifetime values of glioma, metastasis and meningioma were shorter than their controls and at 375 nm we did not find any difference; (iii) multimodal nonlinear analysis of human brain samples provided new insights in the tissue architecture upon analyzing FLIM, two-photon fluorescence and second harmonic generation signal. Altogether, those results suggest multimodal optical analysis as a promising tool to help the intra-operative identification of tumor margins.

Our study confirmed that fluorescence emission was significantly reduced in tumor tissue as compared to healthy tissue in accordance with previous reports [122, 124–126, 135, 137, 242, 246]. The autofluorescence decrease we observed in tumor tissues had been ascribed to reduction of NADH amount in tumor cells due to the Warburg effect, the increased metabolization, almost tenfold, of glucose to lactate by neoplastic tissue compared with healthy tissue in aerobic condition [116, 247]. However, this point is still a matter of debate with a recent review quoting a possible increase of NADH with mitochondrial dysfunction in tumor [248]. It might be possible that tumor necrosis (up to 87% of glioblastoma in the present series), tumor hyperperfusion or neoangiogenesis explained, at least in part, the observed lower emission fluorescence [158, 249]. Previous studies reported a shift in the emission wavelength between the different tissue types [122, 242]. In the present series, we observed a redshift using one photon excitation. This trend was less evident with two-photon excitation but the main peak was centered at 540 nm for metastasis and glioma versus 520 nm for the control samples. Even if analysis of fluorescence intensity seems promising to discriminate tumor infiltration from normal zones, some drawbacks must be taken into account: spectral shape was quite variable, blood contamination during surgery can drastically decrease the collected signal. Distinguishing tumor borders from healthy tissue should be more difficult than differentiating solid tumor and healthy tissue. In this way, multimodal analysis seems mandatory [250].

Fluorescence lifetime is a sensitive technique for recording low-level signals with high precision [251]. To our knowledge, our lifetime measurements are the only ones using 375 and 405 nm excitation wavelengths. The absence of any previous work using the same excitation wavelengths makes harder comparison with literature. Lifetime values that we obtained are in accordance with general review on this topic but not with the previous work on human brain samples [131, 135–137, 252, 253]. However, the values remained in the same order of magnitude. For instance, Yong et al. used a 337 nm excitation wavelength and found out lifetime values at 390 nm emission wavelength equal to 1.27 ns for cerebral cortex; 2.3 ns for normal white matter; 1.4 ns for low grade glioma; 1.4 ns for high grade glioma and 2.0 ns for high grade glioma with necrotic change. At 440 nm and 460 nm, emission wavelengths closer to the studied emission wavelength in this paper, this trend was less evident. In our multivariate analysis, 470 nm corresponding to NADH, 520 nm corresponding to flavins and 580 nm corresponding to lipopigments had significantly longer lifetime values in the control group than tumor groups using 405 nm as excitation wavelength. This is in accordance with a previous work by our team on rats tissues and literature [128, 231]. NADH lower lifetime in neoplastic tissue can be explained by change in NADH bound/free ratio or changes in the distribution of NADH enzyme binding sites [231, 232]. Our literature review found out some works of multimodal nonlinear optical microspectroscopy on brain or nervous system [254, 255] but only one multiphoton analysis of human brain samples was performed with 750 nm excitation wavelength using the DermaInspect set-up [256]. FLIM results ranged from 1.4 ns (brain parenchyma sample) to 2.1 ns (glioblastoma sample) [256]. Correlation between gold standard histopathology was made only on rat samples and no second harmonic generation study was performed. We worked on a dedicated set-up for nonlinear analysis and we recorded four different types of signals: second harmonic generation, FLIM, one and two-photon fluorescence imaging. This preliminary study confirmed the potential of nonlinear microscopy for human brain investigation: mosaics composed of second harmonic generation signal and fluorescence signal at 890 nm excitation wavelength are presented in Fig. 5. Second harmonic generation signal revealed collagen fibers, present in necrosis for example. Fluorescence showed multiple focal points, corresponding to cell cytoplasm or mitochondria. A pathologist made a comparison between nonlinear images and H&E slides. Matching mosaics and H&E slides was possible in the ten cases. No macroscopic tissue alteration was found

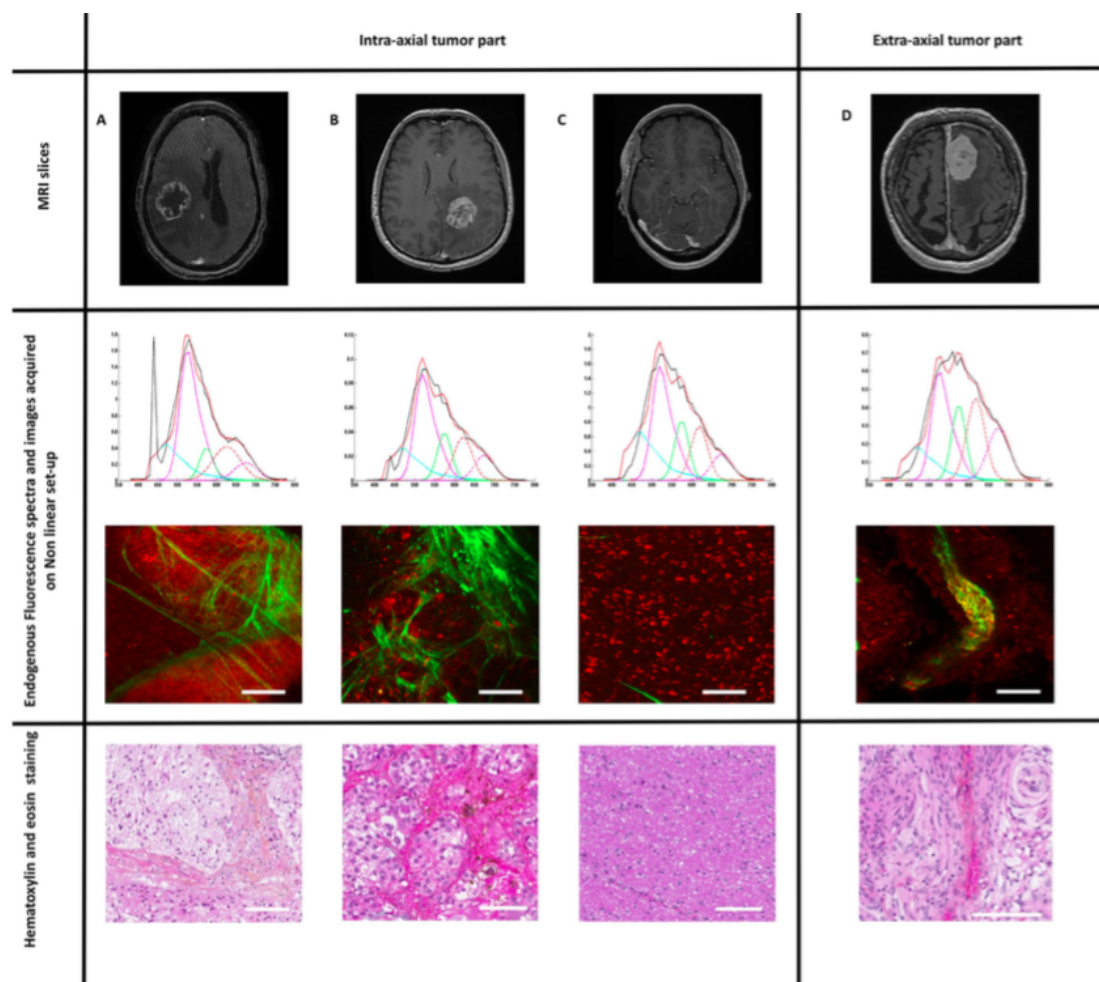


Figure 3.8 – Multimodal analysis of intra and extra-axial tumor analysis of glioma(A) and metastasis(B) samples versus control samples (C) and meningioma control sample (D). From top to bottom: Axial MR slice on contrast enhanced T1-weighted sequence. Spectra at 890 nm excitation wavelength from nonlinear set-up showing a clear peak of SHG at 445 nm. Image from nonlinear set-up showing SHG signal in green and fluorescence in red. Hematoxylin-Eosin staining Images. Scale bars: 100  $\mu\text{m}$ . Spectra analysis: X-axis: emission wavelength (nm) and Y-axis: Fluorescence intensity (a.u.); Fitted by Matlab so ware: blue, purple and green line represent respectively NADH, FAD and lipopigment fluorescence emission spectra. Red and purple dot lines for porphyrin I and porphyrin II.

out after two-photon excitation. Despite the limits of such macroscopic analysis, this results was in accordance with previous results [257, 258]. Our FLIM measurements were in accordance with a previous study performed on fixed meningioma samples [216]. Two-photon FLIM measurement differed from the results of endoscopic visible set-up due to several reasons: (1) the excitation wavelength and the focal volume (due to the different setup configuration) were not the same and by consequence the lifetime could differ; (2) the absorption effective section of the various molecules was different under two-photon excitation; (3) under two-photon excitation, we collected the global emission spectra without any selective filter in front of detectors as in the endoscopic set-up. *Ex vivo* condition was the major limitation of this study. However, the whole process took less than two hours ensuring the fresh condition of our samples [259] and this delay was essentially due to the transportation of samples. Even if we presented the largest cohort of *ex vivo* fresh human brain samples to date, another limit was the definition of our groups: gliomas vary by subtypes and grade and metastases vary by their primary. Such subgroup analyses were not possible to maintain robust statistical analyses. The same consideration remained true for the effects of oncological treatment on fluorescence signal. Finally the control group (healthy brain tissue) used in the study could not have same fluorescence/optical characteristics as the normal brain tissue surrounding the tumor but this control group definition ensured that our control samples were healthy, without any tumoral infiltration. Moreover, the small number of samples analyzed on the multimodal microscopic setup precluded any relevant statistical calculations.

These results represent the first step in producing optical signatures from human brain tissue with multimodal analyses using one and two-photon excitation. This emerging database needs to be widened. A nonlinear endomicroscope adapted to the intra-operative condition is under development by our group. Given that the aim of this surgical tool is to distinguish infiltrated and healthy tissue, it seems mandatory to combine second harmonic generation signal, spectral analysis, lifetime values and two-photon fluorescence to detect infiltrated tissue and not only solid tumor. Multimodal analysis may potentially help differentiating tumor infiltration from healthy zones, allowing the improvement of the quality of life and the survival of patients harboring a central nervous system tumor. Such nonlinear endomicroscopy presents obvious advantages: (1) easy to use in the operating room; (2) fast time acquisitions; (3) and low cost [125]. Moreover, subcellular investigation of human brain can help current research on many topics such as age related diseases or psychiatric diseases.

## Chapter 4

# Could mono and bi-photon excitation discriminate label-free fluorescence emission of meningioma tumor grade ?

### 4.1 Context of the study

As presented in the introduction of this thesis, Meningioma is one of the most common brain tumors. So large cohort of patients were available thanks to the collaboration with the Sainte-Anne Hospital.

In the literature, there are few studies on this tumors. Using a 337nm excitation, Butte et al. showed the discrimination between meningioma and healthy dura matter with a 90% level of confidence [252]. In an exploratory study on *ex vivo* brain tumor tissue, Kantelhardt et al. looked at one WHO grade I meningioma using a two-photon microscope. They showed high fluorescence intensity of the cytoplasm of tumor cells and low-signal-intensity nuclei in the TPEF images, and distinctly longer lifetimes than for tumor-adjacent brain [134, 256]. The scarcity of detailed literature on the endogenous response of meningioma leaves place for more in-depth work.

In the previous chapter, the performed quantitative discrimination on freshly extracted tissue using one-photon endoscopic configuration was presented, and it was hinted that similar results could be obtained using a two-photon excitation. Moreover, two-photon excitation allows to obtain a multi-contrast image (TPEF-SHG), revealing structures which are very close to H&E gold standard. To grade meningioma based on the H&E images, neuropathologists use structures such as fiber arrangement, vessels organization and cells density. These structures have been identified in TPEF-SHG of the previous chapter exploratory study. There the clinical need of grading meningioma tumor would be a suited challenge to perform a first complete study using a two-photon configuration.

The questions that arise are : is it possible to detect these structures with a two-photon imaging system, without any coloration of the tissue and then to perform a diagnosis ? Could quantitative



discrimination be found and lead to further automated decisions ? To evaluate the potential of the two-photon microscopy, and compare it to the previous one-photon technique, a study on grading meningioma tumor was designed. The chosen meningioma tumor cohort contained WHO grade I and II samples. Neuropathologist compared the TPEF-SHG images obtained to find standard hallmark of grade. Quantitative spectral and FLIM measurements were then acquired to test if discriminative indicator could be extracted.

This study does not answer yet the complete problem set in thesis, the discrimination of brain tumors from healthy regions, but it could be seen as a starting point to evaluate the capabilities of two-photon endomicroscopy. Answering this challenges will be the first step to tackle larger clinical problem such as the discrimination of primary and secondary brain tumor.

**Methods** Nine formaldehyde fixed meningioma samples were used in this study, four WHO grade I and five WHO grade II. The samples were analyzed using 405nm excitation wavelength on the bi-modal set-up presented in the two previous chapters. Then they were analyzed using a two-photon bench-top microscope using 810 and 890 nm excitation, performing fluorescence, SHG and FLIM imaging, as well as spectral and fluorescence lifetime measurements. H&E staining were performed on the samples, as well as a Ki-67 immunohistochemical staining to calculate the mean Ki-67 proliferative index.

**Results and discussion** In this study, the question of the discrimination of meningioma grade was tackled for the first time by monitoring endogenous fluorescence with multimodal optical set-ups. The study showed: 1) that merged images of TPEF and SHG are comparable to H&E histological standard; 2) that the spectral response with both one and two photon excitation resulted in a higher intensity for grade II than I; 3) that fluorescence lifetime resulted in a shorter value for grade II than grade I; and 4) that when fluorescence intensity was compared to a histological proliferative indicator, Ki-67, a correlation was found.

Using two photon-excitation gave access to another imaging modality besides TPEF, the SHG response. The molecules producing fluorescence were predominant in cells cytoplasm and interconnective tissue, where the SHG is generated by non-centrosymmetric structures, such as fibers or vessels walls. These secondary signals were particularly advantageous in meningioma tumor, where fibrillar collagen is dominant and where changes in its architecture are a strong marker of tumor grade. Different structures were identified in the TPEF images that serve for neuropathological diagnosis on H&E images: whorls, psammoma and winding fibers of collagen. Moreover blood vessels walls also resulted in SHG, and thus could be used as a diagnosis marker since vascular architecture is strongly modified through the tumor process. With this study it has been shown that the visual grading of meningioma done on H&E stained images could also be performed directly on the TPEF-SHG images. An H&E image requires chemical manipulation and long preparation time, several hours to a day, while the optical image combining TPEF and SHG is acquired in a few seconds and can be measured directly on the tissue without any manipulation. Being able to perform the diagnosis on TPEF-SHG images will speed up considerably the process of histopathology analysis and reduce the bias due to chemical manipulation, resulting in faster medical decision and better care for the patient.

However the real advantage of the optical method is the possibility to use quantitative measurements that will be more reliable than the human judgement. As in one-photon, two-photon excitation was used to measure the spectral response of tissue. In both configurations the grade II tissue resulted in a higher fluorescence signal than the grade I. The grade II meningioma in

this study were defined as "intrinsic", tumor marked by an increased in mitotic activity, and a denser cellularity [260]. These two characteristics of grade II are sources of a higher intensity of fluorescence, due to a higher concentration of cells and increased metabolic activity explaining the higher signal in grade II tumor. In histopathology, techniques have been developed to get access to indicators offering quantitative results and assessing changes at a molecular scale. One direction has been to monitor antigen in tissue using an antibody binding technique. This is called immunohistochemistry (IHC) and localizes specific proteins in cells or tissue [261]. IHC can highlight cells proliferation, proteins of regulatory cycle, hormone receptors and growth factors, it has been used to improve routine histological grading. In meningioma, a proliferation marker is used, the Ki 67, a nuclear protein active during the mitotic phase and showing different values for cell proliferation in each grade of meningioma [262]. The mean Ki-67 proliferative index was calculated to grade the tumors, and the tissue spectral intensity detected by our set-up was compared to this value. A correlation was found. Higher were the proliferative index (translating to higher grade), higher the spectral intensity was. These results are very encouraging. In histopathology two staining techniques are used: first the H&E staining to evaluate the type of tumor and then an IHC staining to have molecular information and give a grading to the tumor. With the multimodal optical microscope, one set-up can give the spatial and molecular information at the same time.

As with the one-photon set-up, fluorescence lifetime is also measured with the two-photon configuration. In the previous study longer lifetime values were found in healthy tissue compared to tumor, so here it was expected to find longer value for grade I than grade II. This was the case at 375 and 810nm excitation wavelength, however at 405 and 890nm, this trend could be seen for some molecules but was not always significant. Still, a distinction could be done between grades by also using the fluorescence lifetime imaging.

With this study, two-photon microscopy has shown potential to help answer a relatively simple clinical question which is the grading of meningioma using fixed tissue. These results bring us a step closer to the larger objective of discriminating any brain tumor from healthy tissue. The next step took was to design a study to find optical criteria discriminating primary and secondary tumor from healthy tissue, using two-photon microscope configuration and freshly extracted tumor samples. The results of this campaign will be the object of the next chapter.

## 4.2 Paper: Multimodal optical analysis of meningioma and comparison with histopathology

J. Biophotonics **10**, No. 2, 253–263 (2017) / DOI 10.1002/jbio.201500251



### FULL ARTICLE

### Multimodal optical analysis of meningioma and comparison with histopathology

Marc Zanello<sup>\*,1</sup>, Fanny Poulon<sup>\*,1</sup>, Pascale Varler<sup>3,5</sup>, Fabrice Chretien<sup>3,5</sup>, Felipe Andreiuolo<sup>3,5</sup>,  
Mélanie Pages<sup>3,5</sup>, Ali Ibrahim<sup>1</sup>, Johan Pallud<sup>4,5</sup>, Edouard Dezamis<sup>4,5</sup>,  
Georges Abi-Lahoud<sup>4,5</sup>, François Nataf<sup>4,5</sup>, Baris Turak<sup>4,5</sup>, Bertrand Devaux<sup>4,5</sup>,  
and Darine Abi Haidar<sup>\*,1,2</sup>

<sup>1</sup> IMNC Laboratory, UMR8165-CNRS, Orsay, France

<sup>2</sup> University Paris 7-Paris DIDEROT, F-75013, Paris, France

<sup>3</sup> Neuropathology Department, Sainte-Anne Hospital, France

<sup>4</sup> Neurosurgery Department, Sainte-Anne Hospital, France

<sup>5</sup> Paris Descartes University, Paris, France

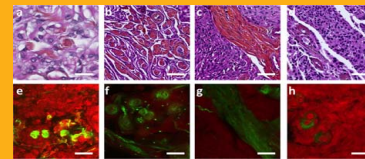
Received 21 September 2015, revised 17 December 2015, accepted 11 January 2016

Published online 15 February 2016

**Key words:** Fluorescence, meningioma, spectroscopy, fluorescence lifetime, multiphoton microscopy, histology

Meningioma is the most frequent primary central nervous system tumor. The risk of recurrence and the prognosis are correlated with the extent of the resection that ideally encompasses the infiltrated dura mater and, if required, the infiltrated bone. No device can deliver real-time intraoperative histopathological information on the tumor environment to help the neurosurgeon to achieve a gross total removal. This study assessed the abilities of nonlinear microscopy to provide relevant and real-time data to help resection of meningiomas. Nine human meningioma samples (four World Health Organization Grade I, five Grade II) were analyzed using different optical modalities: spectral analysis and imaging, lifetime measurements, fluorescence lifetime imaging microscopy, fluorescence emitted under one- and two-photon excitation and the second-harmonic generation signal imaging using a multimodal setup. Nonlinear microscopy produced images close to histopathology as a gold standard. The second-harmonic generation signal delineated the collagen background and two-photon fluorescence underlined cell cytoplasm. The matching between fluorescence images and Hematoxylin and Eosin staining was possible in all cases. Grade I meningioma emitted less autofluorescence than Grade II meningioma and Grade II meningioma exhibited

a distinct lifetime value. Autofluorescence was correlated with the proliferation rates and seemed to explain the observed differences between Grade I and II meningiomas. This preliminary multimodal study focused on human meningioma samples confirms the potential of tissue autofluorescence analysis and nonlinear microscopy in helping intraoperatively neurosurgeons to reach the actual boundaries of the tumor infiltration.



Correspondence between H&E staining (top pictures) and the two-photon fluorescence imaging (bottom pictures).

\* Corresponding author: e-mail: abihaidar@imnc.in2p3.fr

\*\* These authors participated equally to this work.

### 4.2.1 Introduction

Meningioma represents the most frequent primary central nervous system tumor [263]. Meningioma arises from arachnoid cells and their progressive enlargement compresses adjacent structures, leading to clinical revelation through epileptic seizures, neurological deficits, or increased intracranial pressure [264]. These tumors are histologically classified into three grades, from Grade I to Grade III, according to the World Health Organization (WHO) classification. Most meningiomas are classified as Grade I tumors and up to 10% exhibit a more aggressive pattern, leading to their classification as atypical (Grade II) or anaplastic/malignant (Grade III) meningiomas [264]. These latter have a greater risk of recurrence with increased mortality: The five-year survival rates are 78% and 44% respectively for Grade II and Grade III meningiomas [21].

The gold standard for therapeutic management of meningiomas is gross total surgical resection encompassing, whenever possible, the dural insertion, the perilesional dura mater and the overlying bone if infiltrated. The postoperative management consisted of radiotherapy, if required, for grade II and Grade III cases [265]. The extent of the dural resection, measured by the Simpson grading system, is correlated with the risk of recurrence [266, 267]. However, repeated surgeries and extensive resections are associated with operative risks and quality of life impairment [268]. To improve the benefit-to-risk ratio, neurosurgeons used intra-operative tools such as ultrasonography, neuro-navigation, macroscopic induced fluorescence using 5-aminolevulinic acid or indocyanine green, radioisotope, intraoperative magnetic resonance imaging (MRI) or intraoperative computed tomography [269–275]. None of these devices can currently deliver sufficient information on the histopathological nature of the perilesional dura mater. An intra-operative tool, able to provide real-time multiple data on dural infiltration, extrinsic brain invasion, or histopathological grade during surgery could help the neurosurgeon to achieve gross total removal of a meningioma.

Progresses in optical technologies make it possible and optical devices are currently being explored in the field of surgical neuro-oncology [137, 170, 174, 244] 18 . Their micrometric resolution offers a new type of medical imaging and allows for quickly obtaining details on the tumor environment and architecture with fast time acquisition. However, they are frequently associated with the use of external markers, such as 5-aminolevulinic acid or indocyanine green, and their devices are a wide-field or a laser scanning confocal microscopy system [270, 276]. Nonlinear microscopy presents several advantages: visualization of deeper structures, reduced phototoxicity due to better localization of the excitation and additional imaging modalities [170]. However, multiphoton endomicroscopy is still under development [196, 197]. On the other hand, the analysis of tissue fluorescence emitted by endogenous brain fluorophores, namely autofluorescence, seems to be a promising way to avoid any bias and metabolic alteration related to external markers [137]. To our knowledge, no series investigating human meningioma samples has combined autofluorescence and nonlinear multimodal microscopy.

In this exploratory analysis, we first assessed the ability of multimodal optical analyses (spectral analysis, fluorescence lifetime imaging microscopy (FLIM), time-domain measurement, second-harmonic generation (SHG) imaging, and fluorescence under one- and two-photon excitation) to individualize pathological features associated with meningioma and we compared the images to histopathology as the gold standard. Secondly, we investigated the differences between the optical signatures of Grade I and Grade II meningiomas.

## 4.2.2 Material and methods

### 4.2.2.1 Samples

Nine formalin zinc-fixed meningioma samples (4 Grade I, 5 Grade II) were included. None of the patients had familial history of meningioma, neurofibromatosis or previous oncological treatment, including surgery or radiotherapy. We collected only the samples taken two months ago in the Sainte Anne Hospital Neurosurgery Department with enough material to allow complementary analysis if necessary. All samples had an immunohistochemical staining of Ki-67 (1 : 200, MIB-1, Dako Denmark A/S, Glostrup, Denmark). Immunostainings were performed and evaluated semiquantitatively (number of labeled cells per total number of tumor cells, excluding endothelial and lymphomonocytic cells). Mean Ki-67 proliferative index was less than 1% (range: < 1% to 4%) for Grade I meningioma and was 13% (range: 5% to 20%) for Grade II meningioma. The institutional review board of the Sainte-Anne Hospital Center - University Paris Descartes approved the study protocol (number SC3227).

### 4.2.2.2 Spectroscopic and time resolved measurements on a visible setup

The visible setup consisted of two-pulsed laser diodes from Picoquant used as laser sources. One emitted at 405nm (LDHP-C-405B, FWHM 60 ps, Picoquant GmbH, Berlin, Germany) and the other emitted at 375nm (LDHP-C-375B, FWHM 45 ps, Picoquant GmbH, Berlin, Germany) with a maximum power of 1 mW. The diodes were driven by PDL-808 Sepia (PicoQuant GmbH, Berlin, Germany). The power and the repetition frequency could be adjusted. The repetition frequency could be set between 2.5 MHz and 40 MHz. Excitation was performed via a first fiber and fluorescence was collected via a second fiber (silica/silica step index fibers of inherent spatial resolution of 0.5 mm). A long-pass filter (SR 420, Semrock, New York, USA) was used to remove the laser excitation's contribution to fluorescent signal. A beam splitter divided and sent the collected fluorescence into two detectors: 70% of the signal for spectroscopic analysis and 30% for lifetime measurement. For spectroscopic measurement, the collected fluorescence was directed toward a computer-controlled cooled spectrometer (QE 6500, Ocean Optics, Dunedin, USA) of 1.5 nm spectral resolution over a 200-1000 nm spectral range. A specific mechanical support was mounted on a motorized microtranslator stage (Thorlabs, Newton, USA) for XY scanning. The X-dimension scanning velocity was 100  $\mu\text{m/s}$  and the acquisition time during X-line scanning was 3 s per fluorescence spectrum. Spectral acquisition was accomplished for several longitudinal lines of each sample. For time-resolved measurements, the collected fluorescence was guided to a photomultiplier tube (PMA-182 NM, PicoQuant GmbH, Berlin, Germany). The temporal resolution of the photomultiplier tube was 220 ps. The synchronization output signal from the diode driver and the start signal from the photomultiplier tube were connected to their respective channels on the data acquisition board time-correlated single-photon counting (TimeHarp 200, PicoQuant GmbH, Berlin, Germany). A motorized filter wheel (FW102C, Thorlabs, Newton, USA) was placed in front of the photomultiplier tube allowing selection of the spectral emission band. With a 405 nm excitation wavelength, we used five filters (Semrock, New York, USA):  $450 \pm 10$  nm,  $520 \pm 10$  nm,  $550 \pm 30$  nm,  $620 \pm 10$  nm and  $680 \pm 10$  nm. With a 375 nm excitation wavelength, we worked only with the  $450 \pm 10$  nm and  $520 \pm 10$  nm filters. Lifetime and spectroscopic measurements were acquired on the same setup and 2 s were required to measure each fluorophore lifetime.

### 4.2.2.3 Confocal, two-photon microscopy and fluorescence lifetime imaging on a multimodal setup

A Mai Tai DeepSee Ti:sapphire laser with automated dispersion compensation (Spectra-Physics, Santa Clara, USA) and a TCS SP8 MP confocal microscope (Leica Microsystems, Wetzlar, Germany) performed confocal microscopy as well as two-photon microscopy and fluorescence lifetime imaging of the samples. The laser cavity had over 2.4 W of average power at 800 nm and was tunable from 690 nm to 1040 nm. The repetition rate was 80 MHz and the temporal width at the output of the cavity was around 70 fs. The laser was controlled with the Leica software, including easy adjustment of the prechirp unit. Two supersensitive Leica hybrid non-descanned (HyD NDD) detectors recorded the faintest structures from deep-tissue sections. For two-photon imaging experiments, fluorescence was collected after the microscope objective via a dichroic beamsplitter, transparent to wavelengths greater than 680 nm. The collected visible spectrum was split by another dichroic cube (FF495-Di03-25 x 36, Semrock, New York, USA) into two channels toward the HyD NDD detectors. This configuration minimized loss in the fluorescence collection. The presence of two additional filters (FF01-448/20-25 and FF01-520/35-25, Semrock, New York, USA) on the dichroic cube set the detection band. Microscope objectives were long working distance water-immersion Leica objectives (HCX IRAPO L 25X NA 0.95 or HC PL APO 40X NA 1.1 CORR CS2). An electro-optical modulator adjusted the laser power at the entrance of the confocal system. This was particularly useful to automatically compensate for energy loss due to scattering as the focus moved inside the samples. Spectral unmixing software allowed elaboration of multicolor multiphoton experiments. The spectral acquisition was performed using an internal hybrid detector. Fluorescence was dispersed by a prism and a specific motorized split mirror selected the spectral detected band before the hybrid detector. With this spectral detection we made different images of selected fluorescence for XY imaging plane. The system coupled the single-photon counting technology fluorescence lifetime imaging with spectral acquisition: it integrated hardware and software (PicoQuant GmbH, Berlin, Germany) with the high-end confocal system Leica TCS SP8 MP. This optical setup recorded four different optical signals on the region of interest (ROI): 1) one and two-photon spectral analysis, 2) two-photon fluorescence lifetime imaging measurement, 3) SHG imaging, and 4) fluorescence imaging under one- and two-photon excitation.

### 4.2.2.4 Data analysis

#### 4.2.2.4.1 Analysis of spectroscopic measurements from a visible setup

The spectral measurements were processed using a homemade Matlab program, as previously described [128]. These spectra represented the different endogenous fluorophores emissions. To determine the contribution of each fluorophore (intensity, maximum wavelength emission and integral under the curve), we adjusted data following Eq. 4.1 where  $S_{total}(\lambda)$  was the measured spectrum,  $i$  the fluorophore,  $S_i(\lambda)$  the emission spectrum of the fluorophore  $i$  and  $f_i$  a multiplicative factor of this spectra. Five fluorophores were considered: reduced Nicotinamide adenine dinucleotide (NADH), flavins, lipopigment, porphyrin and chlorin. We did not use an appropriate excitation wavelength to excite the fluorescence of collagen. For both excitation wavelengths of 375 nm and 405 nm, the spectrum of flavins ( $S_{Flav}(\lambda)$ ) is adjusted by an emission spectrum taken from literature [105], while for NADH ( $S_{NADH}(\lambda)$ ) we used the spectra obtained during our previous experiment on rat under 375 nm excitation [128]. The other 3 peaks, ( $S_{Lipo}(\lambda)$ ), ( $SP_{620}(\lambda)$ ) and ( $SP_{680}(\lambda)$ ), are fitted by Gaussians.

$$S_{total}(\lambda) = \sum_i 1(f_i.S_i(\lambda)) \quad (4.1)$$

#### 4.2.2.4.2 Analysis of lifetime measurement from a visible setup

Data were adjusted by a monoexponential fit via FluoFit software (PicoQuant, GmbH, Berlin, Germany) to recover the lifetimes from the measured fluorescence decays. The criteria for an acceptable fit were: 1) a  $\chi^2$  value less than 1.0 and 2) residuals randomly distributed around 0 within the interval +4 and -4. The instrument response function was calculated by placing the probe on a Teflon block and on a mirror. The instrument response function of our system, measured with 1.1  $\mu$ W excitation power at 405 nm, was around 240 ps (FWHM = 120 ps).

#### 4.2.2.4.3 Analysis of lifetime measurements from a multimodal setup

For fluorescence lifetime imaging measurements, two positions at least per sample were analyzed using appropriate excitation wavelengths. The depth was equal to that used for spatial image acquisition. The image size was 128 x 128 pixels, at 100 Hz and represented the average of 20 frames. The data were collected and analyzed via the software Symphotime (PicoQuant, GmbH, Berlin, Germany). On each fluorescence lifetime image, twelve ROI were selected on the different structures and fitted by a mono- or biexponential decay to extract the fluorescence lifetime. The criteria for an acceptable fit were: 1) a  $\chi^2$  value less than 1.0 and 2) residuals randomly distributed around 0 within the interval +4 and -4. Results were the mean of the twelve selected ROI.

#### 4.2.2.4.4 Analysis of spectral analysis, SHG imaging, and fluorescence imaging under one- and two-photon excitation from a multimodal setup

All the analyses were performed by the dedicated Leica software (Leica Microsystems, Wetzlar, Germany). Spectra were obtained from spectral acquisition using the Leica software, then they were fitted using the described methodology. Fluorescence and SHG images reconstruction were acquired by using the dedicated Leica software as well as an open source-image-processing program ImageJ.

### 4.2.3 Results

#### 4.2.3.1 Determination of optimal excitation wavelength on a multimodal setup

The optimal excitation wavelength to work on human brain samples is not perfectly known as endogenous fluorescence of each tissue type is the combination of different fluorophores. To define the optimal excitation wavelength, we used two NDD HyD detectors, each one sensitive in a specific wavelength range. Figure 4.1a and b show, respectively, the emission fluorescence intensity of one sample collected by every detector at each excitation wavelength of the tunable laser cavity from 690 nm to 1040 nm. At a 810 nm excitation wavelength, the NADH fluorescence emission was lower compared with a 405 nm excitation wavelength and chlorin was not excited. At a 890 nm excitation wavelength, fluorescence emission of endogenous fluorophores was lower compared with a 810 nm excitation wavelength, except for chlorin. At a 890 nm excitation wavelength, SHG emission related to noncentrosymmetric molecules like collagen was visible around 440 nm. We decided, as shown in

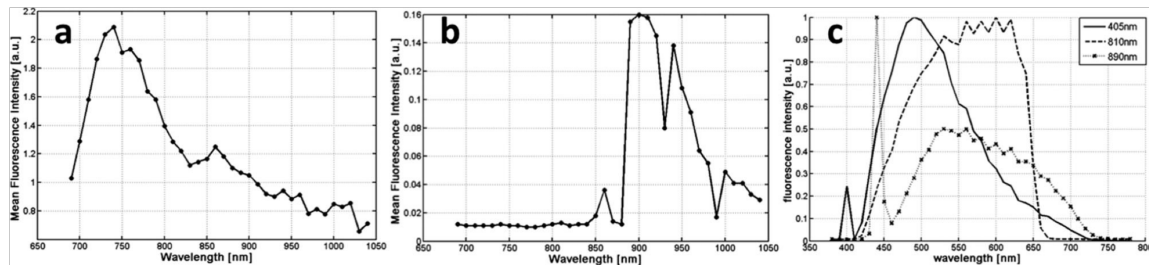


Figure 4.1 – (a) Average fluorescence intensity (in arbitrary unit) detected by non-descanned hybrid detector 1 according to the excitation wavelength. (b) Average fluorescence intensity detected by non-descanned hybrid detector 2 according to the excitation wavelength. (c) Superposition and normalization of the emitted fluorescence by a WHO Grade I meningioma sample using different excitation wavelengths: 405 nm (black line), 810 nm (dotted line) and 890 nm (line with points). The peak around 400 nm at 405 nm excitation wavelength was the laser reflection. The peak around 440 nm at a 890 nm excitation wavelength was the second-harmonic generation signal.

Figure 4.1c, to use two different excitation wavelengths: 1) 810 nm, the double of one wavelength of the visible setup (405 nm) and 2) 890 nm with emission of fluorescence as well as the SHG signal.

#### 4.2.3.2 Multimodal optical imaging on a multimodal setup

The correspondence between H&E staining and the acquisitions made on a multimodal setup is represented in Figure 4.2 .

Different images representing features of meningiomas such as collagen fascicles (Figure 4.2a, c, e and g), whorls (Figure 4.2b and f), and blood vessels (Figure 2d and h) were quite recognizable by neuropathologists on the corresponding two-photon fluorescence images. The histopathology slices and fluorescence images were similar.

Figure 4.3 represents a mosaic of numerous images combining the two-photon fluorescence signal and SHG. The size of the two-photon fluorescence signal images was enlarged to fit gold standard histopathology. As shown in Figure 4.3, the SHG signal in green delineated whorls and collagen fibers and two-photon emitted fluorescence in red delineated meningothelial lobules. This resolved image is matched with the correspondent H&E slides.

#### 4.2.3.3 Optical signature of Grade I and Grade II meningioma on both setups

##### 4.2.3.3.1 Multimodal analysis

Figure 4.4 represents the MRI characteristics, the macroscopic appearance and fluorescence images obtained with the multimodal setup with corresponding histopathological slices of representative cases of Grade I and Grade II meningiomas. The protocol for matching fluorescence to histology was previously described [244]. It appeared that the MRI and macroscopic appearance were similar, whereas the fluorescence images were quite different: the SHG signal was stronger and cell-emitted fluorescence emitted was brighter in Grade II meningioma than in Grade I meningioma due to more abundant collagen fascicles and cell density, as demonstrated on histopathological slices.



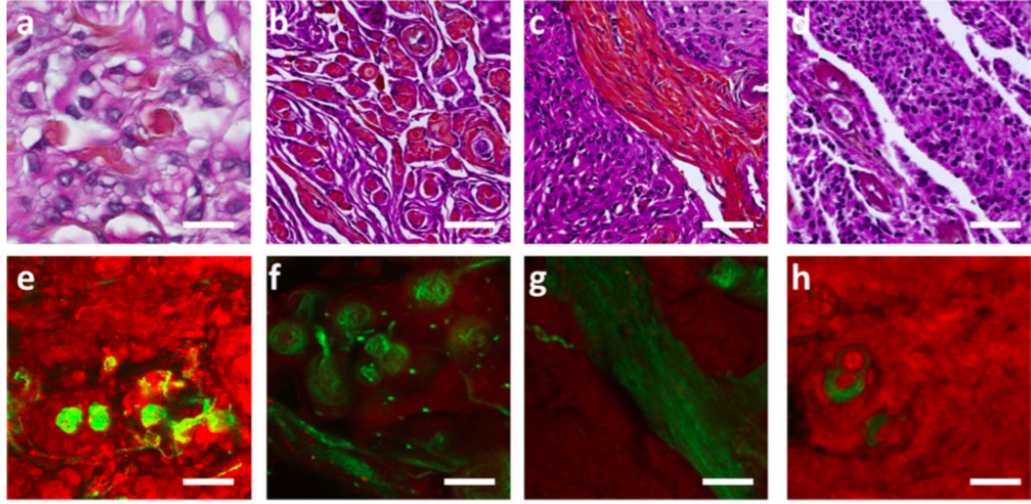


Figure 4.2 – Correspondence between H&E staining (top pictures) and the two-photon fluorescence imaging (bottom pictures) are, respectively, presented. Bundles of collagen (Figure 2a and e), psammoma bodies (Figure 2b and f), winding collagen fiber (Figure 2c and g) and vessels walls (Figure 2d and h). Scale bars at  $100\mu\text{m}$  for fluorescence images and Hematoxylin and Eosin staining.

These modalities were complementary. For instance, some bright fibrillary formations appeared discreetly with confocal imaging. These formations were whorls, formed by the rolling-up of some cells flattened around a big round cell or around a small vessel with a fibrous wall and were clearly discriminated with two-photon excitation, thanks to the SHG signal of the collagen fibers. Another example of this complementarity was the possibility to distinguish round collagen fibers from vessel walls with FLIM.

#### 4.2.3.3.2 Spectral emission using visible and multimodal setups

Figure 4.5 highlights representative cases of emission spectrum with 405 nm (Figure 4.5a and b) and 890 nm (Figure 4.5c and d) excitation wavelengths and the mean spectrum for Grade I and Grade II meningiomas at the same wavelengths. Two Ki-67 stains, one weak and the other strong, are showed in Figure 4.7A with the correlation between fluorescence intensity and Ki-67 staining (Figure 4.7B).

The mean spectrum of each grade was measured on three ROI for each sample ( $n = 27$ ) at the 405 nm excitation wavelength on the visible setup. As observed, we globally collected a high-emitted fluorescence from Grade II meningioma. On average, Grade II samples were 26.6% more fluorescent than Grade I. Using the 890 nm excitation wavelength, the five endogenous fluorophores (NADH, flavins, lipopigment, porphyrins and chlorins) were observed as well as SHG. We observed the SHG at 445 nm and the emitted autofluorescence under two-photon excitation. On average, Grade II samples were 84.6% more fluorescent than Grade I samples. The signal from Grade I samples was lower than the signal from Grade II samples in all cases. Given the difference of Ki-67 proliferative index between our Grade I and Grade II meningioma, we investigated the relationship

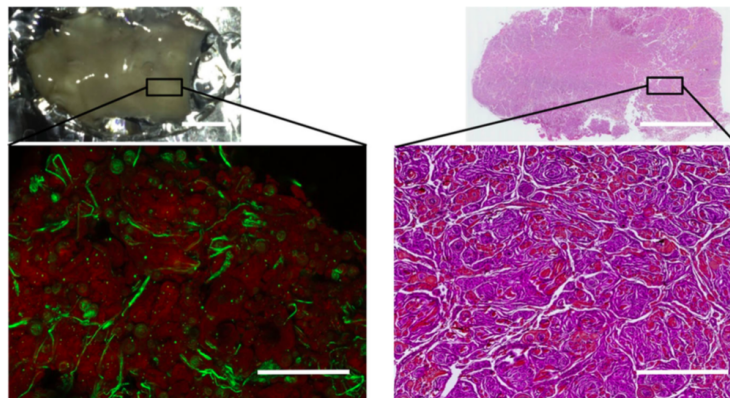


Figure 4.3 – Correspondence between the macroscopic view of a meningioma sample, the superimposition of two-photon fluorescence and second-harmonic generation, and the histopathology as a gold standard. **Left top** image shows the macroscopic view of the meningioma sample. **Left bottom** image shows the superimposition of the two-photon fluorescence (fluorescence signal in red) and the second-harmonic generation (signal in green). **Right top** image shows the macroscopic view of the Hematoxylin and Eosin staining of the same meningioma sample. **Right bottom** image shows the enlarge Hematoxylin and Eosin staining. Scale bars at 500  $\mu\text{m}$  for macroscopic views (**top**). Scale bars at 100  $\mu\text{m}$  for microscopic views (**bottom**).

between the Ki-67 proliferative index and fluorescence intensity. This latter increased with the Ki-67 proliferative index.

#### 4.2.3.3.3 Lifetime of the different excited endogenous fluorophores with visible and multimodal setups

The fluorescence lifetime characteristics of our cohort are summarized in figure 4.6 . On the visible setup, at the 375 nm excitation wavelength, lifetime values of NADH and flavins of Grade I samples were always longer than the lifetime values of Grade II samples: 5% and 10%, respectively. At the 405 nm excitation wavelength, NADH, flavins, lipopigments; porphyrin, but not chlorin of Grade meningioma I samples had longer lifetime values than Grade II samples. On the multimodal setup, at the 810 nm excitation wavelength, NADH and flavins were the two excited fluorophores. At the 890 nm excitation wavelength, the best fit was obtained with three components for Grade I meningioma, interpreted like NADH, flavins and SHG signal. For Grade II meningioma, a fourth component ( $\tau_2$ ) appeared for all studied samples with a fluorescence lifetime of 1.8 ns. The lifetime values from Grade I and Grade II meningiomas were similar.

## 4.2.4 Discussion

The present study described, for the first time, multimodal optical imaging on a series of human meningioma samples. We showed that: 1) an excitation wavelength of 890 nm allowed two-photon fluorescence and a SHG signal to be obtained; 2) multimodal analysis could be easily compared with

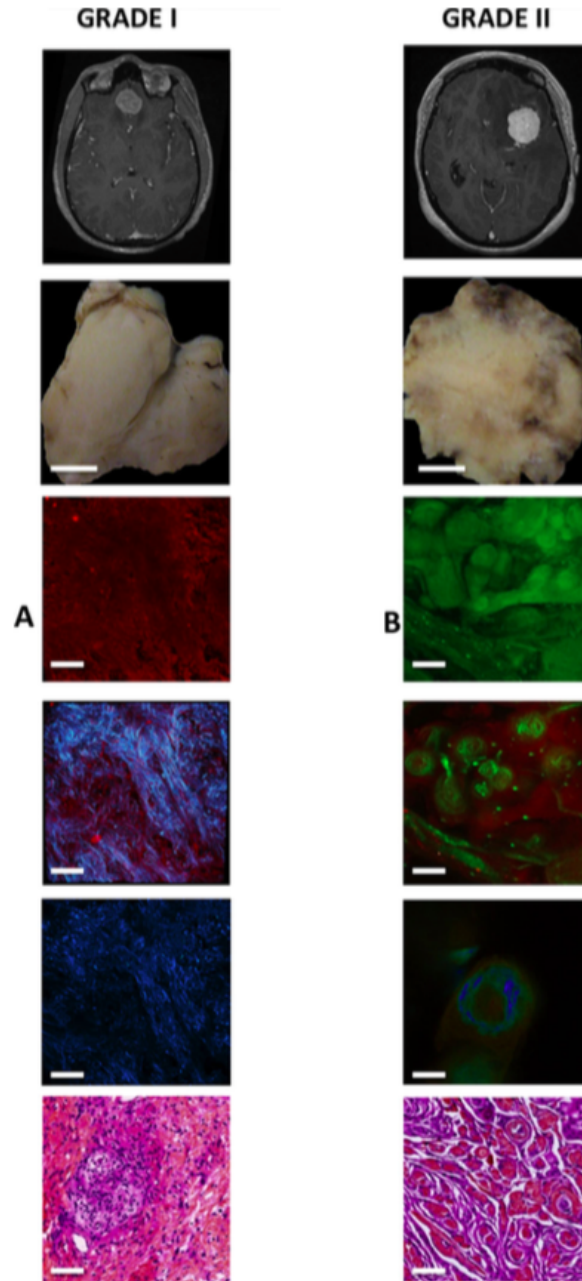


Figure 4.4 – Illustrative case of WHO Grade I meningioma (A). From top to bottom: Axial MR image on contrast enhanced T1-weighted sequence; macroscopic view of meningioma sample; fluorescence image at 405 nm excitation wavelength; two-photon fluorescence image at a 890 nm excitation wavelength with fluorescence in red and second-harmonic generation signal in blue; fluorescence lifetime imaging microscopy; gold standard Hematoxylin and Eosin staining. Illustrative case of WHO Grade II meningioma (B). From top to bottom: Axial MR image on contrast enhanced T1-weighted sequence; macroscopic view of meningioma sample; fluorescence image at a 405 nm excitation wavelength; two-photon fluorescence image at a 890 nm excitation wavelength with the fluorescence signal in red and the second-harmonic generation signal in green; fluorescence lifetime imaging microscopy of the square in F with different lifetime values in the same structure; gold standard Hematoxylin and Eosin staining. Scale bars at 100  $\mu\text{m}$  for fluorescence images and Hematoxylin and Eosin stainings. Scale bars at 500  $\mu\text{m}$  for macroscopic views.

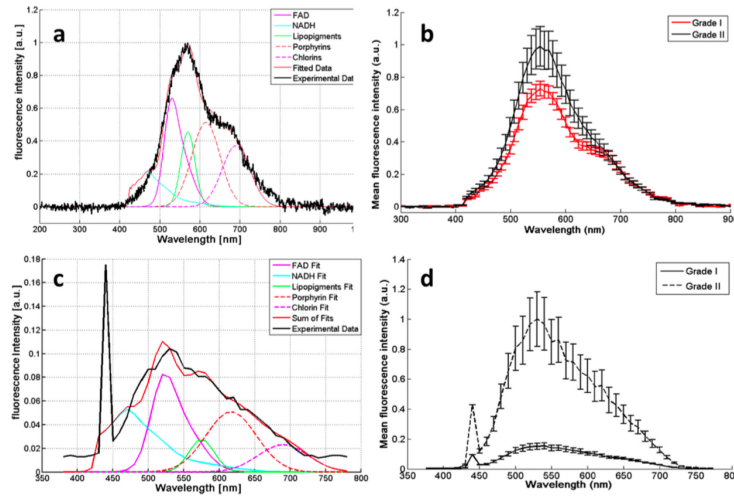


Figure 4.5 – Representative emission spectrum of a sample (a) at a 405 nm excitation wavelength on a visible setup and the fits of the five endogenous fluorophores; (b) Mean emission fluorescence intensity of WHO Grade I meningiomas (red line) and WHO Grade II meningiomas (black line) at 405 nm excitation wavelength on the visible setup; (c) Representative emission spectrum of a sample at a 890 nm excitation wavelength on the multimodal setup and the fits of the five endogenous fluorophores (the peak at 445 nm was the second-harmonic generation signal); (d) Mean emission fluorescence intensity of WHO Grade I meningioma (continuous line) and WHO Grade II meningioma (dotted line) at a 890 nm excitation wavelength on the multimodal setup.

Setup	Excitation wavelength (nm)	Filter: wavelength (nm)	ROI (n)	Lifetimes values: WHO Grade I meningioma (ns, mean $\pm$ SD)	ROI (n)	Lifetimes values: WHO Grade II meningioma (ns, mean $\pm$ SD)	Fluorophore
Visible setup	375	450 $\pm$ 10	9	4.680 ( $\pm$ 0.082)	6	4.440 ( $\pm$ 0.177)	NADH
		520 $\pm$ 10	9	4.672 ( $\pm$ 0.174)	6	4.159 ( $\pm$ 0.186)	FAD
	405	450 $\pm$ 10	9	3.998 ( $\pm$ 0.178)	6	3.639 ( $\pm$ 0.104)	NADH
		520 $\pm$ 10	9	4.214 ( $\pm$ 0.061)	6	3.873 ( $\pm$ 0.189)	FAD
		550 $\pm$ 30	9	7.569 ( $\pm$ 2.103)	6	7.211 ( $\pm$ 0.707)	Lipopigment 1
			9	4.324 ( $\pm$ 1.858)	6	2.236 ( $\pm$ 0.178)	Lipopigment 2
		620 $\pm$ 10	9	3.326 ( $\pm$ 0.296)	6	3.287 ( $\pm$ 0.144)	Porphyrin
		680 $\pm$ 10	9	2.890 ( $\pm$ 0.162)	6	3.065 ( $\pm$ 0.134)	Chlorin
Multi-modal setup	810	–	16	2.670 ( $\pm$ 0.151)	10	2.550 ( $\pm$ 0.137)	NADH
		–	16	0.507 ( $\pm$ 0.035)	10	0.441 ( $\pm$ 0.047)	FAD
	890	–	30	2.321 ( $\pm$ 0.116)	22	2.264 ( $\pm$ 0.044)	NADH
		–	22	0.341 ( $\pm$ 0.066)	22	0.417 ( $\pm$ 0.038)	FAD
		–	14	0.084 ( $\pm$ 0.004)	12	0.098 ( $\pm$ 0.009)	SHG
		–	–	–	10	1.794 ( $\pm$ 0.032)	Not known: $\tau_2$

Figure 4.6 – Fluorescence lifetime characteristics of our cohort under visible and IR excitation wavelength. ROI: Region of interest.

gold standard histopathology; 3) Grade II meningioma emitted more autofluorescence than Grade I meningioma; 4) the fluorescence lifetime of Grade I meningioma was longer than the fluorescence lifetime of Grade II meningioma and Grade II meningioma exhibited a distinct lifetime value on the visible setup; and 5) the fluorescence intensity and Ki-67 proliferative index seemed to be correlated in meningioma.

Since the early 1990s, only sparse studies have investigated the capacity of autofluorescence to distinguish between pathological and healthy brain tissue [122, 125, 137, 241]. Only three references studied brain neoplasms with visible setups. Nazeer et al. worked with two excitation wavelengths: 320 nm and 410 nm [126]. The first detected collagen, NADH, and flavins around 380nm, 460nm, and 510nm, respectively. Excitation at 410 nm gave the emission values of flavins, phospholipids and porphyrin around 500 nm, 590 nm and 630 nm to 695 nm, respectively. Collagen and phospholipid peaks were less intense for tumor tissue than healthy tissue. Nazeer et al. concluded that collagen and lipid levels in brain decreased as tissue became tumoral. Less porphyrin but more collagen was present in extra-axial tumors, such as meningioma, as compared to intra-axial tumors, such as glioblastoma. No analysis was performed based on the WHO grading system. Butte et al. performed a two modalities analysis: spectral and lifetime analysis [252]. They had a clear peak of fluorescence around 390 nm for Grade I meningioma whereas two peaks (390 nm and 440 nm) existed for dura mater. Lifetime analysis revealed that the fluorescence intensity time-decay characteristics were wavelength dependent and clearly distinct between dura mater and meningioma. Butte et al. concluded that there were at least two distinct types of collagens and their crosslinks contributing to fluorescence emission of dura mater and meningioma and that these fluorophores were not the same between these two tissues. For dura mater, "P" and "M" fluorophores were cited based on a previous chromatography study [277]. For meningioma, collagen type I and collagen type III were responsible of the most important part of the meningioma fluorescence emission according to Butte et al. Using spectral and time-resolved values, the sensitivity and the specificity to diagnose meningioma were equal to 89% and 100%, respectively, far better than spectral analysis used alone with a sensitivity of 61% and a specificity of 73%. Saraswathy et al. reported a statistically significant difference in spectral emission between meningioma (without a clear WHO Grading) and surrounding normal tissue: meningioma exhibited less autofluorescence than normal tissue and the peak around 600 nm, attributed to porphyrins, was more intense than the two other detected peaks (500 nm and 550 nm attributed to collagen and flavins) in meningioma contrary to the normal tissue spectrum [246]. Only one previous work reported signal of a Grade I meningioma under two-photon excitation [256]. Kantelhardt et al. showed that the cytoplasm of meningioma cells exhibited high fluorescence intensity, contrary to the low signal from the nuclei. Lifetime increased at higher excitation wavelengths and the tumor had longer lifetime than tumor-adjacent brain. This study was performed with a nondedicated setup, designed for dermatologic analysis (DermaInspect) and did not explore spectral and SHG signals.

The present work was the more complete optical analysis made on Grade I and Grade II meningioma samples. Non-centrosymmetric fibrillar collagen possesses a tremendous nonlinear susceptibility. This is of particular interest in the field of neuro-oncology since, apart from the high proportion of collagen presented in meningioma; this signal underlines vessel walls and necrotic zones, two classical signs of aggressive behavior for brain neoplasms. In the present study, neuropathologists were able to compare fluorescence images under nonlinear excitation with different histopathological key criteria. Here, Grade II meningiomas showed a significant increase of autofluorescence intensity as compared to Grade I ones. This is of particular interest since there are two types of Grade II meningiomas: 1) intrinsic ones with increased mitotic activity or three or

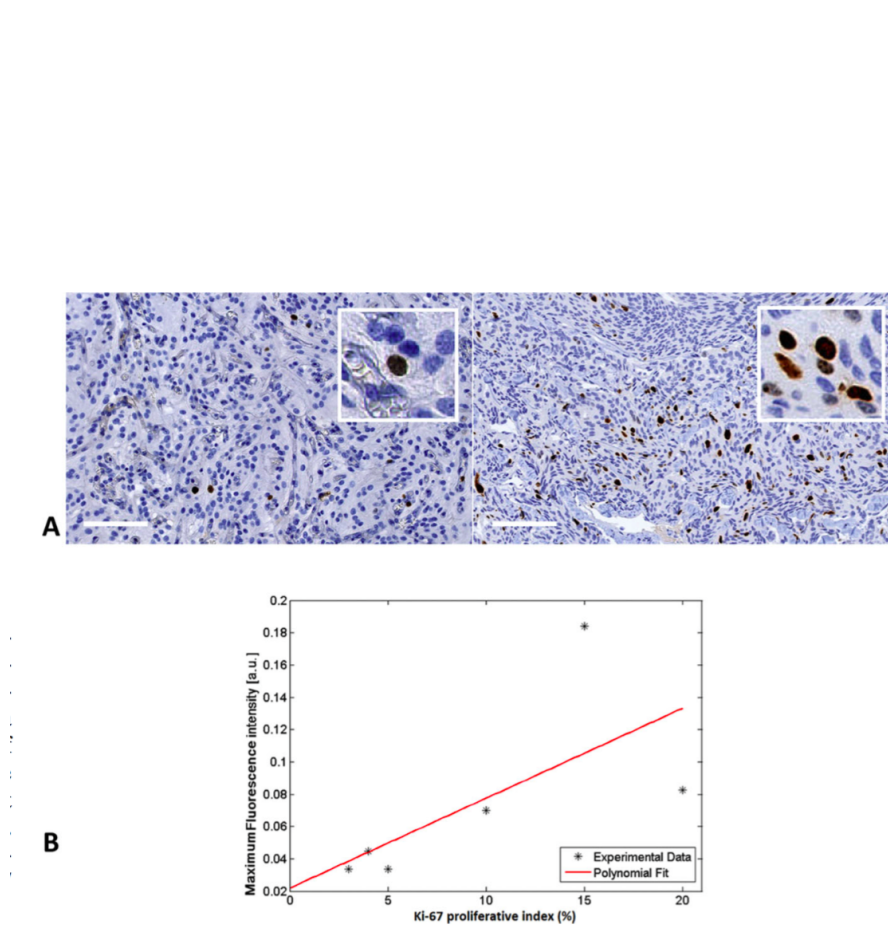


Figure 4.7 – (A) From left to right: Representative case of a Grade I meningioma sample weak Ki-67 stain- ing with the insert showing a stained cell; Representative case of a Grade II meningioma sample strong Ki-67 staining with the insert showing numerous stained cells. (B) Relationship between fluorescence intensity at 890 nm and Ki-67 proliferative index.

more of the following features: increased cellularity, small cells with a high nuclear/cytoplasmic ratio, prominent nucleoli, uninterrupted patternless or sheet-like growth and foci of 'spontaneous' or 'geographic' necrosis [260], 2) extrinsic ones with brain invasion [260]. The Grade II meningiomas under study consisted exclusively of "intrinsic" Grade II. Hence, the observed difference in autofluorescence intensity was probably explained by the increased cell density with an increased level of metabolic activity in Grade II meningiomas as compared to Grade I ones. NADH and flavins had been widely used to evaluate oxidative metabolic state in cells and tissues [278] and NADH was considered as the most prevalent endogenous fluorophore. The correlation between Ki-67 staining and spectroscopic fluorescence intensity corroborated this assessment. The Ki-67 antigen is a nuclear protein present only during mitosis [262]. The lower fluorescence intensity found with the multimodal setup compared with the visible setup could be explained by a small two-photon absorption section of NADH at a 810 nm excitation wavelength [279]. The variation in fluorescence intensity could be a potential criterion to differentiate WHO Grade I and Grade II meningiomas with nonlinear excitation, as with the visible setup. We did not rely on the collected autofluorescence of meningioma in this study to collagen because we did not use excitation wavelengths able to excite the collagen fluorescence [102] and this explained why we ascribed the major part of the spectral response to NADH and FAD, two well-known endogenous fluorophores. However, endogenous fluorescence of human tissue is always due to several fluorophores and it may be possible that collagen crosslinks contributed to the collected signal.

The lowering of lifetime values between Grade I and Grade II meningioma on the visible setup was in accordance with our previous work on mouse brain tumor model [128]. The healthy tissue had longer lifetime values than tumoral tissue so it seemed logical that Grade I meningioma exhibited longer lifetime values than Grade II meningioma. Our results on the multimodal setup were close to those previously described [256] but we did not find the same decrease in lifetime values between Grade I and Grade II meningiomas. During oncogenesis, a shift from cellular oxidative phosphorylation to cellular glycolysis for ATP production occurs. This is called the Warburg effect [248]. The endogenous fluorophore NADH is the principal electron acceptor in glycolysis and an electron donor in oxidative energy metabolism. NADH has two lifetime components: 1) short when it is in its free state and 2) long in a protein-bound state [132]. The changes in metabolism due to tumor growth modified the equilibrium between free and bound form of NADH and the conformation of protein-bound NADH [118]. Considering that Grade II meningiomas are more aggressive than Grade I ones and that the distinct lifetime value found in Grade II meningiomas (1.8ns) was closer to free NADH, the greater amount of free NADH could explain this distinct fluorescence lifetime value presented only in Grade II meningiomas. Another explanation of this distinct fluorescence lifetime value could be the presence of elastin in Grade II meningioma due to the numerous vessels present in these tumors.

These results have to be confirmed *in vivo*, if possible during neurosurgical procedures, formalin fixation altering tissues fluorescence. An easier first step could be the study of meningioma cells implanted in an alive rat brain, having an optical window and the tracking of the optical answer evolution over several weeks. Despite the limits of the present study, multimodal optical imaging could overcome the current limits of actual optical technics and could provide clinically useful intra-operative information.

## Chapter 5

# Could two-photon imaging match the performance of H&E standard in discriminating primary and secondary brain tumor ? Could multimodal quantitative detection improve brain tumor diagnosis ?

### 5.1 Context of the study

In the two previous chapters, it has been proved that the combination of TPEF-SHG imaging shows a high resolution and the capability to highlight typical tissue structures comparable to those seen in H&E stain. In the literature two-photon microscopy has already been used on other types of tumor to find cellular and tissular architecture comparable to the histological standard. Different studies went further than just highlighting similar structures and performed pathological analysis directly on the TPEF images, evaluating the accuracy of such method compared to the results of the H&E standard.

A first team used only the fluorescence response imaging to match H&E diagnosis with unstained images.

Hong et al. studied gallbladder cancer [280]. They identified high fluorescence signal in cytoplasm and a lack of signal in nuclei which gave enough contrast to identify cells morphology and organization. The mucosa, muscularis and serosa were also distinguished using TPEF. The modification in shape and organization of these structures could be tracked as in H&E images to evaluate cancer presence and stage. A pathological diagnosis based on TPEF images, and blind to histology results, was performed and resulted in 96.4% precision [280].

Other teams used the combined TPEF-SHG images to have the closest correlation to H&E-



stained images.

Wu et al. looked at breast masses [281]. Breast tissue presented a lot of fibrous structures resulting in high SHG signal, where changes could be tracked as in H&E slices. They asked a pathologist to analyze TPEF-SHG images, blind to H&E diagnosis. The sensitivity, specificity and accuracy of these diagnoses were evaluated at 88.89%, 83.33%, 87.50%, respectively. The false negative rate was 11.11%.

Yan et al. studied liver cancer [282]. They identified cells architecture, hepatocyte cords, blood-filled sinusoids, glandular and tubular structure of vascular septa in the TPEF image and collagen architecture in the SHG channel. Based on these observations they performed a blind analysis on the TPEF-SHG images and classified them between two states: cancerous or benign, obtaining a 96.32% sensitivity, 96.43% specificity, and 96.34% accuracy.

The standard in histology and the previous described methods were all based on human judgement to perform diagnosis. Some teams used another approach to diagnose tumor using two-photon microscopy to avoid this limitation. They used all the possibilities of optical detection and developed a quantitative method to have an automated diagnosis.

Yan et al. used the TPEF signal to measure [282], in each image, the redox ratio between the NADH and FAD component, using NADH/FAD formula. They found a higher ratio in cancerous cells, with a  $p < 0.001$ .

Other teams used SHG signal to extract quantitative information and build scoring system to evaluate tissue nature. Strupler et al. looked at the SHG organization in renal tissue and build a three-parameters scores to discriminate tissues [283]. Xu et al. evaluated neck margin in pancreatic cancer measuring the pixel density of collagen between in SHG images [284]. Xu et al. identified intramural metastasis in esophageal carcinoma using the quantification of fiber 3D-orientation and directional variance [285].

In the two previous chapter of this thesis it was shown that a bi-modal detection of the spectral response and fluorescence lifetime could discriminate tissues. Moreover structures in brain tissue such as neurons, extracellular matrix arrangement, necrosis, blood vessels or dense regions of tumor cells could be identified in the TPEF-SHG images. To get the most of a two-photon analysis of brain tissue, the two approaches of the literature were considered in the design of this study. A qualitative and quantitative analysis of the biopsy samples would be performed to find a scoring system that could discriminate different tumor types. Here a larger clinical question, than the grading of one tumor type in the previous chapter, was chosen : the discrimination of primary and secondary brain tumor compared to control cortex tissue. TPEF-SHG modality was firstly used to characterize typical structures and perform a blind reading and diagnosis. Then quantitative measurements were analyzed computing different powerful indicators of molecular states in the tissues. The spectral intensity of NADH and FAD were used to monitor metabolic activity, the SHG intensity was used to quantify the fiber organization and density and the average fluorescence lifetime to translate the molecular distribution. The combination of these quantitative answers was tried as a scoring system of tissue nature.

**Methods** A protocol for samples to arrive fresh few hours after excision at the IMNC laboratory was designed in collaboration with the Sainte-Anne Hospital. The cohort for this study contained 25 patients, 7 control biopsies issued from cortex, 10 metastasis and 8 glioblastoma. A dedicated transporter was chosen (360°) to bring the samples from Paris to Orsay (Essonne,

France). Once in the lab, a multiphoton bench-top microscope was used with a Ti-sapphire pulse laser, as an excitation source, to perform a multi-modal analysis on the biopsy samples. TPEF and SHG images were acquired, spectral emission-excitation matrix were analyzed over the 690 to 1040 nm excitation range and fluorescence lifetime images were acquired under 890 nm excitation wavelength.

**Results and discussion** The two-photon imaging results on brain tissue highlighted neuronal cells as a hypo-intense structure in TPEF images, vessel walls as an intense signal in the SHG channel, and disorganized stroma and dense blood vessels of metastasis as an SHG signal. Cellular disorganization with vascular proliferation of GBM was observed with combined intense signal in TPEF and SHG images. Based on all these observations, a neuropathologist was asked to perform a diagnosis on TPEF-SHG images while blind to the H&E diagnosis. Pathologists answered two questions on the TPEF-SHG images : Were tissues tumoral or healthy ? If tumoral, was it a primary or secondary tumor ? For the healthy vs. tumoral discrimination, they could achieve a sensitivity of 76%, a specificity of 50% and an accuracy of 72%. The lack of sensitivity was due to 27% of false negative, that were tissues in which the pathologist couldn't decide on any diagnosis. And the lack of specificity is due to 28% of false positive that were healthy tissues diagnosed as glioblastoma tumor. The rate of false negative could be reduced with a longer training of neuropathologist on recognizing important structures in TPEF-SHG images. In the literature the study with the best results, an accuracy higher than 95% [282], had trained the neuropathologist on 60 samples before performing the blind analysis. Training in this study used only 25 samples. The discrimination between primary or secondary tumor types resulted in sensitivity of 89%, a specificity of 71% and a accuracy of 81%. An already very promising results on a small cohort.

Another direction improving the performance of the direct diagnosis on TPEF-SHG images and avoiding the issue of training neuropathologists, is to use algorithms to create virtual H&E images from the fluorescence images [286, 287]. Two studies can be referred: Rivenon et al. used wide-field microscopy images and transformed them into virtual H&E, and Jones or Masson's trichome stains with a deep-learning algorithm [286]; Bocklitz et al. them, transformed CARS/TPEF/SHG multimodal images into pseudo-H&E images using multivariate statistics [287]. In the first study [286], once a tissue type is trained in the algorithm, for any new images the computing time is on the order of 0.6 s. Comparison of results with traditional H&E stains resulted in a difference lower than 5%. They used the pseudo-H&E to show to the medical community that optical images can recoup the same amount of detail as in the standard stains in histology. With these results it was shown that without any staining, two-photon imaging can quickly produce images providing the same details as H&E standards for a precise diagnosis. A direction that could be investigated in the future to improve the accuracy of the diagnosis based on TPEF-SHG images found in this chapter.

However to have a robust and reproducible diagnosis, there is a need for quantification and automation of the process. The two-photon set-up used in this chapter gave access to two quantitative techniques : spectral measurements and fluorescence lifetime imaging. The first quantitative measurement was to evaluate cerebral energetic metabolism, using the ratio of the spectral intensity of NADH and FAD, an indicator already studied by our team on rat brain tissue [128]. In this study, a higher ratio was observed in tumoral tissue compared to control samples. A second indicator extracted from the spectral response, was the SHG intensity, to indicate tissue organization. The highest was detected in metastasis, and GBM tended to be slightly higher than control, however this difference was not significant in all GBM. These two quantitative measurements did not give significant discrimination in all tissue types and could not be used alone as a diagnosis tool.

Another modality, fluorescence lifetime, was explored in this study to try to find a reliable quantitative optical response. In this article average lifetime obtained from bi-exponential fit was monitored in all tissue types. Longer values were found in tumoral tissue compared to control ( $p < 0.001$ ). Moreover GBM and metastasis had distinguishable values ( $p < 0.001$ ). This modality which depends only on conformational change, environmental factors (pH, temperature, viscosity) and ionization was more robust in the exploration of brain tissue. In the literature few groups have looked at brain tumor spectral and fluorescence lifetime measurements. Butte et al. performed a study on meningioma healthy dura matter and cortex using these two contrasts [252]. Using the spectral intensity they discriminated tissue with a sensitivity of 61% and a specificity of 73% [252]. Looking at the fluorescence lifetime they discriminate tumor tissue with a sensitivity of 84% and a specificity of 100% [252]. They also found that fluorescence lifetime is more suited to brain tumor tissue than spectroscopy alone. They developed an algorithm combining the spectral response and the fluorescence lifetime and found a discrimination for tumor tissue of 90% sensitivity and 100% specificity.

The conclusion of these results is that taking advantage of multimodal detection results in a reliable discrimination algorithm. To best exploit the data on this study a similar strategy was applied, adding SHG emission as a third modality in addition to spectral response and fluorescence lifetime. Three quantitative indicators were extracted : metabolic (redox ratio), structural (SHG intensity) and conformational (lifetime measurements), to build a 3D scoring system. In this 3D-plot each tissue type occupied a specific region of the space, which highlighted the possibility of automated discrimination using analysis of endogenous fluorescence.

In this chapter the possibility of discriminating primary and secondary tumor was demonstrated. However it was also learned how sensitive statistical analysis could be and how there was a large variability from one type of tissue to another. These observations lead to the realization of needing to go further in data analysis and to find other molecules that could help to confirm the diagnosis. To achieve more data for analysis why not look at a larger range of excitation, from the deep-UV to the NIR ? And try new analysis methods such as spectral clustering on the phasor approach ?

## 5.2 Paper : Real-time Brain Tumor imaging with endogenous fluorophores: a diagnosis proof-of-concept study on fresh human samples

www.nature.com/scientificreports

# SCIENTIFIC REPORTS

OPEN

## Real-time Brain Tumor imaging with endogenous fluorophores: a diagnosis proof-of-concept study on fresh human samples

Received: 8 May 2018  
Accepted: 20 September 2018  
Published online: 05 October 2018

Fanny Poulon<sup>1</sup>, Johan Pallud<sup>2,4,5</sup>, Pascale Varlet<sup>3,4,5</sup>, Marc Zanella<sup>1,2,5</sup>, Fabrice Chretien<sup>3,5</sup>, Edouard Dezamis<sup>2,5</sup>, Georges Abi-Lahoud<sup>2,5</sup>, François Nataf<sup>2,5</sup>, Baris Turak<sup>2,5</sup>, Bertrand Devaux<sup>2,5</sup> & Darine Abi Haidar<sup>1,6</sup> 

The primary line of therapy for high-grade brain tumor is surgical resection, however, identifying tumor margins *in vivo* remains a major challenge. Despite the progress in computer-assisted imaging techniques, biopsy analysis remains the standard diagnostic tool when it comes to delineating tumor margins. Our group aims to answer this challenge by exploiting optical imaging of endogenous fluorescence in order to provide a reliable and reproducible diagnosis close to neuropathology. In this study, we first establish the ability of two-photon microscopy (TPM) to discriminate normal brain tissue from glioblastomas and brain metastasis using the endogenous fluorescence response of fresh human brain sample. Two-photon fluorescence images were compared to gold standard neuropathology. "Blind" diagnosis realized by a neuropathologist on a group of TPM images show a good sensitivity, 100%, and specificity, 50% to discriminate non tumoral brain tissue versus glioblastoma or brain metastasis. Quantitative analysis on spectral and fluorescence lifetime measurements resulted in building a scoring system to discriminate brain tissue samples.

Surgical resection aims to maximize tumor removal while minimizing morbidity for both primary and metastatic brain tumors<sup>1,2</sup>. Such an approach requires the identification of the surgical margins that can be defined by the limits of normal tissue and/or the extent of tumor infiltration. For normal tissue, particularly eloquent areas, that represent the corticocortical functional pathways, need to be preserved. Even if eloquent cortico-subcortical pathways can be identified intraoperatively using brain mapping with direct electrical stimulations under awake conditions<sup>3,4</sup>, the identification of tumor boundaries remains challenging. Nowadays, tumor margins are identified based on the neurosurgeon's experience and with the aid of operating microscopes, MRI-based and/or ultrasonography-based neuronavigation, and intraoperative MRI<sup>5</sup>. Unfortunately, none of these techniques have sufficient spatial resolution to identify tumor infiltration at the cellular level and to discriminate infiltrating tumor from surgically-induced brain tissue alterations (i.e. contusion, ischemia or edema)<sup>6,7</sup>. The assessment of tumor borders at the cellular scale can be performed using pathological intraoperative examination, however this technique is not adapted for use during surgery due to time and sampling technique constraints.

The inspection of endogenous brain fluorophores, such as reduced Nicotinamide Adenine Dinucleotide (NADH), Flavin Adenine Dinucleotide (FAD), lipopigments, and porphyrins I and II, all of which considered as biomarkers of cell energy metabolism<sup>8,9</sup>, is a promising key to perform optical imaging at the cellular scale. Interestingly, by examining tissue autofluorescence, one is avoiding prejudice that results from the use of external markers, such as 5-Aminolevulinic Acid (5-ALA) that enhances protoporphyrin IX (PpIX) fluorescence. In addition, although such markers induce fluorescence, they do so through molecular links or processes that are not natural and could therefore result in artifact in the fluorescence response. Evaluating intrinsic optical signals using two photon microscopy (TPM) gives access to two imaging contrasts; fluorescence and second

<sup>1</sup>IMNC Laboratory, UMR 8165-CNRS/IN2P3, Paris-Saclay university, 91405, Orsay, France. <sup>2</sup>Neurosurgery Department, Sainte-Anne Hospital, Paris, France. <sup>3</sup>Neuropathology Department, Sainte-Anne Hospital, Paris, France. <sup>4</sup>IMA BRAIN, INSERMU894, Centre de Psychiatrie et de Neurosciences, Paris, France. <sup>5</sup>Paris Descartes University, Paris, France. <sup>6</sup>Paris Diderot University, Sorbonne Paris Cité, F-75013, Paris, France. Correspondence and requests for materials should be addressed to D.A.H. (email: [abihaider@imnc.in2p3.fr](mailto:abihaider@imnc.in2p3.fr))

### 5.2.1 Introduction

Surgical resection aims to maximize tumor removal while minimizing morbidity for both primary and metastatic brain tumors [288, 289]. Such an approach requires the identification of the surgical margins that can be defined by the limits of normal tissue and/or the extent of tumor infiltration. For normal tissue, particularly eloquent areas, that represent the corticosubcortical functional pathways, need to be preserved. Even if eloquent cortico-subcortical pathways can be identified intraoperatively using brain mapping with direct electrical stimulations under awake condition [290, 291], the identification of tumor boundaries remains challenging. Nowadays, tumor margins are identified based on the neurosurgeon's experience and with the aid of operating microscopes, MRI-based and/or ultrasonography-based neuronavigation, and intraoperative MRI [74]. Unfortunately, none of these techniques have sufficient spatial resolution to identify tumor infiltration at the cellular level and to discriminate infiltrating tumor from surgically-induced brain tissue alterations (i.e. contusion, ischemia or edema) [82, 237]. The assessment of tumor borders at the cellular scale can be performed using pathological intraoperative examination, however this technique is not adapted for use during surgery due to time and sampling technique constraints. The inspection of endogenous brain fluorophores, such as reduced Nicotinamide Adenine Dinucleotide (NADH), Flavin Adenine Dinucleotide (FAD), lipopigments, and porphyrins I and II, all of which considered as biomarkers of cell energy metabolism [102, 218], is a promising key to perform optical imaging at the cellular scale. Interestingly, by examining tissue autofluorescence, one is avoiding prejudice that results from the use of external markers, such as 5-Aminolevulinic Acid (5-ALA) that enhances protoporphyrin IX (PpIX) fluorescence. In addition, although such markers induce fluorescence, they do so through molecular links or processes that are not natural and could therefore result in artifact in the fluorescence response. Evaluating intrinsic optical signals using two photon microscopy (TPM) gives access to two imaging contrasts; fluorescence and second harmonic generation, which both act as complementary modalities giving high resolved spatial information. This has motivated its use in real-time optical biopsy in different cancer types, such as breast tumor masses [281], liver cancer[282] or even pancreatic cancer[284]. Moreover, the ability to combine this technique to quantitative measurements such as spectroscopy and fluorescence lifetime, results in reliable and reproducible discrimination in clinical settings based on an endogenous contrast. Compared to other endomicroscopy techniques, such as confocal laser endoscope . TPM provides multiple advantages [177] such as 1) intrinsic sectioning up to 1 mm; 2) no out-of-focus photobleaching and photodamage; 3) localized phototoxicity and photobleaching; 4) deeper penetration into biological tissue compared with confocal microscopy (up to 1mm) [292], and 5) no spectral overlapping between excitation and emission signals. To top it up, four different optical contrast mechanisms which are: 1) spectral analysis; 2) two photon Fluorescence Lifetime Imaging Microscopy (FLIM); 3) Second Harmonic Generation (SHG) imaging [293], and 4) Two Photon Excitation Fluorescence (TPEF), can be extracted with the use of TPM to provide complementary information for improved tissue characterization. The aim of the present study was to evaluate the ability of TPM in differentiating tumorous brain tissue from normal tissue in order to support the development of an intraoperative two-photon endomicroscope, that will be able to give a real-time answer to the surgeon. We investigated TPM autofluorescence signal analysis from the visible to the infrared domains, exploring all known endogenous molecules coming from freshly extracted brain tissue, including normal (control) tissue, glioblastoma (GBM), and brain metastasis collected from adult patients. In this study, we evaluated: 1) the capacity of TPM in distinguishing between tumorous and normal tissue; 2) the correlation between the optical signatures extracted from TPM and the histopathological diagnosis derived from the gold standard, whereby we can evaluate the

Metastasis (n=10)	Origin	Number
	Thyroid carcinoma	1
	Larynx and esophagus carcinoma	1
	Bronchial adenocarcinoma	2
	Mammary adenocarcinoma	1
	colon carcinoma	2
	Heel melanoma	1
	Otorinolaringologia carcinoma	1

Table 5.1 – Origin of the metastasis tissues used in this study

clinical relevance of TPM as a more robust intraoperative diagnosis modality, and 3) the predictive power of TPM imaging features in differentiating malignant gliomas from normal tissue as well as from brain metastasis.

## 5.2.2 Materiel and methods

### 5.2.2.1 Samples

This prospective longitudinal study was conducted at a tertiary referral neurosurgical center for brain tumor patients, between March 2015 and May 2017. The human research institutional review board of the Sainte-Anne Hospital – University Paris Descartes (CPP Ile de France 3, S.C.3227) approved the study protocol. All methods were carried out in accordance with relevant guidelines and regulations. An informed written consent was obtained from all patients prior to enrollment. Twenty-five individuals (25 patients, 13 males, 12 females; mean,  $51.2 \pm 15.2$  year-old; range, 19-69 year-old) were included. Fresh human tumor brain tissue specimens (n=18 from 18 individuals) were obtained from the planned surgical margin surrounding the tumor core (10 metastasis samples, originating from thyroid, larynx, oesophagus, colon and otorinolaringologia carcinoma, bronchial and mammary adenocarcinoma and heel melanoma, summed up in Table 5.1; and 8 glioblastoma samples, GBM). The gross location of each specimen was recorded intraoperatively with MRI-based neuronavigation (BrainLAB, AG, Feldkirchen, Germany). Control brain tissue specimens (7 patients with no history of brain cancer) were obtained during surgical removal of drug-resistant mesial temporal lobe epilepsy.

Fresh samples in excess to what was needed for routine histopathological diagnosis were obtained directly from the operating room. Half of each fresh sample under study was sent to histopathology (solution of serum Physio, ambient temperature, black box), where it was formalin-fixed (4% paraformaldehyde), paraffin-embedded, stained with H&E for histopathological analysis, and digitized using Digital Slide Scanner NanoZoomer 2.0 (Hamamatsu Photonics K.K, Hamamatsu, Japan). The other half was carried to the PIMPA platform under similar conditions (solution of serum Physio, ambient temperature, black box) and imaged with TPEF, SHG, FLIM and spectral imaging without tissue fixation. No specimen was excluded from TPM or histopathological analysis. Samples were  $1.25 \pm 0.45$  cm (range, 0.5-2.0) in size and  $3.36 \pm 1.05$  mm (range, 2-5) thick. TPEF, SHG, FLIM and spectral imaging were recorded sequentially without tissue processing within a mean time interval of  $1 \pm 0.2$  s (range, 0.8-1.2s).

### 5.2.2.2 Correlation between TPM and histopathology

We initially collected 25 paired TPM and H&E images from 25 samples (10 metastasis, 8 glioblastomas, 7 controls). A senior neuropathologist performed an initial histopathological analysis, while blind to the TPM results. No specimen was excluded due to lack of histopathological representativity. To control for intra-observer bias, we presented a Web-based survey of TPM images (png file of the superimposed image of TPM and SHG response) to two senior neuropathologists six months after the initial H&E based diagnosis pertaining to 25 randomly selected patients (control, n=7, GBM, n=8, metastasis, n=10). They were asked to classify the sampled tissue in four categories: 1) GBM; 2) metastasis; 3) healthy tissue; or 4) unclassified. The neuropathologist had access to clinical data typically available along with the TPM images. This includes patients' age, gender, clinical presentation, tumor location, and the pre-operative MR images. The neuropathological blind analysis of TPM images and its corresponding ability to discriminate between control, GBM, and metastasis tissues was evaluated using the classification properties defined as the sensitivity, specificity and the accuracy of a diagnostic test, respectively following Eq. 5.1 , Eq. 5.2 and Eq. 5.3.

$$S_e = \frac{TP}{TP + FN} \quad (5.1)$$

$$S_p = \frac{TN}{TN + FP} \quad (5.2)$$

$$Acc = \frac{TN + TP}{TN + FN + TP + FP} \quad (5.3)$$

TP = True Positive, FP= False Positive, TN= True Negative and FN= False Negative. Their signification depended on:

- Discriminating tumor tissues (GBM, metastasis) from control tissues: TP=tumoral tissue classified as tumoral, FP=control tissue classified as tumoral, TN=control tissue classified as healthy and FN=tumoral tissue classified as healthy.
- Discriminating GBM tissues from metastasis tissues: TP=metastasis classified as metastasis, FP=GBM tissue classified as metastasis, TN=GBM tissue classified as GBM and FN=metastasis classified as GBM.

### 5.2.2.3 Fluorescence and SHG image acquisition

This study was conducted on the multimodal two-photon microscope at the PIMPA (multiphotonic imaging platform for small animals) platform of the IMNC laboratory, Orsay, France. A Mai Tai DeepSee Ti:Sapphire laser source with automated dispersion compensation was used for two-photon excitation. The source's average power was 2.4 W at 800 nm excitation and was tunable from 690 nm to 1040 nm. The repetition rate of the laser source was 80 MHz and the output pulse duration was set to 70 fs. The laser was combined to a confocal and multiphoton microscope, the TCS SP8 MP (Leica Microsystems, Germany) and was controlled through the Leica software, Symphotime x64. Different visible excitation diodes were also included in the setup, including the 405 nm excitation wavelength. Two super sensitive non-descanned hybrid detectors (Leica, Germany) were used to collect the two-photon fluorescence signal. The collected signal passed through a transparent dichroic filter ( 680 nm.) to laser reflection, then through a second dichroic filter (FF495-Di03-25x36) to direct the light towards the two hybrid detectors. An additional filter

(Semrock, FF01-448/20-25, FF01-520/35-25) was placed in front of the detector to define specific spectral bands. Two different water-immersion Leica objectives were used (HCX IRAPO L 20X NA 0.95 and HC PL APO 40X NA 1.1 CORR CS2). Images were 512 by 512 pixels in size. The speed scan was 400 Hz and the pixel size was 866.65 nm by 866.65 nm (no zoom factor). The pixel dwell time was 1.20  $\mu$ m and the frame rate was 0.52 frames per second. Large regions of interests were selected with Leica's acquisition software for image and spectral

#### 5.2.2.4 Spectral imaging and analysis

The spectrally-resolved fluorescence intensities were detected by a hybrid detector (HyD, Leica, Germany) placed in the confocal head of the microscope piloting the grating and mirror in front of the detector. The spectral resolution was 10 nm, covering the range from 380 nm to 780 nm. A spectral mosaic was acquired on a 3x3 image area i.e. a spectral measurement was made for each image of the mosaic then the software merged the information to give its mean fluorescence spectrum. The spectral excitation-emission matrix was acquired by varying the excitation wavelength and detecting the fluorescence across the whole emission band. The power at the output of the microscope objective was measured using a power meter (Nova II, Ophir, USA) so that the fluorescence spectra were adjusted according to the corresponding excitation power. The acquired spectra were treated with Matlab scripts developed at the IMNC laboratory [128], where the fluorescence and SHG signal of five endogenous molecules were spectrally decomposed (NADH, FAD, lipopigments, porphyrins I and II). Five ROIs, each corresponding to 200  $\mu$ m in diameter were chosen for spectral analysis. The SHG, NADH and FAD peak intensities were extracted at 890nm excitation wavelength to calculate two quantitative markers, the SHG peak intensity and the redox ratio (ROx) [217]. The ROx is defined in Eq. 5.4 as:

$$ROx = \frac{NADH}{FAD} \quad (5.4)$$

#### 5.2.2.5 FLIM acquisition

The microscope integrated a FLIM module from PicoQuant (GmbH, Berlin, Germany), in order to acquire fluorescence lifetime imaging. Each ROI (512x512 pixels) was also imaged in FLIM mode at a repetition rate of 100 Hz, where the final image was the result of averaging twenty single frames. For each pixel, the fluorescence decay profiles were fit to a mono- or bi-exponential function using the Symphotime software (Symphotime x64 bit, PicoQuant, GmbH, Berlin, Germany) to recover the lifetime values. Ten to fifteen ROIs were selected from different structures observed in the FLIM image. The goodness of fit was assessed by calculating  $\chi^2$ -value as defined in Eq. 5.5:

$$\chi^2 = \sum_i \frac{(x_i - \mu_i)^2}{\sigma_i^2} \quad (5.5)$$

$\mu_i$ : mean,  $\sigma^2$ : variance

The criterion for an acceptable fit was having  $\chi^2$ -values of around 1.0 ( $\chi^2$  range 0.8 to 1.6). Additionally, the residuals had to be randomly distributed around zero within the intervals 4 and -4. The average lifetime ( $\tau_{avg}$ ) for each ROI was measured using Eq. 5.6.



$$\tau_{avg} = \frac{\sum_i a_i \tau_i}{\sum_i a_i} \quad (5.6)$$

### 5.2.2.6 Scoring system

Three quantitative indicators were used: (1) Redox ratio: NADH/FAD, (2) fitted SHG intensity and, (3) the average lifetime, all under an 890nm excitation wavelength. The three measurements were performed on the same region of interest that could be projected in a 3D space with these values as coordinates. The scatter cloud of a group was fitted by a Gaussian ellipsoid using the mean and the standard deviation as parameters for the covariance so that the ellipse can cover 95% of the total probability mass. The percentage of overlap between the ellipses for each group was then calculated to assess of the performance of such algorithm.

### 5.2.2.7 Statistical analysis

Statistical analyses of the SHG and fluorescence intensities, along with the spectral widths were performed in Matlab (R 2013a), using an ANOVA test for the three tissue groups. This was followed by applying the Bonferroni method to determine which mean values are significantly different within a 95% confidence interval. The statistical values found in Figure 7 (B, C, D) were computed using the software R (x64 3.2.0), where the computed p-values  $< 0.05$  were considered to be statistically significant.

## 5.2.3 Results

The routines of the TPM procedure match the requirements for clinical use of freshly resected brain tissue. Specimens from twenty-five patients, comprising 10 metastasis, 8 GBM, and 7 epileptic patients with no history of brain tumors, were included in the cohort. Fresh samples were either sent to histopathology and/or to the multimodal imaging platform (PIMPA), providing similar imaging conditions for TPEF, SHG, FLIM and spectral imaging. In the histopathology circuit, the samples followed a first protocol of fixation, paraffin embodiment and hematoxylin and eosin (H&E) coloration that lasts several hours, then the stained samples were imaged and analyzed by neuropathologists. In the multimodal imaging platform circuit, the samples were directly placed (without any preparation or chemical modification) under the multiphoton microscope, from which a multimodal imaging protocol (TPEF/SHG, spectral, FLIM) was performed within several seconds, after which the results were analyzed. Being a crucial point to take into account, the time required to obtain imaging data from brain samples was compared in each of the above circuits. The standard histological H&E staining method, that results in the most precise diagnostic and that yields the nature and the grading of the tumor, required  $450 \pm 30$  min. Surgeons can also use a faster method during surgery, with the help of a neuropathologist, based on frozen sections that can be evaluated in 20 min in parallel to the operation and yield some information on the lesioned nature of tissue. However, both these techniques were more time consuming than the required time of  $0.01 \pm 0.005$  min for the optical analysis method by TPM, which included data from TPEF, SHG, FLIM and spectral imaging ( $p < 0.001$ ), with a real-time discriminating algorithm. Additionally, TPM has a

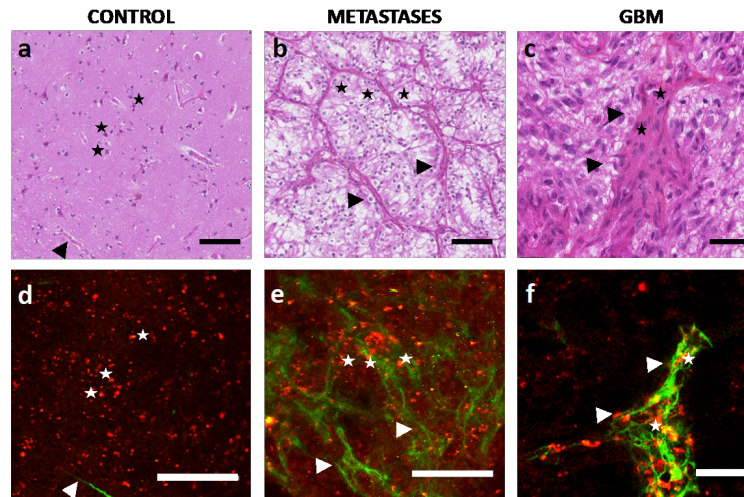


Figure 5.1 – Comparative H&E (a,b,c) and TPM images (d,e,f) . (a,d) Control sample, stars: neurons, arrow: brain vessels in the SHG, scale bar 100 microns, (b,e) Brain carcinoma metastasis: scale bar 100 microns, stars: tumor cells, arrow : dense vascularization forming a dense network around the tumor cells, (c,f) GBM sample scale bar 40microns: stars : proliferative endothelial cells, arrow : zoom on a proliferating vessel.

major advantage over both histological techniques, the analysis is performed *in vivo* on unlabeled tissue.

*TPM images match standard histopathology with H&E staining* The work then comprised a thorough comparison between the TPM based images and the H&E-stained images. The PIMPA platform provides simultaneously two different images obtained by the two external hybrid detectors: a TPEF image at the maximum fluorescence peak (filter  $520 \pm 20 \text{ nm}$ ) to capture tissue characteristics; and a SHG image (filter  $448 \pm 20 \text{ nm}$ ) to detect non centrosymmetric structures such as collagen fibers and vessels walls. The TPEF and SHG images were merged using ImageJ to obtain a superimposed image showing the complete morphological structures of the tissue. For each sample, a senior neuropathologist was asked to identify normal or tumorous cellular components (neuron oligodendrocyte, astrocyte; endothelial cell, carcinoma cell) and/or a particular morphological aspect (necrosis, neo-angiogenesis and microvascular proliferation, calcification) on H&E-stained images that served as a reference, and was then asked to localize these patterns in the merged TPEF and SHG images. In all samples ( $n=25$ ), the senior neuropathologist was able to identify in TPEF and SHG images the features that were first identified on H&E-stained images. Examples are shown in Figure 5.1.

In control non tumoral brain samples, cellular nuclei appeared as hypointense structures in a homogeneous matrix-dominated background. Neuronal cells were easily discernable in both H&E stained images as well as merged TPEF-SHG images (black and white stars in figure 5.1 A-B). In brain metastasis, typical cytoarchitecture hallmarks such as hypercellularity and disorganized stroma with numerous blood vessels generated a particular SHG signal (black and white arrows in figure 5.1 C-D). In GBM samples, a highly cellular disorganized tumoral cell architecture was observed with microvascular proliferation. In general, the SHG signal highlights collagen structure

<b>a</b>			
$N_{\text{images}}=25$			
		Real tissue nature	
		Tumor (n=18)	Healthy (n=7)
TPM test	Tumor	TP=16	FP=2
	Healthy	FN=2	TN=5
$Se = 88\%, Sp = 71\%, Acc = 72\%$			

<b>b</b>			
$N_{\text{images}}=18$			
		Real tissue nature	
		GBM (n=8)	Metastasis (n=10)
TPM test	GBM	TP=5	FP=2
	Metastasis	FN=3	TN=8
$Se = 62\%, Sp = 80\%, Acc = 72\%$			

Figure 5.2 – "Blind" histological analysis on TPM images. (a) Flowchart summarizing the results of the pathologists' diagnosis based on TPM images, sensitivity (Se, Sew), specificity (Sp) and accuracy (Acc, Accw) of this method were calculated with the unknown classification (Non-diagnosed, n=5) either excluded (Se, Acc) or taken into account as False Negative (Sew, Accw). (b) Results of the pathologists' diagnosis of tumoral tissue, discriminating GBM from Brain metastasis. The sensitivity (Se), specificity (Sp) and accuracy (Acc) were also calculated.

and metastasis samples had the densest collagen network. The control and GBM samples revealed sparse SHG signals representative of vessel walls.

#### 5.2.3.1 "Blind" analysis of TPM images

We next assessed the clinical application of TPM imaging and its capacity to show specific patterns of the different brain tumors needed in clinical practice to discriminate them. Twenty-five TPM images (control, n=7, GBM, n=8, metastasis, n=10) were given to neuropathologists blind to the nature of tissue. They were asked to classify the tissue in four categories: 1) GBM; 2) Brain metastasis; 3) Normal brain parenchyma or 4) impossible diagnosis. The neuropathologists were asked to use TPM derived markers, as determined in the previous section (cell, cell density, collagen fiber density and organization, angiogenesis, microvascular proliferation, and necrosis) to propose a diagnosis. The results are summarized in 5.2. Discriminating tumorous tissue from control tissue using TPM resulted in a sensitivity of 88% and a specificity of 71%. The accuracy of this procedure, which means the probability to correctly classify tissues, was 72%. Interestingly, from the results of the neuropathologists, the ability to discriminate GBM tissues from metastasis tissues using TPM could also be evaluated. This resulted in a sensitivity of 62% and a specificity of 80%. The accuracy of this procedure, was found to be 72%.

#### 5.2.3.2 Quantitative analyses of TPM signals

To determine reliable discriminating criteria, quantitative analyses of spectral and FLIM images were performed on each sample (n=25; n=10 metastasis, n=8 GBM and n=7 control). Different wavelengths (from 730 nm to 960 nm) were applied to the three subgroups to define the optimal excitation wavelength for collecting spectral and FLIM images as well as the SHG signals. The variation of endogenous fluorescence was measured in order to build an excitation-emission matrix for control, GBM, and metastasis samples. The results are presented in Figure 5.3.

The fluorescence intensity decreased by 70% as the excitation wavelength changed from 730 to 900 nm. However, secondary maximal fluorescence intensity was present at 890 nm (60% of the maximum intensity) in a region where SHG signal peaks. Control samples and GBM samples had a comparable decrease of 15% in the fluorescence intensity when the excitation wavelength varied from 730nm to 760nm. Interestingly, metastasis samples had a faster rate of decrease (30%) in the

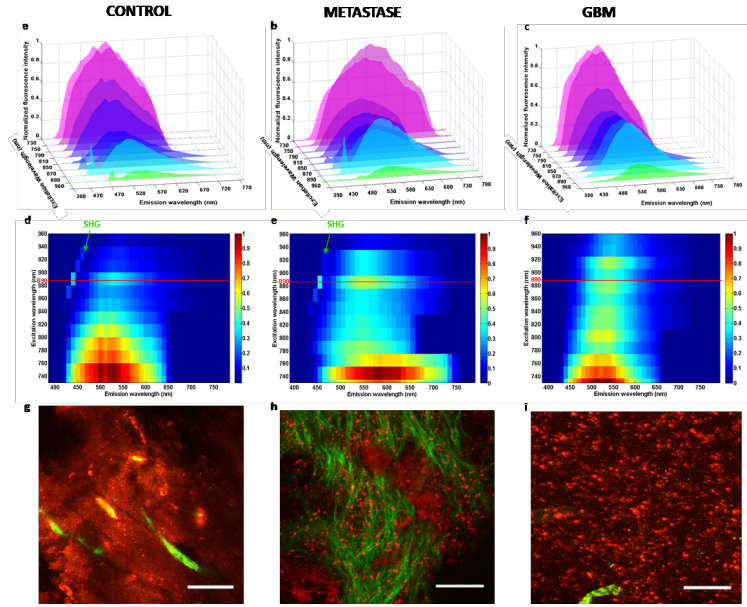


Figure 5.3 – Analysis of emitted fluorescence for the different groups. (a,b,c) Topological representation of the emitted fluorescence spectra at different excitation wavelength for the control group (a,d,g), the metastasis group (b,e,h) and the GBM group (c,f,i). (d,e,f) represent colormaps of the Emission-Excitation matrix for each type of tissue. The ideal excitation wavelength is highlighted by a red line and the part of the map corresponding to the SHG signal is identified by a green arrow. TPEF images (g,h,i) of the selected region is also shown with a scale bar of 100 microns.

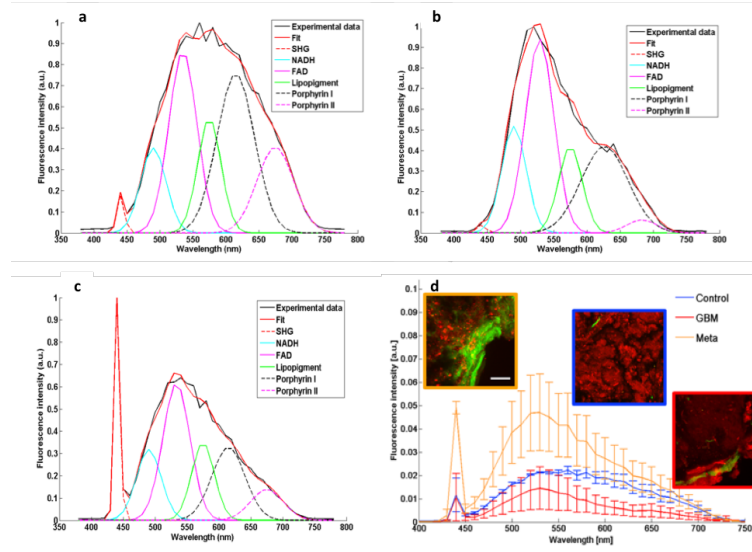


Figure 5.4 – Spectral decomposition and comparison of emitted spectra at 890nm for each group. (a,b,c) Example of fitted spectra for control (a), metastasis (b), and GBM (c), under 890 nm excitation. (d) Mean spectra and standard deviations determined from 25 fresh human samples (10 metastasis samples, 8 GBM samples and 7 cortex samples) along with representative images of TPEF (red) and SHG (green) corresponding to each tissue group.

fluorescence intensity. In all three subgroups, the overall emitted fluorescence intensities remained similar upon excitations ranging from 850 nm to 900 nm. The emission spectra then decreases when fluorophores are excited at longer wavelengths. This optimal 850-900 nm spectral range for excitation coincides with the emission spectral range optimized for SHG detection. Consequently, further TPM based imaging were conducted under an 890 nm excitation. It is clear that the emission spectra are red-shifted when the longest excitation wavelengths are used. Additionally, fluorescence emitted around 470 nm, which is mainly attributed to NADH autofluorescence is greatly suppressed. This is explained by NADH's suboptimal absorption cross section at wavelengths longer than 800 nm. FAD on the other hand showed a second maximal absorption cross section around 900nm [294].

In all cases, the spectral shape differed between subgroups indicating the differences in the relative amounts of individual fluorophores present in the three tissue groups. An example of the fitted spectra at 890 nm of each subgroup is shown in 5.4.

Figures 5.4a,b,c show a spectrally decomposed fitted spectra ( $n=1$ ) for a sample from each tissue group. The fluorescence coming from five endogenous fluorophores was recovered, namely, NADH, FAD, lipopigments, porphyrins I and II. The SHG peaks were also extracted. The control samples (Fig. 5.4.a) presented a broader fluorescence spectrum compared to both metastatic and GBM samples. Spectra from GBM and metastasis samples (Fig. 5.4.b and c) were particularly dominated by FAD fluorescence followed by Porphyrin I. The metastatic samples showed a uniquely high SHG peak corresponding to the presence of dense vessels network, as shown in the TPEF/SHG image, which was always significantly higher than that from healthy and GBM tissue ( $p < 0.001$ : SHG signal:  $M_{metastasis}=0.057$ ,  $M_{GBM}=0.0069$  and  $M_{Control}=0.0054$ ). ). GBM and healthy tissues

exhibited similar SHG peaks suggesting that both types have comparable microvascular density. GBM did show larger blood vessels, facilitating angiogenesis on the corresponding TPEF/SHG images. Moreover, the full width at half maximum,  $L$ , computed from the total fluorescence spectra of control samples were found to be significantly different from the ones extracted in Metastatic and GBM tissue ( $L_{metastasis}=128\text{nm}$ ,  $L_{GBM}=134\text{nm}$ ,  $L_{Control}=185\text{nm}$ ). A summary of the spectral analysis at the reference excitation wavelength of 890 nm is presented in Figure 5.4.d. GBM samples exhibited an overall lower fluorescence intensity than control samples supposedly due to the necrotic areas in these samples. This was confirmed by the TPEF images showing a global darker background. In the emission range of 600 to 650nm, the mean emitted fluorescence was significantly lower ( $p<0.001$ ) in the GBM samples as compared to control and metastasis samples ( $M_{GBM}=0.0055$ ,  $M_{metastasis}=0.0221$  and  $M_{Control}=0.0160$ ). Metastasis samples exhibited an overall higher fluorescence intensity than control samples due to the higher tumor cell density as previously confirmed by the TPEF images showing a high density of bright red spot, identified as tumor cells. In the emission range of 500 to 550 nm, the mean emitted fluorescence was significantly higher ( $p<0.001$ ) in the metastasis samples as compared to control and GBM samples ( $M_{metastasis}=0.0435$ ,  $M_{GBM}=0.0035$  and  $M_{Control}=0.0045$ ). One limitation to spectral response studies prevails in identifying tissue samples, the intensity is dependent on the fluorophore concentration, which can be very low in peripheral tumor volumes and in tumor margins. To overcome such an obstacle, we studied fluorescence lifetime, which is a quantitative optical measurement that depends on environmental conditions such as pH, temperature, viscosity, and structural changes including molecular conformation and binding partners, but not on fluorophore concentration. We quantified the fluorescence lifetime on all samples ( $n=25$ ;  $n=10$  metastasis,  $n=8$  GBM and  $n=7$  Control) through the FLIM technique. Figure 5.5 shows representative results for each tissue group.

The control samples had the broadest FLIM distribution ( $\text{FWHM}_{Control}=0.856$  ns compared to  $\text{FWHM}_{metastasis}=0.764$  ns and  $\text{FWHM}_{GBM}=0.557$  ns) due to a heterogenous range of components with short and long lifetime values that were present in similar quantity. GBM samples had a narrow FLIM distribution; the blue-green structures represented neo-angiogenesis. The metastasis samples had the shortest average lifetime at maximum (metastasis=0,7344 ns compared to GBM=1,47 ns and Control=1,78 ns) compared to the Control and GBM samples as a result of the presence of a dense vascular network. However, the tissue background color in between vessels corresponds to longer fluorescence lifetimes than that of GBM samples ( $\text{FWHM}_{metastasis}=0,764$  ns  $>$   $\text{FWHM}_{GBM}=0,557$  ns).

### 5.2.3.3 TPM signals scoring system

To translate TPM imaging into the operating room, we aimed to develop quantitative parameters derived from the spectral analysis and the fluorescence lifetime imaging to construct a scoring system combining three quantitative tissue dependent variables: the redox ratio, the average lifetime and the SHG intensity. The redox ratio and the SHG intensity were calculated from the spectral fitting results whereas the average lifetime was calculated from the exponential-decay fit of the lifetime measurements. The three derived values were used as coordinates to plot each sample in a 3D space. Figure 5.6 summarizes these results.

Taken separately, each of the quantitative indicators were not always statistically significant while discriminating between the different tissue types. The average lifetime of both GBM samples and metastasis samples were notably shorter than those of Control samples ( $\tau_{GBM}=1.13\text{ns}$  -

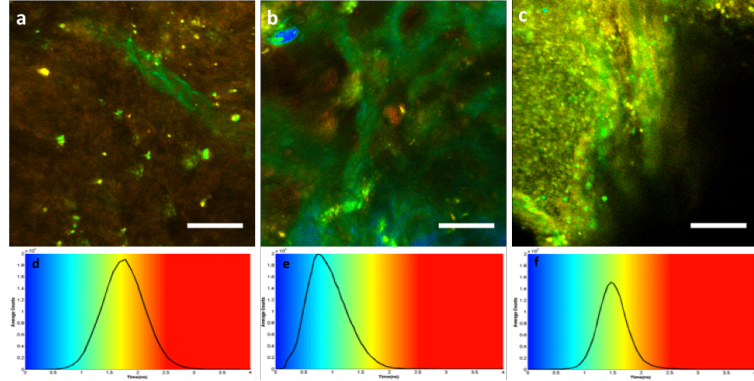


Figure 5.5 – FLIM representation at 890nm for each tissue type. (a,b,c) FLIM images of control sample (a), metastasis sample (b), and GBM (c). Scale bars 100  $\mu\text{m}$ , (d,e,f) give the color scale of FLIM imaging with the histogram of the average lifetime; shorter lifetimes (blue) are on the left side of the color scale, and longer lifetime (red) on the right side, two measurements were taken and the full width at half maximum of distribution and the average lifetime of the maximum. SHG is not a fluorescent but diffusing process, appearing as very short lifetime corresponding to the instrument response function (IRF), which is of the order of 0.06 ns and shown in blue in the FLIM images. The typical vascular structures of each tissue are consequently as recognizable as in the TPEF images.

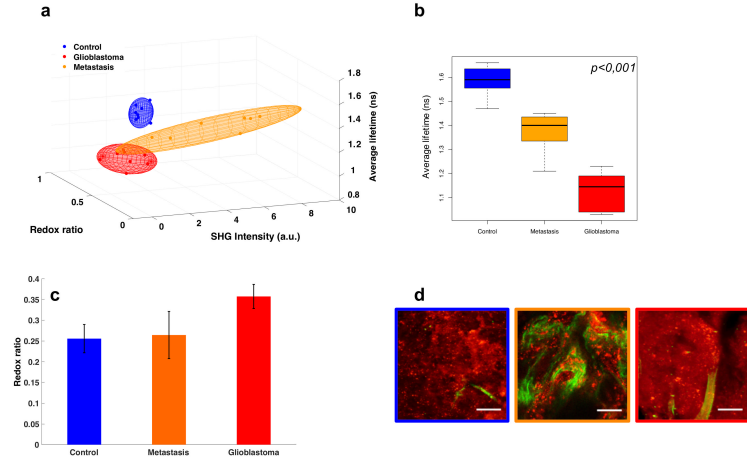


Figure 5.6 – (a) 3D scatter plot of three quantitative tissue indicators: the redox ratio, fluorescence lifetime, and SHG signal averaged for each tissue subgroup, (b) box plot of the average lifetimes, (c) bar graph of the redox ratios for each tissue type with the errors corresponding to the standard deviations across all measurements, and (d) overlaid TPEF and SHG intensity images.

$\tau_{control}=1.59\text{ns}$ ,  $p<0.001$ ;  $\tau_{metastasis}=1.37\text{ns}$  -  $\tau_{control}=1.59\text{ns}$ ,  $p<0.001$ ). In addition, the average lifetime of GBM samples was remarkably shorter than those of metastasis samples ( $\tau_{GBM}=1.13\text{ns}$  -  $\tau_{metastasis}=1.37\text{ns}$ ,  $p<0.001$ ). On average, cancerous tissues had higher redox ratios ( $\text{ROX}_{control}=0.256\pm0.030$ ,  $\text{ROX}_{Meta}=0.264\pm0.030$  and  $\text{ROX}_{GBM}=0.357\pm0.030$ ), compared to normal tissues. Although it did not reach statistical significance, the larger trend was observed between GBM and control cases ( $\text{ROX}_{control}=0.256$ ,  $\text{ROX}_{GBM}=0.357$ ,  $p=0.08$ ). On the other hand, the SHG intensities were particularly helpful in discriminating metastatic samples from the remaining two types ( $\text{SHG}_{metastasis}=3.8$ ,  $\text{Control}=0.35$ ,  $p<0.001$  and  $\text{SHG}_{metastasis}=3.8$  -  $\text{SHG}_{GBM}=0.46$ ). Consequently, in order to have a more vigorous mean of discrimination, these separate indicators were combined in a unique scoring system, Figure 5.6.a. The performances of the multimodal algorithm were generated using a Gaussian ellipsoid fit, where the control tissue never overlapped with any tumorous type in 95% confidence, and GBM-metastasis only had 16,6% of overlap.

### 5.2.4 Discussion

In this prospective study, we compared TPM derived optical contrasts measured from different fresh human brain tumoral and non tumoral samples to gold standard neuropathology. We have demonstrated that: 1) TPM can readily be integrated into the operating room as the acquisition times are short; 2) The merged TPEF and SHG images showed some similar features as those observed by standard neuropathology particularly the vascular and stromal network 3) TPM imaging was capable of discriminating tumorous from normal tissue at a sensitivity and specificity of 88% and of 71% respectively. Interestingly, TPM also allowed the discrimination between GBM and metastasis tissues with a sensitivity of 62% and a specificity of 80%; 4) Quantitative TPM signals also categorized tissues according to their groups (control, GBM, metastasis) ; and lastly, 5) the combined scoring system, i.e. combining redox ratios, average lifetimes, and SHG intensities, allowed tissue samples to be discriminated, with no overlap between control and both GBM and metastasis response.

An important point to firstly stress on is the clinical benefit in acquiring TPEF in real-time compared to standard histological examination ( $t_{TPM}=0.01\text{min} < t_{H\&E}=450\text{min}$ ). A classical H&E image is time and labor consuming given the multiple steps and resting time that are required in order to obtain a stained slice. On the contrary, optical images are recorded in a few seconds without any tissue manipulation of the sample, samples being imaged freshly resected directly under the microscope. This point demonstrates the power of optical imaging in giving quick and highly resolved images as well as its ability to be used intraoperatively.

Second, having established the technical advantages of TPM, it was crucial to evaluate its capacity in discriminating tissues. Therefore, a typical comparison between TPEF-SHG images and histology gold standard H&E staining was performed, and a strong correlation was established between the two imaging modalities for each tissue type. The cortex could be identified by the presence of numerous neurons associated with thin branched vessels highlighted by SHG signal. Glioblastoma are characterized by a high cellularity and large glomerular vessels. Brain metastasis by contrast show the dense collagen vascular stroma, resulting in a very strong SHG signal. The tissue specific signatures found in this comparison were used by a neuropathologist to perform a blind analysis of the TPM images. The statistical results of this diagnostic procedure gave promising results, with high sensitivity (between 75 and 100%) to discriminate tumor from control tissue, opening the doors to real-time optical biopsy. The low specificity (50%) of the technique can be improved by training the neuropathologist with these images as the standard practice for H&E.



A major common limitation between image comparison and H&E staining is the subjective diagnosis. For this reason, a real advantage of TPM is the combination of images with quantitative measurements to build a computed diagnosis that could be used directly *in vivo* by the surgeon. In this study, we explored two quantitative measurements, the spectral emission and the fluorescence lifetime to build a discriminative algorithm. The spectral measurement is sensitive to the nature and the concentration of fluorophores measured, thus giving access to information on the metabolic evolution of tissues, such as indicators of redox status by following NADH and FAD [102, 218, 295]. On the other hand the FLIM measurement is sensitive to binding states, molecular interferences, and other aspects of the molecular environment such as temperature, molecular liaisons, viscosity of the medium, and pH [296–300]. Therefore, TPM-FLIM data can provide important complementary information about the local biochemical medium that may aid in distinguishing healthy from tumorous tissues. Time-resolved fluorescence of endogenous response is a useful complementing tool that separates pathological tissues based on their metabolism [104, 118]. The extra quantitative dimensions of information provided by spectral and lifetime imaging could facilitate diagnostic judgments. Consequently, three of the most significant quantitative indicators found in the exploratory analysis were combined to build a scoring system of brain tissue nature. These indicators were the redox ratio to monitor the metabolic state [118, 217, 222, 295], the SHG intensity to evaluate the density of collagen structures [299, 301] and the average fluorescence lifetime to track environmental and conformational changes [296–300]. Taken separately these numerical indicators gave us mixed results when discriminating tissues. For example, the Redox ratio failed to be robust, although it did discriminate GBM from control most accurately, with the tumors having higher ratios. This result is in accordance with literature [217] and is explained by increased tumoral metabolic needs (Warburg effect) resulting in changes in the NADH/FAD ratios [247]. The SHG intensity on the other hand gave us a statistical difference between control and metastasis, corresponding to the strong net of vessels and collagen matrix that form around the tumors cells as also referred to in the literature [302]. The average lifetime was the most robust classifier, where the values for tumor and control tissues were significantly different with a shorter lifetime found in tumor tissue. Nevertheless, when accounting for all three quantitative markers, as displayed in the 3D scatter plot of Figure 6a, classifying brain tissue was achieved. ., one could easily classify brain tissues. These results underline the necessity of developing an endomicroscope with multimodality capabilities for robust *in vivo* tissue interrogation.

All in all, these results based on tissue autofluorescence signals coming from brain tumors are taking part in the construction of an optical database that will be implemented in a two-photon multimodal endomicroscope. A first prototype of this intraoperative surgical tool is under development in our laboratory and has shown great performances when it comes to collecting signals [198, 221]. Compared to the different diagnostic techniques such as frozen sections or formaldehyde fixed H&E stains performed by neuropathologists today, this method does not require any tissue resection. On the contrary, the probe can be directly put in contact with the human brain while performing a measurement. Another advantage is the turnaround time required to diagnose a tissue, which is estimated to be less than a minute from the moment the surgeon holds the probe until the results are displayed on the screen, as compared to at least thirty minutes for the above listed methods. Additionally, compared to other techniques developed for the same purpose such as MRI [82], PET [41] or exogenous fluorescence guided endoscopy [279], our tool does not require the use of any external agents, thus simplifying the work and limiting any biased classification. As for the techniques based on intrinsic signals such as OCT [139], or intraoperative ultrasound [238], these simply act as imaging tools that demand the interference of an expert to fully interpret the results.

By focusing the work on TPEF, this method gave us the possibility to combine imaging modalities to quantitative measurements to reach unsupervised discrimination in real-time.

In conclusion, this preliminary study highlights the interest of a multimodal two-photon excitation tool to guide intraoperative delineation of tumors' margins. It may be useful to tailor intraoperatively the surgical resection of malignant brain tumors in addition to brain mapping. In time to come, the present study will be extended to a larger cohort that includes different brain tumor subtypes. This study will address the question of whether the quantitative optical markers studied here can be applied to infiltrating brain tissue located at tumor margins. The final challenge will be to translate the endomicroscope into the operating room and to be approved for *in vivo* clinical studies.

## 5.2. PAPER : REAL-TIME BRAIN TUMOR IMAGING WITH ...

## Chapter 6

# Could multimodal and multiscale optical analysis from DUV to NIR, be a reliable tool for diagnosis of primary and secondary tumor ?

### 6.1 Context of the study

In the previous chapters, the analyze of the autofluorescence both spatially and quantitatively, from visible to NIR, has been shown. It resulted in a discrimination between healthy tissue, primary and secondary tumor. These results showed that the accuracy of the diagnosis could be improved with a more in-depth study, exploiting the relationship between the different molecules and analyzing a larger excitation range. A campaign with an excitation from DUV to NIR was consequently designed to increase the quantity of informations collected on tissue and to improve the discrimination. A collaboration with DISCO beamline scientists from synchrotron SOLEIL was initiated to analyze our tissues under DUV excitation. Moreover, in the last chapter it was concluded that multimodality is a key to develop reliable and robust algorithms. Consequently in this chapter, the development of discrimination algorithms, which could be implemented intra-operatively, using the multi-range excitation and the multi-modal detection, were explored more in-depth.

Previous we showed that NADH, FAD, Lipopigments and porphyrins, were the analyzed molecules under one and two-photon excitations. These molecules gave an insight on tissue structure and metabolism, elements impacted during tumor development. However using a DUV excitation will excite other types of molecules present in tissue. For instance amino acids are also fluorescent when excited in the DUV range. In the brain two amino-acids are present and can consequently be excited, the tyrosin and tryptophan which are structural units forming proteins. Monitoring their signal can give information about new protein structure and dynamic [104]. Tryptophan is also linked to NADH in tissue, enzymes carrying tryptophan favor  $\text{NAD}^+$  to NADH conversion during oxydo-reduction, consequently metabolic changes involving NADH will result in variations in tryptophan autofluorescence response too. This observation has been at the origin of FLIM-

FRET detection method based on the Trp-NAD(P)H interactions [303, 304]. Being able to register the information of tryptophan autofluorescence on the brain biopsy tissue will help to understand the results found in the NADH/FAD variation. However with our two-photon set-up presented in the previous chapter, tryptophan couldn't be detected, this is due to the fact that its fluorescence emission is around 355 nm which is outside our detectors spectral range (390 nm to 790 nm).

DUV excitation gave also access to the fluorescence of structural proteins of collagen. In the previous one and two-photon study collagen was only accessible through the SHG signal to highlight its fibrillar structure. However collagen is a major component of the extracellular matrix (ECM), holding organs and cells together. The ECM is an important part of angiogenesis and neoplasia mechanisms. The fibrils of collagen are stabilized by cross-linking that results in autofluorescence signal and that can be a tool to monitor cancerous structural mechanisms [104]. In literature monitoring of collagen with DUV excitation was demonstrated for two other types of tumor. Georgakoudi et al. looked at endogenous fluorescence emission in cervical lesions and Barrett's esophagus. Excitations between 340 and 420nm were used to build emission-excitation matrix and extract collagen and NADH signal. A lower collagen signal was obtained in high-grade dysplastic lesions [305]. Another study from Pu et al. on patients suffering from prostate cancer, showed that the collagen decrease in tumor region using a 340nm excitation wavelength. They looked at the NADH/collagen ratio for a robust quantitative indicator of tissue nature [306]. Both study showed that in parallel of a collagen decrease, an NADH increase could be associated to tumoral presence. These two modifications resulted in a higher NADH/collagen ratio in prostate cancerous regions. In brain tumor tissues this has never been observed in the literature yet, motivating study with larger range of excitation.

To exploit all the possibilities of endogenous fluorescence and highlight as seen the link between the signal of the different molecules, a large study with an excitation from the DUV to the NIR was put in place. For this study, samples from patient with consent from the large frozen database of the Sainte-Anne hospital were accessible and used, making it possible to have a statistically significant cohort. This large cohort allowed us to build a study testing more robust algorithms and finding discriminative threshold that could be replicate clinically. These algorithms are based on spectral molecular analysis from the DUV to the NIR, combining several indicators to discriminate tissue nature and also fluorescence lifetime in the NIR range.

**Methods** Frozen samples from the Saint-Anne database were brought to the IMNC lab in Orsay. Thin slices of 10 microns were cut and fixed in order to be analyzed on the different set-ups. The cohort contained biopsy from 51 patients (13 control from cortex, 17 GBM and 21 metastasis). We first analyzed the samples under DUV excitation using 275 $\mu$ m wavelength at the synchrotron SOLEIL. In this excitation range were performed, a wide-field imaging of the emitted fluorescence and a spectroscopic measurements on the same region. The slices were then imaged using the two-photon bench-top microscope combined to a Ti-Sapphire laser. Images combining TPEF and SHG signal were acquired at 890nm. Spectral response and fluorescence lifetime were acquired at 810 and 890nm excitation. All these quantitative data were analyzed using homemade algorithms optimizing the discrimination between tissue nature, the algorithms are based on spectral and fluorescence decay fitting, spectral clustering and phasor approach for fluorescence lifetime. The slices were then stained using the hospital protocol for H&E staining.

**Results and discussion** Under DUV excitation, a deconvolution was applied on the spectral response to monitor each molecule. Different ratio giving a discrimination between control, pri-

primary and secondary tumor were calculated : tryptophan/collagen, tryptophan/NADH and tryptophan/tyrosin ratio. A discrimination based on the combination of these three significant ratio resulted in a sensitivity of 90% and a specificity of 73% and accuracy of 84%. In the two-photon range two quantitative measurements were accessible the spectral and fluorescence lifetime. Different molecular ratio were tested, the redox ratio to express the metabolic state of tissue and the optical index to translate the vascularity in tissue. An algorithm based on the two spectral indicators was tested and resulted in a sensitivity of 92% and a specificity of 95% and accuracy of 92%. However as seen in the literature [252], combining the spectral lifetime to the spectral measurements improved the results of the discriminative algorithm. Therefore in this chapter, a 3D-scoring system based on the two spectral ratio and the average lifetime was build and resulted in sensitivity of 97% and a specificity of 100% and accuracy of 98.3%. In our results the most accurate algorithm has been to that point the multi-contrast using a two-photon excitation. Having access to the DUV measurements on the same region make it possible to try the performances of a multi-range multimodal algorithm. A discrimination was made based on a the tryptophan-collagen ratio, the optical index and the fluorescence lifetime. This 3D-algorithm resulted in a 98,2% of accuracy to discriminate tumor from control tissue. Results of the different algorithms are summarized in the Table 6.1.

	<b>UV- spectral only</b>	<b>TPEF - spectral only</b>	<b>TPEF- spectral and lifetime</b>	<b>TPEF-UV and spectral- lifetime</b>
<b>Sensitivity</b>	90%	92%	97%	-
<b>Specificity</b>	73%	95%	100%	-
<b>Accuracy</b>	84%	92%	98,3%	98,2%

Table 6.1 – Performances of the different algorithms tried of this chapter

Looking at the accuracy of each algorithm, the spectral response using the two-photon excitation gave more precision than the DUV excitation. This is the consequence of a higher rate of false negative, 15,4%, in the DUV algorithm. This is a critical point in the perspective of improving surgical resection, it will result in leaving in place regions which are tumorous, because diagnose as healthy intra-operatively. Looking at algorithm only based on the spectral response, two-photon excitation between 800 and 900nm gave the most accurate discrimination. However, as seen in the conclusion of the previous chapter, the use of multimodal detection can improve the discrimination of tumor tissue. In this study, the precision of bi-modal algorithm based on spectral and lifetime detection was quantified to answer the question of discriminating primary and secondary tumor from control tissues. These algorithms resulted in an improved accuracy from 92% to 98,3% with a very low rate of false positive, 4,3%, which is very encouraging to translate the technology to the clinic. The last used algorithm test the impact of adding a DUV information to a multimodal algorithm. The data could be discriminated with the same accuracy (98,2%) than the two-photon model. However it gave a complete discrimination between secondary tumor and control, where the

two-photon multimodal algorithm gave a complete discrimination of the primary tumor compared to the control and had showed false positive cases for secondary tumor discrimination. This shows that depending on the tumor type, the molecules monitored with the DUV excitation could brought more precision than the ratio accessible with the two-photon excitation.

This large scale study provide a large amount of data to test different algorithms. All the previous analysis based on quantitative measurements were done using fitting algorithms [117, 128]. Fitting methods are known to be very dependent of initial parameters and so result in a low reliability and reproducibility. In intra-operative diagnosis the repeatability and reliability are important points to a successful technological transfer and failing to achieve that could kill a development towards clinical use. In this study, non-fitting algorithms were adapted and used on both the spectral and fluorescence lifetime data. For spectral data, a method was tested on UV spectral maps to find a discrimination, the cluster analysis. The clustering method has been already extensively explored on the infrared spectra to answer questions like the differentiation of colon cancer [307], the tumor heterogeneity in skin cancer [308] and tumor progression [309]. This method resluted in high precision to differentiate structure and a possibility of automation for a systemic diagnosis in clinical condition [308]. On our DUV data acquired at SOLEIL, a cluster algorithm based on the k-mean method was used and highlighted variations in the tryptophan/collagen ratio from healthy to tumoral regions. This observation on the cluster analysis resulted in a classification based on the quantification of the tryptophan/collagen ratio that gave a threshold to separate healthy region from tumoral regions.

For FLIM analysis, two methods of non-fitting can be found in the literature, the Laguerre deconvolution [135] and the phasor approach [310]. Fereidouni et al. compared the performances of the two methods to find their advantages and limitations [311]. They conclude that the phasor approach resulted in a very accurate estimation of the lifetime value and gave access to a graphical 2D representation of the results compared to Laguerre coefficients. The future user of such technology will be surgeons who do not have the same technical background than us, having access to a graphical results easy to interpret for non specialist will get their approval faster. For these reasons, phasor approach was the one tested and developed on the data of this study. The two-photon FLIM data were analyzed with this approach, and five distinct regions could be observed on the phasor plot. It could be identified that two of them were dominant in tumor and the other three in control tissue, resulting in a discrimination criteria that could significantly differentiate the tumor from control ( $p < 0.05$ ). However this method to extract a discrimination from FLIM analysis failed to differentiate the tumor types (primary and secondary). So there is still work to do on this non-fitting method to get to the precision of previous presented fitting method. In the literature other teams have used the phasor with other criteria of discrimination for example determining the fraction of free-bound NADH [115], this other approach could bring the precision needed in the analysis of the phasor results. It would be a perspective study.

The algorithm found here based on multimodal and multi-range approaches resulted in reliable discrimination between control, primary and secondary tumor. The reliable results especially using multimodal algorithm, with false negative rate lower than 5%, is opening the way to automation of brain tissue nature diagnosis. This is reinforced with the development of non-fitting algorithm such as the clustering that can be the first step of automated classification algorithms. However this study presented the first stage of algorithms development : the training phase. To get closer to a reliable clinical use, the found discriminative thresholds and criteria should be tested on a new set of data to evaluate algorithm robustness. These results and perspectives open the doors to the idea of a diagnosis performed by an artificial intelligence and not a human operator.

Through the chapter 2 to 6 a large database on the evaluation of primary and secondary tumor compared to control tissue was build and resulted on the development of discriminative algorithm that could be automated in an endomicrosper. These results support the development of two-photon endomicroscope to provide to the surgeon automatized discriminative algorithms during the surgery.



## 6.2 Paper: Multimodal analysis of central nervous system tumor tissue endogenous fluorescence with multiscale excitation



ORIGINAL RESEARCH  
published: 09 October 2018  
doi: 10.3389/fphy.2018.00109



### Multimodal Analysis of Central Nervous System Tumor Tissue Endogenous Fluorescence With Multiscale Excitation

Fanny Poulon<sup>1</sup>, Audrey Chalumeau<sup>1</sup>, Frederic Jamme<sup>2</sup>, Johan Pallud<sup>3,4,5</sup>, Pascale Varlet<sup>4,5,6</sup>, Hussein Mehdine<sup>1,7</sup>, Marjorie Juchaux<sup>1</sup>, Bertrand Devaux<sup>3,5</sup>, Matthieu Refregiers<sup>2</sup> and Darine Abi Haidar<sup>1,7\*</sup>

<sup>1</sup> IMNC Laboratory, UMR 8165-CNRS/IN2P3, Paris-Saclay University, Orsay, France, <sup>2</sup> DISCO Beamline, Synchrotron SOLEIL, Gif-sur-Yvette, France, <sup>3</sup> Neurosurgery Department, Sainte-Anne Hospital, Paris, France, <sup>4</sup> IMA BRAIN, INSERMU894, Centre de Psychiatrie et de Neurosciences, Paris, France, <sup>5</sup> Paris Descartes University, Paris, France, <sup>6</sup> Neuropathology Department, Sainte-Anne Hospital, Paris, France, <sup>7</sup> Paris Diderot University, Sorbonne Paris Cité, Paris, France

#### OPEN ACCESS

##### Edited by:

Qiyin Fang,  
McMaster University, Canada

##### Reviewed by:

Eleni Drakaki,  
National Technical University of  
Athens, Greece  
Oxana Sernyachkina-Glushkovskaya,  
Saratov State University, Russia

##### \*Correspondence:

Darine Abi Haidar  
abihaidar@imnc.in2p3.fr

##### Specialty section:

This article was submitted to  
Biomedical Physics,  
a section of the journal  
Frontiers in Physics

Received: 12 July 2018

Accepted: 10 September 2018

Published: 09 October 2018

##### Citation:

Poulon F, Chalumeau A, Jamme F,  
Pallud J, Varlet P, Mehdine H,  
Juchaux M, Devaux B, Refregiers M  
and Abi Haidar D (2018) Multimodal  
Analysis of Central Nervous System  
Tumor Tissue Endogenous  
Fluorescence With Multiscale  
Excitation. *Front. Phys.* 6:109.  
doi: 10.3389/fphy.2018.00109

The primary therapeutic approach for high-grade brain tumor is surgical resection. However, identifying tumor margins *in vivo* remains a major challenge. Biopsy analysis remains the standard diagnostic technique on tumor margins. This *ex vivo* analysis is time consuming and delays treatment. The aim of this study is tissue discrimination using label free autofluorescence and application in intraoperative optical probe for optical biopsy. Biopsy samples from 51 patients who underwent brain tumor surgery (21 metastasis tumors, 17 glioblastoma tumors, GBM, and 13 control samples) were included in this study. The samples underwent a multiscale and multi-contrast optical analysis. The excitation were performed with a deep-UV synchrotron beam, at 275 nm, and a near-infrared Ti:sapphire pulsed laser, from 690 to 1,040 nm. The detection modalities were fluorescence imaging, spectroscopy and fluorescence lifetime. Using deep-UV excitation, and combining three molecular ratios (tyrosin-tryptophan, tryptophan-collagen, tryptophan-NADH) resulted in discrimination with a sensitivity of 90% and a specificity of 73%. Using a two-photon excitation, and combining average lifetime, NADH-FAD ratio and Porphyrin-NADH ratio, resulted in discrimination with a sensitivity of 97% and a specificity of 100%. A multiscale algorithm resulted in an overlap of only 1.8% between control and tumor samples.

**Keywords:** deep-UV, synchrotron, Multi-photon, autofluorescence, brain tumor, phasor analysis, cluster, spectral analysis

#### INTRODUCTION

Many Central Nervous System (CNS) tumors, such as glioblastoma and metastasis both primary and secondary, are infiltrating. Surgical resection is the main course of treatment for such tumors. The outcome and life expectancy after these operations is very low and their improvements is one of the major challenges in modern medicine. In recent years many new technologies such as intraoperative ultrasound [1], intraoperative magnetic resonance imaging (MRI) [2], confocal endoscopy [3] have been brought into the operating room to help guide surgeons in resecting tumors. However none of these tools has been able to discriminate infiltrating tumors

### 6.2.1 Introduction

Many Central Nervous System (CNS) tumors, such as glioblastoma and metastasis both primary and secondary, are infiltrating. Surgical resection is the main course of treatment for such tumors. The outcome and life expectancy after these operations is very low and their improvements is one of the major challenges in modern medicine. In recent years many new technologies such as intra-operative ultrasound [87], intra-operative magnetic resonance imaging (ioMRI) [82], confocal endoscopy [173] have been brought into the operating room to help guide surgeons in resecting tumors. However none of these tools has been able to discriminate infiltrating tumors margins (ITMs). These techniques have failed to offer cellular-level resolution, and to detect the low concentrations of tumor cells in infiltrating regions. As a consequence, the chosen surgical approach is to maximize the extent of tumor removal while minimizing intrusion on the eloquent brain area[312]. And while resection improves the outcome and life expectancy of the patient, the surgeon still operates "blind" on the true nature of margins. To meet the challenge of discriminating ITM's intra-operatively, there has been a boom in developing surgical medical imaging tools that can contrast brain tissues and discriminate cell types. Examining tissue autofluorescence with optical microscopy techniques is one answer to the demand for intra-operative ITM discrimination. Several molecules produce an endogenous fluorescence signal in the brain [102] and this signal can change from one type of tissue to another. This difference can be used to distinguish tumoral regions from healthy ones [103, 122, 135] . Following that direction, our group miniaturized two-photon microscopy into a fibered configuration for intra-operative purpose. This endomicroscope enables two imaging contrasts: two-photon autofluorescence emission (TPEF) and second harmonic generation(SHG), with an excitation in the near infrared (NIR). The NIR excitation lies in the tissue therapeutic window, resulting in less photodamage and a better penetration depth. In our set-up we also choose to include several types of measurements: full field imaging, micro-spectroscopy and fluorescence lifetime to provide the most reliable and reproducible response. To validate this technical approach we built, in parallel, an optical database of the autofluorescence response from brain tissues which will be used to develop and test robust algorithms to automatically discriminate tissue and validate automatic tissue analysis, potentially eliminating subjective reading of images by a human operator. Multimodal study of endogenous fluorescence on human tissue is relatively new and, according to the literature, only a few tissue types have been explored. Our lab focused on brain tissue endogenous fluorescence by partnering with 1) the Saint-Anne hospital (Paris, France) who provided biopsy samples and medical knowledge, and 2) Synchrotron SOLEIL who provided access to a deep UV imaging platform at DISCO beamline, while the IMNC, performed two-photon microscopy with a bench-top microscope.

This study searched for an objective optical marker to discriminate tumor from healthy tissue, and to discriminate primary from secondary tumors. A large study on fixed biopsy tissue of primary (glioblastoma), secondary (metastasis) tumor and control cortex was performed, with large scale excitation ranging from deep-UV (DUV) to near infrared (NIR), and several modalities of detection from qualitative, fluorescence and lifetime imaging, to quantitative, spectral and lifetime measurements. Finding a discriminating optical marker was made possible by exploiting multiple contrast and building 2D and 3D discriminative algorithms for the DUV and NIR excitations individually, and then in combination. Discrimination specificity and sensitivity were in the 70 to 100% range, highlighting the power of optical analysis to discriminate the nature of tissue with enough precision to be clinically useful. The qualitative results of our study were also used to compare optical microscopy technology to the gold standard H&E staining. This comparison highlighted discriminative histological structure in the optical images, and a "blind" pathologic analysis was

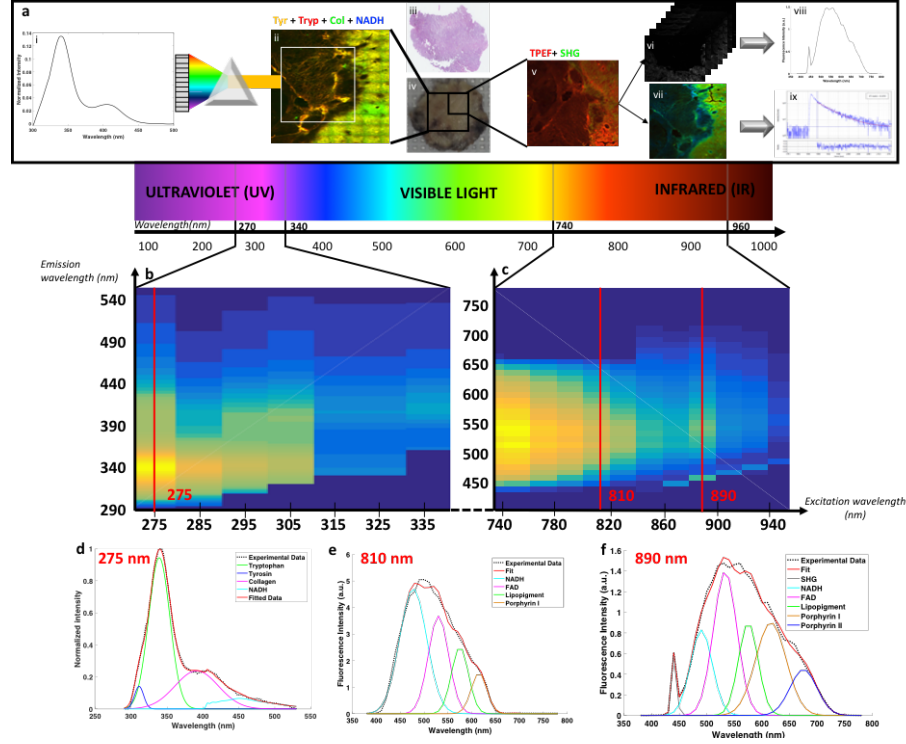


Figure 6.1 – (a) Schematic of the acquisition-analysis protocol from deep-UV to infrared excitation (b) Deep-UV excitation-emission matrix. (c) Two-photon (NIR excitation) excitation-emission matrix. The bottom line present how were fitted tyrosin, tryptophan, collagen crosslinks and NADH at 275nm (d), NADH, FAD, lipopigments, porphyrin I and porphyrin II at 810 nm (e) and SHG, NADH, FAD, lipopigments, porphyrin I and porphyrin II at 890nm (f).

then performed directly on our images.

## 6.2.2 Materiel and methods

### 6.2.2.1 Study design

The samples were excited in the deep-ultraviolet (DUV) and the near infrared (NIR) range on two different platforms. The design of the study is presented in Figure 1. On both platforms an excitation emission matrix was performed to highlight the different excited components and to select the optimal wavelengths for our study. Under DUV excitation we chose 275nm as the optimal wavelength, being the most efficient in set-up, and in exciting four components simultaneously: Tyrosin (Tyr), Tryptophan (Trp), Collagen crosslinks (Col) and NADH.

In the NIR range we chose two excitation wavelengths: 810nm and 890 nm. Four molecules and SHG were tracked: NADH, FAD, Lipopigments, Porphyrin. At 810nm excitation NADH was optimally detected and at 890nm we obtained the best tradeoff between SHG and emitted fluorescence [216]. Samples (Fig5.a.iv) underwent the following process : (1) large mosaic at 275nm

Type	Nb Patient	Age	Men	Women
Control	13	35,2±7,4	9	4
Primary Tumor : GBM	17	68,3±11,4	12	5
Secondary Tumor : Metastasis	21	58,8±12,2	10	11
TOTAL	51	54,1±17	31	20

Table 6.2 – Description of samples

in the four detection channel (Tyr, Tryp, Col, NADH) (Fig6.1.a.ii) (2) selection of a region of interest and spectral measurements at 275nm (Fig6.1.a.i) (3) Large mosaic at 890 nm (Fig6.1.a.v) (4) selection of the same region of interest as in DUV to perform spectral (Fig6.1.a.vi) and FLIM measurements (Fig6.1.a.vii) at 810 and 890 nm. Once data acquisition was completed, analysis followed : (i) spectral fitting of the data at each wavelength using homemade Matlab program (Fig6.1.a.i & viii) (ii) Fitting of the lifetime data with Symphotime software (Fig6.1.a.ix) (iii) Phasor analysis of the lifetime data (iv) construction of discriminative algorithm combining the different analysis results and (v) comparison with the gold standard histology (Fig6.1.a.iii).

### 6.2.2.2 Samples preparation

A collaboration with the anatomopathology and neurology departments of the Saint-Anne Hospital (Paris, France) provide a large cohort of human biopsy samples. The protocol of experimentation was approved by the Institutional Review Board of Sainte Anne Hospital (Ref CPP S.C.3227). Fifty-one individuals (31 males, 20 females; age average 54.1±17 year-old) were included and an informed written consent was obtained from all patients prior to enrollment. Frozen human brain tissues, conserved at -80°C, were obtained from two types of tumor (21 metastasis samples, Meta; 17 glioblastoma samples, GBM) and Control specimens (13 patients with no history of tumor) selected from epileptic surgery. The metastases were originated from lung, breast, bladder and skin. The characteristics of the cohort are summarized in Table 6.2 . A dedicated transport (360°, France) brought the selected cohort to the IMNC laboratory (Orsay, France). Samples were conserved at -80°C, before being transferred to a -20° freezer 24 hours before being cut with a cryostat (Leica CM 1950). Ten-micron slices were deposited on quartz coverslips and microscope slides, and fixed with an ethanol solution (100%). The quartz coverslips were brought to the Synchrotron in a dedicated box, and the microscope slides were used for H&E staining and two-photon imaging on the PIMPA platform.

### 6.2.2.3 Histological Process: Hematoxylin and Eosin Staining

A gold standard Hematoxylin and Eosin (H&E) staining was performed on one of the microscope slices following the Sainte-Anne hospital protocol [61] whose steps are hydration, H&E staining, dehydration, and toluene fixation. Once stained the samples were imaged in a Digital Slide Scanner NanoZoomer 2.0 (Hamamatsu Photonics K.K, Hamamatsu, Japan).

### 6.2.2.4 Deep-Ultraviolet imaging and spectral measurements

The Deep-Ultraviolet (DUV) measurements were performed on the DISCO beamline at the Synchrotron SOLEIL [313]. Two set-ups, a full-field microscope (Zeiss Axio-observer Z-1) and a

microspectrofluorimeter (Olympus IX71), were used for this study. The samples were excited with the continuous emittance from the DISCO beamline bending magnet between 275nm and 335nm. The details of the set-up have been presented in other studies [314, 315]. A large mosaic of the sample was made under the full field microscope with an excitation wavelength of 275nm and four emission filters (307-323nm, 323-357nm, 408-438nm and 435-455nm, Semrock, USA) in front of a detector (CCD camera, Pixis BUV, Princeton Instrument, USA). Regions of interest were then selected in this mosaic and spectral measurements were done with the microspectrofluorimeter at the same excitation wavelength. One second integration time and a ten microns lateral step size were applied. An Excitation-Emission matrix was also measured using the microspectrofluorimeter. An emission spectrum was acquired for each excitation wavelength from 275nm to 335nm every 10nm.

#### 6.2.2.5 Two-photon imaging and quantitative measurements

A two-photon benchtop microscope (TCS SP8 MP microscope, Leica Microsystems, Wetzlar, Germany) combined with a Ti:sapphire laser source (Mai Tai DeepSee, Spectra-Physics, Santa Clara, USA) was used to perform fluorescence imaging (TPEF), emission spectra and fluorescence lifetime imaging (FLIM). The set-up and acquisition methods are described thoroughly in our previous work [216, 223]. The measurements were recorded on the same region of the sample as the one imaged with the DUV excitation. On each region TPEF and SHG image were recorded using 890 nm excitation wavelength. Then spectral and FLIM analyses were performed using 810 and 890nm excitation wavelength. Excitation-Emission matrices were also measured by acquiring a spectral stack at excitation wavelengths between 740 and 940 nm every 20 nm.

#### 6.2.2.6 Data analysis

##### 6.2.2.6.1 DUV analysis

DUV full-field images were processed, using Image J, to create a merged image of the fourth detection filter and to visually identify any difference between tissue regions. The spectral results were analyzed using lab-written Matlab script and the PLS toolbox (Eigenvector Research Inc., WA, United-States). Two types of analyses were performed on the data. First was a cluster analysis to extract spectral signature of tumoral region, and second was a fitting analysis to compare tissues at a molecular scale. In the first method, the data were first preprocessed using lab-written scripts developed by SOLEIL and IMNC teams, in order to: (1) reduce the noise, (2) suppress dead pixels, (3) set-up a baseline, and (4) normalize to the maximum of the cohort. Then a discriminative cluster analysis (DCA, K-Means) was applied to all the pixels of every images using the PLS toolbox. The number of input clusters was chosen iteratively looking at the results, and fixed at five in our case. The second analysis applied on the spectral data was a spectral fitting of the different molecular contributions. The fit was performed using a lab-written Matlab script previously used on visible and near infrared autofluorescence data [216, 223] and adapted to the DUV data. The results of the fit were used to compare different molecular ratios. The ratio between tryptophan and collagen crosslinks was given a particular attention, but tyrosin/tryptophan and tryptophan/NADH ratio were also computed to build a robust discriminative marker.

##### 6.2.2.6.2 Two-photon analysis

TPEF images were processed using Image J, in order to produce both a good quality and scaled image of the merged TPEF-SHG signal. The images were then compared with H&E images.

After highlighting the histological structure on the TPEF images, a neuropathologist was asked to perform a blind analysis. The analysis was done on paired TPEF and H&E images from 25 samples (10 metastases, 8 glioblastomas, 7 controls). First, a senior neuropathologist, blind to the TPM results, performed an initial histopathological analysis. No specimen was excluded due to lack of histopathological representativeness. Then, six months later, we presented a web-based survey of the TPEF images (PNG TPEF/SHG images) and the participant was asked to classify the sampled tissue in four categories: 1) GBM ; 2) Meta; 3) healthy tissue; or 4) unclassified. Although completely blind to the initial histological analysis, the participants had access along with the TPM images, to typical clinical data including patient's age, gender, clinical presentation, tumor location, and pre-operative MRI images. These results were then compared to initial histological analysis to calculate the accuracy of the diagnosis on TPEF images.

The spectral stacks were opened in Image J to extract five spectral region of interest (ROIs) in each of the 810 and 890nm images, and then processed in Matlab. The obtained spectra were fitted using a lab-written Matlab script previously published and used on meningioma samples [216]. Five autofluorescent molecules were fitted: NADH, Flavin adenine dinucleotide (FAD), Lipopigments, Porphyrin I and Porphyrin II. The results of the fit were used to compute two indicators according to the literature [117, 222]. The oxydo-reduction ratio between NADH and FAD:

$$ROx = \frac{FAD_{890}}{FAD_{890} + NADH_{810}} \quad (6.1)$$

And the optical index ratio between NADH and porphyrin:

$$OI = \frac{PorphyrinI_{890}}{NADH_{810}} \quad (6.2)$$

The NADH values were extracted from the emission spectrum using 810 nm excitation wavelength and the FAD and Porphyrin from the emission spectrum using 890 nm excitation wavelength. To be comparable, the spectra were normalized by the excitation power.

As with spectral data, the FLIM data were analyzed using two methods, fitting and non-fitting, which were developed. First, bi-exponential fitting – the method implemented in the acquisition software (Symphotime Vx64, Picoquant)-was used. On each image the same five ROI as for spectral measurements were selected, and on each ROI the fluorescence decay histogram was bi-exponentially fitted. The amplitude average lifetime was extracted from this fit using a method previously published on bladder tumor [316]. The second implemented method used a non-fitting process, called phasor analysis. We started with the time-correlated single-photon counting (TCSPC) detection of fluorescence decay curves at each pixel of a 3\*3 mosaic image. The intensity of a 32\*32 pixel (a 28±m-side) square was added together to obtain the decay I(t) at each reduced pixel. In the phasor approach, the decay I(t) at each pixel is transformed into two coordinates in a Cartesian plot according to the following equations:

$$S_i(w) = \frac{\int_0^\infty I(t)\cos(\omega t)dt}{\int_0^\infty I(t)dt} \quad (6.3)$$

$$G_i(w) = \frac{\int_0^\infty I(t)\sin(\omega t)dt}{\int_0^\infty I(t)dt} \quad (6.4)$$

where,  $S_i(\omega)$  and  $G_i(\omega)$  are the x and y coordinates of the phasor in the phasor plot, respectively;  $\omega$  is the angular repetition frequency linked to the signal length (L) and the sampling period ( $T_s$ ) by the relation:  $\omega = 2\pi/(LT_s)$ . We stored for each pixel  $S_i(\omega)$ ,  $G_i(\omega)$  and  $M_i$  - the normalized integration under the decay of each pixel to provide the phasor histogram of the 3\*3 mosaic image. A global phasor histogram grouping the data of all the samples (n=51) was plotted. Five areas were selected on this global phasor histogram and the images were reconstructed with a five colors-scale corresponding to selected area. Pixel colors criteria following Eq. 6.5 were used to compare the data from each group.

$$\log \frac{\%green\ pixel + \%blue\ pixel}{\%red\ pixel + \%yellow\ pixel} \quad (6.5)$$

Value of fluorescence lifetime was also determined in this analysis using an error ellipse method. An ellipse that should contain 95% of phasor counts in each area was fitted on the five areas of the global histogram. The two intersections between the major axis and the circle segment are linked to the two lifetimes and their contributions.

#### 6.2.2.7 Statistical analysis

The different computed ratios were compared statistically with t-test in Matlab to obtain a p-value with a criteria of significance at  $p < 0.5$ . The representation in scatter plot and the blind analysis were evaluated by defining the sensitivity (Se) and specificity (Sp) of the discrimination criteria, following Eq. 6.6 and Eq. 6.7.

$$S_e = \frac{TP}{TP + FN} \quad (6.6)$$

$$S_p = \frac{TN}{TN + FP} \quad (6.7)$$

The variables were TP = True Positive, FP= False Positive, TN= True Negative and FN= False Negative, defined as: TP=Tumoral tissue classified as tumoral, FP=Control tissue classified as tumoral, TN=Control tissue classified as healthy and FN=Tumoral tissue classified as healthy.

#### 6.2.2.8 Multiscale discriminative algorithm

In the various excitation ranges the three best indicators were chosen: (1) Porphyrin/NADH ratio using two-photon excitation, (2) Tryptophan/collagen crosslinks ratio at DUV excitation and (3) the average lifetime using 890nm excitation. A region of interest measured in our protocol could be then represented in the 3D-scatter plot with these three indicators as its coordinate. The scatter cloud of a group was fitted by a Gaussian ellipsoid using the mean and the standard deviation as parameters for the covariance with the ellipse to cover 60% of the total probability mass. The percentage of overlap between the ellipses for each group was then calculated to assess of the performance of such algorithm.

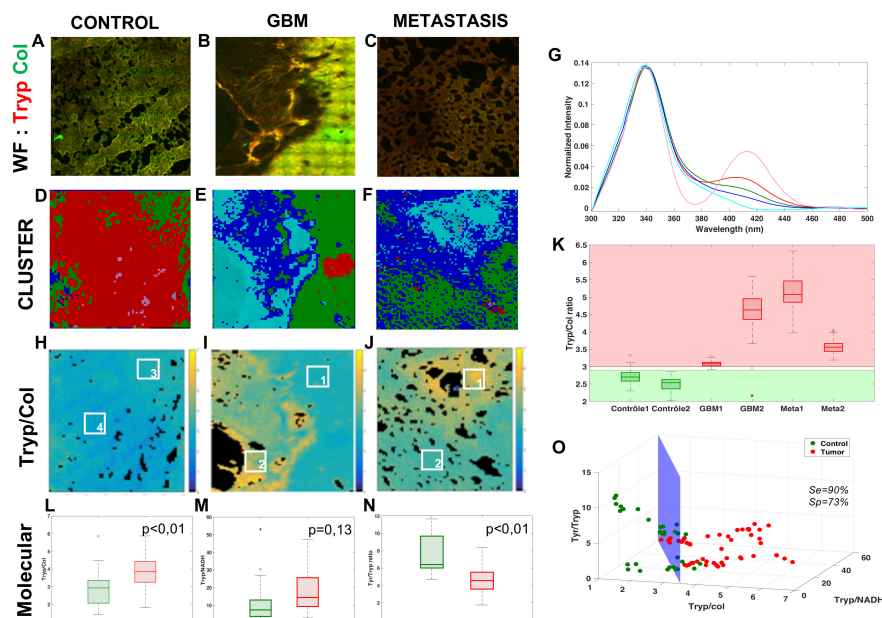


Figure 6.2 – Analysis of the Deep-UV data. Comparison of the three tissue groups control (a,d,h), glioblastoma (b,e,i) and metastasis (c,f,j) with different analysis methods: wide-field(WF) imaging (a,b,c), spectral clustering (d,e,f) with a 5-cluster decomposition shown on a graph (g), map of the tryptophan/collagen ration (h,i,j) with comparison of selected ROIs(k). Molecular analysis of the tryptophan/collagen ratio (l), the tryptophan/NADH ratio(m) and the tyrosin/tryptophan ratio(n) combined in 3-D scatter discrimination plot (o).

### 6.2.3 Results

In this large study, we first look at the results under DUV excitation. The Figure 6.2 presents a summary of the analysis results and discrimination reached in this excitation range.

Figure 6.2a.b.c shows an example of the superposition of the tryptophan (green) and collagen channel of wide-field (WF) image in each group. The control image presents an homogeneous color, while in primary and secondary tumor some regions show a different color, exposing a variation in the tryptophan-collagen ratio in tumoral tissue. Based on this observation a method of clustering was applied to the spectral data to validate this hypothesis and to see if two types of spectral signatures were highlighted.

The figure 6.2.d.e.f shows the results of the spectral cluster analysis on the same region as the one on the WF images. The spectra corresponding to each color are superposed in the figure 6.2.g. The two dominant colors in control (red and pink) correspond to spectrum with a main peak in the tryptophan range and a secondary peak in the collagen crosslinks range, where the different dominant colors (blue and cyan) in tumor correspond to spectrum with only one main peak in the tryptophan range. These results led us to track the ratio between the two main peaks of the DUV spectral response, the Tryptophan/collagen ratio.

Figure 6.2h.i.j gives an example of the Tryptophan/collagen ratio in a tissue of each group,



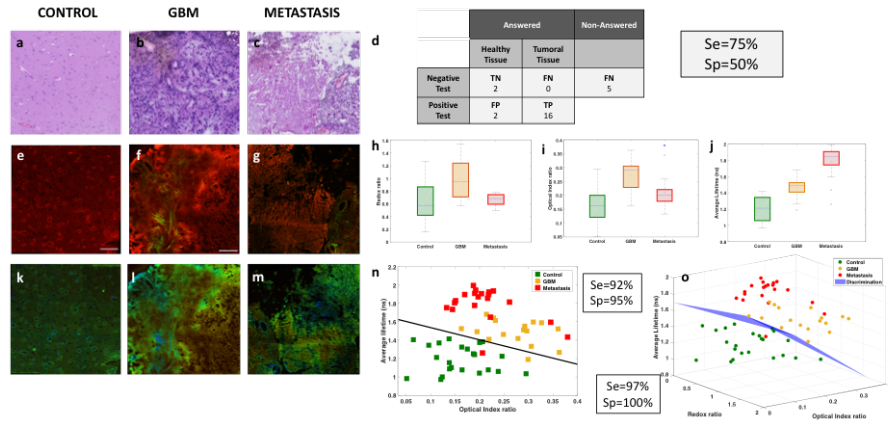


Figure 6.3 – Analysis of NIR data. Comparison of three tissue groups : control (a,e,k), glioblastoma(b,f,l) and metastasis (c,g,m) with different imaging techniques H&E (a,b,c), TPEF imaging (a,f,g) and FLIM (k,l,m). Results of the "blind" analysis on TPEF for diagnosis (d). Boxplot of the spectral molecular analysis, redox ratio (h) and optical index (i), these results were combined in a scatter plot (n). Boxplot of the average lifetime (j). 3D-scatter of the two molecular indicators and the average lifetime to build a discriminative algorithm (o).

the ratio being higher in tumoral groups than in control group. The results of the selected ROI are plotted in the Fig.6.2.k. A threshold value distinguishes tissue type: below 2.8 the tissue is healthy, above 3 the tissue is tumoral. After validation of this method a larger statistical analysis was performed on all the sets of tissue and new molecular ratios were tested. The results are shown in Fig.6.2.l.m.n. The Tryptophan/collagen ratio showed a significantly higher ratio in control tissue ( $p < 0.01$ ). The Tryptophan/NADH ratio also showed the same trend but with less statistical significance ( $p = 0.13$ ). The third ratio, Tyrosine/Tryptophan, showed a lower value in tumoral tissue than control ( $p < 0.01$ ). To find a discriminative algorithm with statistical significance, these three molecular ratios were extracted in five ROI in different types of tissue, and projected as the coordinate of the ROI in a 3D-scatter plot (Fig.6.2.o). A discriminative cross-section could be drawn between tumoral tissue (red dots) and control tissue (green dots), with calculated algorithm specificity of 73% and sensitivity of 90%. This discriminative algorithm has a high sensitivity, making it a good diagnosis tool, ruling out tumor presence with precision. However it still gave a non-negligible level of false positives.

The data obtained in the NIR excitation range were tested with similar approaches. The results are shown in Figure 6.3.

The first approach was to compare the TPEF images to the histological gold standard H&E images to find the structure used to discriminate tissues. The TPEF images are a merger of autofluorescence emission, red contrast, and SHG signal, green contrast. In the control, typical cortical arrangement of neurons (dark violet triangular spot in H&E), showed a strong uorescent spot on the TPEF images. In the glioblastoma, large vessels, identified by light pink structures in H&E and lamen in SHG green channel. The vessels are surrounded by a high density of tumor cells, identified with an intense signal in the uorescence image. In the metastasis, strong neovascularization with tumor cells entangled, light pink signal signal in H&E surrounded by high density of cells, were iden-

tied on the TPEF images by a strong SHG signal with bright uorescent spots. Thereafter the TPEF were given to senior neuropathologist for blind diagnosis in order to evaluate the capability of direct diagnosis on TPEF images. The senior pathologist was able to discriminate tissues with a specificity of 50% and a sensitivity of 75%. Next the quantitative results were analyzed on each TPEF image region. A spectral response with a 810 and 890nm excitation was measured and different molecular indicators were calculated at different regions of interest for every tissue. The two spectral markers calculated were the redox ratio and the optical index. In Figure 6.3.h, the redox tended to be higher in tumoral tissue and discriminative between tumor types ( $p_{control-GBM} < 0.01$ ,  $p_{control-meta} = 0.06$ ,  $p_{GBM-meta} < 0.01$ ). The optical index is also higher in tumoral tissue and can discriminate primary from secondary tumor ( $p_{control-GBM} < 0.01$ ,  $p_{control-meta} = 0.01$ ,  $p_{GBM-meta} < 0.01$ ). Complementary quantitative measurements were performed on the samples: extraction of the average lifetime using a fitting method applied on the various regions of interest, and boxplot comparison of different tissue types, as shown in Figure.6.3.j. This method could discriminate the three types of tissue ( $p_{control-GBM} < 0.01$ ,  $p_{control-meta} < 0.01$ ,  $p_{GBM-meta} < 0.01$ ). The results were combined to develop a discriminative algorithm. First we used the two most efficient indicators, optical index and average lifetime (Figure 6.3.n.). Results with specificity and sensitivity respectively of 92 and 95% are shown in a 2D-scatterplot. To improve the diagnostic algorithm, a third piece of information was added to represent the data in a 3D-plot (Figure 6.3.o.). A cross-section was drawn to obtain a sensitivity of 97% and specificity of 100%.

The best method to directly discriminate tissue types was shown to be lifetime measurements. We decided to investigate it more in detail by implementing another analysis method, called the phasor approach [133] which helped to uncover a discriminative indicator without fitting of data. The results are shown in Figure 6.4.

Control, GBM and Metastasis decays were gathered on a global phasor counts, Fig.6.4.a. In this phasor plot five local maximums of counts were observed and selected in order to assign a different color to pixels within each region. Each image using the phasor plot was displayed with this color code. Examples are shown in Figure 6.4.b,c,d,I,j,k. and compared to the fast FLIM images obtained by the microscope software. The images show green and blue dominant in control, while red and yellow are more present in tumoral tissue. To quantify this difference a color ratio was defined and calculated in each sample. The results, comparing the tissue groups, are presented in Figure 6.4.l. Each tumor could be differentiated from the control tissue (Control-GBM :  $p=0.03$  and Control-Metastasis :  $p=0.02$ ). However it did not give a significant discrimination between primary and secondary tumor. The green and blue areas, occupying the majority of healthy tissue, had an average lifetime around 1.4-1.6 ns, while control had a mean average lifetime around 1.3ns in the fitting method. Yellow and red areas, occupying the majority of tumoral tissue, had average lifetimes around 1.8-2 ns, while the GBM mean was around 1.6 ns and the metastasis mean around 1.9 ns in the fitting method.

From DUV to NIR, various interesting discriminative indicators were highlighted. To improve the capacity to discriminate not only control from tumor, but also tumor types from one another, the three most efficient indicators were combined for scatter plotting the groups in 3D space to highlight discrimination. The results with the indicators, Porphyrin-NADH ratio at two-photon excitation (Optical Index), Tryptophan collagen ration at DUV excitation (DUV ratio) and the average lifetime at 890nm, are shown in the Figure 6.5.

This 3D algorithm was used to find an accurate discrimination between a healthy region and any tumoral region, Figure 6.5.a., the points of each type were approximated by an ellipsoid giving an overlap of only 1.8%, resulting in high rate of tumor discrimination. This algorithm was also

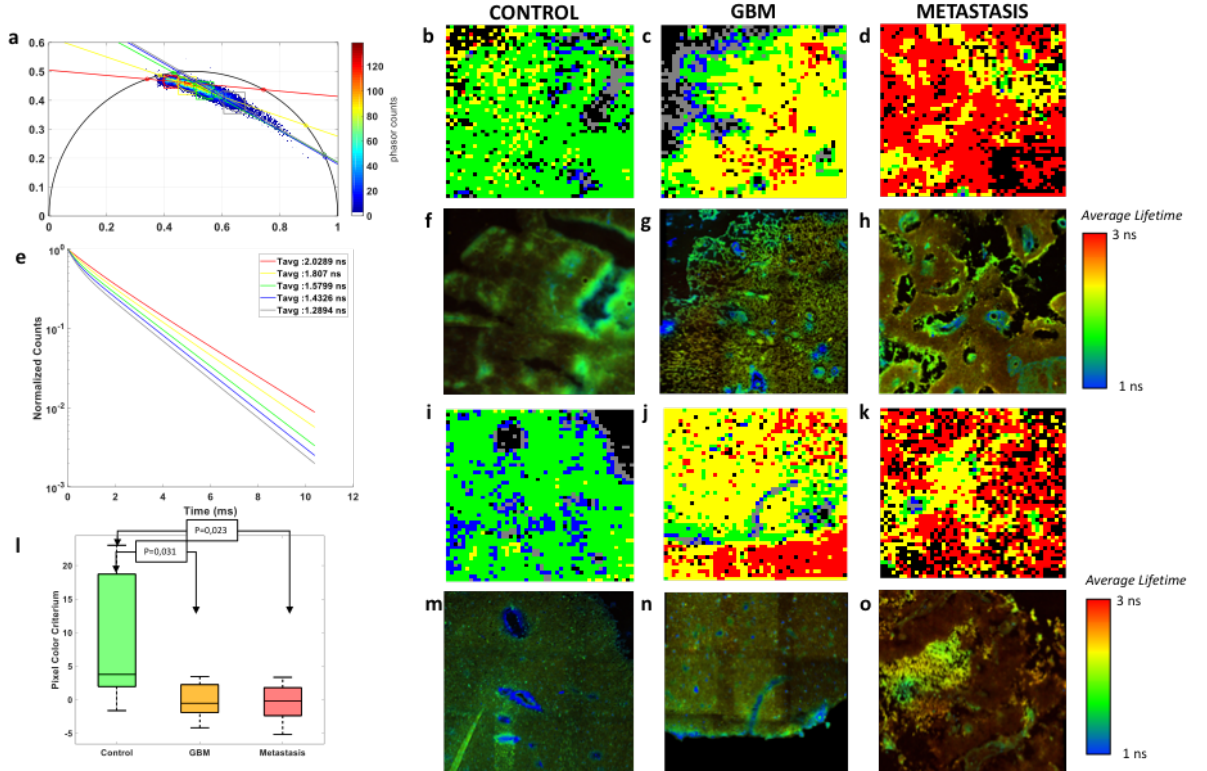


Figure 6.4 – Phasor analysis of the FLIM : (a) Global phasor histogram with the selected zones and the error ellipses. (e) Average lifetime fluorescence decay calculated in each zones. (l) Boxplot of the pixel colors criterion with p-values of the control-tumor test. Comparison of three tissue groups control (b,f,i,m), glioblastoma (c,g,j,n) and metastasis (d,h,k,o) with rebuilt images of the phasor analysis (b,c,d,i,j,k) and Fast FLIM of the microscope (f,g,h,m,n,o).

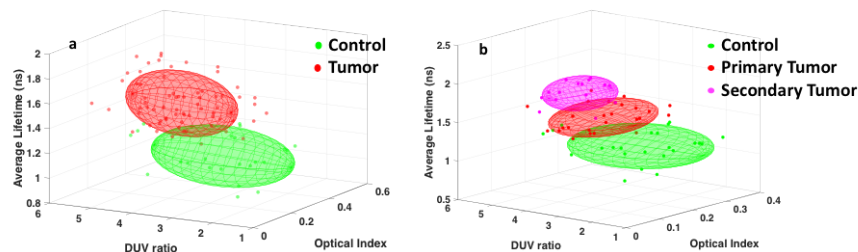


Figure 6.5 – Discrimination of tissue types combining three indicators: Porphyrin/NADH ratio using two-photon excitation (Optical Index), Tryptophan/collagen ratio at DUV excitation (DUV ratio) and the average lifetime using 890nm excitation. (a) Results comparing Control and any tumor types. (b) Results for Control, primary tumor (GBM) and secondary tumor (Metastasis).

used to look for discrimination between tumor types, Figure 6.5.b., primary tumors had only 6.7% overlap with secondary tumors. This second 3D-plot also showed that the secondary tumors could be unambiguously discriminated from the control tissue.

#### 6.2.4 Discussion

In this study excitation ranging from DUV to NIR, various detection contrasts, and multiple methods of analysis were applied to biopsied brain tissue of three types: primary tumors ( $n=17$ ), secondary tumors ( $n=21$ ) and controls ( $n=13$ ). We demonstrated that: 1) Tumor could be discriminated from control in the DUV excitation range using molecular ratio 2) The merged TPEF-SHG images revealed features similar to those seen in standard neuropathology, and could discriminate tumor from normal tissue 3) Quantitative TPM signals also discriminated between tissue types combining molecular ratio and average lifetime 4) Lifetime measurements analyzed with a phasor method gave a discriminating criteria significantly ( $p<0.05$ ) distinguishing control from tumor tissue. 5) A multiscale discriminative algorithm, could graphically separate the tissue types in a 3D plot.

First, using DUV spectral response and cluster analysis, we showed that a distinguishing spectral signature for tumoral versus healthy tissues, quantified in the tryptophan and collagen peaks ratio calculated on all spectral mosaic, with  $<2.8$  being healthy, and  $>3$  being tumoral. Few studies have exploited DUV excitation of Tryptophan. Pradhan et al. [317] studied Tryptophan/NADH and found a higher ratio in metastasis tissue, similar to our findings in ex vivo human brain tumor. The autofluorescence of collagen has also been studied in tumor with a UV excitation. Georgakoudi et al. looked at cervical lesions and Barrett's esophagus and found lower collagen signal in high-grade dysplastic lesions [340]. Pu et al. collagen emission in prostate cancer, and showed a decrease in tumor region. They looked at the NADH/collagen ratio for a robust quantitative indicator of tissue nature [306]. The actual state of art is often comparing one or two molecules to find discrimination. A four molecule analysis was performed to get closer to clinical expectations of accuracy and repeatability. A 3D discriminative algorithm using three molecular ratios achieved specificity of 73% and sensitivity of 90% and thus could be used as diagnostic tool. However, low specificity indicates significant false-positives when a tumor is detected.

Secondly, we used the NIR images superposing two modalities: fluorescence emission and second

harmonic generation, to highlight tissue structure comparable to the histological standard for tumor diagnosis. A neuropathologist was asked to perform a histological diagnosis blind to the H&E results. This test showed discrimination with a sensitivity of 75% and a specificity of 50%. Training neuropathologists on TPEF images could improve these results since this trial was a first time experience using this imaging modality. Blind analysis of TPEF-SHG images have never been performed before on brain tumor, but on other types of cancer, such as gallbladder cancer [280], breast masses [281], and liver cancer [282]. In these analysis, they found even higher results than us with accuracy of discrimination around 90%, due to training of the neuropathologist on bigger sets of data. Analysis directly on TPEF images have advantages over staining technique, such as time management and tissue preservation, however it still requires a trained neuropathologist to diagnose based on visual observation. The real advantage of optical microscopy in our study is the capacity to provide more parameters and new measurements, feeding into data analysis and visualization that support automated distinguishing of tissues. Two-photon excitation provides other parameters besides fluorescence intensity: the fluorescence lifetime and SHG. We use the power of these techniques to achieve a better discrimination of the nature of tissue by combining the results of molecular analysis on emitted spectrum and the lifetime analysis of the same region. The combination in 3D-plot of: (1) the average lifetime, (2) the FAD/NADH ratio and (3) the Porphyrin/NADH gave the best discrimination with a 97% sensitivity and 100% specificity. This type of analysis were already published only with visible, one-photon excitation [135]. Other groups tried to build a 2D algorithm, using visible excitation : Liu et al [117] studied redox ratio and spectral shape with a 89% sensitivity and a 97% specificity. Lin et al [124] analyzed fluorescence intensity and reflectance at 337nm, with a one-step algorithm yielding sensitivity and specificity under 85%. A two-steps algorithm gave them better results (sensitivity, 100%, specificity, 76%). However we can achieve similar results with a one-step algorithm, which is easier to implement in a clinical workflow. Thirdly, using two photons imaging, only the fluorescence lifetime produced significant discrimination among the three types of tissue ( $p < 0.01$ ). Due to their independence from concentration, fluorescence lifetime measurements have been the most popular technique. Several teams have tried to implement it with various analysis algorithms to answer the question of glioma margin resection. Sun et al [136] used the Laguerre coefficient value and found a longer lifetime in GBM than normal tissue with a  $p\text{-value} < 0.05$ . They preferred this technique because there is no deconvolution process of the data, avoiding any assumption on the decay shape. Another non-fitting technique is the phasor approach [133]. This is the second method we tried, since it offers a very graphical representation of data. The phasor approach showed five distinct regions, with some being predominant in tumor and others in control tissue. From this a numerical indicator from region repartition was exploited and resulted in a significant difference between tissue types ( $0.023 < p\text{-value} < 0.031$ ). However, compared to the exponential fitting, primary and secondary tumor could not be discriminate. Other exploitations of phasor plot exist [318], that could be implemented to improve these results.

We took advantage of our multiscale analysis and designed a graphical discriminating algorithm based on spectral DUV measurements, spectral NIR measurements, and lifetime NIR measurements. We distinguished an ellipsoid region for each type of tissue. Primary tumor and control had only 1.8% of overlap. Secondary tumor and control had 0% overlap and primary and secondary tumor had 6.7% overlap.

This study highlights the capability of discriminating brain tissue type from one another, tumoral from control, but also tumor types from one another. This was achievable by combining the different quantitative and qualitative measurements accessible with optical microscopy. The technique used

in this study can be implemented in real-time in the operating room with fast and direct analysis. These results are bringing us closer to clinical use and could improve the surgical practice of tumor resection. The perspective of this study are to extend the work to fresh tissues and other tissue types to get information closer to the in vivo condition and improve the discriminating algorithm.



## Chapter 7

# Discussion and Conclusion

In this thesis project intrinsic fluorescence signal of tissue has been extensively analyzed using different excitations and contrasts. Three goals can be extracted from this project : 1) to show autofluorescence signal, as a powerful contrast for brain tissues diagnosis, 2) to develop data analysis and robust algorithms required to fit into surgical workflow, providing reliable *in vivo* guidance, and 3) comforting the development of the multimodal two-photon endomicroscope, presenting an architecture resolving current issues in a clinical setting. Interesting and promising results have been obtained for each step. In this last chapter, I will discuss their significance, where they fit in the literature landscape, and look at the prospects of getting closer to clinical use.

### 7.1 Autofluorescence as a diagnosis tool

At present, the key limitation of intra-operative techniques is the lack of cellular level resolution imaging. To discriminate areas with very low concentrations of tumor cells, the standard is still H&E-stained histopathology, an ex-vivo technique also used to diagnose tumor types and grades. The aim of this work is to address this challenge and to present a technique that could be implemented in the operating room and result in direct discrimination for the surgeon.

Two approaches have been explored and combined to answer this question. First, finding a label-free imaging technique showing the same cellular features as the techniques now used in histology. Secondly, being able to quantify and monitor cellular energetic metabolism, hemodynamic, or even structural changes in order to identify anomaly in the tissue at a cellular scale and give an automated answer to the surgeon. For this second point different quantitative measurements were performed on the autofluorescence response of tissue using a large range of excitation from the deep-UV to the NIR and on different brain tissue cohorts.

#### 7.1.1 Qualitative analysis of label-free fluorescence images compared to gold standard H&E-stained

Neuropathologists use H&E-stained images as a gold standard to identify brain tumor type and grade. These diagnosis are based on the observation of tissue architecture observed by a pathologist. Looking at three important groups of brain tumors, the different features that are highlighted by



pathologist are described here :

Glioblastoma tumor, a WHO grade IV glial tumor, is identified by [319] :

- Coagulation necrosis or microvascular proliferation with thickened vascular walls due to increase in nuclei in vessel wall
- Hyper cellular with mitotic figures
- Pseudopalisading necrosis : tumor cells around necrotic zones.

Meningioma WHO grade I and II are identified by [320]:

- Lobulated architecture, often containing "meningothelial" whorls
- Syncytial cells with indistinct cell membranes
- Psammoma bodies
- Grade II have increased mitoses, cellularity and sheet-like growth pattern
- Grade II have areas of spontaneous necrosis

Metastasis, secondary brain tumor, revealed structures such as [321, 322]:

- Sharply demarcated from the surrounding brain
- Surrounding brain shows tissue depletion, neovascularization and gliosis
- Epithelial cells with discrete cell boundaries
- Dense vascular regions

Neuro-pathologic analysis happens ex-vivo and H&E staining is a long process, that takes several hours to days. In order to have a shorter processing time to produce an image, the label-free technique was explored. In this thesis two-photon microscopy was chosen to do the work. This method gives access to the autofluorescence of tissue but also to the diffuse signal of SHG from non-centrosymmetric structures.

The two-photon imaging technique was used on three cohorts, first to explore the possibility of it on a large scope of brain tumors, second to discriminate the grade of meningioma and thirdly to discriminate primary tumor glioblastoma and secondary metastasis tumor. In the **chapter 3**, GBM, metastasis and meningioma were imaged in a first exploratory study with a two-photon excitation. In the TPEF-SHG images, area presenting organization and structure close to the H&E standard were found. In the **chapter 4**, WHO grade I and WHO grade II of meningioma were studied and TPEF-SHG images were compared to gold standard H&E. The SHG signal highlighted the collagen whorls and psammoma, the sheet like architecture typical of grade II. In the **chapters 5 and 6**, primary and secondary brain tumor were discriminated using a two-photon microscope. The TPEF-SHG images in glioblastoma highlighted typical structures such as enlarged vessels walls (SHG) with surrounding dense cells (high TPEF intensity), and palisadic necrosis with circular-like intense regions in TPEF images. The metastasis features could also be precisely highlighted with SHG signal revealing the dense vascularity, and the cells architecture showing in the TPEF signal. These observations were convincing enough to imagine the possibility of a diagnosis derived directly from the two-photon images. In the literature on two-photon microscopy analysis of other cancer types, blind analysis directly on the TPEF images has already been performed [280–282], and these studies resulted in high accuracy of diagnosis. The same approach was used in the **chapter 5** to perform the first blind analysis on brain tumor TPEF-SHG images, and this resulted in an accuracy of 72% to discriminate tumor from healthy tissue. Tumor types were also differentiated one from another resulting in an accuracy of 80%. The factor limiting higher accuracy was the high rate of false positive 28% during this analysis. There were tissues that, based on the image, could not result in any diagnosis. The solution for improvement at this point was better training of the neuropathologist on the TPEF-SHG images as they are with the H&E images, using a larger cohort of tissue. Another approach presented in **chapter 5** proposes to use a deep-learning

## CHAPTER 7. DISCUSSION AND CONCLUSION

algorithm to transform the autofluorescence images in a virtual histological stained image that the neuropathologist could analyze with this already-known expertise.

Still, diagnosis based on a human judgement on an image presents high variability and often low reliability among different observers. Even the gold standard H&E analysis is subject to discrepancies. Pathological analysis and reports are still the crucial central core of an oncological diagnosis and choice of treatment course, making it a very sensitive point in the process and in need of high accuracy [323]. However the diagnosis of CNS disease is the most challenging even for the most experienced neuropathologist, and most especially in tumor diagnosis. A study was made to look at the accuracy of diagnosis based on H&E stain between two different observers. A second opinion was performed on 500 cases and a major diagnostic error was found in 25% of cases [324]. The Childhood Brain Tumor Consortium looked at another source of discrepancies in intra-observer reliability. Neuropathologists had to re-evaluate a large number of their cases sometime after the original, and it resulted in the same diagnosis in only 76% of cases [325]. The most errors were in the glioma subtype, a crucial point given that most adult brain tumors fall into the glioma category [323]. So even if H&E were to remain the gold standard, efforts should be done to improve diagnostic reliability, and strong challenges still remain in using such a subjective technique for diagnosis.

Even if the first direction was to improve the pathologist recall of diagnosis criteria and to regularly edit the database and classification of cancers, another direction taken was to use an additional quantitative indicator as an added method for diagnosis. Immuno-histochemistry (IHC) methods have appeared in the last two decades, as complementary to H&E-stained histology. These methods are used to precisely identify the tumor cell type/origin, and to quantify cell proliferation. They are even used to evaluate the boundary between tumor and the surrounding tissue using specific antibodies to target proteins involved in important tumor process [326]. IHC brought molecular information to the morphologic information provided by H&E-stained images to improve accuracy of neuropathologist diagnosis. However these tests require a second set of staining and so a longer process to arrive at a pathology report for the oncology team. We have seen before that two-photon imaging can provide morphologic information close to the H&E standard in few minutes or seconds. If this could be combined with an optical measure that provides molecular information, this would result in accurate discrimination using only one label-free technique that could be used in-vivo.

In the **chapter 4**, the grading of meningioma was explored and an IHC method, the Ki-67 proliferative index, was used to precisely assess the tumor grade. The spectral intensity of each tissue was compared to the proliferative index and a direct correlation was found between the two measurements, hinting that spectral response and more generally autofluorescence emission could translate molecular processes happening in tissue and give a precise quantification of the tissue nature. Based on that observation and knowledge of the molecules contributing to the spectral emission, quantitative studies were performed on brain tissue using optical microscopy methods to elaborate an automated discrimination method.

### 7.1.2 Quantitative measurements based on autofluorescence emission

#### 7.1.2.1 Redox ratio to monitor energetic metabolism

Two important cofactors of cellular energy metabolism are the NADH and FAD that can be present in the cells in oxidized form ( $\text{NAD}^+$ , FAD) or reduced form (NADH,  $\text{FADN}_2$ ), playing donor and acceptor in ATP formation [114, 327]. Glycolysis and oxidative phosphorylation are the

two main processes involved in energy metabolism. In the glycolysis process  $\text{NAD}^+$  is consumed to produce NADH, and in the mitochondria at the end of the process FAD is consumed to produce  $\text{FADN}_2$ . In the oxidative phosphorylation process to produce ATP, NADH is the main donor while FAD is the main electron and proton acceptor. Difference between healthy and tumor tissue is the equilibrium between these two energy producing reactions. It has been shown that tumor cells privilege glycolysis even in normal oxygen conditions, making NADH dominant compared to FAD [114, 116]. NADH and FAD are two molecules that can produce an autofluorescence signal when excited at suited wavelength. Because they are complementary molecules in the cell energy metabolism process, monitoring their fluorescence ratio will translate the state of metabolism in tissue. It can be deduced if the tissue is privileging a glycolysis or oxidative process and thus showing if the tissue is tumoral or healthy. Different ratios have been explored in the literature depending on the tissue explored and the setup used.

- $\text{FAD}/(\text{NADH}+\text{FAD})$  [328]
- $(\text{FAD}-\text{NADH})/(\text{FAD}+\text{NADH})$  [217]
- $\text{NADH}/\text{FAD}$  [329, 330]

The ratio with NADH at the denominator resulted in higher response in tumor than in healthy tissue [329, 330], translating a glycolysis dominant pathway in energy production in tumor. On the contrary, ratio with FAD in the denominator, resulted in lower response in tumor than healthy tissue [217, 328], translating of the reduced use of oxidation phosphorylation pathway to produce ATP.

In this thesis the redox ratio was used to discriminate the different brain tumor regions from healthy regions using different formula of the redox ratio. In **chapter 2**, fixed brain biopsies of different tumor types were studied under visible excitation (375 and 405nm) and the spectral response was measured. NADH and FAD contribution to the spectrum were extracted using a fitting algorithm, and the redox ratio was calculated using the equation  $(\text{FAD}-\text{NADH})/(\text{FAD}+\text{NADH})$ . All the tumor tissue resulted in a lower redox ratio than the one found in control tissue ( $p < 0.001$ ), which correlated with results in the literature [217]. However the types of tumor couldn't be discriminated from one another significantly. In **chapter 5**, a similar analysis was performed on fresh tissue to compare primary and secondary tumor to healthy tissue, and the  $\text{NADH}/\text{FAD}$  ratio was used to monitor the cellular metabolism. Control tissue had the lowest redox ratio, while secondary tumor and primary had the highest ratios and could be significantly discriminated from healthy tissue. These results are correlated to the hypothesis of a favored glycolysis pathway in tumor tissue, as already shown in the literature for other types of tumor [329, 330] and in rat brain tumor [117, 128].

Even if the redox ratio can highlight differences between tumor and healthy tissue and gives a significant discrimination in some cases, it is not reliable enough to be used alone as a definite discrimination tool in the operating room. Other parameters of fluorescence and molecular ratio have been quantified to be complementary to the metabolic response and bring more reliability to discrimination based on the intrinsic optical response.

### 7.1.2.2 Quantification of fiber organization

Collagen is one of the main proteins of the ECM in tissue, varying in types and structures. Collagen of type I and III are composed of triple-helical macromolecules that are non-centrosymmetric and result in a SHG signal [301]. This optical modality can consequently be used to monitor ECM organization in tissue and highlights changes due to cancer. In some major cancer types, systematic

## CHAPTER 7. DISCUSSION AND CONCLUSION

methods of quantification have been developed to quantify different cancer types [331]. Some teams have looked at the ratio between SHG collagen signal and fluorescence signal from elastic tissue, sometime called the SAAID (SHG-to-AF Aging Index of Dermis) value [331]. It is a method used in skin cancer for example to identify margins of basal cell carcinoma, with the highest SAAID value in tumor [332, 333]. In breast [285] and ovarian cancer [331], the orientation of fibers at tumor-stroma boundaries (TACS) was used to quantify and classify into three stages of tumor from early disease (TACS-1) to highly invasive tumor (TACS-3). Some teams also measured the organization of fiber using a Fourier transform method, for example in colonic cancer showing a certain organization in cancer tissue compared to random organization of healthy regions [334]. In other tumors, they only calculated the density of SHG pixels in the studied regions. With for example in renal fibrous, density and average value of SHG computed in three scores [283]. In the evaluation of neck margin in pancreatic cancer, pixel density of collagen was evaluated [284].

In brain tumors, collagen fiber structures are not as present as in other tumor types such as breast cancer or bladder cancer. The main groups showing significant SHG signals are the metastasis that developed dense vascular organization to migrate and also meningiomas that arise from dura matter in a region made of highly fibered organization. GBM could still result in more SHG signal than control due to the thickened vessels walls. From these observations, a quantitative indicator of SHG was used in the study of fresh biopsies from primary and secondary tumor. It was chosen to track the intensity of SHG and resulted in significant discrimination of the metastasis tissue. GBM in some cases gave a higher intensity, however it was not always significantly different than healthy tissue. In the literature, two studies looked closely at collagen fibrillar formation in glioma [335] especially GBM structures [336] and quantified the signal. In the first study they looked at TPEF-SHG images of glioma tissue compared to healthy cortex [335], and calculated the ratio of SHG pixels to overall pixels in each analyzed region. The ratio was higher in glioma than cortex tissue. This was explained by the fact that in cortex tissue the ECM has a special composition made up mostly of hyaluronic acid, and is usually devoid of the fibrillar proteins, such as collagen, usually found in the rest body [337]. However glioma are presented with collagen deposition in connective tissue and newly formed vessels, which will produce a stronger SHG signal. Another feature of GBM is the enlargement of vascular structures compared to normal tissue. A study showed that fibrillar structures will form in the vascular elements of GBM and quantify the formation using the ratio of SHG pixels to the number of TPEF pixels in the vascular region, finding non-zero values, and confirming that SHG could be a means to discriminate GBM based on its vascular formation [336].

### 7.1.2.3 Indicator of the molecular compositions

Using visible or two-photon NIR infrared excitation, another molecule that plays a role in cancer metabolism can be excited, the porphyrin. In a lot of tumor investigation, it has been shown that porphyrin will accumulate more in the tumoral tissue compared to healthy ones [128, 330]. This makes porphyrin an interesting tumoral marker. Teams have started to look at the ratio of NADH over porphyrin as another molecular indicator. In tumor, this ratio has been found to be lower, due to the higher accumulation of porphyrin compared to NADH. In **chapters 2 and 6** this indicator was measured on fixed tissues of primary and secondary tumor using visible and two-photon excitation. Tumor tissue showed a lower NADH/porphyrin ratio than the control tissues, concurring with the literature.

In this thesis we looked at other excitation ranges, such as the deep-UV, to be able to monitor more molecules emitting autofluorescence. These results are presented in the **chapter 6**. In the deep-UV range three new molecules could be excited: tyrosin, tryptophan, and collagen. These molecules were explored to find more reliable ratios or correlations between different molecules excited from DUV to NIR. This will possibly result in more reliable discriminations or a greater understanding of molecular interactions and metabolism in tumor tissue. In this study the tryptophan/collagen ratio has shown the best results for discriminating tissue. A non-fitting method, called clustering, was applied to the spectral map and it highlighted variations in the spectral response of the tryptophan/collagen ratio. This ratio was also calculated using a fitting method and a statistical analysis between primary and secondary tumor. The tryptophan/collagen ratio was higher in tumor than control ( $p < 0,01$ ), which is in correlation with the studied literature [305].

Using a non-fitting method such as spectral cluster analysis is an interesting and powerful method to reach automated diagnosis, that will be based on an artificial intelligence rather than a human judgement. This technique has shown a growing development, in infrared spectroscopy techniques, such as Raman and FT-IR [338, 339], applied to tumor tissue discrimination. Studies presented results with unsupervised and automated algorithms, based on spectral lap clustering, even more precise than histology in some cases to identify presence of tumor, highlighting also inhomogeneity in the tumor regions [308]. In our work, the possibility to apply the cluster to DUV-visible autofluorescence spectroscopy was demonstrated. The automated algorithms developed in infrared spectroscopy, could consequently be now transferred to the DUV-visible spectroscopy to obtained also unsupervised discrimination with 2D representation.

#### 7.1.2.4 Fluorescence lifetime

Spectral measurements have provided interesting indicators to discriminate tumoral from healthy tissue. However, it has often failed to discriminate between tumor types, limiting the reliability and specificity of this method. Another problem is the difficulty of separating the response at a molecular level due to the spectral overlap between the fluorescence emission of each of the molecules. Molecules like NADH can be presented in two forms in tissue, free or bound to a protein, and the spectral emission of each form is only separated by 20nm, making it difficult to separate them spectrally [114]. Finally, spectral measurements are strongly dependent of the concentration of fluorophores, and regions with a low density of tumor cells failed to give a significant discrimination.

To improve these results and to take advantage of all the possibilities of autofluorescence, another parameter, the fluorescence lifetime, was tracked in a different study. This measure is independent from the concentration of fluorophore but is mainly dependent on the fluorophore microenvironment: pH, temperature, concentrations of ions and oxygen, binding to other molecules or conformation [114]. Combining this method with spectral measurements could offer a powerful tool to study tissue nature. Table 7.1, illustrates the obtained results using fluorescence lifetime to discriminate brain tissue types.

On fresh tissue, using either one or two-photon excitation, the fluorescence lifetimes of NADH, FAD, and porphyrin at 405nm, or their average two-photon lifetimes at 890 nm, were always lower in tumor than in healthy tissue. Higher grades of meningioma also presented a lower fluorescence lifetimes, leading to the assumption that the more aggressive is the tumor, the lower is the fluorescence lifetime.

The results tracking the NADH component showed a decrease in tumor tissue. This decrease could be related to the different forms of NADH, which presents different lifetime values, 0.3 ns for

Compared tissue	tissue state	$\tau_{NADH}$ 405nm	$\tau_{FAD}$ 405nm	$\tau_{Pph}$ 405nm	$\tau_{avg}$ 890nm
<b>Control to Primary Glioma</b>	fresh	$\searrow$	$\searrow$	$\searrow$	$\searrow$
	fixed	$\approx$		$\searrow$	$\nearrow$
<b>Control to Secondary Meta</b>	fresh	$\searrow$	$\searrow$	$\approx$	$\searrow$
	fixed			$\searrow$	$\nearrow$
<b>Primary G to Secondary M</b>	fresh	$\searrow$	$\approx$	$\searrow$	$\searrow$
	fixed				$\nearrow$
<b>Control to Meningioma</b>	fresh	$\searrow$	$\searrow$	$\searrow$	
	fixed				
<b>Meningioma GI to Meningioma GII</b>	fresh				
	fixed	$\searrow$	$\searrow$	$\searrow$	

Table 7.1 – Summary of the fluorescence lifetime results for the different brain tissue discrimination studied in this thesis.  $\searrow$  : decrease ,  $\nearrow$  : increase ,  $\approx$  : same order in lifetime value.

the free form and 1.8 for the bound form [114]. Free NADH is localized in the cytosol and plays a major role in the glycolysis process, while the bound form is localized in mitochondria and is an actor in oxidative phosphorylation [114, 340]. It has been explained previously that tumor tend to favor a glycolysis state, resulting in more abundant free NADH and therefore shorter lifetimes.

It could be possible to monitor metabolic state by studying the fluorescence lifetime of free and bound form of molecules. To exploit the free-bound fraction of NADH in fluorescence lifetime, more graphical analysis methods have been developed. The lifetime results presented until this point have been extracted with a bi-exponential fitting method. However a non-fitting method has been developed and provides direct graphical results of the free/bound fraction of NADH or FAD. This method is called the phasor FLIM [133, 310, 341].

This method was implemented in the study described in **chapter 6** of my thesis, looking at the discrimination between primary and secondary fixed brain tumor tissues. The phasor plot showed five distinct regions in the pixel analysis that were associated with different colors and re-projected on false-color images. From that color criteria were used to separate tumor from healthy region. This method showed a high accuracy in separating tumoral from healthy tissue, however was not specific enough to differentiate primary from secondary tumor. To improve the accuracy of phasor plot analysis and to take advantage of its graphical representation, teams have developed a method to easily access the free-bound fraction of NADH [341]. This technique can also be applied to the measurements of the free-bound FAD fraction and is currently under development in the lab for further tissue studies.

### 7.1.3 From multimodal detection to automated algorithms

In the literature, studies based on fluorescence spectroscopy or fluorescence lifetime have been able to highlight some discrimination [105, 130, 131, 332, 342]. Combining these two modalities improves significantly the sensitivity and specificity of a discriminative algorithm, as shown, for example, by Butte et al. [252]. See table 7.2.

Other teams have tried using multi-contrast techniques for discriminating the nature brain tissue in order to improve the accuracy of their discriminative algorithm. Using a multi-contrast

## 7.1. AUTOFLUORESCENCE AS A DIAGNOSIS TOOL

		Meningioma	Normal Dura	Normal Cortex
		N=75	N=17	N=5
Spectral values only	Sensitivity	61%	65%	100%
	Specificity	73%	66%	98%
Time resolved values only	Sensitivity	84%	77%	100%
	Specificity	100%	91%	90%
Spectra+time-resolved values	Sensitivity	89%	100%	100%
	Specificity	100%	91%	99%

Table 7.2 – Comparison of discrimination algorithm on a study of meningioma and dura matter [252]

approach based on reflectance and spectral analysis, Lin et al. performed a pilot clinical trial on 26 brain tumor patients [124]. two excitation wavelengths of 460nm and 620nm, and built a two-steps algorithm combining the fluorescence emission and the reflectance at each excitation wavelength. This algorithm gave a sensitivity of 100% and a specificity of 76% between glioma infiltrative margin and normal brain tumor [124]. Toms et al. tried two modality of discrimination using 337nm excitation wavelength [125]. For glioma solid tumor regions compared to healthy cortex they obtained a sensitivity of 80% and specificity of 89%, and for glioma infiltrative regions, a sensitivity of 94% and specificity of 93% [125]. This method gave promising results but wasn't able to produce the same performance as the combination of spectroscopy and lifetime measurements shown previously.

In this thesis, the approach of spectral and lifetime measurements was chosen to discriminate tissue. In the **chapters 2, 3 and 4**, it was shown that each technique was able to give discrimination on fixed and fresh tissue with statistical significance. The first multimodal algorithm for tissue discrimination was tried in the **chapter 5**, where freshly extracted biopsies of primary and secondary brain tumor were observed using two-photon excitation, and combining spectral, fluorescence lifetime and SHG signals. A 3D representation combining the redox ratio, the SHG intensity and average lifetime gave a clear distinction between healthy tissue, primary tumor and secondary tumor. In **chapter 5**, a large cohort of fixed brain tumor tissue was accessible and an algorithm developed using multi-range and multi-modal analysis from deep-UV to NIR. The results are summarized in table 7.3.

Our results showed that the multi-modal algorithm combining spectral and fluorescence lifetime provided the best accuracy, higher than 98%. It was then tried a multi-modal and multi-range algorithm that combined NIR previous indicator to a molecular ratio in the DUV excitation range. This resulted in a similar 98% accuracy, which confirmed our results using two-photon excitation, but did not improve it.

In the development of a discriminative algorithm, several stages are necessary to reach clinical use. First is the training phase where the discriminative thresholds are determined. This were done in the various chapters of this thesis, where thresholds have been tested using different algorithms.

	Spectral only (275nm)	Spectral only (810- 890nm)	Spectral- lifetime(810 and 890nm)	Spectral- lifetime(275, 810 and 890nm)
<b>Sensitivity</b>	90%	92%	97%	
<b>Specificity</b>	73%	95%	100%	
<b>Overlap</b>				1,8%

Table 7.3 – Different algorithm tried on fixed tissue for discrimination between primary and secondary brain tumor in **chapter 5**.

Second, the test phase, where the thresholds have to be tested on a larger cohort. This stage is a continuing part of the work of this study. Next, the algorithms have to be automated and implemented in a measuring tool, which will lead to the stage of clinical trials. A prototype is under development in my research team in order to reach *in vivo* test. The last phase during these tests will be algorithm optimization to achieve the most reliable tool and certification for clinical use.

## 7.2 Optical development towards an intra-operative endomicroscope

### 7.2.1 First bi-modal non linear endomicroscope

I have had the opportunity to conduct my research project in a dynamic team, around an idea that has received substantial financial support. Several PhD candidates and interns were involved with the project before and during my PhD, giving me the possibility to participate to their work in order to be able to take part in all the different aspects of such a large project. When I started my PhD at the lab, the development of the two-photon endomicroscope had already started. The architecture of the first prototype had been chosen and put in place in a lab setting. See figure 7.1.

The chosen architecture was a pulsed MaiTai laser tunable from 690 to 1040nm. A pre-compensation unit was used at the output of the laser. The unit was made of a 50cm SMF fiber and a GRISM line [195]. A 2 m DCF fiber was used to excite tissue using a GRIN lens as an objective. The emitted fluorescence was collected by the same GRIN and DCF fiber to be sent into a spectrometer for this first prototype. The first endomicroscope prototype provides bi-modal spectral and lifetime detection. However the final goal is to add to it two PMTs to image fluorescence and SHG signal.

Using this setup two studies were performed previously to my PhD. In the first one various commercially available DCF's were tested and compared to determine if one of them might be suited for two-photon excitation and detection at the same time [196]. In the second study the collection capacities were further tested looking at the resolution obtained combining the fiber to



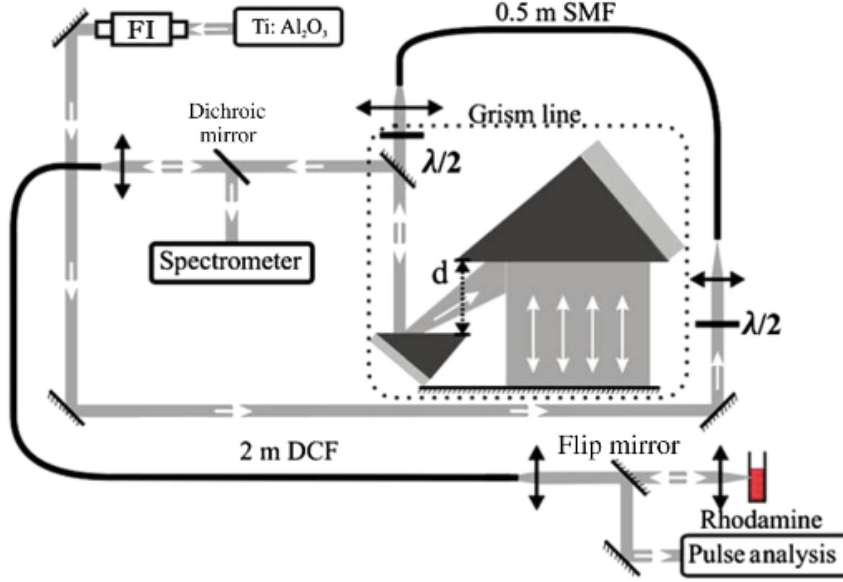


Figure 7.1 – Set-up of the first developed two-photon endoscope [196].

different GRIN lenses [197]. The tested fibers were three step-index DCF's (Fibercore, Liekki, Nufern) and one micro-structured DCF (Crystal Fiber). Measured optical characteristics using 800nm excitation wavelength were summarized in table 7.4.

The comparison showed that the micro-structured Crystal Fiber gave the best features at the excitation, with the shortest pulse to date in the literature (24 fs) and a very good average power (50mW) for exciting tissues [196]. The Crystal Fiber DCF was also characterized at the collection using various GRIN lenses and showed poorer lateral resolution compared to other fibers [197]. The better performances of the Crystal Fiber were due to the high NA of the inner cladding, which is needed for two-photon detection [196], where its poorer lateral resolution was due to a too large core diameter,  $16\mu\text{m}$ . The Crystal Fiber is also the most expensive of the four fibers, which is a drawback for its prospective use in clinical settings [197]. These two studies showed that an adequate fiber did not yet exist, but that it should ideally have a configuration close to the Crystal Fiber DCF with a smaller core diameter. To achieve that, a collaboration was put in place with the group of Alexandre Kudlinsky (PHLAM, UMR8523, Lille) to build a customized DC-PCF. The characteristics of such fiber are detailed below :

- Micro-structured crystal fiber : hole-to-hole spacing and hole diameter respectively  $3.5\mu\text{m}$  and  $0.41\mu\text{m}$ .
- Central core diameter =  $6.4\mu\text{m}$  (single-mode at 800 nm), NA core (800 nm) = 0.097
- NA inner cladding (450nm) = 0.27

During my PhD, I participated in the work of the team post-doc on the characterization of the customized DC-PCF in the endomicroscope setup. Two papers were published and are presented in **appendix A and B**.

In the first study, **appendix A**, five meters of this new DC-PCF fiber were placed in the two-

## CHAPTER 7. DISCUSSION AND CONCLUSION

Manufacturer	Core-Inner cladding $\emptyset$ ( $\mu\text{m}$ )	Core-Inner cladding NA	Pulse dura- tion(fs)	Average power(mW)- Pulse energy(nJ)
<b>Fibercore</b>	3,6 - 100	0,19 - 0,25	40	9 - 0,11
<b>Liekki</b>	5,5 - 125	0,15 - 0,46	37	5 - 0,06
<b>Crystal Fiber</b>	16 - 163	0,04 - 0,64	24	50 - 0,14
<b>Nufern</b>	9 - 105	0,12 - 0,2	31	11 - 0,14

Table 7.4 – Comparison of pulses characteristics at the output of four commercial DCF using a 800nm excitation wavelength with the first bi-modal endomicroscope prototype [196].

photon endomicroscope setup. The same characterization as for the commercial fibers was applied to be able to compare the results and reach some conclusions on the performance of this custom made one. Measurements were performed using two laser pulse durations, 100 and 300 fs, with an excitation wavelength from 750 to 900nm. At a preferred wavelength of 800nm the endoscope was able to produce 33 fs pulse duration, at the output of a five meter of DC-PCF, without any objective lens, and 40fs using a GRIN lens. Over the entire range of excitation wavelength, the pulse was under 60 fs at the fiber output. The customized DC-PCF gave a better simulated lateral resolution (0.58  $\mu\text{m}$  with a GRIN) than the most-suited commercial fibers. Using very short pulses to excite fluorophores resulted in a higher collection efficiency. These results met all the specifications defined as having the best excitation-collection performance in a two-photon configuration. These results answered all the specifications defined to have the best excitation-collection performance in a two-photon configuration.

To detail the high collection efficiency of such a fiber, a second study was conducted where the DC-PCF was placed in the visible endoscope used in **chapter 2 and 3** and compared to the bi-fiber configuration and to a multimode commercial configuration. The results are presented in **appendix B**. Moreover, in this study, the first spectral and lifetime measurements on tissue using this custom-made fiber with visible excitation were presented. The use of the DC-PCF in the endoscopic configuration showed collection efficiency four times better than the two other configurations. This result is due to the small core, 6.4  $\mu\text{m}$ , allowing excitation in a small focal volume and the large clad, allowing optimal collection of emitted fluorescence.

Using this setup, quantitative measurements were performed on the exogenous fluorophores, fluorescein and rhodamine B, then on brain freshly extracted ex-vivo tissues. Lower fluorescence intensity was found in tumor tissue with a different spectral shape for each group. The lifetime values of each fluorophore were also shorter in tumor than control. This result showed that our custom DC-PCF was the best candidate to optimize autofluorescence collection. Moreover it was also shown that the combination of fluorescence intensity, spectral width and fluorescence lifetime could give a reliable discrimination between tumor and healthy region.

### 7.2.2 Position and improvement of our set-up compared to two-photon endomicroscopy state of the art

In the literature, few studies presenting the architecture of an endomicroscope based on a DCF fiber can be found. Two groups have developed endomicroscopes based on the commercial fibers mentioned earlier. Fu et al. developed a two-photon endomicroscope based on the Crystal Fiber DCF [190]. They used 1 m of fiber to send 80 fs pulse at the output of a MaiTai laser at 800 nm to a sample. They found a 6  $\mu\text{m}$  axial resolution and approximately 1  $\mu\text{m}$  lateral resolution. Collection efficiency was improved compared to a SMF, but not compared to other commercially available DCF's. They were able to perform TPEF-SHG imaging using a MEMS as a scanning system and this endomicroscope was then used in *in vitro* studies on cancerous cells [343] and on mice with gastrointestinal abnormalities [180, 344]. Chang et al. developed an endomicroscope with the Liekki DCF to perform FCS measurement [345]. Comparing the DCF to a SMF, they found increased collection and better resolution. This endomicroscope until that time had been tested only on cytometry measurements *in vitro* and *in vivo* in mice [346]. Two other groups took the same direction as we did and based their development on a customized DCF. Liang et al. used a customized DCF and compared it to the Nufern and Fibercore commercial DCFs [347]. They used 75cm of DCF with a core diameter of 5  $\mu\text{m}$ , a core NA of 0,12 and an inner cladding NA of 0,35. They obtained a lateral resolution of 0,7  $\mu\text{m}$  and an axial resolution of 6,5  $\mu\text{m}$ . Compared to the other DCF, they found an improved two-photon excitation and collection efficiency, and a reduced fiber background noise. In this prototype they used a piezoelectric system to scan the sample and obtained TPEF-SHG images. They also calculated the redox ratio in order to have a quantitative indicator. The endomicroscope has been tested only on samples of *ex vivo* mouse liver and *in vivo* experiments have been done on anesthetized mouse kidney. Ducourthial et al. also developed an endomicroscope using a customized DC-PCF from the PhLAM laboratory, but with a different architecture than ours. The fiber used in their set-up has an inner core of 3,5  $\mu\text{m}$  diameter and 0,13 NA at 800 nm and a microstructure to maintain polarization. They used 5 m of this fiber with a GRISM pre-compensation unit to obtain a 38 fs pulse at the output with 800nm excitation. Their endomicroscope had transverse and axial resolutions respectively of 0,8  $\mu\text{m}$  and 12  $\mu\text{m}$ . The system was tested on *ex vivo* and *in vivo* on the kidney of an anesthetized mouse.

With our configuration we obtained better lateral and axial resolution than in the literature, with an improved collection efficiency compared to the commercial DCF. Compared to literature we also: 1) implemented and presented a multimodality of detection to obtained more reliable and reproducible discrimination. 2) Build an optical database on brain tissue autofluorescence response, that will be implemented in the endomicroscope. And 3) reached a miniaturization suited to slide the probe into existing clinical tools. Another advantages is the use of a 5-meter long fiber. Only one other group used this length. Other fibers were 1 meter long or less, which is not suitable to fit in the operating room environment. The teams using short fibers did not assess the pulse duration at the output, which in our study appeared to be an important factor for improving the excitation and collection efficiency. However using sub-100fs pulses is uncommon compared to classical two-photon microscopy configurations that generally use pulses of 100 fs or more. There is therefore only little knowledge of the impact of this ultra-short pulses on a biological material, such as animal or human tissue. One study can be found in the literature looking at the impact of pulse duration between 15 and 400 fs on human skin excised tissue [348]. The study first showed as in our study that shorter pulses resulted in higher TPEF and SHG emitted signal. Then the study looked at the tissue autofluorescence response using sub-20fs pulses and 120fs pulses at different

penetration depths. They didn't find any distortion in the spectral response using sub-20fs pulses. This ultra short pulses, on the contrary, resulted in a higher intensity and penetration depth for both the SHG and TPEF response, improving the quality of detected signal [348]. Even if this study seems to hint that sub-20 fs will not have a negative impact on tissue and will result in a better TPEF-SHG response, this still a very limited study and some other parameters should be evaluated. For instance, no measurements were made on the photobleaching that could be induced with such pulses, neither on the local temperature changes. In order to confirm the clinical applicability of our designed endomicroscope, a study was conducted with the post-doc of the group on brain biopsy tissue monitoring the spectral response and the fluorescence lifetime to evaluate the position and negative effect of these interesting short pulse for clinical applications. The endomicroscope was used to excite ex-vivo fixed samples from 40 to 200 fs, and the spectral and fluorescence lifetime responses were evaluated. The spectral measurements resulted in similar conclusions as in the literature. Shorter pulses improved 8 times the collected intensity but did not affect the spectral shape. Fluorescence lifetime detection acted as a probe of any environmental changes, such as temperature, viscosity and broken molecular links. The lifetime results were not affected by the sub-100 fs pulses, revealing that no local damage was done to the tissue with these shorter pulses.

As of this point we have developed a bi-modal endoscope able to perform two-photon excitation with collection efficiency and without causing any tissue damage. The next step for the instrument development is to implement a scanning system in order to combine spatial response with quantitative measurements and to offer a known and comfortable modality to surgeons. Two types of scanning systems have been favored in the literature for implementation in endomicroscopes. These are the piezoelectric system [347] and the MEMS [190]. The PZT systems have been able to reach smaller probe diameter [203, 347]. However the algorithms to reconstruct the images and the overall stability of the system is better using MEMS, making it an interesting choice too [190]. We have been working at first on a piezoelectric solution to reach a miniaturization of the probe to under 2mm of diameter, a size not available in a MEMS probe. However MEMS have recently been used in a millimetric-diameter OCT probe [349], opening the door to a collaboration in order to adapt this technology into a two-photon endomicroscope probe. This solution would offer more stability than a piezo probe and a more accessible computing system. The two configurations are currently being developed in the group. The scanning system remains a technological barrier to overcome. This step requires overcoming several technical challenges: miniaturization, speed, and a large field of view, all in order to provide synchronized images in a multimodal instrument.

### 7.3 Towards other problematics : the bladder cancer

Our method and resulting technology are not limited to answering questions on brain tumor tissue. This is a universal technology that could address the differing expectations of surgeons and solve issues such as lack of micro-scale resolution, slow acquisition time, and reliability of intra-operative feedback. Taking a step back from the problem of brain tumor discrimination, the area of bladder tumor surgery also presents intra-operative challenges that could improve the quality of patient management. The surgeons need to evaluate the grade of the tumor to understand how it has infiltrated the bladder tissues and to choose the appropriate surgical protocol. Getting this information in real-time during the first surgery, will shorten patient management time and improved surgical outcomes.

### 7.3. TOWARDS OTHER PROBLEMATICS : THE BLADDER...

Miniature intraoperative tools going through the urinary tract have already been developed to give surgeons a method of assessing tumor nature before the surgical intervention. One endomicroscopy technique has made it beyond the exploratory phase, is currently nearing completion of clinical validation, and will start to be implemented in a multi-center study. It is confocal laser endomicroscopy (CLE) using fluorescein as a contrast agent [350].

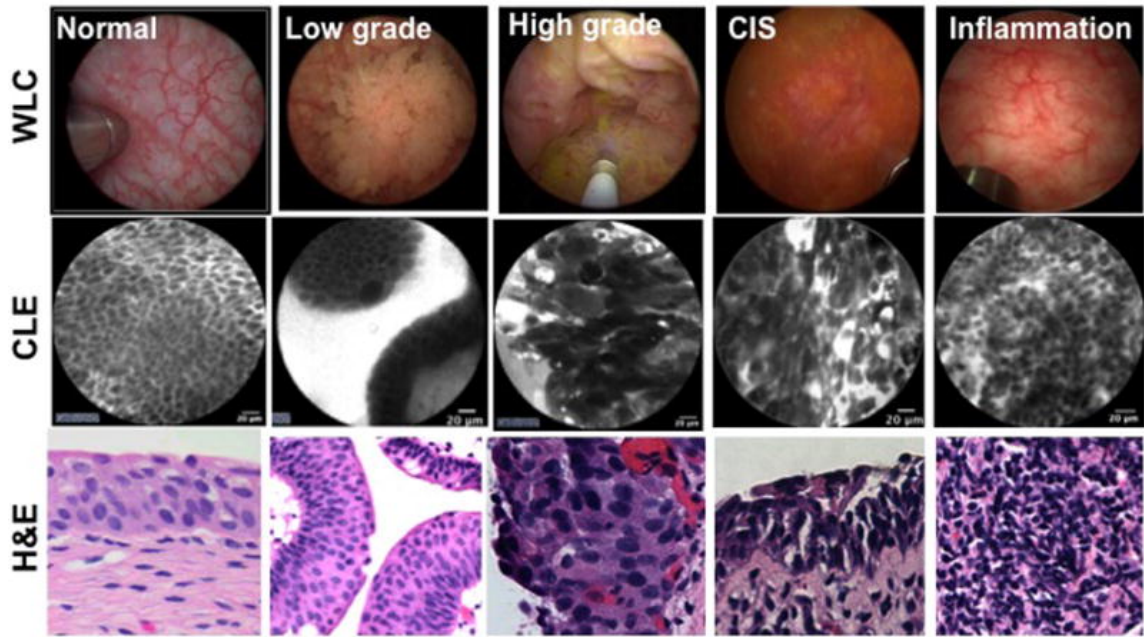


Figure 7.2 – Optical biopsy of bladder mucosa using probe-based confocal laser endomicroscopy (CLE). CLE of normal, low/high grade papillary bladder cancer, CIS, and inflammation shown with corresponding white light cystoscopy (WLC) and hematoxylin and eosin (HE) staining of the biopsy [351].

This technique has been used to provide images showing structures similar to the ones used in H&E-stained images as shown in figure 7.2. Basing a diagnosis on an imaging modality is relatively subjective. In order to make it a standard, as reliable as possible, an atlas of the diagnostic features for normal, benign, and cancerous tissue has been presented in the literature [352]. Still this technique showed some limitations : 1) The contrasts until now have been obtained with exogenous contrast agents, introducing bias and requiring ethics committee approvals; and 2) there is only one detection contrast, resulting in low reliability and reducing the possibility of automated diagnosis. In order to address the first limitation of CLE, an optical technique based on intrinsic optical signal, the OCT, has been developed and used intra-operatively in bladder cancer evaluation. Nevertheless this technique still provides only an imaging technique and consequently lacks the possibility of an automated diagnosis. Moreover the image provided by OCT requires an expert to be interpreted.

At the exploratory stage, few studies can be found using label-free microscopy techniques with quantitative detection [217, 222, 353]. Aboumarzouk et al. used a visible excitation to perform spectral measurements on bladder tissue [353]. They tried three quantitative indicators to dis-

## CHAPTER 7. DISCUSSION AND CONCLUSION

criminate malignant regions from benign ones: the area under the fluorescence intensity curve, the mean emission wavelength, and the ratio between emitted porphyrin and NADH intensity. The means emission wavelengths and porphyrin/NADH ratio gave the most significant discrimination. The ratio was higher in malignant tissue supporting the idea of porphyrin accumulation in tumor. Palmer et al., in another study, used UV excitation to look at the NADH and FAD spectral response and NIR excitation to monitor the porphyrin. Two indicators were computed to discriminate tissue, the redox ratio (NADH/FAD) and the NADH/porphyrin ratio [222]. They found a higher NADH/porphyrin ratio in tumor, a result agreeing with the previous study in literature. They also showed discrimination with the redox ratio but with an opposite trend than in other studies.

The study used various excitation wavelengths to determine three quantitative indicators: the SAAID ratio to look at the density of SHG signal compared to the autofluorescence, the redox ratio (FAD-NADH/FAD+NADH) and the lifetime measurement of free-bound fraction of NADH and FAD. Each of these indicators resulted in a discrimination between healthy mucosa and carcinoma in situ tumor.

These few studies demonstrated that optical endomicroscopy could be applied to bladder tissue discrimination. We therefore decided to test the acquisition and analysis methods developed on brain tumor to bladder tissue discrimination, in order to test the power and robustness of such techniques. The first explorative study designed, was set to answer the clinical question of grade identification among healthy tissue, low grade and high grade bladder tumors. The results obtained with a two-photon microscope are presented in **appendix C**.

A cohort of sixteen biopsies was explored and composed of five low grade, five high grade urothelial carcinoma and six non-tumoral urothelium. The samples were examined under 870nm excitation wavelength using a two photon microscope. TPEF-SHG images were compared to the H&E standard. The organization of the urothelial cells were highlighted in the TPEF image and served as criteria of differentiation between grades, similar to the H&E standard. The SHG image gave access to the architecture of the stroma and the lamina propria, other important structures in the diagnosis of tumor type and grade in bladder. These findings and comparisons to the H&E stained images are presented in figure 7.3.

A quantitative analysis was also performed and combined with the spatial the spatial results. The spectral response and FLIM images were acquired, and the redox ratio and average lifetime were determined. The redox ratio was significantly higher in the healthy urothelium compared to tumor samples ( $p < 0.001$ ). Moreover, it was able to discriminate low grade from high grade tumors. The low grade has a significantly higher redox ratio ( $p = 0.002$ ) than high grade tumor. The second quantitative measurement was the average fluorescence lifetime, which translated the balance between free and bound FAD. The average lifetime was shorter in healthy tissue compared to tumor ( $p = 0.002$  and  $p < 0.001$ ), and the low grade had a shorter lifetime value than high grade ( $p < 0.001$ ). These results mean that the free FAD form was more prevalent in tumor tissue, which agrees with the findings of Cicci et al. in their analysis of CIS [217].

With this study, it was shown that the spatial and quantitative techniques developed using a two-photon excitation can be transferred to other types of cancer. These results opened a bit more the door to a clinical transfer of two-photon endomicroscopy, assuring the clinical relevance of such project.

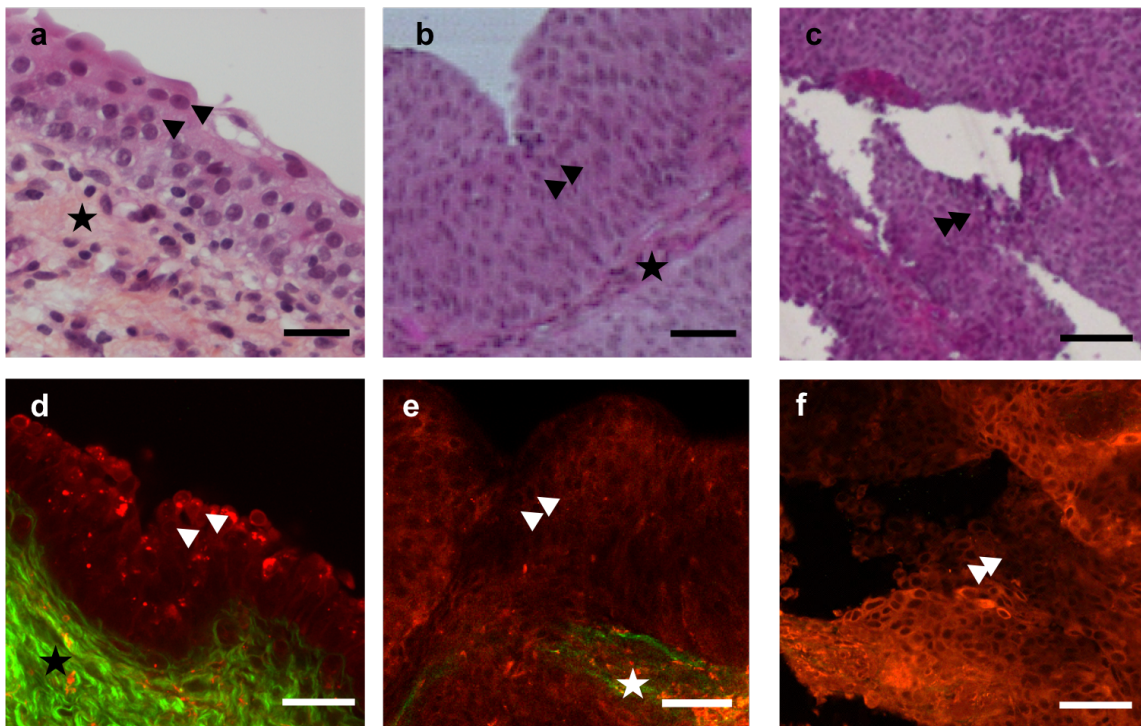


Figure 7.3 – Comparison between hematoxylin-eosin Safran staining (a-c) with two-photon fluorescence images at 870 nm excitation wavelength, red color for the fluorescence signal and green color for the SHG signal (d-f) of three tissue types: healthy (a, d), low-grade tumor (b, e) and high-grade tumor (c, f). Scale: 100  $\mu\text{m}$ . Star: Fibrovascular cores, arrow: Urothelial cells.

## 7.4 Conclusion

**Technical conclusion** This work presents the largest database, known to this day, on the autofluorescence response of brain tissue to answer the question of tumor demarcation. The database groups results into several brain tissue types : healthy cortex and dura matter, primary glioma and meningioma tumor and secondary metastasis tumor. The analysis contains measurements of 1) optical coefficients, 2) spectral response with one-photon, deep-UV and visible excitation and two-photon NIR excitation, 3) two-photon imaging of fluorescence, 4) results on SHG signal, and 5) fluorescence lifetime with one and two-photon excitation. These large sets of data multimodal algorithms were developed to find relevant thresholds and to highlight the possibility of providing reliable automated discrimination of brain tissue types. Combined with the technical developments achieved by the research team to develop a multimodal two-photon endomicroscope, clinical transfer can be considered and supported. Moreover such methods were also able to produce an answer on bladder tumor grading, showing the capacity to be a universal tool answering different surgical challenges. Multimodal two-photon endomicroscopy is presenting itself as a major technical breakthrough for intra-operative diagnosis.

## CHAPTER 7. DISCUSSION AND CONCLUSION

**Personnal conclusion** In this PhD, I was able to work in a strong multi- disciplinary environment. I discovered the interaction on a daily basis with a team of surgeons and neuropathologists to be a completely "other" type of science that requires adapting one's communication and to reach compromise in the team's work. Developing technology to improve medical imaging has to be based on strong collaboration with a hospital team. These collaborations are very enriching scientifically and push you to develop better communication skills, to work productively with people with different kinds of knowledge and scientific backgrounds. This collaborative work was extended to a third part, DISCO beamline, and started during my master's thesis. I was there from the start of the collaboration and was able to learn how to build a project with different parties, and make it into a successful collaboration using the different expertise of each person. Working on such a dynamic project, involving several parties and a large research team, gave me the opportunity to work on a large set of publications and to present my work in several international conferences even getting the chance to be awarded best student poster in a session of 2017 Photonic West conference.

This thesis was also built by overcoming difficulties, which was part of the learning process. One of the first difficulties was in collaborating with the hospital. The studies were based on biopsy sample imaging and it implies that several factors come together: surgery has to happen, the patient had to be contacted to sign a consent, and the sample had to be large enough to get a piece for research. All these requirements have made it difficult sometimes to have a dataset large enough for statistics in a short period of time. Working around these difficulties required finding solutions with the medical teams to optimize the process and the communication. The other major difficulties were with natural catastrophe. I had to face the consequences of two floods, slowing work, creating administrative challenge and difficulties in collaboration. However this is bound to happen in a long project and consequently developed capacity in project management.

In conclusion, this was a successful PhD thesis and a strong learning experience in a dynamic, experienced and very welcoming research team. I have truly committed to this project during these three years and I would like to continue working on it and be a part of those people who will bring it to the clinical setting as a regular tool.





# Bibliography

1. *Une campagne pour changer la représentation du cancer* fr. <http://www.e-sante.fr/campagne-pour-changer-representation-cancer/actualite/373> (2018).
2. Papavramidou, N., Papavramidis, T. & Demetriou, T. Ancient Greek and Greco-Roman Methods in Modern Surgical Treatment of Cancer. *Annals of Surgical Oncology* **17**, 665–667. ISSN: 1068-9265 (Mar. 2010).
3. Weiderpass, E. Lifestyle and cancer risk. eng. *Journal of Preventive Medicine and Public Health = Yebang Uihakhoe Chi* **43**, 459–471. ISSN: 1975-8375 (Nov. 2010).
4. *Qu'est-ce que le cancer? | Fondation contre le Cancer* <https://www.cancer.be/le-cancer/quest-ce-que-le-cancer> (2018).
5. *World cancer report* (eds Stewart, B. W., Kleihues, P. & for Research on Cancer, I. A.) OCLC: ocm52122625. ISBN: 978-92-832-0411-4 (IARC Press, Lyon, 2003).
6. *~QU'EST CE QUE LE CANCER ? QU'AFPECTE-T-IL ?~ - Le Lymphome de Hodgkin* <http://lymphomehodgkin.eklablog.com/qu-est-ce-que-le-cancer-qu-affecte-t-il-c29141044> (2018).
7. *WHO | Cancer* <http://www.who.int/mediacentre/factsheets/fs297/en/> (2018).
8. *Cancer Facts & Figures 2018 | American Cancer Society* en. <https://www.cancer.org/research/cancer-facts-statistics/all-cancer-facts-figures/cancer-facts-figures-2018.html> (2018).
9. *Brain Tumor Statistics | American Brain Tumor Association* <http://www.abta.org/about-us/news/brain-tumor-statistics/> (2018).
10. Spine, M. B. *Brain tumors: overview of types, diagnosis, treatment options | Cincinnati, OH Mayfield Brain & Spine* <http://www.mayfieldclinic.com/pe-braintumor.htm> (2018).
11. *Brain metastases - Symptoms and causes* en. <http://www.mayoclinic.org/diseases-conditions/brain-metastases/symptoms-causes/syc-20350136> (2018).
12. Giese, A., Bjerkvig, R., Berens, M. & Westphal, M. Cost of Migration: Invasion of Malignant Gliomas and Implications for Treatment. en. *Journal of Clinical Oncology* **21**, 1624–1636. ISSN: 0732-183X, 1527-7755 (Apr. 2003).
13. Ichimura, K., Narita, Y. & Hawkins, C. E. Diffusely infiltrating astrocytomas: pathology, molecular mechanisms and markers. en. *Acta Neuropathologica* **129**, 789–808. ISSN: 0001-6322, 1432-0533 (June 2015).

14. Rapalino, O., Batchelor, T. & González, R. G. en. in *Handbook of Clinical Neurology* 253–274 (Elsevier, 2016). ISBN: 978-0-444-53485-9. doi:10.1016/B978-0-444-53485-9.00014-3. <http://linkinghub.elsevier.com/retrieve/pii/B9780444534859000143> (2018).
15. Wesseling, P., Bent, M. v. d. & Perry, A. Oligodendroglioma: pathology, molecular mechanisms and markers. en. *Acta Neuropathologica* **129**, 809–827. ISSN: 0001-6322, 1432-0533 (June 2015).
16. Grimm, S. A. & Chamberlain, M. C. Anaplastic astrocytoma. en. *CNS Oncology* **5**, 145–157. ISSN: 2045-0907, 2045-0915 (July 2016).
17. Omuro, A. & DeAngelis, L. M. Glioblastoma and other malignant gliomas: a clinical review. eng. *JAMA* **310**, 1842–1850. ISSN: 1538-3598 (Nov. 2013).
18. Ellor, S. V., Pagano-Young, T. A. & Avgeropoulos, N. G. Glioblastoma: Background, Standard Treatment Paradigms, and Supportive Care Considerations. en. *The Journal of Law, Medicine & Ethics* **42**, 171–182. ISSN: 1073-1105, 1748-720X (July 2014).
19. Bauer, S., Wiest, R., Nolte, L.-P. & Reyes, M. A survey of MRI-based medical image analysis for brain tumor studies. *Physics in Medicine and Biology* **58**, R97–R129. ISSN: 0031-9155, 1361-6560 (July 2013).
20. Shapiro, W. R. & Shapiro, J. R. Biology and treatment of malignant glioma. eng. *Oncology (Williston Park, N.Y.)* **12**, 233–240; discussion 240, 246. ISSN: 0890-9091 (Feb. 1998).
21. Durand, A. *et al.* WHO grade II and III meningiomas: a study of prognostic factors. eng. *Journal of Neuro-Oncology* **95**, 367–375. ISSN: 1573-7373 (Dec. 2009).
22. Bi, W. L. & Dunn, I. F. Current and emerging principles in surgery for meningioma. en. *Chinese Clinical Oncology* **6**. ISSN: 2304-3873. doi:10.21037/cco.v0i0.15463. <http://cco.amegroups.com/article/view/15463> (2018) (July 2017).
23. Langley, R. R. & Fidler, I. J. The Biology of Brain Metastasis. en. *Clinical Chemistry* **59**, 180–189. ISSN: 0009-9147, 1530-8561 (Jan. 2013).
24. Geiger, T. R. & Peeper, D. S. Metastasis mechanisms. en. *Biochimica et Biophysica Acta (BBA) - Reviews on Cancer* **1796**, 293–308. ISSN: 0304419X (Dec. 2009).
25. Preusser, M. *et al.* Brain metastases: pathobiology and emerging targeted therapies. eng. *Acta Neuropathologica* **123**, 205–222. ISSN: 1432-0533 (Feb. 2012).
26. Perkins, A. & Liu, G. Primary Brain Tumors in Adults: Diagnosis and Treatment. *American family physician* **93** (2016).
27. DeAngelis, L. M. Brain tumors. *New England Journal of Medicine* **344**, 114–123 (2001).
28. Chandana, S. R., Movva, S., Arora, M. & Singh, T. Primary brain tumors in adults. *American family physician* **77** (2008).
29. Jacobs, A. H. *et al.* Imaging in Neurooncology. *NeuroRx* **2**, 333–347. ISSN: 1545-5343 (Apr. 2005).
30. Zani, A., Biella, G. & Proverbio, A. M. en. in *The Cognitive Electrophysiology of Mind and Brain* 417–422 (Elsevier, 2003). ISBN: 978-0-12-775421-5. doi:10.1016/B978-012775421-5/50022-4. <http://linkinghub.elsevier.com/retrieve/pii/B9780127754215500224> (2018).

## BIBLIOGRAPHY

31. Holtrop, J. L. & Sutton, B. P. High spatial resolution diffusion weighted imaging on clinical 3 T MRI scanners using multislabs spiral acquisitions. *Journal of Medical Imaging* **3**. ISSN: 2329-4302. doi:10.1117/1.JMI.3.2.023501. <https://www.ncbi.nlm.nih.gov/pmc/articles/PMC4828939/> (2018) (Apr. 2016).
32. Li, K.-L. *et al.* An improved coverage and spatial resolution-using dual injection dynamic contrast-enhanced (ICE-DICE) MRI: A novel dynamic contrast-enhanced technique for cerebral tumors. en. *Magnetic Resonance in Medicine* **68**, 452–462. ISSN: 07403194 (Aug. 2012).
33. Hu, J. *et al.* A high spatial resolution 1H magnetic resonance spectroscopic imaging technique for breast cancer with a short echo time. *Magnetic resonance imaging* **26**, 360–366. ISSN: 0730-725X (Apr. 2008).
34. Mabray, M. C., Barajas, R. F. & Cha, S. Modern Brain Tumor Imaging. *Brain Tumor Research and Treatment* **3**, 8–23. ISSN: 2288-2405 (Apr. 2015).
35. Hygino da Cruz, L. C., Vieira, I. G. & Domingues, R. C. Diffusion MR Imaging: An Important Tool in the Assessment of Brain Tumors. en. *Neuroimaging Clinics of North America* **21**, 27–49. ISSN: 10525149 (Feb. 2011).
36. *Role of Imaging in Brain Tumors* <http://www.medscape.org/viewarticle/776272> (2018).
37. Horská, A. & Barker, P. B. Imaging of Brain Tumors: MR Spectroscopy and Metabolic Imaging. *Neuroimaging clinics of North America* **20**, 293–310. ISSN: 1052-5149 (Aug. 2010).
38. *A history full of revolutions* en. Generic Template. <https://www.medmuseum.siemens.com/en/stories-from-the-museum/ct-history> (2018).
39. Wijdicks, E. F. M. The First CT Scan of the Brain: Entering the Neurologic Information Age. en. *Neurocritical Care*. ISSN: 1541-6933, 1556-0961. doi:10.1007/s12028-017-0495-3. <http://link.springer.com/10.1007/s12028-017-0495-3> (2018) (Dec. 2017).
40. Flohr, T. & Ohnesorge, B. en. in *Multi-slice and Dual-source CT in Cardiac Imaging* 41–69 (Springer Berlin Heidelberg, Berlin, Heidelberg, 2007). ISBN: 978-3-540-25523-9. doi:10.1007/978-3-540-49546-8\_3. [http://link.springer.com/10.1007/978-3-540-49546-8\\_3](http://link.springer.com/10.1007/978-3-540-49546-8_3) (2018).
41. Fink, J. R., Muzi, M., Peck, M. & Krohn, K. A. Continuing Education: Multi-modality Brain Tumor Imaging – MRI, PET, and PET/MRI. *Journal of nuclear medicine : official publication, Society of Nuclear Medicine* **56**, 1554–1561. ISSN: 0161-5505 (Oct. 2015).
42. Luiten, A. L. en. in *Magnetic Resonance Imaging* 1–7 (Springer Berlin Heidelberg, Berlin, Heidelberg, 1999). ISBN: 978-3-662-03802-4 978-3-662-03800-0. doi:10.1007/978-3-662-03800-0\_1. [http://link.springer.com/10.1007/978-3-662-03800-0\\_1](http://link.springer.com/10.1007/978-3-662-03800-0_1) (2018).
43. Drevelegas, A. & Papanikolaou, N. en. in *Imaging of Brain Tumors with Histological Correlations* (ed Drevelegas, A.) 13–33 (Springer Berlin Heidelberg, Berlin, Heidelberg, 2011). ISBN: 978-3-540-87648-9 978-3-540-87650-2. doi:10.1007/978-3-540-87650-2\_2. [http://link.springer.com/10.1007/978-3-540-87650-2\\_2](http://link.springer.com/10.1007/978-3-540-87650-2_2) (2018).
44. Mori, S. & Zhang, J. Principles of Diffusion Tensor Imaging and Its Applications to Basic Neuroscience Research. *Neuron* **51**, 527–539. ISSN: 0896-6273 (Sept. 2006).
45. Jahng, G.-H., Li, K.-L., Ostergaard, L. & Calamante, F. Perfusion Magnetic Resonance Imaging: A Comprehensive Update on Principles and Techniques. *Korean Journal of Radiology* **15**, 554–577. ISSN: 1229-6929 (2014).

46. Girouard, H. & Iadecola, C. Neurovascular coupling in the normal brain and in hypertension, stroke, and Alzheimer disease. eng. *Journal of Applied Physiology (Bethesda, Md.: 1985)* **100**, 328–335. ISSN: 8750-7587 (Jan. 2006).
47. Pak, R. W. *et al.* Implications of neurovascular uncoupling in functional magnetic resonance imaging (fMRI) of brain tumors. eng. *Journal of Cerebral Blood Flow and Metabolism: Official Journal of the International Society of Cerebral Blood Flow and Metabolism* **37**, 3475–3487. ISSN: 1559-7016 (Nov. 2017).
48. Berger, A. Positron emission tomography. *BMJ : British Medical Journal* **326**, 1449. ISSN: 0959-8138 (June 2003).
49. Salmon, E., Bernard Ir, C. & Hustinx, R. Pitfalls and Limitations of PET/CT in Brain Imaging. en. *Seminars in Nuclear Medicine* **45**, 541–551. ISSN: 00012998 (Nov. 2015).
50. Krieger, M. D., Chandrasoma, P. T., Zee, C.-S. & Apuzzo, M. L. J. Role of stereotactic biopsy in the diagnosis and management of brain tumors. en. *Seminars in Surgical Oncology* **14**, 13–25. ISSN: 1098-2388 (Jan. 1998).
51. Rahman, M., Murad, G. J. A. & Mocco, J. Early history of the stereotactic apparatus in neurosurgery. *Neurosurgical Focus* **27**, E12 (Sept. 2009).
52. *Frame and Frameless Stereotactic Brain Biopsy* en-US. Mar. 2015. <https://clinicalgate.com/frame-and-frameless-stereotactic-brain-biopsy/> (2018).
53. Brown, R. A. & Nelson, J. A. Invention of the N-localizer for stereotactic neurosurgery and its use in the Brown-Roberts-Wells stereotactic frame. eng. *Neurosurgery* **70**, 173–176. ISSN: 1524-4040 (June 2012).
54. Heper, A. O. *et al.* An analysis of stereotactic biopsy of brain tumors and nonneoplastic lesions: a prospective clinicopathologic study. en. *Surgical Neurology* **64**, S82–S88. ISSN: 00903019 (Nov. 2005).
55. Yuen, J. *et al.* A sequential comparison on the risk of haemorrhage with different sizes of biopsy needles for stereotactic brain biopsy. eng. *Stereotactic and Functional Neurosurgery* **92**, 160–169. ISSN: 1423-0372 (2014).
56. *How Neurosurgeons Perform a Stereotactic Brain Biopsy* en. <https://www.aans.org/> (2018).
57. Kreth, F. W. *et al.* The Risk of Haemorrhage after Image Guided Stereotactic Biopsy of Intra-Axial Brain Tumours – A Prospective Study. en. *Acta Neurochirurgica* **143**, 539–546. ISSN: 0001-6268, 0942-0940 (June 2001).
58. Ross, M. H. & Pawlina, W. *Histology: a text and atlas: with correlated cell and molecular biology* 5th ed. OCLC: ocm60516651. ISBN: 978-0-7817-5056-1 (Lippincott Williams & Wilkins, Baltimore, MD, 2006).
59. Titford, M. The long history of hematoxylin. en. *Biotechnic & Histochemistry* **80**, 73–78. ISSN: 1052-0295, 1473-7760 (Jan. 2005).
60. Chan, J. K. C. The Wonderful Colors of the Hematoxylin–Eosin Stain in Diagnostic Surgical Pathology. en. *International Journal of Surgical Pathology* **22**, 12–32. ISSN: 1066-8969, 1940-2465 (Feb. 2014).

## BIBLIOGRAPHY

61. Fischer, A. H., Jacobson, K. A., Rose, J. & Zeller, R. Hematoxylin and Eosin Staining of Tissue and Cell Sections. en. *Cold Spring Harbor Protocols* **2008**, pdb.prot4986–pdb.prot4986. ISSN: 1559-6095 (May 2008).
62. Ritz, S. HISTOLOGY AND TISSUE STAINING, 78.
63. Mitra, S., Kumar, M., Sharma, V. & Mukhopadhyay, D. Squash preparation: A reliable diagnostic tool in the intraoperative diagnosis of central nervous system tumors. *Journal of Cytology / Indian Academy of Cytologists* **27**, 81–85. ISSN: 0970-9371 (July 2010).
64. Lee, H. S. & Tihan, T. The Basics of Intraoperative Diagnosis in Neuropathology. en. *Surgical Pathology Clinics* **8**, 27–47. ISSN: 18759181 (Mar. 2015).
65. Ghosal, N., Hegde, A. S., Murthy, G. & Furtado, S. V. Smear preparation of intracranial lesions: A retrospective study of 306 cases. en. *Diagnostic Cytopathology* **39**, 582–592. ISSN: 87551039 (Aug. 2011).
66. Novis, D. A. & Zarbo, R. J. Interinstitutional comparison of frozen section turnaround time. A College of American Pathologists Q-Probes study of 32868 frozen sections in 700 hospitals. eng. *Archives of Pathology & Laboratory Medicine* **121**, 559–567. ISSN: 0003-9985 (June 1997).
67. Dikondwar, A. R. *et al.* Utility and challenges in intraoperative consultation of spinal lesions by crush smear cytology. *Asian Journal of Neurosurgery* **11**, 129–133. ISSN: 1793-5482 (2016).
68. Jaafar, H. Intra-Operative Frozen Section Consultation: Concepts, Applications and Limitations. *The Malaysian Journal of Medical Sciences : MJMS* **13**, 4–12. ISSN: 1394-195X (Jan. 2006).
69. DiNardo, L. J., Lin, J., Karageorge, L. S. & Powers, C. N. Accuracy, utility, and cost of frozen section margins in head and neck cancer surgery. eng. *The Laryngoscope* **110**, 1773–1776. ISSN: 0023-852X (Oct. 2000).
70. Chand, P., Amit, S., Gupta, R. & Agarwal, A. Errors, limitations, and pitfalls in the diagnosis of central and peripheral nervous system lesions in intraoperative cytology and frozen sections. *Journal of Cytology / Indian Academy of Cytologists* **33**, 93–97. ISSN: 0970-9371 (2016).
71. Watts, C. & Sanai, N. en. in *Handbook of Clinical Neurology* 51–69 (Elsevier, 2016). ISBN: 978-0-12-802997-8. doi:10.1016/B978-0-12-802997-8.00004-9. <http://linkinghub.elsevier.com/retrieve/pii/B9780128029978000049> (2018).
72. Shakarami, M., Suratgar, A. & Talebi, H. Estimation of intra-operative brain shift based on constrained Kalman filter. en. *ISA Transactions* **55**, 260–266. ISSN: 00190578 (Mar. 2015).
73. Reinges, M. H. T. *et al.* Course of brain shift during microsurgical resection of supratentorial cerebral lesions: limits of conventional neuronavigation. en. *Acta Neurochirurgica* **146**, 369–377. ISSN: 0001-6268, 0942-0940 (Apr. 2004).
74. Berger, M. S. & Hadjipanayis, C. G. SURGERY OF INTRINSIC CEREBRAL TUMORS. en. *Neurosurgery* **61**, SHC–279–SHC–305. ISSN: 0148-396X, 1524-4040 (July 2007).
75. Mandonnet, E., Winkler, P. A. & Duffau, H. Direct electrical stimulation as an input gate into brain functional networks: principles, advantages and limitations. en. *Acta Neurochirurgica* **152**, 185–193. ISSN: 0001-6268, 0942-0940 (Feb. 2010).
76. Pallud, J. & Dezamis, E. Functional and oncological outcomes following awake surgical resection using intraoperative cortico-subcortical functional mapping for supratentorial gliomas located in eloquent areas. en. *Neurochirurgie* **63**, 208–218. ISSN: 00283770 (June 2017).

77. TAMURA, M. *et al.* Strategy of Surgical Resection for Glioma Based on Intraoperative Functional Mapping and Monitoring. *Neurologia medico-chirurgica* **55**, 383–398. ISSN: 0470-8105 (May 2015).
78. Weidle, U. H., Niewöhner, J. & Tiefenthaler, G. The Blood–Brain Barrier Challenge for the Treatment of Brain Cancer, Secondary Brain Metastases, and Neurological Diseases. en. *Cancer Genomics - Proteomics* **12**, 167–177. ISSN: 1109-6535, 1790-6245 (Jan. 2015).
79. Rampling, R., James, A & Papanastassiou, V. THE PRESENT AND FUTURE MANAGEMENT OF MALIGNANT BRAIN TUMOURS: SURGERY, RADIOTHERAPY, CHEMOTHERAPY. *Journal of Neurology, Neurosurgery, and Psychiatry* **75**, ii24–ii30. ISSN: 0022-3050 (June 2004).
80. Vasefi, F., MacKinnon, N., Farkas, D. L. & Kateb, B. Review of the potential of optical technologies for cancer diagnosis in neurosurgery: a step toward intraoperative neurophotonics. *Neurophotonics* **4**. ISSN: 2329-423X. doi:10.1117/1.NPh.4.1.011010. <https://www.ncbi.nlm.nih.gov/pmc/articles/PMC5184765/> (2018) (Jan. 2017).
81. Lipson, A. C., Gargollo, P. C. & Black, P. M. Intraoperative magnetic resonance imaging: considerations for the operating room of the future. *Journal of Clinical Neuroscience* **8**, 305–310. ISSN: 0967-5868 (July 2001).
82. Kubben, P. L. *et al.* Intraoperative MRI-guided resection of glioblastoma multiforme: a systematic review. *The lancet oncology* **12**, 1062–1070 (2011).
83. Eljamel, M. S. & Mahboob, S. O. The effectiveness and cost-effectiveness of intraoperative imaging in high-grade glioma resection; a comparative review of intraoperative ALA, fluorescein, ultrasound and MRI. eng. *Photodiagnosis and Photodynamic Therapy* **16**, 35–43. ISSN: 1873-1597 (Dec. 2016).
84. Coburger, J. *et al.* Linear array ultrasound in low-grade glioma surgery: histology-based assessment of accuracy in comparison to conventional intraoperative ultrasound and intraoperative MRI. eng. *Acta Neurochirurgica* **157**, 195–206. ISSN: 0942-0940 (Feb. 2015).
85. Hall, W. A. & Truwit, C. L. Intraoperative MR-guided neurosurgery. en. *Journal of Magnetic Resonance Imaging* **27**, 368–375. ISSN: 10531807, 15222586 (Feb. 2008).
86. Garzon-Muvdi, T., Kut, C., Li, X. & Chaichana, K. L. Intraoperative imaging techniques for glioma surgery. en. *Future Oncology* **13**, 1731–1745. ISSN: 1479-6694, 1744-8301 (Aug. 2017).
87. Silas, A. M., Kruskal, J. B. & Kane, R. A. INTRAOPERATIVE ULTRASOUND. English. *Radiologic Clinics* **39**, 429–448. ISSN: 0033-8389, 1557-8275 (May 2001).
88. Petridis, A. K., Anokhin, M., Vavruska, J., Mahvash, M. & Scholz, M. The value of intraoperative sonography in low grade glioma surgery. en. *Clinical Neurology and Neurosurgery* **131**, 64–68. ISSN: 03038467 (Apr. 2015).
89. Gerganov, V. M., Samii, A., Giordano, M., Samii, M. & Fahlbusch, R. Two-dimensional high-end ultrasound imaging compared to intraoperative MRI during resection of low-grade gliomas. *Journal of Clinical Neuroscience* **18**, 669–673. ISSN: 0967-5868 (May 2011).
90. Belykh, E. *et al.* Intraoperative Fluorescence Imaging for Personalized Brain Tumor Resection: Current State and Future Directions. *Frontiers in Surgery* **3**. ISSN: 2296-875X. doi:10.3389/fsurg.2016.00055. <https://www.ncbi.nlm.nih.gov/pmc/articles/PMC5066076/> (2018) (Oct. 2016).

## BIBLIOGRAPHY

91. Behbahaniinia, M. *et al.* Intraoperative fluorescent imaging of intracranial tumors: A review. *Clinical Neurology and Neurosurgery* **115**, 517–528. ISSN: 0303-8467 (May 2013).
92. Moore, G. E. & Peyton, W. T. The clinical use of fluorescein in neurosurgery; the localization of brain tumors. eng. *Journal of Neurosurgery* **5**, 392–398. ISSN: 0022-3085 (July 1948).
93. Luscan, R. ICG cine-angiography demonstrates choroidal reperfusion after vortex vein occlusion in AMD. eng. *Journal Francais D’ophtalmologie* **38**, e131. ISSN: 1773-0597 (June 2015).
94. Saito, M. *et al.* Quantitative Blood Flow Assessment by Multiparameter Analysis of Indocyanine Green Video Angiography. English. *World Neurosurgery* **0**. ISSN: 1878-8750. doi:10.1016/j.wneu.2018.04.148. [https://www.worldneurosurgery.org/article/S1878-8750\(18\)30868-4/fulltext](https://www.worldneurosurgery.org/article/S1878-8750(18)30868-4/fulltext) (2018) (May 2018).
95. Degett, T. H., Andersen, H. S. & Gögenur, I. Indocyanine green fluorescence angiography for intraoperative assessment of gastrointestinal anastomotic perfusion: a systematic review of clinical trials. eng. *Langenbeck’s Archives of Surgery* **401**, 767–775. ISSN: 1435-2451 (Sept. 2016).
96. Eyüpoglu, I. Y. *et al.* Intraoperative vascular DIVA surgery reveals angiogenic hotspots in tumor zones of malignant gliomas. eng. *Scientific Reports* **5**, 7958. ISSN: 2045-2322 (Jan. 2015).
97. Liu, J. T., Meza, D. & Sanai, N. Trends in Fluorescence Image-guided Surgery for Gliomas. *Neurosurgery* **75**, 61–71. ISSN: 0148-396X (July 2014).
98. Stummer, W. *et al.* Intraoperative detection of malignant gliomas by 5-aminolevulinic acid-induced porphyrin fluorescence. eng. *Neurosurgery* **42**, 518–525; discussion 525–526. ISSN: 0148-396X (Mar. 1998).
99. Stummer, W. *et al.* Fluorescence-guided surgery with 5-aminolevulinic acid for resection of malignant glioma: a randomised controlled multicentre phase III trial. en. *The Lancet Oncology* **7**, 392–401. ISSN: 14702045 (May 2006).
100. Kantelhardt, S. R. *et al.* Multiphoton excitation fluorescence microscopy of 5-aminolevulinic acid induced fluorescence in experimental gliomas. en. *Lasers in Surgery and Medicine* **40**, 273–281. ISSN: 1096-9101 (Apr. 2008).
101. Stummer, W. The Fear of 5-ALA—Is It Warranted? en. *World Neurosurgery* **81**, e30–e31. ISSN: 18788750 (May 2014).
102. Croce, A. & Bottiroli, G. Autofluorescence spectroscopy and imaging: a tool for biomedical research and diagnosis. *European Journal of Histochemistry* **58**. ISSN: 2038-8306, 1121-760X. doi:10.4081/ejh.2014.2461. <http://ejh.it/index.php/ejh/article/view/2461> (2016) (Dec. 2014).
103. Monici, M. in *Biotechnology Annual Review* 227–256 (Elsevier, Jan. 2005). doi:10.1016/S1387-2656(05)11007-2. <http://www.sciencedirect.com/science/article/pii/S1387265605110072> (2018).
104. Chorvatova, A. & Chorvat, D. en. in *Fluorescence Lifetime Spectroscopy and Imaging* (eds Marcu, L., French, P. & Elson, D.) 47–84 (CRC Press, July 2014). ISBN: 978-1-4398-6167-7 978-1-4398-6168-4. <http://www.crcnetbase.com/doi/abs/10.1201/b17018-5> (2016).
105. Wagnieres, G. A., Star, W. M. & Wilson, B. C. In Vivo Fluorescence Spectroscopy and Imaging for Oncological Applications. en. *Photochemistry and Photobiology* **68**, 603–632. ISSN: 1751-1097 (Nov. 1998).



106. Bottirolì, G. & Croce, A. C. in *Comprehensive Series in Photochemical & Photobiological Sciences* (eds Palumbo, G. & Pratesi, R.) 189–210 (Royal Society of Chemistry, Cambridge, 2007). ISBN: 978-0-85404-321-7. doi:10.1039/9781847551207-00189. <http://ebook.rsc.org/?DOI=10.1039/9781847551207-00189> (2018).
107. Shin, S. J., Kanomata, N & Rosen, P. P. Mammary carcinoma with prominent cytoplasmic lipofuscin granules mimicking melanocytic differentiation. en. *Histopathology* **37**, 456–459. ISSN: 1365-2559 (Nov. 2000).
108. Matsumoto, Y. Lipofuscin pigmentation in pleomorphic adenoma of the palate. English. *Oral Surgery, Oral Medicine, Oral Pathology and Oral Radiology* **92**, 299–302. ISSN: 2212-4403, 2212-4411 (Sept. 2001).
109. Patil, R. *et al.* Advances in Imaging: Brain Tumors to Alzheimer's Disease. *The Bangkok medical journal* **10**, 83–97. ISSN: 2228-9674 (Sept. 2015).
110. Tilbury, K., Lien, C.-H., Chen, S.-J. & Campagnola, P. J. Differentiation of Col I and Col III Isoforms in Stromal Models of Ovarian Cancer by Analysis of Second Harmonic Generation Polarization and Emission Directionality. *Biophysical Journal* **106**, 354–365. ISSN: 0006-3495 (Jan. 2014).
111. Leppert, J. *et al.* Multiphoton Excitation of Autofluorescence for Microscopy of Glioma Tissue. en. *Neurosurgery* **58**, 759–767. ISSN: 0148-396X, 1524-4040 (Apr. 2006).
112. Giannoni, L., Lange, F. & Tachtsidis, I. Hyperspectral imaging solutions for brain tissue metabolic and hemodynamic monitoring: past, current and future developments. *Journal of Optics* **20**, 044009. ISSN: 2040-8978, 2040-8986 (Apr. 2018).
113. Miyamoto, O. & Auer, R. N. Hypoxia, hyperoxia, ischemia, and brain necrosis. en. *Neurology* **54**, 362–362. ISSN: 0028-3878, 1526-632X (Jan. 2000).
114. Lukina, M., Shirmanova, M., Sergeeva, T. & Zagaynova, E. Metabolic Imaging in the Study of Oncological Processes (Review). *Sovremennye tekhnologii v medicine* **8**, 113–126. ISSN: 20764243 (Dec. 2016).
115. Liu, Z. *et al.* Mapping metabolic changes by noninvasive, multiparametric, high-resolution imaging using endogenous contrast. eng. *Science Advances* **4**, eaap9302. ISSN: 2375-2548 (Mar. 2018).
116. Koppenol, W. H., Bounds, P. L. & Dang, C. V. Otto Warburg's contributions to current concepts of cancer metabolism. en. *Nature Reviews Cancer* **11**, 325–337. ISSN: 1474-1768 (May 2011).
117. Liu, Q. *et al.* Compact point-detection fluorescence spectroscopy system for quantifying intrinsic fluorescence redox ratio in brain cancer diagnostics. *Journal of Biomedical Optics* **16**. ISSN: 1083-3668. doi:10.1117/1.3558840. <https://www.ncbi.nlm.nih.gov/pmc/articles/PMC3173890/> (2018) (Mar. 2011).
118. Skala, M. C. *et al.* In vivo multiphoton microscopy of NADH and FAD redox states, fluorescence lifetimes, and cellular morphology in precancerous epithelia. *Proceedings of the National Academy of Sciences* **104**, 19494–19499 (2007).
119. Ranji, M. *et al.* Fluorescence spectroscopy and imaging of myocardial apoptosis. eng. *Journal of Biomedical Optics* **11**, 064036. ISSN: 1083-3668 (Dec. 2006).

## BIBLIOGRAPHY

120. Drezek, R. *et al.* Autofluorescence Microscopy of Fresh Cervical-Tissue Sections Reveals Alterations in Tissue Biochemistry with Dysplasia¶. en. *Photochemistry and Photobiology* **73**, 636–641. ISSN: 1751-1097 (June 2001).
121. Chung, Y. G., Schwartz, J. A., Gardner, C. M., Sawaya, R. E. & Jacques, S. L. Diagnostic potential of laser-induced autofluorescence emission in brain tissue. *Journal of Korean Medical Science* **12**, 135–142. ISSN: 1011-8934 (Apr. 1997).
122. Croce, A. C. *et al.* Diagnostic Potential of Autofluorescence for an Assisted Intraoperative Delineation of Glioblastoma Resection Margins¶. en. *Photochemistry and Photobiology* **77**, 309–318. ISSN: 1751-1097 (Mar. 2003).
123. Evers, D., Hendriks, B., Lucassen, G. & Ruers, T. Optical spectroscopy: current advances and future applications in cancer diagnostics and therapy. *Future Oncology* **8**, 307–320 (Mar. 2012).
124. Lin, W.-C., Toms, S. A., Johnson, M., Jansen, E. D. & Mahadevan-Jansen, A. In Vivo Brain Tumor Demarcation Using Optical Spectroscopy¶. en. *Photochemistry and Photobiology* **73**, 396. ISSN: 0031-8655 (2001).
125. Toms, S. A. *et al.* Intraoperative optical spectroscopy identifies infiltrating glioma margins with high sensitivity. eng. *Neurosurgery* **61**, 327–335; discussion 335–336. ISSN: 1524-4040 (July 2007).
126. Nazeer, S. S., Saraswathy, A., Gupta, A. K. & Jayasree, R. S. Fluorescence spectroscopy as a highly potential single-entity tool to identify chromophores and fluorophores: study on neoplastic human brain lesions. en. *Journal of Biomedical Optics* **18**, 067002. ISSN: 1083-3668 (June 2013).
127. Nazeer, S. S., Saraswathy, A., Gupta, A. K. & Jayasree, R. S. Fluorescence spectroscopy to discriminate neoplastic human brain lesions: a study using the spectral intensity ratio and multivariate linear discriminant analysis. *Laser Physics* **24**, 025602. ISSN: 1054-660X, 1555-6611 (Feb. 2014).
128. Haidar, D. A., Leh, B., Zanello, M. & Siebert, R. Spectral and lifetime domain measurements of rat brain tumors. eng. *Biomedical Optics Express* **6**, 1219–1233. ISSN: 2156-7085 (Apr. 2015).
129. Berezin, M. Y. & Achilefu, S. Fluorescence Lifetime Measurements and Biological Imaging. *Chemical reviews* **110**, 2641–2684. ISSN: 0009-2665 (May 2010).
130. Chen, L.-C., Lloyd, W. R., Chang, C.-W., Sud, D. & Mycek, M.-A. Fluorescence lifetime imaging microscopy for quantitative biological imaging. eng. *Methods in Cell Biology* **114**, 457–488. ISSN: 0091-679X (2013).
131. Marcu, L. *et al.* Fluorescence Lifetime Spectroscopy of Glioblastoma Multiforme¶. en. *Photochemistry and Photobiology* **80**, 98–103. ISSN: 00318655, 17511097 (Apr. 2007).
132. Elson, D., Marcu, L. & French, P. en. in *Fluorescence Lifetime Spectroscopy and Imaging* (eds Marcu, L., French, P. & Elson, D.) 3–22 (CRC Press, July 2014). ISBN: 978-1-4398-6167-7 978-1-4398-6168-4. doi:10.1201/b17018-3. <http://www.crcnetbase.com/doi/abs/10.1201/b17018-3> (2018).
133. Digman, M. A., Caiolfa, V. R., Zamai, M. & Gratton, E. The Phasor Approach to Fluorescence Lifetime Imaging Analysis. English. *Biophysical Journal* **94**, L14–L16. ISSN: 0006-3495 (Jan. 2008).

134. Kantelhardt, S. R. *et al.* In vivo multiphoton tomography and fluorescence lifetime imaging of human brain tumor tissue. en. *Journal of Neuro-Oncology* **127**, 473–482. ISSN: 0167-594X, 1573-7373 (May 2016).
135. Butte, P. V. *et al.* Intraoperative delineation of primary brain tumors using time-resolved fluorescence spectroscopy. en. *Journal of Biomedical Optics* **15**, 027008. ISSN: 10833668 (2010).
136. Sun, Y. *et al.* Fluorescence lifetime imaging microscopy for brain tumor image-guided surgery. *Journal of Biomedical Optics* **15**. ISSN: 1083-3668. doi:10.1117/1.3486612. <https://www.ncbi.nlm.nih.gov/pmc/articles/PMC2966493/> (2018) (2010).
137. Butte, P. V. *et al.* Fluorescence lifetime spectroscopy for guided therapy of brain tumors. *Neuroimage* **54**, S125–S135. ISSN: 1053-8119 (Jan. 2011).
138. Fujimoto, J. G., Pitris, C., Boppart, S. A. & Brezinski, M. E. Optical Coherence Tomography: An Emerging Technology for Biomedical Imaging and Optical Biopsy. *Neoplasia (New York, N.Y.)* **2**, 9–25. ISSN: 1522-8002 (Jan. 2000).
139. Böhrringer, H. J. *et al.* Time-domain and spectral-domain optical coherence tomography in the analysis of brain tumor tissue. en. *Lasers in Surgery and Medicine* **38**, 588–597. ISSN: 1096-9101 (July 2006).
140. Valdés, P. A., Roberts, D. W., Lu, F.-K., PhD & Golby, A. Optical technologies for intraoperative neurosurgical guidance. en. *Neurosurgical Focus* **40**, E8. ISSN: 1092-0684 (Mar. 2016).
141. Matz, H. *et al.* Intraoperative Applications of OCT in Ophthalmic Surgery. *Biomedical Engineering / Biomedizinische Technik* **57**. ISSN: 1862-278X, 0013-5585. doi:10.1515/bmt-2012-4460. <https://www.degruyter.com/view/j/bmte.2012.57.issue-s1-P/bmt-2012-4460/bmt-2012-4460.xml> (2018) (Jan. 2012).
142. Zagaynova, E., Gladkova, N., Shakhova, N., Gelikonov, G. & Gelikonov, V. Endoscopic OCT with forward-looking probe: clinical studies in urology and gastroenterology. en. *Journal of Biophotonics* **1**, 114–128. ISSN: 1864063X, 18640648 (May 2008).
143. Terashima, M., Kaneda, H. & Suzuki, T. The Role of Optical Coherence Tomography in Coronary Intervention. en. *The Korean Journal of Internal Medicine* **27**, 1. ISSN: 1226-3303, 2005-6648 (2012).
144. Kut, C. *et al.* Detection of Human Brain Cancer Infiltration ex vivo and in vivo Using Quantitative Optical Coherence Tomography. *Science translational medicine* **7**, 292ra100. ISSN: 1946-6234 (June 2015).
145. Carignan, C. S. & Yagi, Y. Optical endomicroscopy and the road to real-time, in vivo pathology: present and future. *Diagnostic Pathology* **7**, 98. ISSN: 1746-1596 (Aug. 2012).
146. Fan, Y. *et al.* Optical coherence tomography for precision brain imaging, neurosurgical guidance and minimally invasive theranostics. eng. *Bioscience Trends* **12**, 12–23. ISSN: 1881-7823 (Mar. 2018).
147. Valdés, P. A. *et al.* -aminolevulinic acid-induced protoporphyrin IX concentration correlates with histopathologic markers of malignancy in human gliomas: the need for quantitative fluorescence-guided resection to identify regions of increasing malignancy. *Neuro-Oncology* **13**, 846–856. ISSN: 1522-8517 (Aug. 2011).

## BIBLIOGRAPHY

148. Minsky, M. Memoir on inventing the confocal scanning microscope. en. *Scanning* **10**, 128–138. ISSN: 1932-8745.
149. *Confocal Microscopy - Introduction* <https://www.olympus-lifescience.com/de/microscope-resource/primer/techniques/confocal/confocalintro/> (2018).
150. Flusberg, B. A. *et al.* Fiber-optic fluorescence imaging. *Nature methods* **2**, 941–950. ISSN: 1548-7091 (Dec. 2005).
151. Loterie, D. *et al.* Digital confocal microscopy through a multimode fiber. EN. *Optics Express* **23**, 23845–23858. ISSN: 1094-4087 (Sept. 2015).
152. Fu, L. & Gu, M. Fibre-optic nonlinear optical microscopy and endoscopy. en. *Journal of Microscopy* **226**, 195–206. ISSN: 1365-2818 (June 2007).
153. Sung, K. B. *et al.* Near real time in vivo fibre optic confocal microscopy: sub-cellular structure resolved. en. *Journal of Microscopy* **207**, 137–145. ISSN: 1365-2818 (Aug. 2002).
154. Bird, D. & Gu, M. Two-photon fluorescence endoscopy with a micro-optic scanning head. en. *Optics Letters* **28**, 1552. ISSN: 0146-9592, 1539-4794 (Sept. 2003).
155. Xie, H., Pan, Y. & Fedder, G. K. Endoscopic optical coherence tomographic imaging with a CMOS-MEMS micromirror. *Sensors and Actuators A: Physical. Micromechanics section of Sensors and Actuators, based on contributions revised from the Technical Digest of the 15th IEEE International conference on Micro Electro mechanical Systems (MEMS 2002)* **103**, 237–241. ISSN: 0924-4247 (Jan. 2003).
156. Fu, L. & Gu, M. Double-clad photonic crystal fiber coupler for compact nonlinear optical microscopy imaging. EN. *Optics Letters* **31**, 1471–1473. ISSN: 1539-4794 (May 2006).
157. Piyawattanametha, W. *et al.* Fast-scanning two-photon fluorescence imaging based on a microelectromechanical systems two-dimensional scanning mirror. EN. *Optics Letters* **31**, 2018–2020. ISSN: 1539-4794 (July 2006).
158. Wang, J. *et al.* A Confocal Endoscope for Cellular Imaging. *Engineering* **1**, 351–360. ISSN: 2095-8099 (Sept. 2015).
159. Rouse, A. R., Kano, A., Udovich, J. A., Kroto, S. M. & Gmitro, A. F. Design and demonstration of a miniature catheter for a confocal microendoscope. en. *Applied Optics* **43**, 5763. ISSN: 0003-6935, 1539-4522 (Nov. 2004).
160. Kyrish, M. *et al.* Needle-based fluorescence endomicroscopy via structured illumination with a plastic, achromatic objective. en. *Journal of Biomedical Optics* **18**, 096003. ISSN: 1083-3668 (Sept. 2013).
161. Yang, L. *et al.* Five-lens, easy-to-implement miniature objective for a fluorescence confocal microendoscope. en. *Optics Express* **24**, 473. ISSN: 1094-4087 (Jan. 2016).
162. Yu, H., Zhou, G., Leung, H. M. & Chau, F. S. Tunable liquid-filled lens integrated with aspherical surface for spherical aberration compensation. en. *Optics Express* **18**, 9945. ISSN: 1094-4087 (May 2010).
163. Jabbour, J. M. *et al.* Optical axial scanning in confocal microscopy using an electrically tunable lens. *Biomedical Optics Express* **5**, 645–652. ISSN: 2156-7085 (Jan. 2014).
164. Kim, M. *et al.* Miniature objective lens with variable focus for confocal endomicroscopy. *Biomedical Optics Express* **5**, 4350–4361. ISSN: 2156-7085 (Nov. 2014).

165. Cheong, L. S. *et al.* Embedded Computing for Fluorescence Confocal Endomicroscopy Imaging. en. *Journal of Signal Processing Systems* **55**, 217–228. ISSN: 1939-8018, 1939-8115 (Apr. 2009).
166. Thong, P. S. P. *et al.* Toward real-time virtual biopsy of oral lesions using confocal laser endomicroscopy interfaced with embedded computing. en. *Journal of Biomedical Optics* **17**, 056009. ISSN: 10833668 (2012).
167. Sharma, P. *et al.* Real-time increased detection of neoplastic tissue in Barrett’s esophagus with probe-based confocal laser endomicroscopy: final results of an international multicenter, prospective, randomized, controlled trial. *Gastrointestinal endoscopy* **74**, 465–472. ISSN: 0016-5107 (Sept. 2011).
168. Liem, E. I. *et al.* Confocal Laser Endomicroscopy for the Diagnosis of Urothelial Carcinoma in the Bladder and the Upper Urinary Tract: Protocols for Two Prospective Explorative Studies. *JMIR Research Protocols* **7**. ISSN: 1929-0748. doi:10.2196/resprot.8862. <https://www.ncbi.nlm.nih.gov/pmc/articles/PMC5822038/> (2018) (Feb. 2018).
169. Tan, J., Quinn, M. A., Pyman, J. M., Delaney, P. M. & McLaren, W. J. Detection of cervical intraepithelial neoplasia in vivo using confocal endomicroscopy. eng. *BJOG: an international journal of obstetrics and gynaecology* **116**, 1663–1670. ISSN: 1471-0528 (Nov. 2009).
170. Zehri, A. *et al.* Neurosurgical confocal endomicroscopy: A review of contrast agents, confocal systems, and future imaging modalities. en. *Surgical Neurology International* **5**, 60. ISSN: 2152-7806 (2014).
171. Sankar, T. *et al.* Miniaturized Handheld Confocal Microscopy for Neurosurgery. en. *Neurosurgery* **66**, 410–418. ISSN: 0148-396X, 1524-4040 (Feb. 2010).
172. Pavlov, V. *et al.* Intraoperative Probe-Based Confocal Laser Endomicroscopy in Surgery and Stereotactic Biopsy of Low-Grade and High-Grade Gliomas: A Feasibility Study in Humans. eng. *Neurosurgery* **79**, 604–612. ISSN: 1524-4040 (2016).
173. Sanai, N. *et al.* Intraoperative Confocal Microscopy for Brain Tumors: A Feasibility Analysis in Humans: en. *Operative Neurosurgery* **68**, ons282–ons290. ISSN: 2332-4252 (June 2011).
174. Sanai, N. *et al.* Intraoperative confocal microscopy in the visualization of 5-aminolevulinic acid fluorescence in low-grade gliomas. *Journal of neurosurgery* **115**, 740–748 (2011).
175. Paull, P. E., Hyatt, B. J., Wassef, W. & Fischer, A. H. Confocal Laser Endomicroscopy: A Primer for Pathologists. en. *Archives of Pathology & Laboratory Medicine* **135**, 1343–1348. ISSN: 0003-9985, 1543-2165 (Oct. 2011).
176. Sako, Y. *et al.* Comparison of two-photon excitation laser scanning microscopy with UV-confocal laser scanning microscopy in three-dimensional calcium imaging using the fluorescence indicator Indo-1. en. *Journal of Microscopy* **185**, 9–20. ISSN: 0022-2720, 1365-2818 (Jan. 1997).
177. Gu, M., Bao, H. & Kang, H. Fibre-optical microendoscopy. en. *Journal of Microscopy* **254**, 13–18. ISSN: 1365-2818 (Apr. 2014).
178. Zipfel, W. R., Williams, R. M. & Webb, W. W. Nonlinear magic: multiphoton microscopy in the biosciences. *Nature Biotechnology* **21**, 1369–1377. ISSN: 1087-0156 (Nov. 2003).
179. Centonze, V. E. & White, J. G. Multiphoton excitation provides optical sections from deeper within scattering specimens than confocal imaging. *Biophysical journal* **75**, 2015–2024 (1998).

## BIBLIOGRAPHY

180. Bao, H., Boussioutas, A., Reynolds, J., Russell, S. & Gu, M. Imaging of goblet cells as a marker for intestinal metaplasia of the stomach by one-photon and two-photon fluorescence endomicroscopy. eng. *Journal of Biomedical Optics* **14**, 064031. ISSN: 1560-2281 (Dec. 2009).
181. Moreaux, L., Sandre, O., Charpak, S., Blanchard-Desce, M. & Mertz, J. Coherent scattering in multi-harmonic light microscopy. eng. *Biophysical Journal* **80**, 1568–1574. ISSN: 0006-3495 (Mar. 2001).
182. Thomas, G., van Voskuilen, J., Gerritsen, H. C. & Sterenborg, H. Advances and challenges in label-free nonlinear optical imaging using two-photon excitation fluorescence and second harmonic generation for cancer research. en. *Journal of Photochemistry and Photobiology B: Biology* **141**, 128–138. ISSN: 10111344 (Dec. 2014).
183. Williams, R. M., Zipfel, W. R. & Webb, W. W. Interpreting Second-Harmonic Generation Images of Collagen I Fibrils. *Biophysical Journal* **88**, 1377–1386. ISSN: 0006-3495 (Feb. 2005).
184. Both, M. *et al.* Second harmonic imaging of intrinsic signals in muscle fibers in situ. eng. *Journal of Biomedical Optics* **9**, 882–892. ISSN: 1083-3668 (Oct. 2004).
185. Brown, R. M., Millard, A. C. & Campagnola, P. J. Macromolecular structure of cellulose studied by second-harmonic generation imaging microscopy. eng. *Optics Letters* **28**, 2207–2209. ISSN: 0146-9592 (Nov. 2003).
186. Nadiarnykh, O., LaComb, R. B., Brewer, M. A. & Campagnola, P. J. Alterations of the extracellular matrix in ovarian cancer studied by Second Harmonic Generation imaging microscopy. *BMC Cancer* **10**, 94. ISSN: 1471-2407 (Mar. 2010).
187. Conklin, M. W. *et al.* Aligned Collagen Is a Prognostic Signature for Survival in Human Breast Carcinoma. *The American Journal of Pathology* **178**, 1221–1232. ISSN: 0002-9440 (Mar. 2011).
188. Ouzounov, D. G. *et al.* Delivery of nanojoule femtosecond pulses through large-core microstructured fibers. eng. *Optics Letters* **27**, 1513–1515. ISSN: 0146-9592 (Sept. 2002).
189. Tai, S.-P. *et al.* Two-photon fluorescence microscope with a hollow-core photonic crystal fiber. eng. *Optics Express* **12**, 6122–6128. ISSN: 1094-4087 (Dec. 2004).
190. Fu, L., Jain, A., Xie, H., Cranfield, C. & Gu, M. Nonlinear optical endoscopy based on a double-clad photonic crystal fiber and a MEMS mirror. EN. *Optics Express* **14**, 1027–1032. ISSN: 1094-4087 (Feb. 2006).
191. Wadsworth, W. J. *et al.* Supercontinuum generation in photonic crystal fibers and optical fiber tapers: a novel light source. en. *Journal of the Optical Society of America B* **19**, 2148. ISSN: 0740-3224, 1520-8540 (Sept. 2002).
192. Knight, J. C. APPLIED OPTICS: New Ways to Guide Light. *Science* **296**, 276–277. ISSN: 00368075, 10959203 (Apr. 2002).
193. Lelek, M. *et al.* Coherent femtosecond pulse shaping for the optimization of a non-linear micro-endoscope. EN. *Optics Express* **15**, 10154–10162. ISSN: 1094-4087 (Aug. 2007).
194. Le, T., Tempea, G., Cheng, Z., Hofer, M. & Stingl, A. Routes to fiber delivery of ultra-short laser pulses in the 25 fs regime. en. *Optics Express* **17**, 1240. ISSN: 1094-4087 (Feb. 2009).
195. Lefort, C., Mansuryan, T., Louradour, F. & Barthelemy, A. Pulse compression and fiber delivery of 45 fs Fourier transform limited pulses at 830 nm. en. *Optics Letters* **36**, 292. ISSN: 0146-9592, 1539-4794 (Jan. 2011).

196. Lefort, C., Hamzeh, H., Louradour, F., Pain, F. & Haidar, D. A. Characterization, comparison, and choice of a commercial double-clad fiber for nonlinear endomicroscopy. eng. *Journal of Biomedical Optics* **19**, 076005. ISSN: 1560-2281 (2014).
197. Hamzeh, H., Lefort, C., Pain, F. & Abi Haidar, D. Optimization and characterization of nonlinear excitation and collection through a gradient-index lens for high-resolution nonlinear endomicroscopy. eng. *Optics Letters* **40**, 808–811. ISSN: 1539-4794 (Mar. 2015).
198. Ibrahim, A. *et al.* Characterization of fiber ultrashort pulse delivery for nonlinear endomicroscopy. en. *Optics Express* **24**, 12515. ISSN: 1094-4087 (June 2016).
199. Knorr, F., Yankelevich, D. R., Liu, J., Wachsmann-Hogiu, S. & Marcu, L. Two – photon excited fluorescence lifetime measurements through a double-clad photonic crystal fiber for tissue micro – endoscopy. *Journal of biophotonics* **5**, 14–19. ISSN: 1864-063X (Jan. 2012).
200. *Jenlab: Multiphoton Tomography* <http://www.jenlab.de/Home.6.0.html?&L=ru%27A%3D0> (2018).
201. Konig, K. & Riemann, I. High-resolution multiphoton tomography of human skin with sub-cellular spatial resolution and picosecond time resolution. eng. *Journal of Biomedical Optics* **8**, 432–439. ISSN: 1083-3668 (July 2003).
202. Koenig, K. *et al.* *Optical tomography of human skin with subcellular spatial and picosecond time resolution using intense near infrared femtosecond laser pulses* in (eds Periasamy, A. & So, P. T. C.) (June 2002), 191–201. doi:10.1117/12.470692. <http://proceedings.spiedigitallibrary.org/proceeding.aspx?articleid=871888> (2018).
203. Ducourthial, G. *et al.* Development of a real-time flexible multiphoton microendoscope for label-free imaging in a live animal. *Scientific Reports* **5**. ISSN: 2045-2322. doi:10.1038/srep18303. <https://www.ncbi.nlm.nih.gov/pmc/articles/PMC4682136/> (2018) (Dec. 2015).
204. Zhao, Y., Sheng, M., Huang, L. & Tang, S. Design of a fiber-optic multiphoton microscopy handheld probe. *Biomedical Optics Express* **7**, 3425–3437. ISSN: 2156-7085 (Aug. 2016).
205. Brusatori, M. *et al.* Intraoperative Raman Spectroscopy. en. *Neurosurgery Clinics of North America* **28**, 633–652. ISSN: 10423680 (Oct. 2017).
206. Jacques, S. L. Optical properties of biological tissues: a review. eng. *Physics in Medicine and Biology* **58**, R37–61. ISSN: 1361-6560 (June 2013).
207. Eggert, H. R. & Blazek, V. Optical properties of human brain tissue, meninges, and brain tumors in the spectral range of 200 to 900 nm. eng. *Neurosurgery* **21**, 459–464. ISSN: 0148-396X (Oct. 1987).
208. Bevilacqua, F. *et al.* In vivo local determination of tissue optical properties: applications to human brain. eng. *Applied Optics* **38**, 4939–4950. ISSN: 0003-6935 (Aug. 1999).
209. Yaroslavsky, A. N. *et al.* Optical properties of selected native and coagulated human brain tissues in vitro in the visible and near infrared spectral range. eng. *Physics in Medicine and Biology* **47**, 2059–2073. ISSN: 0031-9155 (June 2002).
210. Gebhart, S. C., Lin, W. C. & Mahadevan-Jansen, A. In vitro determination of normal and neoplastic human brain tissue optical properties using inverse adding-doubling. en. *Physics in Medicine & Biology* **51**, 2011. ISSN: 0031-9155 (2006).

## BIBLIOGRAPHY

211. Zee, P. v. d., Essenpreis, M. & Delpy, D. T. *Optical properties of brain tissue* in *Photon Migration and Imaging in Random Media and Tissues* **1888** (International Society for Optics and Photonics, Sept. 1993), 454–466. doi:10.1117/12.154665. <https://www.spiedigitallibrary.org/conference-proceedings-of-spie/1888/0000/Optical-properties-of-brain-tissue/10.1117/12.154665.short> (2018).
212. Cheong, W., Prahl, S. & Welch, A. A review of the optical properties of biological tissues. *IEEE Journal of Quantum Electronics* **26**, 2166–2185. ISSN: 00189197 (Dec. 1990).
213. Bashkatov, A. N., Genina, E. A. & Tuchin, V. V. OPTICAL PROPERTIES OF SKIN, SUBCUTANEOUS, AND MUSCLE TISSUES: A REVIEW. en. *Journal of Innovative Optical Health Sciences* **04**, 9–38. ISSN: 1793-5458, 1793-7205 (Jan. 2011).
214. Swartling, J., Pålsson, S., Platonov, P., Olsson, S. B. & Andersson-Engels, S. Changes in tissue optical properties due to radio-frequency ablation of myocardium. eng. *Medical & Biological Engineering & Computing* **41**, 403–409. ISSN: 0140-0118 (July 2003).
215. Solonenko, M. *et al.* In vivo reflectance measurement of optical properties, blood oxygenation and motexafin lutetium uptake in canine large bowels, kidneys and prostates. eng. *Physics in Medicine and Biology* **47**, 857–873. ISSN: 0031-9155 (Mar. 2002).
216. Zanello, M. *et al.* Multimodal optical analysis of meningioma and comparison with histopathology. en. *Journal of Biophotonics*, n/a–n/a. ISSN: 1864063X (Mar. 2016).
217. Cicchi, R. *et al.* Time- and Spectral-resolved two-photon imaging of healthy bladder mucosa and carcinoma in situ. eng. *Optics Express* **18**, 3840–3849. ISSN: 1094-4087 (Feb. 2010).
218. Papayan, G., Petrishchev, N. & Galagudza, M. Autofluorescence spectroscopy for NADH and flavoproteins redox state monitoring in the isolated rat heart subjected to ischemia-reperfusion. en. *Photodiagnosis and Photodynamic Therapy* **11**, 400–408. ISSN: 15721000 (Sept. 2014).
219. Taddeucci, A. Optical properties of brain tissue. en. *Journal of Biomedical Optics* **1**, 117. ISSN: 10833668 (1996).
220. Barrio, J. R., Tolman, G. L., Leonard, N. J., Spencer, R. D. & Weber, G. Flavin 1, N 6 -ethenoadenine dinucleotide: dynamic and static quenching of fluorescence. eng. *Proceedings of the National Academy of Sciences of the United States of America* **70**, 941–943. ISSN: 0027-8424 (Mar. 1973).
221. Ibrahim, A. *et al.* Spectral and fluorescence lifetime endoscopic system using a double-clad photonic crystal fiber. en. *Optics Letters* **41**, 5214. ISSN: 0146-9592, 1539-4794 (Nov. 2016).
222. Palmer, S. *et al.* Optical redox ratio and endogenous porphyrins in the detection of urinary bladder cancer: A patient biopsy analysis. eng. *Journal of Biophotonics*. ISSN: 1864-0648. doi:10.1002/jbio.201600162 (Oct. 2016).
223. Zanello, M. *et al.* Multimodal optical analysis discriminates freshly extracted human sample of gliomas, metastases and meningiomas from their appropriate controls. *Scientific Reports* **7**. ISSN: 2045-2322. doi:10.1038/srep41724. <https://www.ncbi.nlm.nih.gov/pmc/articles/PMC5288720/> (2018) (Feb. 2017).
224. Farbiszewski, R., Skrzydlewska, E. & Roszkowska, A. Formaldehyde-induced modification of hemoglobin in vitro. eng. *Acta Biologica Hungarica* **49**, 345–352. ISSN: 0236-5383 (1998).



225. Filippidis, G. *et al.* Effect of liquid-nitrogen and formalin-based conservation in the in vitro measurement of laser-induced fluorescence from peripheral vascular tissue. eng. *Journal of Photochemistry and Photobiology. B, Biology* **47**, 109–114. ISSN: 1011-1344 (Dec. 1998).
226. Majumder, S. K., Ghosh, N. & Gupta, P. K. N2 laser excited autofluorescence spectroscopy of formalin-fixed human breast tissue. eng. *Journal of Photochemistry and Photobiology. B, Biology* **81**, 33–42. ISSN: 1011-1344 (Oct. 2005).
227. Xu, M. G., Williams, E. D., Thompson, E. W. & Gu, M. Effect of handling and fixation processes on fluorescence spectroscopy of mouse skeletal muscles under two-photon excitation. eng. *Applied Optics* **39**, 6312–6317. ISSN: 1559-128X (Dec. 2000).
228. Gabrecht, T., Andrejevic-Blant, S. & Wagnières, G. Blue-Violet Excited Autofluorescence Spectroscopy and Imaging of Normal and Cancerous Human Bronchial Tissue after Formalin Fixation. en. *Photochemistry and Photobiology* **83**, 450–459. ISSN: 1751-1097.
229. Gabrecht, T., Andrejevic-Blant, S. & Wagnières, G. Blue-violet excited autofluorescence spectroscopy and imaging of normal and cancerous human bronchial tissue after formalin fixation. eng. *Photochemistry and Photobiology* **83**, 450–458. ISSN: 0031-8655 (Apr. 2007).
230. Wang, H.-W. *et al.* Differentiation of apoptosis from necrosis by dynamic changes of reduced nicotinamide adenine dinucleotide fluorescence lifetime in live cells. eng. *Journal of Biomedical Optics* **13**, 054011. ISSN: 1083-3668 (Oct. 2008).
231. Skala, M. C. *et al.* In vivo multiphoton fluorescence lifetime imaging of protein-bound and free nicotinamide adenine dinucleotide in normal and precancerous epithelia. eng. *Journal of Biomedical Optics* **12**, 024014. ISSN: 1083-3668 (Apr. 2007).
232. Vishwasrao, H. D., Heikal, A. A., Kasischke, K. A. & Webb, W. W. Conformational dependence of intracellular NADH on metabolic state revealed by associated fluorescence anisotropy. eng. *The Journal of Biological Chemistry* **280**, 25119–25126. ISSN: 0021-9258 (July 2005).
233. Uehlinger, P. Optimisation de la photothérapie dynamique et de la photodétection de cancers précoces par spectroscopie résolue en temps de luminophores endogènes et exogènes. fre. doi:10.5075/epfl-thesis-3149. <http://infoscience.epfl.ch/record/33618> (2018) (2004).
234. Wilson, T. A., Karajannis, M. A. & Harter, D. H. Glioblastoma multiforme: State of the art and future therapeutics. eng. *Surgical Neurology International* **5**, 64. ISSN: 2229-5097 (2014).
235. Lin, J., Jandial, R., Nesbit, A., Badie, B. & Chen, M. Current and emerging treatments for brain metastases. eng. *Oncology (Williston Park, N.Y.)* **29**, 250–257. ISSN: 0890-9091 (Apr. 2015).
236. Kuhnt, D. *et al.* Correlation of the extent of tumor volume resection and patient survival in surgery of glioblastoma multiforme with high-field intraoperative MRI guidance. eng. *Neuro-Oncology* **13**, 1339–1348. ISSN: 1523-5866 (Dec. 2011).
237. Uluç, K., Kujoth, G. C. & Başkaya, M. K. Operating microscopes: past, present, and future. eng. *Neurosurgical Focus* **27**, E4. ISSN: 1092-0684 (Sept. 2009).
238. Unsgaard, G. *et al.* Intra-operative 3D ultrasound in neurosurgery. eng. *Acta Neurochirurgica* **148**, 235–253; discussion 253. ISSN: 0001-6268 (Mar. 2006).

## BIBLIOGRAPHY

239. Stummer, W. *et al.* Counterbalancing risks and gains from extended resections in malignant glioma surgery: a supplemental analysis from the randomized 5-aminolevulinic acid glioma resection study. Clinical article. eng. *Journal of Neurosurgery* **114**, 613–623. ISSN: 1933-0693 (Mar. 2011).
240. Kolste, K. K. *et al.* Macroscopic optical imaging technique for wide-field estimation of fluorescence depth in optically turbid media for application in brain tumor surgical guidance. eng. *Journal of Biomedical Optics* **20**, 26002. ISSN: 1560-2281 (Feb. 2015).
241. Andersson-Engels, S., Klinteberg, C. a., Svanberg, K & Svanberg, S. *In vivo* fluorescence imaging for tissue diagnostics. *Physics in Medicine and Biology* **42**, 815–824. ISSN: 0031-9155, 1361-6560 (May 1997).
242. Bottiroli, G. *et al.* Brain tissue autofluorescence: an aid for intraoperative delineation of tumor resection margins. eng. *Cancer detection and prevention* **22**, 330–339. ISSN: 0361-090X (1998).
243. Denk, W, Strickler, J. & Webb, W. Two-photon laser scanning fluorescence microscopy. en. *Science* **248**, 73–76. ISSN: 0036-8075, 1095-9203 (Apr. 1990).
244. Assayag, O. *et al.* Large field, high resolution full-field optical coherence tomography: a pre-clinical study of human breast tissue and cancer assessment. eng. *Technology in Cancer Research & Treatment* **13**, 455–468. ISSN: 1533-0338 (Oct. 2014).
245. Ji, M. *et al.* Rapid, label-free detection of brain tumors with stimulated Raman scattering microscopy. eng. *Science Translational Medicine* **5**, 201ra119. ISSN: 1946-6242 (Sept. 2013).
246. Saraswathy, A., Jayasree, R., Baiju, K., Gupta, A. K. & Pillai, V. M. Optimum Wavelength for the Differentiation of Brain Tumor Tissue Using Autofluorescence Spectroscopy. en. *Photomedicine and Laser Surgery* **27**, 425–433. ISSN: 1549-5418, 1557-8550 (June 2009).
247. Warburg, O., Wind, F. & Negelein, E. THE METABOLISM OF TUMORS IN THE BODY. *The Journal of General Physiology* **8**, 519–530. ISSN: 0022-1295 (Mar. 1927).
248. Gogvadze, V., Orrenius, S. & Zhivotovsky, B. Mitochondria in cancer cells: what is so special about them? eng. *Trends in Cell Biology* **18**, 165–173. ISSN: 1879-3088 (Apr. 2008).
249. Baraghis, E. *et al.* Two-photon microscopy of cortical NADH fluorescence intensity changes: correcting contamination from the hemodynamic response. eng. *Journal of Biomedical Optics* **16**, 106003. ISSN: 1560-2281 (Oct. 2011).
250. Wang, B.-G., Koenig, K., Riemann, I., Krieg, R. & Halhuber, K.-J. Intraocular multiphoton microscopy with subcellular spatial resolution by infrared femtosecond lasers. en. *Histochemistry and Cell Biology* **126**, 507–515. ISSN: 0948-6143, 1432-119X (Oct. 2006).
251. Becker, W. & Shcheslavskiy, V. *Fluorescence lifetime imaging with near-infrared dyes* in (eds Periasamy, A., König, K. & So, P. T. C.) (Feb. 2013), 85880R. doi:10.1117/12.2003608. <http://proceedings.spiedigitallibrary.org/proceeding.aspx?doi=10.1117/12.2003608> (2018).
252. Butte, P. V. *et al.* Diagnosis of meningioma by time-resolved fluorescence spectroscopy. eng. *Journal of Biomedical Optics* **10**, 064026. ISSN: 1083-3668 (Dec. 2005).
253. Yong, W. H. *et al.* Distinction of brain tissue, low grade and high grade glioma with time-resolved fluorescence spectroscopy. *Frontiers in bioscience : a journal and virtual library* **11**, 1255–1263. ISSN: 1093-9946 (May 2006).

254. Lee, J. H., Kim, D. H., Song, W. K., Oh, M.-K. & Ko, D.-K. Label-free imaging and quantitative chemical analysis of Alzheimer's disease brain samples with multimodal multiphoton nonlinear optical microspectroscopy. en. *Journal of Biomedical Optics* **20**, 056013. ISSN: 1083-3668 (May 2015).
255. Bélanger, E. *et al.* Live animal myelin histomorphometry of the spinal cord with video-rate multimodal nonlinear microendoscopy. eng. *Journal of Biomedical Optics* **17**, 021107. ISSN: 1560-2281 (Feb. 2012).
256. Kantelhardt, S. R. *et al.* Imaging of brain and brain tumor specimens by time-resolved multiphoton excitation microscopy ex vivo. *Neuro-oncology* **9**, 103–112 (2007).
257. Thomas, G. *et al.* Estimating the risk of squamous cell cancer induction in skin following nonlinear optical imaging. eng. *Journal of Biophotonics* **7**, 492–505. ISSN: 1864-0648 (July 2014).
258. Fischer, F. *et al.* Assessing the risk of skin damage due to femtosecond laser irradiation. eng. *Journal of Biophotonics* **1**, 470–477. ISSN: 1864-0648 (Dec. 2008).
259. Zanello, M. *et al.* *Spectral and Lifetime Measurements of the Endogenous Fluorescence Variation of Freshly Resected Human Samples over Time - Measuring Endogenous Fluorescence Changes at Different Moment after Tumor or Epileptic Cortex Excision:* in (SCITEPRESS - Science, and Technology Publications, 2016), 13–17. ISBN: 978-989-758-174-8. doi:10.5220/0005654900130017. <http://www.scitepress.org/DigitalLibrary/Link.aspx?doi=10.5220/0005654900130017> (2016).
260. Louis, D. N. *et al.* The 2016 World Health Organization Classification of Tumors of the Central Nervous System: a summary. eng. *Acta Neuropathologica* **131**, 803–820. ISSN: 1432-0533 (June 2016).
261. Ramos-Vara, J. A. & Miller, M. A. When Tissue Antigens and Antibodies Get Along: Revisiting the Technical Aspects of Immunohistochemistry—The Red, Brown, and Blue Technique. en. *Veterinary Pathology* **51**, 42–87. ISSN: 0300-9858, 1544-2217 (Jan. 2014).
262. Commings, D. L., Atkinson, R. D. & Burnett, M. E. Review of meningioma histopathology. en. *Neurosurgical Focus* **23**, E3. ISSN: 1092-0684 (Oct. 2007).
263. Ostrom, Q. T. *et al.* CBTRUS statistical report: Primary brain and central nervous system tumors diagnosed in the United States in 2006-2010. eng. *Neuro-Oncology* **15 Suppl 2**, ii1–56. ISSN: 1523-5866 (Nov. 2013).
264. Whittle, I. R., Smith, C., Navoo, P. & Collie, D. Meningiomas. eng. *Lancet (London, England)* **363**, 1535–1543. ISSN: 1474-547X (May 2004).
265. Sun, S. Q., Hawasli, A. H., Huang, J., Chicoine, M. R. & Kim, A. H. An evidence-based treatment algorithm for the management of WHO Grade II and III meningiomas. eng. *Neurosurgical Focus* **38**, E3. ISSN: 1092-0684 (Mar. 2015).
266. Heald, J. B., Carroll, T. A. & Mair, R. J. Simpson grade: an opportunity to reassess the need for complete resection of meningiomas. eng. *Acta Neurochirurgica* **156**, 383–388. ISSN: 0942-0940 (Feb. 2014).
267. Simpson, D. The recurrence of intracranial meningiomas after surgical treatment. eng. *Journal of Neurology, Neurosurgery, and Psychiatry* **20**, 22–39. ISSN: 0022-3050 (Feb. 1957).

## BIBLIOGRAPHY

268. Sughrue, M. E. *et al.* Outcome and survival following primary and repeat surgery for World Health Organization Grade III meningiomas. eng. *Journal of Neurosurgery* **113**, 202–209. ISSN: 1933-0693 (Aug. 2010).
269. d'Avella, E., Volpin, F., Manara, R., Scienza, R. & Della, A. P. Indocyanine green videoangiography (ICGV)-guided surgery of parasagittal meningiomas occluding the superior sagittal sinus (SSS). eng. *Acta neurochirurgica* **155**, 415–420. ISSN: 0001-6268 (Mar. 2013).
270. Cornelius, J. F. *et al.* Impact of 5-aminolevulinic acid fluorescence-guided surgery on the extent of resection of meningiomas—with special regard to high-grade tumors. eng. *Photodiagnosis and Photodynamic Therapy* **11**, 481–490. ISSN: 1873-1597 (Dec. 2014).
271. Gay, E. *et al.* Intraoperative and postoperative gamma detection of somatostatin receptors in bone-invasive en plaque meningiomas. eng. *Neurosurgery* **57**, 107–113; discussion 107–113. ISSN: 1524-4040 (July 2005).
272. Prada, F. *et al.* From Grey Scale B-Mode to Elastosonography: Multimodal Ultrasound Imaging in Meningioma Surgery—Pictorial Essay and Literature Review. en. *BioMed Research International* **2015**, 1–13. ISSN: 2314-6133, 2314-6141 (2015).
273. Soleman, J., Fathi, A.-R., Marbacher, S. & Fandino, J. The role of intraoperative magnetic resonance imaging in complex meningioma surgery. eng. *Magnetic Resonance Imaging* **31**, 923–929. ISSN: 1873-5894 (July 2013).
274. Sun, G.-c. *et al.* Functional Neuronavigation-Guided Transparieto-Occipital Cortical Resection of Meningiomas in Trigone of Lateral Ventricle. en. *World Neurosurgery* **84**, 756–765. ISSN: 18788750 (Sept. 2015).
275. Uhl, E. *et al.* Intraoperative computed tomography with integrated navigation system in a multidisciplinary operating suite. eng. *Neurosurgery* **64**, 231–239; discussion 239–240. ISSN: 1524-4040 (May 2009).
276. Motekallemini, A. *et al.* The current status of 5-ALA fluorescence-guided resection of intracranial meningiomas—a critical review. en. *Neurosurgical Review* **38**, 619–628. ISSN: 0344-5607, 1437-2320 (Oct. 2015).
277. Sell, D. R. & Monnier, V. M. Isolation, purification and partial characterization of novel fluorophores from aging human insoluble collagen-rich tissue. eng. *Connective Tissue Research* **19**, 77–92. ISSN: 0300-8207 (1989).
278. Chance, B. & Hess, B. Spectroscopic evidence of metabolic control. eng. *Science (New York, N. Y.)* **129**, 700–708. ISSN: 0036-8075 (Mar. 1959).
279. Huang, S., Heikal, A. A. & Webb, W. W. Two-photon fluorescence spectroscopy and microscopy of NAD(P)H and flavoprotein. eng. *Biophysical Journal* **82**, 2811–2825. ISSN: 0006-3495 (May 2002).
280. Hong, Z. *et al.* Optical diagnosis of gallbladder cancers via two-photon excited fluorescence imaging of unstained histological sections. en. *Lasers in Medical Science* **30**, 225–233. ISSN: 0268-8921, 1435-604X (Jan. 2015).
281. Wu, X. *et al.* Label-Free Detection of Breast Masses Using Multiphoton Microscopy. en. *PLoS ONE* **8** (ed Aziz, S. A.) e65933. ISSN: 1932-6203 (June 2013).
282. Yan, J. *et al.* Preclinical study of using multiphoton microscopy to diagnose liver cancer and differentiate benign and malignant liver lesions. en. *Journal of Biomedical Optics* **17**, 026004. ISSN: 10833668 (2012).

283. Strupler, M. *et al.* Second harmonic imaging and scoring of collagen in fibrotic tissues. EN. *Optics Express* **15**, 4054–4065. ISSN: 1094-4087 (Apr. 2007).
284. Xu, J. *et al.* Identifying the neck margin status of ductal adenocarcinoma in the pancreatic head by multiphoton microscopy. en. *Scientific Reports* **7**. ISSN: 2045-2322. doi:10.1038/s41598-017-04771-w. <http://www.nature.com/articles/s41598-017-04771-w> (2018) (Dec. 2017).
285. Xu, J. *et al.* Multiphoton microscopy for label-free identification of intramural metastasis in human esophageal squamous cell carcinoma. EN. *Biomedical Optics Express* **8**, 3360–3368. ISSN: 2156-7085 (July 2017).
286. Rivenson, Y. *et al.* Deep learning-based virtual histology staining using auto- fluorescence of label-free tissue. en, 22.
287. Bocklitz, T. W. *et al.* Pseudo-HE images derived from CARS/TPEF/SHG multimodal imaging in combination with Raman-spectroscopy as a pathological screening tool. *BMC Cancer* **16**. ISSN: 1471-2407. doi:10.1186/s12885-016-2520-x. <https://www.ncbi.nlm.nih.gov/pmc/articles/PMC4962450/> (2018) (July 2016).
288. Hervey-Jumper, S. L. & Berger, M. S. Maximizing safe resection of low- and high-grade glioma. eng. *Journal of Neuro-Oncology* **130**, 269–282. ISSN: 1573-7373 (2016).
289. Ferguson, S. D. *et al.* Neurosurgical management of brain metastases. en. *Clinical & Experimental Metastasis* **34**, 377–389. ISSN: 0262-0898, 1573-7276 (Oct. 2017).
290. Pallud, J. *et al.* Individual Variability of the Human Cerebral Cortex Identified Using Intra-operative Mapping. en. *World Neurosurgery* **109**, e313–e317. ISSN: 18788750 (Jan. 2018).
291. Pallud, J. *et al.* Direct electrical bipolar electrostimulation for functional cortical and subcortical cerebral mapping in awake craniotomy. Practical considerations. eng. *Neuro-Chirurgie* **63**, 164–174. ISSN: 1773-0619 (June 2017).
292. Theer, P., Hasan, M. T. & Denk, W. Two-photon imaging to a depth of 1000 microm in living brains by use of a Ti:Al<sub>2</sub>O<sub>3</sub> regenerative amplifier. eng. *Optics Letters* **28**, 1022–1024. ISSN: 0146-9592 (June 2003).
293. Takahashi, N. *et al.* Two-photon fluorescence lifetime imaging of primed SNARE complexes in presynaptic terminals and cells. eng. *Nature Communications* **6**, 8531. ISSN: 2041-1723 (2015).
294. Xu, C. & Webb, W. W. Measurement of two-photon excitation cross sections of molecular fluorophores with data from 690 to 1050 nm. en. *Journal of the Optical Society of America B* **13**, 481. ISSN: 0740-3224, 1520-8540 (Mar. 1996).
295. Ramanujan, V. K., Zhang, J.-H., Biener, E. & Herman, B. Multiphoton fluorescence lifetime contrast in deep tissue imaging: prospects in redox imaging and disease diagnosis. en. *Journal of Biomedical Optics* **10**, 051407. ISSN: 10833668 (2005).
296. Bastiaens, P. I. & Squire, A. Fluorescence lifetime imaging microscopy: spatial resolution of biochemical processes in the cell. *Trends in cell biology* **9**, 48–52 (1999).
297. Chen, Y. & Periasamy, A. Characterization of two-photon excitation fluorescence lifetime imaging microscopy for protein localization. en. *Microscopy Research and Technique* **63**, 72–80. ISSN: 1059-910X, 1097-0029 (Jan. 2004).

## BIBLIOGRAPHY

298. Van Munster, E. B. & Gadella, T. W. J. Fluorescence lifetime imaging microscopy (FLIM). eng. *Advances in Biochemical Engineering/Biotechnology* **95**, 143–175. ISSN: 0724-6145 (2005).
299. Perry, S. W., Burke, R. M. & Brown, E. B. Two-Photon and Second Harmonic Microscopy in Clinical and Translational Cancer Research. en. *Annals of Biomedical Engineering* **40**, 277–291. ISSN: 0090-6964, 1573-9686 (Feb. 2012).
300. Yan, L., Rueden, C. T., White, J. G. & Eliceiri, K. W. Applications of combined spectral lifetime microscopy for biology. *Biotechniques* **41**, 249 (2006).
301. Keikhosravi, A., Bredfeldt, J. S., Sagar, A. K. & Eliceiri, K. W. en. in *Methods in Cell Biology* 531–546 (Elsevier, 2014). ISBN: 978-0-12-420138-5. <http://linkinghub.elsevier.com/retrieve/pii/B9780124201385000288> (2016).
302. Provenzano, P. P. *et al.* Collagen reorganization at the tumor-stromal interface facilitates local invasion. *BMC medicine* **4**, 1 (2006).
303. Wallrabe, H. *et al.* Segmented cell analyses to measure redox states of autofluorescent NAD(P)H, FAD & Trp in cancer cells by FLIM. *Scientific Reports* **8**. ISSN: 2045-2322. doi:10.1038/s41598-017-18634-x. <https://www.ncbi.nlm.nih.gov/pmc/articles/PMC5758727/> (2018) (Jan. 2018).
304. Jyothikumar, V., Sun, Y. & Periasamy, A. Investigation of tryptophan-NADH interactions in live human cells using three-photon fluorescence lifetime imaging and Förster resonance energy transfer microscopy. eng. *Journal of Biomedical Optics* **18**, 060501. ISSN: 1560-2281 (June 2013).
305. Georgakoudi, I. *et al.* NAD(P)H and Collagen as in Vivo Quantitative Fluorescent Biomarkers of Epithelial Precancerous Changes. en, 7.
306. Pu, Y., Wang, W., Tang, G. & Alfano, R. R. Changes of collagen and nicotinamide adenine dinucleotide in human cancerous and normal prostate tissues studied using native fluorescence spectroscopy with selective excitation wavelength. en. *Journal of Biomedical Optics* **15**, 047008. ISSN: 10833668 (2010).
307. Lasch, P., Haensch, W., Naumann, D. & Diem, M. Imaging of colorectal adenocarcinoma using FT-IR microspectroscopy and cluster analysis. en. *Biochimica et Biophysica Acta (BBA) - Molecular Basis of Disease* **1688**, 176–186. ISSN: 09254439 (Mar. 2004).
308. Sebiskveradze, D. *et al.* Automation of an algorithm based on fuzzy clustering for analyzing tumoral heterogeneity in human skin carcinoma tissue sections. en. *Laboratory Investigation* **91**, 799–811. ISSN: 0023-6837, 1530-0307 (May 2011).
309. Petitbois, C. & Délérès, G. Chemical mapping of tumor progression by FT-IR imaging: towards molecular histopathology. eng. *Trends in Biotechnology* **24**, 455–462. ISSN: 0167-7799 (Oct. 2006).
310. Luo, T., Lu, Y., Liu, S., Lin, D. & Qu, J. Phasor-FLIM as a Screening Tool for the Differential Diagnosis of Actinic Keratosis, Bowen's Disease, and Basal Cell Carcinoma. en. *Analytical Chemistry* **89**, 8104–8111. ISSN: 0003-2700, 1520-6882 (Aug. 2017).
311. Fereidouni, F., Gorpas, D., Ma, D., Fatakdawala, H. & Marcu, L. Rapid fluorescence lifetime estimation with modified phasor approach and Laguerre deconvolution: a comparative study. *Methods and Applications in Fluorescence* **5**, 035003. ISSN: 2050-6120 (Sept. 2017).

312. Hardesty, D. A. & Sanai, N. The Value of Glioma Extent of Resection in the Modern Neurosurgical Era. *Frontiers in Neurology* **3**. ISSN: 1664-2295. doi:10.3389/fneur.2012.00140. <http://journal.frontiersin.org/article/10.3389/fneur.2012.00140/abstract> (2016) (2012).
313. Giuliani, A. *et al.* DISCO: a low-energy multipurpose beamline at synchrotron SOLEIL. eng. *Journal of Synchrotron Radiation* **16**, 835–841. ISSN: 1600-5775 (Nov. 2009).
314. Poulon, F. *et al.* Comparison between fresh and fixed human biopsies using spectral and life-time measurements: Fluorescence analysis using one and two photon excitations in (IEEE, Sept. 2015), 25–28. ISBN: 978-1-4673-6516-1. doi:10.1109/ICABME.2015.7323242. <http://ieeexplore.ieee.org/document/7323242/> (2018).
315. Jamme, F. *et al.* Deep UV autofluorescence microscopy for cell biology and tissue histology: Deep UV autofluorescence microscopy. en. *Biology of the Cell* **105**, 277–288. ISSN: 02484900 (July 2013).
316. Pradère, B. *et al.* Two-photon optical imaging, spectral and fluorescence lifetime analysis to discriminate urothelial carcinoma grades. en. *Journal of Biophotonics*, e201800065. ISSN: 1864063X (May 2018).
317. Pradhan, A. *et al.* Steady state and time-resolved fluorescence properties of metastatic and non-metastatic malignant cells from different species. *Journal of Photochemistry and Photobiology B: Biology* **31**, 101–112. ISSN: 1011-1344 (Dec. 1995).
318. Stuntz, E. *et al.* Endogenous Two-Photon Excited Fluorescence Imaging Characterizes Neuron and Astrocyte Metabolic Responses to Manganese Toxicity. en. *Scientific Reports* **7**. ISSN: 2045-2322. doi:10.1038/s41598-017-01015-9. <http://www.nature.com/articles/s41598-017-01015-9> (2017) (Dec. 2017).
319. *Glioblastoma multiforme* <http://www.pathologyoutlines.com/topic/cnstumorglioblastoma.html> (2018).
320. *Meningioma* <http://www.pathologyoutlines.com/topic/cnstumormeningiomageneral.html> (2018).
321. *Metastases to CNS - General* <http://www.pathologyoutlines.com/topic/cnstumormetastaticcarcinoma.html> (2018).
322. Pekmezci, M. & Perry, A. Neuropathology of brain metastases. *Surgical Neurology International* **4**, S245–S255. ISSN: 2229-5097 (May 2013).
323. Rorke, L. B. Pathologic diagnosis as the gold standard. *Cancer* **79**, 665–667. ISSN: 1097-0142.
324. Bruner, J. M., Inouye, L., Fuller, G. N. & Langford, L. A. Diagnostic discrepancies and their clinical impact in a neuropathology referral practice. eng. *Cancer* **79**, 796–803. ISSN: 0008-543X (Feb. 1997).
325. Intraobserver reproducibility in assigning brain tumors to classes in the World Health Organization diagnostic scheme. The Childhood Brain Tumor Consortium. eng. *Journal of Neuro-Oncology* **7**, 211–224. ISSN: 0167-594X (Sept. 1989).
326. Takei, H. & Powell, S. Z. en. in *Methods of Cancer Diagnosis, Therapy, and Prognosis* 33–51 (Springer, Dordrecht, 2011). ISBN: 978-90-481-8664-8 978-90-481-8665-5. doi:10.1007/978-90-481-8665-5\_4. [https://link.springer.com/chapter/10.1007/978-90-481-8665-5\\_4](https://link.springer.com/chapter/10.1007/978-90-481-8665-5_4) (2018).

## BIBLIOGRAPHY

327. Heikal, A. A. Intracellular coenzymes as natural biomarkers for metabolic activities and mitochondrial anomalies. *Biomarkers in medicine* **4**, 241–263. ISSN: 1752-0363 (Apr. 2010).
328. Varone, A. *et al.* Endogenous two-photon fluorescence imaging elucidates metabolic changes related to enhanced glycolysis and glutamine consumption in precancerous epithelial tissues. eng. *Cancer Research* **74**, 3067–3075. ISSN: 1538-7445 (June 2014).
329. Wu, S. *et al.* Quantitative evaluation of redox ratio and collagen characteristics during breast cancer chemotherapy using two-photon intrinsic imaging. *Biomedical Optics Express* **9**, 1375–1388. ISSN: 2156-7085 (Feb. 2018).
330. Palmer, S., Litvinova, K., Rafailov, E. U. & Nabi, G. Detection of urinary bladder cancer cells using redox ratio and double excitation wavelengths autofluorescence. *Biomedical Optics Express* **6**, 977–986. ISSN: 2156-7085 (Feb. 2015).
331. Adur, J., Carvalho, H. F., Cesar, C. L. & Casco, V. H. Nonlinear optical microscopy signal processing strategies in cancer. eng. *Cancer Informatics* **13**, 67–76. ISSN: 1176-9351 (2014).
332. Lin, S.-J. *et al.* Discrimination of basal cell carcinoma from normal dermal stroma by quantitative multiphoton imaging. EN. *Optics Letters* **31**, 2756–2758. ISSN: 1539-4794 (Sept. 2006).
333. Cicchi, R. *et al.* Nonlinear laser imaging of skin lesions. eng. *Journal of Biophotonics* **1**, 62–73. ISSN: 1864-0648 (Mar. 2008).
334. Liu, N. *et al.* Label-free imaging characteristics of colonic mucinous adenocarcinoma using multiphoton microscopy. en. *Scanning* **35**, 277–282. ISSN: 1932-8745.
335. Jiang, L. *et al.* Label-free imaging of brain and brain tumor specimens with combined two-photon excited fluorescence and second harmonic generation microscopy. *Laser Physics Letters* **14**, 105401. ISSN: 1612-2011, 1612-202X (Oct. 2017).
336. Pointer, K. B. *et al.* Association of collagen architecture with glioblastoma patient survival. eng. *Journal of Neurosurgery* **126**, 1812–1821. ISSN: 1933-0693 (June 2017).
337. Senner, V., Ratzinger, S., Mertsch, S., Grässel, S. & Paulus, W. Collagen XVI expression is upregulated in glioblastomas and promotes tumor cell adhesion. en. *FEBS Letters* **582**, 3293–3300. ISSN: 00145793 (Oct. 2008).
338. Lasch, P., Haensch, W., Naumann, D. & Diem, M. Imaging of colorectal adenocarcinoma using FT-IR microspectroscopy and cluster analysis. eng. *Biochimica Et Biophysica Acta* **1688**, 176–186. ISSN: 0006-3002 (Mar. 2004).
339. Ali, S. M. *et al.* Raman spectroscopic analysis of human skin tissue sections *ex-vivo* : evaluation of the effects of tissue processing and dewaxing. en. *Journal of Biomedical Optics* **18**, 061202. ISSN: 1083-3668 (Nov. 2012).
340. Georgakoudi, I. & Quinn, K. P. Optical Imaging Using Endogenous Contrast to Assess Metabolic State. en. *Annual Review of Biomedical Engineering* **14**, 351–367. ISSN: 1523-9829, 1545-4274 (Aug. 2012).
341. Alonzo, C. A. *et al.* Two-photon excited fluorescence of intrinsic fluorophores enables label-free assessment of adipose tissue function. en. *Scientific Reports* **6**. ISSN: 2045-2322. doi:10.1038/srep31012. <http://www.nature.com/articles/srep31012> (2018) (Nov. 2016).
342. Baker, M. in, – (IOP Publishing, 2016). doi:10.1088/978-1-6817-4071-3ch3. <http://iopscience.iop.org/chapter/978-1-6817-4071-3/bk978-1-6817-4071-3ch3> (2018).



343. Gu, M., Bao, H. C. & Li, J. L. Cancer-cell microsurgery using nonlinear optical endomicroscopy. eng. *Journal of Biomedical Optics* **15**, 050502. ISSN: 1560-2281 (Oct. 2010).
344. Bao, H., Boussioutas, A., Aleixandria, M., Busuttil, R. & Gu, M. GASTROINTESTINAL ABNORMALITIES IDENTIFIED BY FLUORESCENCE ENDOMICROSCOPY. en. *Journal of Innovative Optical Health Sciences* **05**, 1250026. ISSN: 1793-5458, 1793-7205 (Oct. 2012).
345. Chang, Y.-C. *et al.* Two-photon fluorescence correlation spectroscopy through a dual-clad optical fiber. eng. *Optics Express* **16**, 12640–12649. ISSN: 1094-4087 (Aug. 2008).
346. Chang, Y.-C. *et al.* Two-photon in vivo flow cytometry using a fiber probe. *Proceedings of SPIE—the International Society for Optical Engineering* **7173**, 71730I–1–71730I–10. ISSN: 0277-786X (Feb. 2009).
347. Liang, W., Hall, G., Messerschmidt, B., Li, M.-J. & Li, X. Nonlinear optical endomicroscopy for label-free functional histology in vivo. en. *Light: Science & Applications* **6**, e17082. ISSN: 2047-7538 (Nov. 2017).
348. Tang, S., Krasieva, T. B., Chen, Z., Tempea, G. & Tromberg, B. J. Effect of pulse duration on two-photon excited fluorescence and second harmonic generation in nonlinear optical microscopy. eng. *Journal of Biomedical Optics* **11**, 020501. ISSN: 1083-3668 (Apr. 2006).
349. Duan, C., Tanguy, Q., Pozzi, A. & Xie, H. Optical coherence tomography endoscopic probe based on a tilted MEMS mirror. EN. *Biomedical Optics Express* **7**, 3345–3354. ISSN: 2156-7085 (Sept. 2016).
350. Liu, J.-J., Droller, M. J. & Liao, J. C. New Optical Imaging Technologies for Bladder Cancer: Considerations and Perspectives. *The Journal of urology* **188**, 361–368. ISSN: 0022-5347 (Aug. 2012).
351. Hsu, M., Gupta, M., Su, L.-M. & Liao, J. C. Intraoperative Optical Imaging and Tissue Interrogation During Urologic Surgery. *Current opinion in urology* **24**, 66–74. ISSN: 0963-0643 (Jan. 2014).
352. Wu, K. *et al.* Dynamic real-time microscopy of the urinary tract using confocal laser endomicroscopy. eng. *Urology* **78**, 225–231. ISSN: 1527-9995 (July 2011).
353. Aboumarzouk, O. *et al.* Laser-induced autofluorescence spectroscopy: Can it be of importance in detection of bladder lesions? en. *Photodiagnosis and Photodynamic Therapy* **12**, 76–83. ISSN: 15721000 (Mar. 2015).

## Appendix A

Paper : Characterization of fiber  
ultrashort pulse delivery for  
nonlinear endomicroscopy

# Characterization of fiber ultrashort pulse delivery for nonlinear endomicroscopy

A. Ibrahim,<sup>1</sup> F. Poulon,<sup>1</sup> R. Habert,<sup>3</sup> C. Lefort,<sup>4</sup> A. Kudlinski,<sup>3</sup> and D. Abi Haidar<sup>1,2,\*</sup>

<sup>1</sup>Laboratoire IMNC, UMR 8165-CNRS, Orsay, France

<sup>2</sup>Université Paris 7-Paris DIDEROT, F-75013, Paris, France

<sup>3</sup>Université Lille, CNRS, UMR 8523 - PhLAM - Physique des Lasers Atomes et Molécules, F-59000 Lille, France

<sup>4</sup>Laboratoire XLIM, UMR 7252, CNRS, F-87000 Limoges, France

\*[abihaidar@imnc.in2p3.fr](mailto:abihaidar@imnc.in2p3.fr)

**Abstract:** In this work, we present a detailed characterization of a small-core double-clad photonic crystal fiber, dedicated and approved for *in vivo* nonlinear imaging endomicroscopy. A numerical and experimental study has been performed to characterize the excitation and collection efficiencies through a 5 m-long optical fiber, including the pulse duration and spectral shape. This was first done without any distal optics, and then the performances of the system were studied by using two kinds of GRIN lenses at the fiber output. These results are compared to published data using commercial double clad fibers and GRIN lenses.

©2016 Optical Society of America

**OCIS codes:** (190.0190) Nonlinear optics; (120.3890) Medical optics instrumentation; (120.3620) Lens system design; (060.2350) Fiber optics imaging; (130.3120) Integrated optics devices; (170.2150) Endoscopic imaging.

---

## References and links

1. C. Odin, T. Guilbert, A. Alkilani, O. P. Boryskina, V. Fleury, and Y. Le Grand, "Collagen and myosin characterization by orientation field second harmonic microscopy," *Opt. Express* **16**(20), 16151–16165 (2008).
  2. M. Monici, "Cell and tissue autofluorescence research and diagnostic applications," *Biotechnol. Annu. Rev.* **11**, 227–256 (2005).
  3. S. Huang, A. A. Heikal, and W. W. Webb, "Two-photon fluorescence spectroscopy and microscopy of NAD(P)H and flavoprotein," *Biophys. J.* **82**(5), 2811–2825 (2002).
  4. X. Jiang, J. Zhong, Y. Liu, H. Yu, S. Zhuo, and J. Chen, "Two-photon fluorescence and second-harmonic generation imaging of collagen in human tissue based on multiphoton microscopy," *Scanning* **33**(1), 53–56 (2011).
  5. S. Zhuo, J. Chen, T. Luo, D. Zou, and J. Zhao, "Multimode nonlinear optical imaging of the dermis in ex vivo human skin based on the combination of multichannel mode and Lambda mode," *Opt. Express* **14**(17), 7810–7820 (2006).
  6. C. Lefort, H. Hamzeh, F. Louradour, F. Pain, and D. A. Haidar, "Characterization, comparison, and choice of a commercial double-clad fiber for nonlinear endomicroscopy," *J. Biomed. Opt.* **19**(7), 076005 (2014).
  7. H. Hamzeh, C. Lefort, F. Pain, and D. Abi Haidar, "Optimization and characterization of nonlinear excitation and collection through a gradient-index lens for high-resolution nonlinear endomicroscopy," *Opt. Lett.* **40**(5), 808–811 (2015).
  8. H. Choi, S.-C. Chen, D. Kim, P. T. So, and M. L. Culpepper, "Design of a nonlinear endomicroscope biopsy probe," in (Optical Society of America, 2006), p. Tu169.
  9. F. Braud, T. Mansuryan, G. Ducourthial, R. Habert, A. Kudlinski, and F. Louradour, "Double clad photonic crystal fiber for high resolution nonlinear endomicroscopy," in (OSA, 2014), p. SoW3B.2.
  10. G. Ducourthial, P. Leclerc, T. Mansuryan, M. Fabert, J. Brevier, R. Habert, F. Braud, R. Batrin, C. Vever-Bizet, G. Bourg-Heckly, L. Thiberville, A. Druilhe, A. Kudlinski, and F. Louradour, "Development of a real-time flexible multiphoton microendoscope for label-free imaging in a live animal," *Sci. Rep.* **5**, 18303 (2015).
  11. W. J. Wadsworth, R. M. Percival, G. Bouwmans, J. C. Knight, T. A. Birks, T. D. Hedley, and P. St. J. Russell, "Very High Numerical Aperture Fibers," *Photonics Technol. Lett. IEEE* **16**, 843–845 (2004).
  12. C. Lefort, T. Mansuryan, F. Louradour, and A. Barthelemy, "Pulse compression and fiber delivery of 45 fs Fourier transform limited pulses at 830 nm," *Opt. Lett.* **36**(2), 292–294 (2011).
  13. K. König, A. Ehlers, I. Riemann, S. Schenk, R. Bückle, and M. Kaatz, "Clinical two-photon microendoscopy," *Microsc. Res. Tech.* **70**(5), 398–402 (2007).
  14. W. R. Zipfel, R. M. Williams, and W. W. Webb, "Nonlinear magic: multiphoton microscopy in the biosciences," *Nat. Biotechnol.* **21**(11), 1369–1377 (2003).
  15. H. Bao, A. Boussioutas, R. Jeremy, S. Russell, and M. Gu, "Second harmonic generation imaging via nonlinear endomicroscopy," *Opt. Express* **18**(2), 1255–1260 (2010).
-

## 1. Introduction

Two-Photon Microscopy (TPM) has become a standard technique extensively used for imaging optically thick biological tissues [1]. It is able to provide a wealth of information about specific structures without exogenous fluorescent labels. This performance is achieved through various endogenous contrasts: (1) Second Harmonic Generation (SHG), to highlight specific elements, such as myosins and collagens [1], and (2) fluorescence under two photon excitation (TPE), to investigate endogenous fluorophores, such as reduced nicotinamide adenine dinucleotide (NADH) and Flavin, a well-known biomarkers of cellular energy metabolism [3,4]. TPM provide intrinsic sectioning, lack of out-of-focus photobleaching, a localized phototoxicity, important penetration depth due to decreased scattering from long infrared excitation wavelengths and absence of overlapping between excitation and emission. Despite these advantages, the TPM is still limited to laboratory thick tissues testing. Currently, its main applications are focused on fixed or ex vivo samples and in vivo tests are limited to animals. The systems available nowadays to image in vivo human tissues are macroscopic and can only be applied at the skin level [4,5]. A more dedicated solution to study in vivo and in situ human tissues could be nonlinear endomicroscopy. It presents the advantages of TPM and gives the possibility to an in vivo and in situ tissues imaging without resorting to a surgical biopsy, thanks to the use of a thin and elongated optical fiber coupled with miniaturized objective lens instead of the microscope objective. It allows less invasive tests and earlier detection of diseases.

The development of such nonlinear endomicroscopic systems requires a specific attention to the choice of the endoscopic fiber. It should be able to preserve the temporal confinement of short pulses that need to be delivered to the distal optics for different excitation wavelengths. For that, dispersion pre-compensation schemes are usually employed. This fiber should also have a small core diameter to reach high imaging resolution via miniaturized optics as well as a high inner cladding numerical aperture (NA) to be able to collect endogenous weak fluorescence signals. This is usually done using so-called double-clad fibers (DCFs).

By referring to the literature, and to our previous study, different commercially available DCFs were compared and characterized with and without miniaturized objective [6,7]. The DCF DC-165-16-P from NKT Photonics [8], a microstructured fiber, turned out to be the best in terms of single-mode delivery of ultrashort pulses around 800 nm. However, its core diameter (around 16  $\mu\text{m}$ ) is a real problem for the miniaturization of the distal optic. The resulting optical resolution is inevitably altered and worse, compared to a DCF with a smaller core but a doped inner cladding, such as the Fibercore SMM900. Based on these results we were convinced that the ideal fiber did not exist yet. Consequently, it was necessary to conceive a specific DCF combining a small and undoped silica core with a high inner cladding numerical aperture (NA). Such a fiber will deliver high-quality excitation pulses with a low level of optical aberrations in the distal optics, and the highest level of nonlinear signal collection with miniaturized optical lenses. Such a small-core double-clad photonic crystal fiber (DC-PCF), specially designed for the two-photon endomicroscope, has been published recently in the context of the development of an endomicroscope [9,10]. This fiber was able to achieve efficient non-linear endomicroscope images.

This work represents a continuity of our previous studies based on characterization of commercial DCFs [6,7]. Here we extend it to the very recently introduced small-core double-clad photonic crystal fiber (DC-PCF) joined to different GRIN lenses [9,10]. We provide a full characterization of the output short pulse properties and collection efficiency from a scattering sample for input pulse duration in the range 100-300 fs and wavelength of 750-900 nm as a function of pump power, showing efficient femtosecond pulse delivery of the system made of the DC-PCF coupled to a GRISM pre-compensation scheme and GRIN lenses over this whole range of parameters.

## 2. Materials and methods

### 2.1. Customized DC-PCF design

This customized DC-PCF is shown in Fig. 1(a) and 1(b). The hole-to-hole spacing and relative hole diameter are respectively  $3.5\mu\text{m}$  and  $0.41$ . The central core has a diameter of  $6.4\mu\text{m}$  and is single-mode at  $800\text{ nm}$ . It is surrounded by an air/silica microstructured region of  $40\mu\text{m}$  diameter. The DC-PCF used here is  $5\text{ m}$ -long, which is 5 times longer than commercial fibers typically used for the same purpose. The NA of the small core at  $800\text{ nm}$  is  $0.097$ , the second order dispersion coefficient is  $\beta_2 = 2.9 \times 10^{-26}\text{ s}^2/\text{m}$  and the nonlinear parameter is  $\gamma = 10.5\text{ W}^{-1}.\text{km}^{-1}$  at this wavelength. The fiber presents a second microstructure (ring of large air holes) to separate the collecting inner cladding from the outer maintaining cladding. The size of the bridge between the air holes will determine the NA of the inner cladding: the smaller is the bridge, the higher is the numerical aperture [11]. Here the thickness of silica bridges between air holes is around  $500\text{ nm}$ , and the NA of the inner cladding was measured to be  $0.27$  at  $450\text{ nm}$ . This fiber regroups the advantages of a microstructured fiber, by using an undoped core to avoid autofluorescence, but has a smaller core diameter than the NKT Photonics DCF, giving a better axial and lateral resolution.

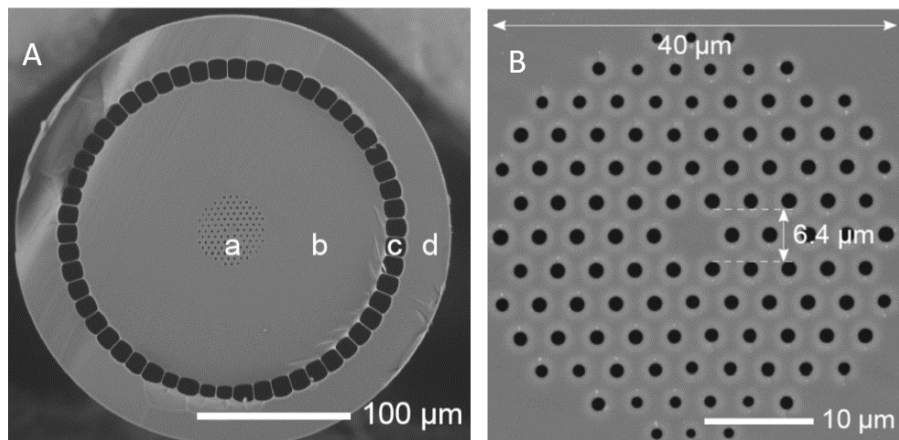


Fig. 1. A. Scanning electron microscope image of the DC PCF. a) Core region surrounded by an air-silica microstructure b) Collecting cladding c) Low index air cladding d) Maintaining cladding. B. Details of the air-silica microstructure around the core.

### 2.2. Setup design for ultra-short pulse delivery characterization

The architecture of the proposed endomicroscope, presented in Fig. 2, is composed of a femtosecond titanium sapphire oscillator (Ti:Sa, Mai Tai DeepSee, eHP, Spectra physics). A Faraday Isolator (FI), placed at the laser output, avoids back reflection from the fiber input face and destabilization of the pulse in the laser cavity.

A pre-compensation unit is used to compensate dispersion (second and third orders simultaneously) and nonlinear effects (mainly self-phase modulation) appearing inside the endoscopic fiber [10]. This unit is composed of a first polarization-maintaining single mode fiber (SMF) ( $0.5\text{ m}$ ) used to broaden the spectrum in order to be able to reach a shorter pulse duration afterwards [12]. It is followed by a GRISM-based anomalous stretcher, consisting in the assembly of a diffraction grating with a prism [6,7,12]. Pulses are then coupled into the endoscopic DC-PCF. It allows simultaneous excitation by the small core and fluorescence collection from the tissue by the inner cladding. The focusing of the light in the specimen is achieved using a specific miniature GRIN lens. The response through the  $5\text{ m}$ -long DC-PCF

and the GRIN lenses was characterized spectrally and temporally using respectively a spectrometer (FLAME-S-VIS-NIR-ES 1, Ocean optics spectrometer, France) and an autocorrelator (Mini-PMT-NIR, AA11.08.01.03, APE). Two different pulse durations were set at the output of the laser cavity using the Deepsee system. The first one, around 300 fs, is a pulse duration used classically in nonlinear microscopy. The second one, around 100 fs, is close to the optimal pulse duration obtained when using a Deepsee after the laser oscillator.

This DC-PCF has been made to excite the sample and collect fluorescence signals at the same time, using a dichroic mirror, Fig. 2. Laser light goes through the GRIN lens to be focused on the sample (Rhodamine) insuring maximum excitation. Fluorescence emitted by the Rhodamine is detected by the second core of the DC-PCF and lead through the dichroic mirror to the spectrometer (QE Pro, Ocean optics spectrometer, France).

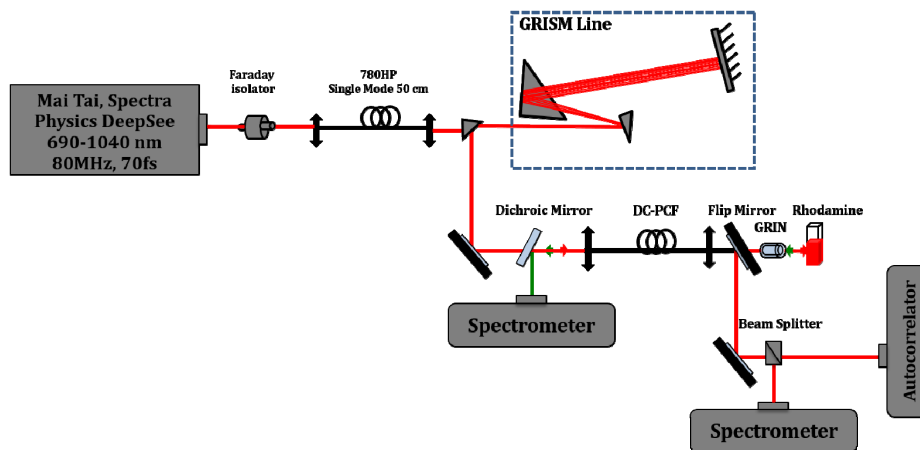


Fig. 2. Experimental setup.

### 2.3. GRIN lenses

Two different GRIN lenses adapted to wavelengths between 800 and 900 nm were used. The first one (GRIN 1) coded GT-MO-080-018-810 has a 1.4 mm diameter. It is a complex optical system with a spherical lens and two GRIN lenses fabricated with a special gradient profile. Its object space NA is 0.8, and the image space NA is 0.18. The total length of this lens is 7.53 mm. In the second lens (GRIN 2) coded GT-MO-080-0415-810, the image space NA is 0.4 and the length is 4 mm. Both GRINs, fabricated by GRINTECH, are mounted in stainless steel tubing. The differences in the image space NA could affect the collection of the fiber output signal. The difference in length could also affect dispersion and pulse duration.

## 3. Results

### 3.1 Efficient excitation using the DC-PCF fiber for different excitation wavelengths and cavity output pulse duration

Two different pulse durations were set at the output of the laser cavity using the Deepsee system. The first one, around 300 fs, is a pulse duration used classically in nonlinear microscopy. The second one, around 100 fs, is close to the optimal pulse duration obtained when using a Deepsee after the laser oscillator. These two extreme durations allow us to estimate the capacity of our system to optimize the pulse at the output of the endoscopic fiber. These measurements were performed for different excitation wavelengths from 750 to 900 nm. The temporal measurements to characterize the fiber and the two GRINs are summarized in Table 1. At each wavelength, the GRISM line mentioned above was optimized in order to get the shortest pulse duration at the output of the system. The pulse duration is obtained by

measuring the full width at half maximum (FWHM) from the autocorrelator data using a Gaussian profile for the deconvolution.

For a pulse duration of 300 fs at the output of the laser cavity, the shortest pulse duration at the output of the endoscopic fiber is approximately 42 fs for a 810 nm excitation wavelength. This value decreases to 33 fs with a laser output cavity pulse at 100 fs, presented in Fig. 3(b). Moreover, by fixing the laser pulse duration at the output of the cavity to 100 fs, we notice that the difference between the shortest and the longest pulse duration at the output of the DC-PCF is 72 fs at the different wavelength, while for a 100 fs laser pulse duration the difference is only 27 fs. The variability of the output pulse duration of the system especially for 100 fs cavity pulse duration is low, highlighting the tenability of our setup. This point is especially important in the context of *in vivo* endogenous fluorescence imaging which frequently requires the use of different excitation wavelengths depending upon the tissue nature.

**Table 1. Measured Pulse Duration at the Output of the Endoscopic Fiber Alone, with Grin 1 and with Grin 2 for Different Laser Cavity Pulse Durations**

	Laser Cavity output pulse at 300 fs			Laser Cavity output pulse at 100 fs		
	DC-PCF	DC- PCF + G1	DC- PCF + G2	DC-PCF	DC-PCF + G1	DC-PCF + G2
750 nm	72 ± 3,6	84 ± 4,2	80 ± 4	60 ± 3	70 ± 3,5	65 ± 3,25
780 nm	69 ± 3,45	76 ± 3,8	74 ± 3,7	55 ± 2,75	62 ± 3,1	59 ± 2,95
800 nm	45 ± 2,25	65 ± 3,25	63 ± 3,15	33 ± 1,65	50 ± 2,5	45 ± 2,25
810 nm	42 ± 2,1	53 ± 2,65	51 ± 2,55	33 ± 1,65	42 ± 2,1	40 ± 2
860 nm	64 ± 3,2	75 ± 3,75	87 ± 4,35	49 ± 2,45	58 ± 2,9	58 ± 2,9
890 nm	85 ± 4,25	136 ± 6,8	93 ± 4,65	55 ± 2,75	75 ± 3,75	70 ± 3,5
900 nm	114 ± 5,7	150 ± 7,5	105 ± 5,25	58 ± 2,9	90 ± 4,5	78 ± 3,9

### 3.2 Coupling GRINs lenses to the DC-PCF

Two conditions are required for nonlinear absorption: spatial and temporal confinement of the excitation pulses. Temporal confinement is obtained thanks to the optimal adjustment of the GRISM line, compensating simultaneously for the second and the third orders of dispersion of the endoscopic system. For spatial confinement, this new fiber was also coupled with GRIN lenses. By that, spatial and temporal confinements of the excitation are acquired for efficient nonlinear excitation. Consequently, imaging of tissues with a high resolution is expected. The GRIN lens with a radial refractive index and a high numerical aperture (NA) has been already validated for clinical use [13] due to their flat surface and small diameter.

Since the 100 fs laser pulses give the best performances as shown above, we chose to analyze the effect of the GRIN lenses on the pulse duration at the endoscopic system output with this laser setup. Adding respectively GRIN1 or GRIN2 at the DC-PCF output affects marginally the response of the pulse duration. For example, at 810 nm, we have the pulse duration values of 33 fs, 42 fs, and 40 fs respectively for the DC-PCF alone, the DC-PCF coupled to the GRIN1 and the DC-PCF coupled to the GRIN2. This difference of 24% or 19% between the fiber alone and the fiber coupled to GRIN 1 or 2 is due to the two distinct dispersion characteristics of these two GRIN lenses. This means that adding GRIN lenses do not affect the pulse duration confinement significantly; subsequently excitation quality is not affected. These results are also highlighted in Fig. 3(c).

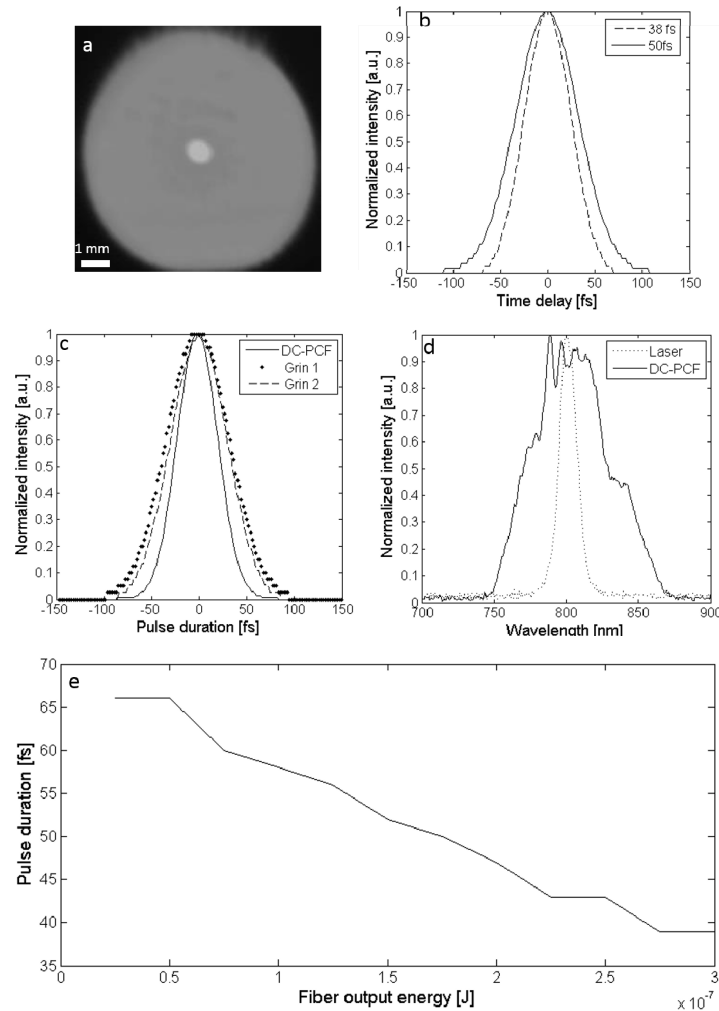


Fig. 3. The laser excitation is set to 800 nm (a) Delivery of the fundamental mode of the light after adjusting the collimation at the first fiber output. (b) The autocorrelation duration of the pulse at the output of DC-PCF obtained by adjusting the laser pulse duration respectively at 300 fs and 100 fs. (c) The optimal pulse duration obtained without GRIN and with GRIN 1 and GRIN 2. (d) Spectral characterization of the laser output and PhLAM fiber output. For these measurements, the wavelength and output power used were 800 nm and 20 mW (e) Pulse duration variation as a function of fiber output.

Experimentally, GRIN 2 gave a slight advantage in pulse duration compared to GRIN 1 at each wavelength, on average 7% shorter for GRIN 2, except at 860 nm where the pulse duration was the same. The spectral analysis performed on the short pulse throughout the setup is shown in Fig. 3(d). This figure presents the spectral shape at the laser cavity and the DC-PCF output. The DC-PCF output spectrum is wider than at the output of the laser thanks to the shaping module before the endoscopic fiber. This allows to obtain shorter compressed pulses. Figure 3(e) shows the variation of the DC-PCF pulse duration at the core with the laser operating at mean power. In the range from 2 mW to 24 mW, we note a reduction of pulse duration with higher power, from 66 fs at 2 and 4 mW, to 39 fs at 22 and 24 mW.



The DC-PCF was also compared numerically to the best commercial DCF presented in our previous study [7]. These numerical tests were performed with a Zemax (Optics Studio 14.2, Zemax LLC) simulation. The DC-PCF was coupled to two different GRIN lenses. The first one was a custom designed (GT-IRLS-050-11-50-NC) in order to be compared with our results previously published results [7], and the second one was the commercial GRIN 1 (GT-MO-080-018-810) used in the experimental measurements. The axial and lateral resolutions of the coupling of the fiber into these GRINs were characterized. These two parameters were computed in accordance with a method taken from the literature [14]. It represents the resolution at the FWHM, calculated from the spot in the focal plane of the GRIN, using a Gaussian beam approximation to simulate the output of the fiber and the propagation through the optics. The results are summarized in Table 2. The DC-PCF has a lateral resolution 2.5 times higher than the NKT Photonics DCF, and is 5-6 times better regarding the axial resolution, and only slightly less resolved than the Fibercore one (1.8 times less resolved).

**Table 2. Resolution of the Excitation Spot in the Focal Plan of the Two GRIN Lenses Coupled to Our Fiber**

Fiber	Core-Cladding diameters	Core NA	Homemade GRIN			GRIN-GT-MO-080-018-810		
			Lateral resolution ( $\mu\text{m}$ )	Axial resolution ( $\mu\text{m}$ )	Waist size ( $\mu\text{m}$ )	Lateral resolution ( $\mu\text{m}$ )	Axial resolution ( $\mu\text{m}$ )	Waist size ( $\mu\text{m}$ )
Fibercore (SMM900)	3.6-100	0.19	0.22	0.33	0.26	0.32	0.80	0.38
Crystal Fiber (DC-165-16 P)	16-163	0.04	1.00	7.99	1.20	1.44	16.61	1.73
DC-PCF (T904B)	6.4-268	0.097	0.40	1.28	0.48	0.58	2.67	0.69

### 3.3 Fluorescence collection efficiency using the DC-PCF

As explained in the introduction, the ability of a DCF to be used as an endoscopic fiber not only depends on its excitation properties, but also on its ability to collect the signal emitted by samples. The collection efficiency depends on the size of the DCF inner cladding (second core) and of its NA. The influence of the pulse duration and average power on the fluorescence emission level is analyzed here using Rhodamine as fluorescent solution. Fluorescent signal emitted by Rhodamine was characterized as a function of (i) the duration of the excitation pulse at the output of the DC-PCF, Fig. 4(a), and (ii) the output average beam power while the pulse duration is kept constant, Fig. 4(b). In this part, we used 1mM of rhodamine placed after the GRIN 2 lens. First we set the beam power at 14 mW at the focal volume, and we changed the pulse duration. We note that the fluorescence signals decrease by increasing pulse duration, but they were still detected until 330 fs, Fig. 4(a). This experiment confirms the importance of using short pulse duration to enhance the fluorescent signal. In second time, we set the pulse duration to 60 fs and we increase the power beam from 1 mW to 20 mW on focal volume. Note that 20 mW is more than sufficient for exciting endogenous fluorophores of tissues. This fiber is not autofluorescent and that was confirmed by measuring the collected fluorescence without sample at the output of the system. This measurement is defining the level of dark current and is not changing when increasing the power. We note that the fluorescence signals emitted decrease by decreasing the beam excitation power, Fig. 4(a). The variation of the excitation power, for fixed pulse duration, shows that it could be possible to reach 40 mW at the output of the DC-PCF while keeping the same spectral shape and without expecting autofluorescence from the fiber.

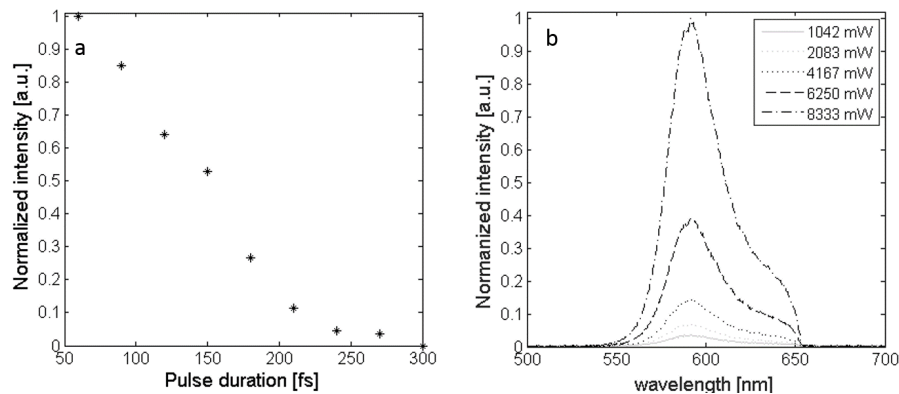


Fig. 4. Backward TPF from Rhodamine with the DC-PCF (a) Fluorescence intensity as a function of the DC-PCF and GRIN output pulse duration, normalized to the TPF intensity at 60 fs, (b) Rhodamine TPF as a function of the pulse peak power at DC-PCF output.

### 3.4 Transmission of the DC-PCF on a wide spectral range

In the majority of the cases, the endoscopic imaging requires to use various excitation wavelengths according to the aim of the study, and especially if based on the analysis of the endogenous molecules. Even when the excitation wavelength is fixed, various endogenous molecules can emit. To verify if this fiber is optimal for a wide range of excitation wavelength or for the collection of the emitted fluorescence by different molecules, a specific study is needed. For this, a spectral lamp (HPX-2000 Family, Ocean Optics, France) was used as sample. For this purpose, a monochromator devices was used to select wavelengths of this spectral lamp. The beam was collected at the output of this monochromator (Scanning Monochromator MonoScan2000, Ocean, Optics, France) and injected in the inner cladding of the DC-PCF. The beam power was measured at the input and output of this fiber to calculate the transmission coefficient every time we change the wavelength. The transmission from different wavelength and at a fixed fiber - sample distance was measured in order to define the transmission coefficient. Results prove that this fiber is able to collect different wavelength ranging from 200 to 1000 nm). We do not have an important variation in transmission coefficient except around wavelengths 340 nm and 850 nm, which presented the maximum of transmission coefficient.

## 4. Discussion and conclusion

A new double-clad photonic crystal fiber for nonlinear imaging has been presented and characterized experimentally and numerically. First, by using the shortest pulse possible at the laser cavity output, combined to a GRISM line, we were able to reach a pulse duration of 33 fs at the output of a 5 m endomicroscopic customized fiber without a miniaturized GRIN lens, and 40 fs at the output of the fiber coupled to a miniaturized GRIN lens. These values represent significant improvements over previously reported two-photon imaging that up to now have been restricted to picosecond pulses [15]. Obviously, we can fix the pulse compression to around 100 fs. In the future, we envisage making a study, which will allow us to estimate the potential benefits of these extremely short pulse durations for tissue imaging. This homemade fiber is 5-meters-long, which is appreciably much longer than the 1-meter-long commercial DCF usually tested in endomicroscopy setups. We have demonstrated that our setup is able to compensate for the dispersion through such long fibers, and to provide pulses as short as those obtained with 1-meter-long fibers. This presents a real advantage in medical imaging applications, indeed a 5-meters-long fiber will allow the placement of the optical head in the operating room, while the laser and compression system can be kept

outside in a non-sterilized environment. Secondly, by comparing our results to those previously reported [6] using a DCF, we note that in our case the spectral broadening after the DC-PCF is approximately the same. With this spectral large band, we hope to be able to excite different endogenous molecules. Thirdly, in order to ensure the coherence in our imaging studies, we can adjust our system in such a way as to minimize pulse duration variation when the excitation wavelength is changed. In addition, for all possible excitation wavelengths, we can obtain pulse durations shorter than 60 fs at the output of our DC-PCF by using laser pulse duration of 100 fs. This ensures a temporal confinement required for an optimal nonlinear excitation. The collection efficiency was measured for different pulses duration showing the importance of using short pulses when we expect tissue imaging. For a fixed pulse duration, experimental results show the enhancement of fluorescence signal with excitation power.

Finally, this new fiber coupled to a GRIN lens has a significantly better simulated resolution than other microstructured DCF (NKT Photonics DC-165-16 P) used in literature for endoscopic imaging and is not far from the performance of the best commercial DCF either, the Fibercore SMM900. Moreover, our fiber delivered shorter pulses than those generated by the Fibercore one [6], thus showing that the new DC-PCF has the advantages of an undoped core fiber, no risk of parasite autofluorescence, while maintaining an acceptable resolution for imaging with the same pulse duration performance.

The influence of the pulse duration and average power on the fluorescence collection was analyzed. We note that the fluorescence signals decrease by increasing pulse duration, but they were still detectable until 330 fs. The fluorescence signals emitted decrease by decreasing the beam excitation power.

Indeed the critical resolution with deep tissue imaging is the axial resolution, it has to be smaller than the characteristic size of the observed sample in order to have a sharp image and achieve z sectioning, here for the DC-PCF the axial resolution is about 1.5  $\mu\text{m}$  and the smallest characteristic size we observe in our biopsy sample, using a classical two-photon microscope, is approximately 10 microns. Finally, the characterization of the excitation and collection path through the DC-PCF shows that we found the homemade architecture to answer our technical specifications.

### Acknowledgments

This Work as a part of the MEVO project was supported by “Plan Cancer” program founded by INSERM (France), by CNRS with “Défi instrumental” grant, and the Institut National de Physique Nucléaire et de Physique des Particules (IN2P3). This work was done in the PIMPA Platform partly funded by the French program “Investissement d’Avenir” run by the “Agence Nationale pour la Recherche” (grant “Infrastructure d’avenir en Biologie Santé – ANR – 11-INBS-0006”). Co-authors from PhLAM acknowledge support from the “Fonds Européen de Développement Economique Régional”, the Labex CEMPI (ANR-11-LABX-0007) and Equipex FLUX (ANR-11-EQPX-0017) through the “Programme Investissements d’Avenir”. We warmly thank James M. Ablett from Synchrotron SOLEIL for valuable discussion.

## Appendix B

Paper : Spectral and fluorescence lifetime endoscopic system using a double-clad photonic crystal fiber

# Optics Letters

## Spectral and fluorescence lifetime endoscopic system using a double-clad photonic crystal fiber

A. IBRAHIM,<sup>1</sup> F. POULON,<sup>1</sup> F. MELOUKI,<sup>1</sup> M. ZANELLO,<sup>5</sup> P. VARLET,<sup>4</sup> R. HABERT,<sup>3</sup> B. DEVAUX,<sup>5</sup>  
A. KUDLINSKI,<sup>3</sup> AND D. ABI HAIDAR<sup>1,2,\*</sup>

<sup>1</sup>IMNC Laboratory, UMR 8165-CNRS/IN2P3, Paris-Saclay University, 91405 Orsay, France

<sup>2</sup>Université Paris Diderot, Sorbonne Paris Cité, F-75013 Paris, France

<sup>3</sup>Université Lille, CNRS, UMR 8523—PhLAM—Physique des Lasers Atomes et Molécules, F-59000 Lille, France

<sup>4</sup>Neuropathology Department, Sainte-Anne Hospital, 75014 Paris, France

<sup>5</sup>Neurosurgery Department, Sainte-Anne Hospital, 75014 Paris, France

\*Corresponding author: abihaidar@imnc.in2p3.fr

Received 3 August 2016; accepted 9 October 2016; posted 12 October 2016 (Doc. ID 270709); published 7 November 2016

**We present a customized small-core double-clad photonic crystal fiber for spectral and fluorescence lifetime measurements of human samples. In this Letter, the new fiber has been characterized on different fluorophores and samples of human brain tumor; a comparison to a bi-fiber homemade system and a commercial fiber probe was made.** © 2016 Optical Society of America

**OCIS codes:** (140.3490) Lasers, distributed-feedback; (060.2420) Fibers, polarization-maintaining; (060.3735) Fiber Bragg gratings; (060.2370) Fiber optics sensors.

<http://dx.doi.org/10.1364/OL.41.005214>

Minimally invasive surgery is becoming the gold standard of surgery today, even in surgical neurological oncology. Surgeons use several techniques to perform operations with a smaller wound opening, making it safer than classical open surgeries. In the 21st century, surgery requires new tools designed to slide into small surgical approaches and capable of giving fast and precise information on the tissue [1]. In order to provide clinically useful data on the human brain, endoscopic systems need to overcome the lack of precise guidance. The new mainstream approach is the use of multimodal optical detection. We aim to develop a multimodal multiphoton endomicroscope by working on a specific customized small-core double-clad photonic crystal endoscopic fiber (DC-PCF) which is able to achieve visible and IR excitation for multimodal analysis. Moreover, if our endoscopic fiber is able to achieve visible and IR excitation, it offers the possibility to add a varifocal objective [2,3] at the output of the system. Thus, it allows a large field of view and a high resolution in the same endomicroscope.

The customized microstructured DC-PCF is based on a central single-mode core with a diameter of 6.4  $\mu\text{m}$ . The core is surrounded by an air/silica microstructured region of 40  $\mu\text{m}$  diameter. The fiber presents a second microstructure (ring of large air holes) to separate the collecting inner cladding from

the outer maintaining cladding. The thickness of the silica bridges between the air holes is around 500 nm. The NA of the inner cladding is around 0.27 at 450 nm.

We prove the efficiency of this fiber to achieve ultrashort pulses for an efficient nonlinear excitation and collection [4].

In this Letter, we focus on the capacity of this fiber to achieve visible excitation, as well as to accomplish spectral and lifetime measurements from endogenous fluorescence of freshly extracted human samples.

In order to do this, the new DC-PCF fiber was brought into a fibered setup at the Saint-Anne hospital to replace a bi-fiber configuration used in a previous study [5–7]. This setup was placed in the Neuropathology Department of Sainte Anne Hospital (Paris, France) near the operating room to achieve measurements, as close as possible, to in vivo conditions. Bimodal optical signature characterization was performed on freshly resected samples taken during surgical resection of human brain tumors. These studies had the approval of the Sainte Anne Hospital Review Board (CPP: S.C. 3227).

The architectures of the new setup and the previously validated setup are presented in Fig. 1. The excitation was accomplished using a diode laser from Picoquant, emitted at 405 nm (LDHP-C-405B, FWHM 60 ps, Picoquant GmbH, Berlin, Germany) with a maximum power of 1 mW. The power and the repetition frequency are tunable. The repetition frequency varies between 2.5 and 40 MHz. The 405 nm excitation was chosen because it is able to excite five different endogenous molecules: nicotinamide adenine dinucleotide (NADH), flavin (FAD), lipopigment, porphyrin, and chlorin. For spectroscopic measurement, the fluorescence was directed toward a computer controlled spectrometer (QE 6500, Ocean Optics, Dunedin, USA) characterized by 1.5 nm as spectral resolution over a 200–1000 nm spectral range. The spectral measurements were processed using a homemade Matlab script [6]. Fluorescence lifetime was measured using an electronic acquisition card (Time Harp 200, Picoquant) that ensures synchronization between the laser and the detector (PMT) from PicoQuant (PMA 182) with a temporal resolution of

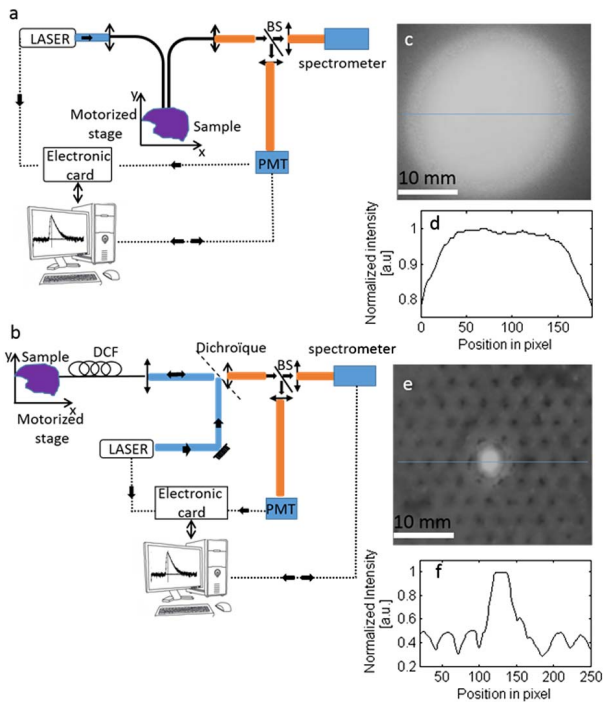


**Fig. 1.** Experimental set-up: (a) system 1 where the excitation and fluorescence collection are done with two different optical fibers and (b) system 2 where the excitation and fluorescence collection are performed with the same optical fiber. (c) Spot at the output of a mono-core optical fiber presenting a Gaussian form. (d) Profile of the spot at the output of a mono-core optical fiber. (e) Spot at the output of the DC-PCF presenting microstructures surrounding the main core. (f) Profile of the spot at the output of the DC-PCF.

220 ps. A motorized filter wheel (FW102C, Thorlabs, Newton, USA) was placed in the collection path, allowing us to select the emission band. We used five filters (Semrock, New York, USA) to separate the five endogenous fluorophores:  $450 \pm 10$  nm,  $520 \pm 10$  nm,  $550 \pm 30$  nm,  $620 \pm 10$  nm, and  $680 \pm 10$  nm. Data were adjusted by a mono-exponential fit via FluoFit software (FluoFit, PicoQuant) to recover the lifetimes from the measured fluorescence decays. The criterion for an acceptable fit was a  $\chi^2$  value less than 1.0, and the residuals were distributed around 0 within the interval 4 and -4. This procedure allows the reconstruction of a histogram of photon counting as a function of the time of fluorescence decay [8].

**System 1 (bi-fiber probe):** this customized bi-fiber system [as shown in Fig. 1(a)] uses a first fiber (HCG M0200T, multi-mode, core  $\varnothing 200$   $\mu\text{m}$ ) for the excitation and a second one (HCG M0365T, multimode, core  $\varnothing 365$   $\mu\text{m}$ ) to collect fluorescence (silica/silica step index fibers of inherent spatial resolution of 0.5 mm). A long pass filter (SR 405, Semrock, New York, USA) is placed in the collection path to remove the reflective signal due to the laser to the fluorescent signal. A beam splitter sends 70% of the fluorescent signal to the spectrometer and the remaining 30% into the PMT for lifetime measurements.

**System 2 (DC-PCF fiber probe):** in this configuration, only one fiber is used [as shown in Fig. 1(b)], to perform the excitation and the collection. We compared a commercial multi-mode fiber (QP600-1-UV-VIS, multi-mode, core  $\varnothing 600$   $\mu\text{m}$ , Ocean Optics) and our customized small-core double-clad photonic crystal fiber (DC-PCF, single mode, core

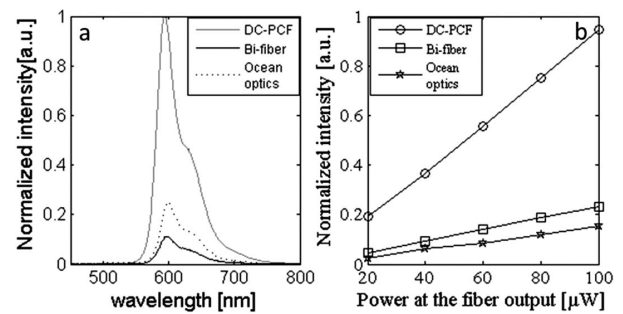


**Fig. 2.** (a) Fluorescence emission from rhodamine B ( $C = 0.1$  mM) collected through three different fibers at a laser excitation power of 40  $\mu\text{W}$ . (b) Maximum of collected fluorescence for different excitation laser power through three different fibers.

$\varnothing 6.4$   $\mu\text{m}$ ) using this setup. As presented in Figs. 1(c)–1(f), the laser beam is injected into the fiber to excite endogenous fluorophores of the human sample. The emitted fluorescent signal is collected by the same optical fiber. A dichroic filter (Di02-R405-25  $\times$  36, Semrock) removes the laser reflection, and only the fluorescent signal provided from the sample reaches the detectors. The remaining part of the setup is the same as in the bi-fiber configuration.

We compared one meter of DC-PCF with the bi-fiber system and the commercial multi-mode fiber described previously. This Letter was performed on a rhodamine B solution. The compared performances were the spectral shape, fluorescence collection efficiency, and fluorescence lifetime measurements. The spectral shape of the collected fluorescence for the same excitation power from rhodamine using these three different fibers is presented in Fig. 2(a). The DC-PCF fiber restitutes a perfect rhodamine spectrum Fig. 2(a), and at each laser power has a collection efficiency four times better than the two other systems Fig. 2(b). This result is due to the small core of DC-PCF, allowing an excitation in a small focal volume and the large clad, allowing an optimal collection of emitted fluorescence.

Table 1 shows the lifetime measurements of a rhodamine solution with different fibers: DC-PCF is able to measure the lifetime of a fluorophore as precisely as the two validated fibers. It gives values in accordance with the literature [9,10].

Specific attention to the robustness of our lifetime acquisition system is required prior to any measurement on human samples. We performed different measurements with the DC-PCF fiber on the well-known fluorophores rhodamine B and fluorescein. The concentration, solvent and pH of the solutions, and parameters affecting the lifetime measurements [6,7,11,12] were varied to validate the accuracy of our system. All other experimental parameters were kept the same.

Table 2 summarizes the lifetime measurements conducted on rhodamine B and the fluorescein solution. Two parameters changed: first, the concentration of the fluorophore in a solution of methanol and, second, the pH. The fluorescence lifetime of rhodamine B in methanol stayed constant over the concentration from  $10^{-4}$  M to  $10^{-6}$  M with a mean value  $2.2 \pm 0.06$  ns which is comparable to the literature value of  $2.38 \pm 0.07$  ns. The only value where it changes is at  $10^{-2}$  M, where the lifetime decrease is due to the reabsorption process at a higher concentration of the fluorophore; this has already



**Table 1. Lifetime Measurements of the Rhodamine B (RdB) with Different Collecting Fibers**

	DC-PCF $\tau$ (ns)	Bi-fiber $\tau$ (ns)	Multi-mode fiber $\tau$ (ns)	Literature $\tau$ (ns)
Rd (B) $c = 0.1$ mM	$1.98 \pm 0.06$	$1.98 \pm 0.04$	$1.93 \pm 0.05$	$1.75 \pm 1.80$

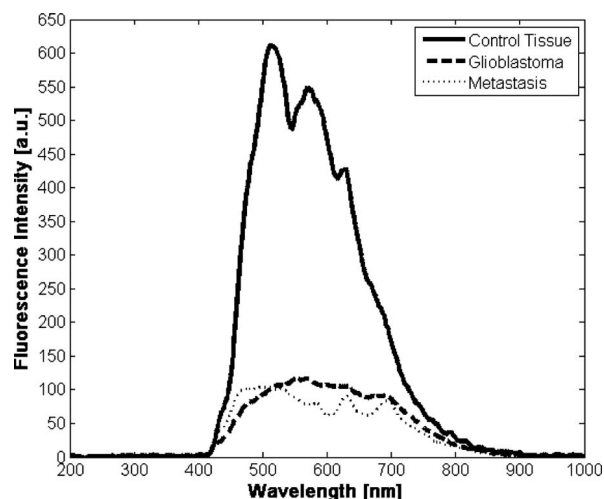
**Table 2. Lifetimes of Rhodamine B (RdB) and Fluorescein in Nanoseconds (ns)**

Concentration (M)	$10^{-2}$	$10^{-4}$	$10^{-5}$	$10^{-6}$
RdB (methanol) Exp.	$1.56 \pm 0.04$	$1.98 \pm 0.05$	$2.24 \pm 0.08$	$2.23 \pm 0.04$
RdB Lit. [14]	$1.68 \pm 0.05$	$2.43 \pm 0.08$	$2.41 \pm 0.07$	$2.32 \pm 0.06$
pH	7		5	
Fluorescence in Exp.	$4.61 \pm 0.05$		$4.16 \pm 0.2$	
Fluorescence in Lit. [10]	$4.2 \pm 0.1$		$3.6 \pm 0.1$	
RdB (PBS) Exp.	$1.79 \pm 0.2$		$1.79 \pm 0.2$	
RdB Lit. [10]	$1.8 \pm 0.1$		$1.8 \pm 0.1$	

been described in the literature [13]. We also made measurements at different pH values to validate the accuracy of our probe. These measurements were compared to the literature. The rhodamine is known to have a constant fluorescence lifetime through changes of pH, where the fluorescein presents a slight change of 0.6 ns from a basic to an acid solution [10]. Table 2 shows that we were able to have this level of precision with our system.

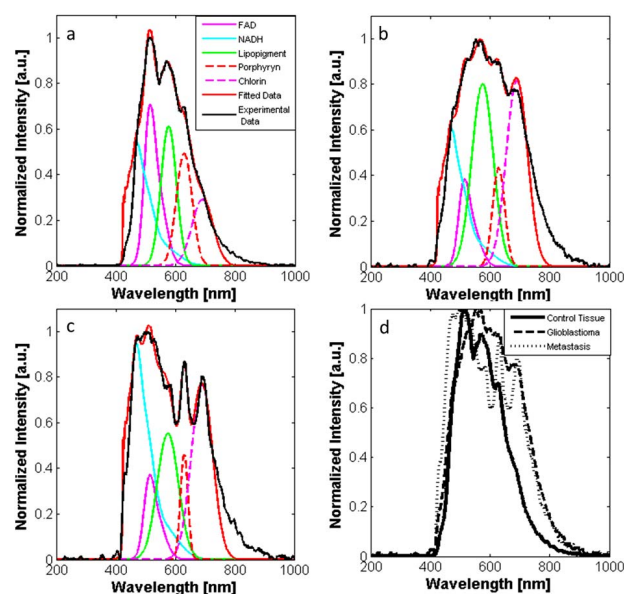
After these promising first results, the system was used on a small cohort of fresh human samples provided by the Sainte Anne Hospital Neurosurgery Department (Paris, France). The cohort had 12 samples from three different groups: two tumor groups glioblastoma ( $n = 4$ ) and metastasis ( $n = 5$ ), and one control group ( $n = 3$ ), provided from epilepsy surgery. The spectral and lifetime measurements were performed on the different samples with an excitation wavelength of 405 nm. After an optical analysis, all tissue specimens were formalin-fixed and returned to the Neuropathology Department of Sainte Anne Hospital. All samples underwent gold standard pathological analysis using both WHO 2007 and Sainte Anne's classifications.

Figure 3 shows the mean emission spectra for each sample group. We see a first distinction between tumorous and control

**Fig. 3.** Emission spectra of different fresh human samples using a 405 nm excitation wavelength.

groups: the maximum intensity of metastasis and glioblastoma groups is six times lower than the maximum intensity of the control group. These measurements show the sensitivity and success of this new DC-PCF fiber to accomplish measurements on endogenous fluorescence in human samples. To go further in the spectral analysis, we used a Matlab script developed in the lab to fit the different endogenous molecules that emit fluorescence in brain tissues. This script has already been used and validated in previous studies [6,7].

Figure 4 regroups the fitted data from metastasis, glioblastoma, and control groups. We note that in the two tumorous groups, porphyrin fluorescent emission is two times higher than in the control group, as shown in Figs. 4(b) and 4(c). In the metastasis group, the NADH is higher than in the control group and the glioblastoma group. Figure 4(d) represents a superposition of the average spectral response from each tissue group. It shows that the tumorous samples have a broader emission spectrum, mainly at the longer wavelength. Each

**Fig. 4.** Spectral emission of (a) the control group, (b) the glioblastoma group, and (c) the metastasis group with the five fluorophores fitted. (d) Superposition of normalized spectrum from each group.

**Table 3. Fluorescence Lifetimes of NADH, Flavin, Lipopigments (Lip), Porphyrin (PPX), and Chlorine in Three Different Groups of Fresh Biopsies**

Samples	NADH	FAD	Lip	PPX	Chlorin
Metastasis $n = 5$	$2.54 \pm 0.24$	$2.95 \pm 0.30$	$3.21 \pm 0.15$	$2.97 \pm 0.29$	$2.49 \pm 0.23$
Glioblastoma $n = 4$	$2.26 \pm 0.16$	$2.99 \pm 0.15$	$2.45 \pm 0.10$	$2.49 \pm 0.15$	$2.69 \pm 0.14$
Control $n = 3$	$3.95 \pm 0.30$	$3.64 \pm 0.15$	$4.09 \pm 0.11$	$3.74 \pm 0.2$	$3.28 \pm 0.13$

group has a specific spectral shape, as previously described [11,12].

Following endogenous spectral modification could allow non-invasive early detection of metabolic anomalies. NADH and FAD [15,16] play important roles in a wide range of cellular oxidation-reduction reaction. These natural biomarkers are diagnostic indicators of anomalies under different pathological conditions [17–19].

Nevertheless, despite first previous promising results [20,21], it seems that spectral analysis alone does not provide sufficient information on the histological nature of the tissue to help surgeons during intervention.

We developed a multimodal setup to obtain more data on the sample. These more complementary data can help building a robust matrix of criteria recognizing the tissue type during surgery: healthy or tumoral. In this setup, fluorescence lifetime measurement has been added to the spectral analysis. On each sample of the three groups (glioblastoma, metastasis and control), four regions of interest have been measured to establish the mean lifetime of the group. Table 3 shows the results of these lifetime measurements. For each endogenous fluorophore, the value of the control group is greater than the two tumorous groups. However, there is no evident trend to discriminate the two tumorous groups. Analyzing each fluorophore within a larger series could be interesting to define the best threshold between different tissue types.

This experiment was conducted at the Sainte-Anne hospital and has given us the opportunity to work with fresh resected samples. Our research raises the possibility that a new micro-structure fiber could be the best candidate to achieve an ideal multimodal endomicroscopic system. In contrast to commercial optical fibers, it allows reduction of the spectral acquisition time and uses a minimum of beam power at the output of the optical fiber. In addition, this fiber proved accurate in spectral and lifetime measurements when compared to the measurements in the literature. With this system, we were also able to give preliminary results on a human cohort and to distinguish three indicators of sample tumoral nature that seem to exist: a lower fluorescence intensity, a broader spectrum, and shorter lifetime value. This Letter represents the preliminary step before a study on more samples and *in vivo* during surgery, in order to help neurosurgeons during tumor resection.

**Funding.** Institut national de la santé et de la recherche médicale (INSERM)—“Plan Cancer” MEVO and IMOP Project; Centre National de la Recherche Scientifique (CNRS) (défi Instrumentation aux limites); Institut National

de Physique Nucléaire et de Physique des Particules (IN2P3); PIMPA platform—Agence Nationale de la Recherche (ANR) (ANR—11-INBS-0006).

## REFERENCES

1. K. W. Li, C. Nelson, I. Suk, and G. I. Jallo, *Neurosurg. Focus* **19**, 1 (2005).
2. D. G. Ouzounov, D. R. Rivera, W. W. Webb, J. Bentley, and C. Xu, *Opt. Lett.* **38**, 3103 (2013).
3. D. G. Ouzounov, D. R. Rivera, W. O. Williams, J. A. Stupinski, T. L. Southard, K. H. Hume, J. Bentley, R. S. Weiss, W. W. Webb, and C. Xu, *Biomed. Opt. Express* **4**, 1494 (2013).
4. A. Ibrahim, F. Poulon, R. Habert, C. Lefort, A. Kudlinski, and D. A. Haidar, *Opt. Express* **24**, 12515 (2016).
5. B. Leh, R. Siebert, H. Hamzeh, L. Menard, M.-A. Duval, Y. Charon, and D. Abi Haidar, *J. Biomed. Opt.* **17**, 108001 (2012).
6. D. A. Haidar, B. Leh, M. Zanello, and R. Siebert, *Biomed. Opt. Express* **6**, 1219 (2015).
7. M. Zanello, F. Poulon, P. Varlet, F. Chretien, F. Andreiulo, A. Ibrahim, J. Pallud, E. Dezamis, G. Abi-Lahoud, and F. Nataf, *J. Biophoton.* (2016).
8. S. Felekyan, R. Kühnemuth, V. Kudryavtsev, C. Sandhagen, W. Becker, and C. Seidel, *Rev. Sci. Instrum.* **76**, 083104 (2005).
9. N. Boens, W. Qin, N. Basarić, J. Hofkens, M. Ameloot, J. Pouget, J.-P. Lefèvre, B. Valeur, E. Gratton, M. vandeVen, N. D. Silva, Y. Engelborghs, K. Willaert, A. Sillen, G. Rumbles, D. Phillips, A. J. W. G. Visser, A. van Hoek, J. R. Lakowicz, H. Malak, I. Gryczynski, A. G. Szabo, D. T. Krajcarski, N. Tamai, and A. Miura, *Anal. Chem.* **79**, 2137 (2007).
10. A. G. Ryder, S. Power, T. J. Glynn, and J. J. Morrison, *Proc. SPIE* **4259**, 102 (2001).
11. P. V. Butte, B. K. Pikul, A. Hever, W. H. Yong, K. L. Black, and L. Marcu, *J. Biomed. Opt.* **10**, 064026 (2005).
12. L. Marcu, J. A. Jo, P. V. Butte, W. H. Yong, B. K. Pikul, K. L. Black, and R. C. Thompson, *Photochem. Photobiol.* **80**, 98 (2004).
13. M. Y. Berezin and S. Achilefu, *Chem. Rev.* **110**, 2641 (2010).
14. A. S. Kristoffersen, S. R. Erga, B. Hamre, and Ø. Frette, *J. Fluoresc.* **24**, 1015 (2014).
15. A. Mayevsky and G. G. Rogatsky, *AJP Cell Physiol.* **292**, C615 (2006).
16. M. A. Yaseen, S. Sakadžić, W. Wu, W. Becker, K. A. Kasischke, and D. A. Boas, *Biomed. Opt. Express* **4**, 307 (2013).
17. R. C. Benson, R. A. Meyer, M. E. Zaruba, and G. M. McKhann, *J. Histochem. Cytochem.* **27**, 44 (1979).
18. A. A. Heikal, *Biomark. Med.* **4**, 241 (2010).
19. S. Huang, A. A. Heikal, and W. W. Webb, *Biophys. J.* **82**, 2811 (2002).
20. E. Salomatina, B. Jiang, J. Novak, and A. N. Yaroslavsky, *J. Biomed. Opt.* **11**, 064026 (2006).
21. Y. Pu, W. Wang, Y. Yang, and R. R. Alfano, *Appl. Opt.* **52**, 1293 (2013).





## Appendix C

Paper : Two-photon optical imaging,  
spectral and fluorescence lifetime  
analysis to discriminate urothelial  
carcinoma grades

# Two-photon optical imaging, spectral and fluorescence lifetime analysis to discriminate urothelial carcinoma grades

**Authors:** B. Pradère<sup>1+</sup>, F. Poulon<sup>2+</sup>, E. Compérat<sup>3</sup>, I. Lucas<sup>4</sup>, D. Bazin<sup>5</sup>, S. Doizi<sup>1</sup>, O. Cussenot<sup>1</sup>, O. Traxer<sup>1</sup> and D. Abi Haidar<sup>2,6,\*</sup>

## Affiliations:

<sup>1</sup>Department of Urology, Hôpital Tenon, HUEP, AP-HP, Sorbonne University, Paris, France

<sup>2</sup>IMNC Laboratory, UMR 8165-CNRS/ IN2P3, Paris-Saclay university, 91405 Orsay, France.

<sup>3</sup> Department of Pathology, Hôpital Tenon, HUEP, AP-HP, Sorbonne University, Paris, France

<sup>4</sup>UPMC Univ Paris 06, Sorbonne Universités, UMR 8235, LISE, Paris, F-75252, France

<sup>5</sup> Laboratoire de Physique des Solides, CNRS UMR 8502, Université Paris Sud XI, Orsay, France; CNRS, Laboratoire de Chimie de la Matière Condensée de Paris, UPMC, Collège de France, Paris, France

<sup>6</sup> Paris Diderot University, Sorbonne Paris Cité, F-75013, Paris, France.

+these authors contributed equally to this work

## \* Corresponding author :

Darine Abi Haidar

IMNC/Université Paris Sud – Bat. 440 - 15 rue Georges Clémenceau 91405 Orsay Cedex, France

Tel : +33 1 69 15 56 29, [abihaider@imnc.in2p3.fr](mailto:abihaider@imnc.in2p3.fr)

**Keywords:** Bladder tumor, two-photon imaging, endomicroscopy, spectroscopy, fluorescence lifetime imaging

## Abstract:

In the framework of urologic oncology, mini-invasive procedures have increased in the last few decades particularly for urothelial carcinoma. One of the essential elements in the management of this disease is still the diagnosis, which strongly influences the choice of treatment. The histopathologic evaluation of the tumor grade is a keystone of diagnosis, and tumor characterization is not possible with just a macroscopic evaluation. Even today intraoperative evaluation remains difficult despite the emergence of new technologies which use exogenous fluorophore. This study assessed an optical multimodal technique based on endogenous fluorescence, combining qualitative and quantitative analysis, for the diagnostic of urothelial carcinoma. It was found that the combination of two photon fluorescence, second harmonic generation microscopy, spectral analysis and fluorescence lifetime

This article has been accepted for publication and undergone full peer review but has not been through the copyediting, typesetting, pagination and proofreading process, which may lead to differences between this version and the [Version of Record](#). Please cite this article as [doi: 10.1002/jbio.201800065](https://doi.org/10.1002/jbio.201800065)

imaging were all able to discriminate tumor from healthy tissue, and to determine the grade of tumors. Spectral analysis of fluorescence intensity and the redox ratio used as quantitative evaluations showed statistical differences between low grade and high grade tumors. These results showed that multimodal optical analysis is a promising technology for the development of an optical fiber setup designed for an intraoperative diagnosis of urothelial carcinoma in the area of endourology.

## 1. Introduction

With more than 79,000 new cases and a projection of 16,390 deaths in 2017 in the US[1], bladder cancer is one of the deadliest cancer worldwide. For urologists, bladder cancer (BC) and upper urinary tract transitional cell carcinoma (UUT-TCC) are principal issues in urologic oncology. It is therefore critical to diagnose these tumors during endoscopy procedures (cystoscopy or ureteroscopy depending of the tumor localization) in order to confirm lesions macroscopically and to collect a tissue sample to confirm histopathologic characteristics. For specific cases of urothelial carcinoma (BC and UUT-TCC), determination of the histopathological grade of urothelial tumors is one of the keystones in the oncological management. The tumor grade impacts the treatment strategy at various levels, from the type of surgery, to the role of chemotherapy, to the chronological steps in management. In the case of a high grade tumor a total ablation of the organ (radical surgery) may be necessary whereas conservative treatment can be a valid option for low grade tumors associated with bladder cancer and upper urinary tract transitional cell carcinoma (UUT-TCC) [2], [3]. A critical step is proper resection of lesions due to a high risk of recurrence[4] particularly for low grade urothelial carcinoma. This is achievable if both lesion detection and diagnosis are optimal. In this framework, peri-operative screening of tumor characteristics could be a valuable support to the surgeon to adapt the surgery and to plan postoperative cares.

With the development of minimally invasive surgery, the use of miniaturized technology has become a standard procedure, especially for UUT-TCC and BC. For UUT-TCC, flexible ureteroscopy with laser photovaporization allows a reduction in both surgical morbidity and renal function impairment [5],

[6]. New technologies have been developed to help the surgeon with intraoperative discrimination of urothelial carcinoma[7], [8]. Enhanced imaging techniques such as Photodynamic diagnosis (PDD) with 5-ALA[9], Narrow Band Imaging system(NBI)[10], real time optical coherence tomography (OCT)[11] and confocal laser endomicroscopy (CLE)[12] are now proposed for diagnosis. However, all of these technologies have limitations including low specificity (NBI), or difficulty of interpretation by the doctors (OCT, CLE), compared to the gold standard histological diagnosis, due to the lack of multimodality and database images.

After two decades of becoming increasingly popular, two photon microscopy (TPM) has now become an important technique for biological tissue imaging. The development of miniaturized high-numerical aperture optics[13], lasers with optimized pulse delivery [14], and miniaturized scanning system[15], [16] has opened the way for clinical applications. Nonlinear microscopy, as classical confocal imaging, can provide an analysis of tissue using only endogenous labels, and thus eliminates the need for exogenous fluorescence labeling. Second Harmonic Generation (SHG) can access characteristics of tissue structure which have a non-centrosymmetric geometry, such as extra-cellular matrix, muscle fibers, walls of blood vessels, while two photon endogenous fluorescence (TPEF) measurements can detect and show the presence of endogenous fluorophores associated with cellular metabolic activity (reduced nicotinamide adenine dinucleotide: NADH and flavin adenine dinucleotide: FAD).

TPM offers several advantages such as intrinsic sectioning, lower photobleaching, lower and localized phototoxicity, higher penetration depth into the tissues, and an absence of overlap between excitation and emission [17]–[20]. Above all, it provides a different endogenous contrast analysis compared to standard microscopy and confocal endomicroscopy. Although the heterogeneity of tissue structure can lead to complex signal interpretation, endogenous fluorescence analysis of urothelial tissue could be a promising way to avoid metabolic alteration related to external markers[21], [22]. The multimodal technique is an improved alternative to the unimodal one since it highlights tumors characteristics more specifically and precisely.

Nevertheless, non-linear flexible endoscopy imaging development remains a challenge. Although some modalities such as SHG have already been evaluated in-vivo[23] and multiphoton microscopy

evaluated on urothelial and prostate samples[24], [25], only one study so far has explored the potential of multimodal optical analysis in the area of uro-oncology[26].

This preliminary study was conducted to establish the efficiency of a multimodal imaging process based on endogenous fluorescence analysis to discriminate grades of urothelial tumours as done in histopathologic grading. For that reason, we conducted a qualitative and quantitative study, using different contrasts to define optical markers of tumours grade. This study show that optical imaging and analysis could provide reproducible and reliable clinical results.

To the best of our knowledge, this preliminary study assesses for the first time the ability of multimodal optical analyses to identify pathological features and histopathological grades associated with urothelial carcinoma, in a manner consistent with classical histopathological evaluation.

## **2. Material and Methods**

### *2.1 Sample management*

This prospective monocentric study had included a collection of samples from patients suspected to have an urothelial carcinoma at fibroscopy or on imagery. The institutional review board (IRB) of the Tenon Hospital center – University Pierre-Marie Curie approved the study (IRB-00003835), all the following methods were performed in accordance with the relevant guidelines and regulations issue in this protocol and informed consent were signed by the patients.

After endoscopic biopsy or resection, urothelial samples were fixed in a formalin zinc solution. Immediately after, the samples were transferred on a specific nonlinear multimodal set-up to perform the acquisitions. After the multimodal optical analysis, the samples were conditioned and analyzed by the pathologist. Detailed clinical data including age at diagnosis, past medical history including urothelial carcinoma and previous treatment were recorded, such as histopathological data.

### *2.2 Confocal, two-photon microscopy and fluorescence lifetime imaging on a microscopic multimodal setup*

A Mai Tai DeepSee Ti:sapphire laser with automated dispersion compensation (Spectra-Physics, Santa Clara, USA) was used as the source for a TCS SP8 MP microscope (Leica Microsystems, Wetzlar, Germany) to perform two-photon microscopy. The set-up allows us to record imaging, emission spectra and lifetime fluorescence. The laser cavity had over 2.4 W of average power at 800 nm and was tunable from 690 nm to 1040 nm. Two supersensitive Leica hybrid nondescanned (HyD NDD) detectors recorded the faintest structures from deep-tissue sections. For two-photon imaging experiments, fluorescence was collected after the microscope objective via a dichroic beamsplitter, transparent to wavelengths greater than 680 nm. The collected visible spectrum was split by another dichroic cube (FF495-Di03-25 × 36, Semrock, New York, USA) into two channels toward the HyD NDD detectors. This configuration minimized loss in the fluorescence collection. The presence of two additional filters (FF01-448/20-25 and FF01-520/35-25, Semrock, New York, USA) on the dichroic cube set the detection band, respectively one to collect Second Harmonic Generation(SHG) signal and the other one to collect the endogenous fluorescence.

A hybrid detector was used to perform the spectral acquisition. A prism dispersed the fluorescence and the spectral detected band was selected with a specific motorized split mirror placed before the hybrid detector. The spectral resolution was 10 nm, covering the range from 380 nm to 780 nm. Spectral acquisition and single-photon counting technology fluorescence lifetime imaging were coupled by a unique system which integrated hardware and software (PicoQuant GmbH, Berlin, Germany) with the high-end confocal system Leica TCS SP8 MP.

A spectral mosaic was acquired on a 3x3 images area selected with the microscope software: a spectral measurement was made for each image of the mosaic then the software merged the information to give a mean spectrum of the mosaic. For fluorescence lifetime imaging measurements, a mosaic of 9 images per sample were analyzed using appropriate excitation wavelengths. The image size was 512×512 pixels, at 100 Hz and represented the average of 10 frames.

Four different optical signals on the region of interest (ROI) were recorded with our multimodal setup: 1) one and two-photon spectral analysis, 2) two-photon fluorescence lifetime imaging measurement,

3) SHG imaging, and 4) fluorescence imaging under one- and two-photon excitation.

### *2.3 Histopathology analysis*

All the samples were analyzed by the same senior uropathologist using hematoxylin-eosin-saffran (HE) staining without prior knowledge of the two-photon analysis status. Results were given according to the WHO 2016 classification for urothelial carcinoma[27]. Correlation between point-to-points optical indexes, imaging abnormalities and pathological examination of biopsy samples in each particular tumor type and grade was performed. All samples were categorized and classified as healthy urothelium or high grade or low grade tumor by the pathologist.

### *2.4 Data Analysis*

#### *2.4.1 Spectral analysis*

Five circular Regions of interest (ROI) of 200 $\mu$ m diameter were placed on each spectral mosaic stack at the 870nm excitation wavelength. A spectrum was generated for each ROI using Image J to calculate the mean intensity of each image of the stack. This spectrum was then fitted using a Matlab script developed in the lab and previously used in rat and human brain tumors[28], [29]. The script was readapted to urothelial tissue, two components were identified in the emitted response: the nicotinamide adenine dinucleotide (NADH) and the flavin adenines dinucleotide (FAD). Indeed, the absence of oxygen or a need to increase glucose catabolism cause an increase in NADH fluorescence. Hence, the redox ratio is already well-known to be associated with malignant transformation[30]–[32]. Different excitation wavelengths were used. For each excitation wavelength a fit was applied to extract the contribution of the different molecules. Figures 1.a.b. show the response of endogenous molecules using two different excitation wavelengths. As shown, 810 nm excitation wavelength doesn't give access to the SHG. Exciting with 870 nm could be reasonable to collect the metabolic molecules as well as SHG. Consequently, to avoid experimental bias and propose the fastest method to analyze tissue only the 870nm wavelength was used in all our analysis. We extracted from this fit the maximum intensity at the max emission wavelength of each component ( $I_{\text{max-NADH}}$ ,  $I_{\text{max-FAD}}$ ) to then calculate a redox ratio, see Figure 1.c.



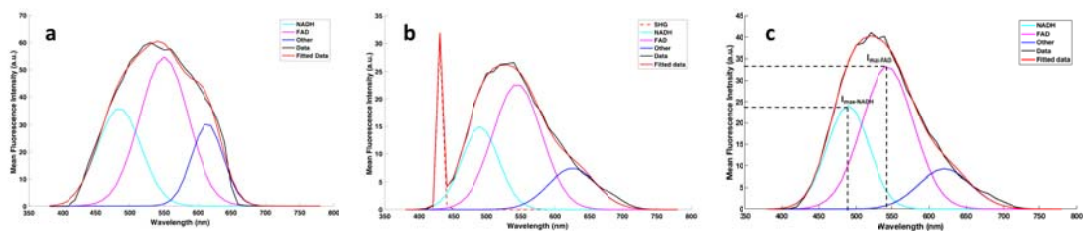


**Figure 1.** Spectral fluorescence response emitted by the tissue using 810nm (a) and 870nm (b) excitation wavelengths. The redox ratio was done under 870nm excitation wavelength, using the NADH and FAD fitted intensity (c).

The redox ratio was then calculated from this value with the most used formula in the literature:

$$\text{Redox} = \frac{I_{\max-FAD} - I_{\max-NADH}}{I_{\max-FAD} + I_{\max-NADH}} \quad [26]$$

#### 2.4.2 Lifetime

The data were collected using the external hybrid dedicated to the fluorescence signal with the filter centered at  $520 \pm 35 \text{ nm}$  and analyzed via the software SymphoTime (PicoQuant, GmbH, Berlin, Germany). On each fluorescence lifetime mosaic of nine images, 5 ROI of a  $200 \mu\text{m}$  diameter were selected on the cells structures and fitted by bi-exponential decay to extract the fluorescence lifetime. The criteria for an acceptable fit were: 1) a  $\chi^2$  value less than 1.0 and 2) residuals randomly distributed around 0 within the interval +4 and -4. The average amplitude lifetime is extracted from fit of each ROI using the following equation:

$$\tau_{avg} = \frac{\sum_i a_i \tau_i}{\sum_i a_i}$$

#### 2.4.3 Statistical analysis

The Chi2 test (or Fisher test) were used to compared qualitative variables, the Student t-test were used for quantitative variables. Redox ratio and average fluorescence lifetime results were evaluated using t-test. A probability value ( $p$ )  $< 0.05$  was considered statistically significant. All statistical analyses were performed using R software.

### 3. Results

#### 3.1 Samples characteristics:

In our study, fourteen patients were enrolled prospectively, including sixteen samples of normal and tumoral urothelium. Among them, fifteen samples were of bladder origin and one from the upper-urinary tract. Amongst them, ten represented urothelial carcinoma (five reported as low grade tumors and five as high grade tumors). Six samples of non tumoral urothelium were also examined.

#### 3.2 Correlation between two-photon fluorescence images and Hematoxylin and Eosin staining

To highlight the performances of non-linear microscopy in tissue diagnosis, we compared our images with the histological analysis, considered as gold standard. Results are shown in Figure 2.

Three major urothelial aspects were identified by fluorescence and compared with the histopathological morphology. First a healthy layer of urothelial cells, second low grade tumor architecture displaying exophytic growth with a fibrovascular core and increased layers of urothelial cells without major atypia or necrosis, and third an invasive high grade tumor, with major atypia and also with exophytic features and a fibrovascular core, typical for pTa tumours (pathologically staged non invasive papillary carcinoma). Moreover, the SHG signal gave us access to the architecture and characteristics of the stroma and the lamina propria and could also be compared with the histological features.

The TPF images were collected through the whole sample, from the epithelial surface to the deepest part, mostly to the detrusor muscle. After the determination of the grade by the multimodal optical analysis, the histopathological images (see Figure 2) were chosen by the pathologist for a better correlation to the TPF images, in order to highlight the specific structures.

Normal urothelium (Figure2; 2a,2d) showed multilayered cells without disorganized architecture, the cells were identify in histological images by dark violet spots and in TPEF images by dark hole in the homogeneous red fluorescent signal, highlighting easily the organization of the layers. There was no

atypia, no disorganization and no mitosis. Umbrella cells were present on the surface, no necrotic features were detected.

Low grade tumor (Figure 2; 2b, 2e) was recognized by the presence of increased number of urothelial cell layers, an architecture which is still recognizable, no cytonuclear atypia, no mitosis. The fibrovascular core is thin, and was highlighted in histological images by pink filament and in two-photon images by the thin green, SHG response, no invasion of the underlying tissue.

High grade tumor (Figure 1; 2c, 2f) is identifiable due to papillary features, the urothelium displays a loss of polarity, cytonuclear atypia can be observed with a modified architecture at the nuclear and epithelial level, this is highlighted in two-photon images by a very irregular form of nuclei of cells, mitosis exist and the fibrovascular core is slightly thickened, the SHG is very difficult to distinguish from the fluorescence, very thin green fiber at the bottom of the image 2.f.

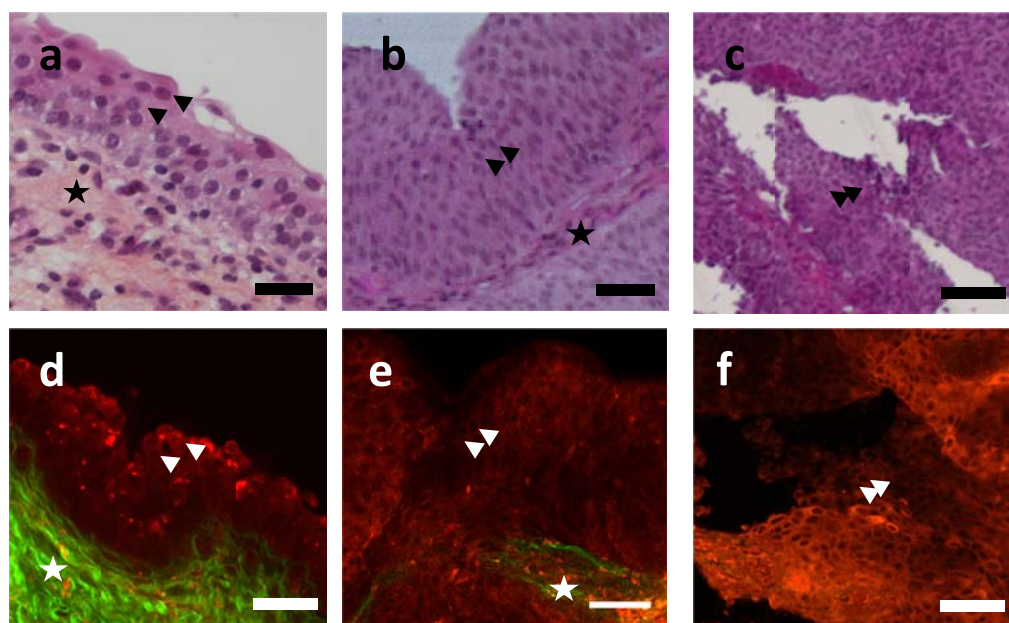


**Figure 2.** Comparison between Hematoxylin - Eosin Saffran staining (a,b,c) with two-photon fluorescence images at 870 nm excitation wavelength, red color for the fluorescence signal and green color for the SHG signal (d,e,f) of three tissue types : healthy (a,d), low grade tumor (b,e) and high grade tumor (c,f). Scale: 100 $\mu$ m. star: Fibrovascular cores, arrow: Urothelial cells.

### 3.3 Quantitative evaluation by spectral analysis and fluorescence lifetime imaging

Once we identified in our images healthy and tumoral urothelium, we performed a quantitative analysis by recording the spectral response and fluorescence lifetime imaging.

A specific wavelength of 870 nm has been chosen for the spectral analysis. This wavelength was chosen after an excitation-emission spectral analysis. We excited the same tissue using all excitation range of the laser from 690 to 1040 nm. The maximum of emission fluorescence was recorded using two hybrid detectors over the excitation range (Figure 3).

The Hybrid1 tracks the SHG and Hybrid2 the emitted endogenous fluorescence. The 870 nm excitation wavelength was chosen to maximize both signal.

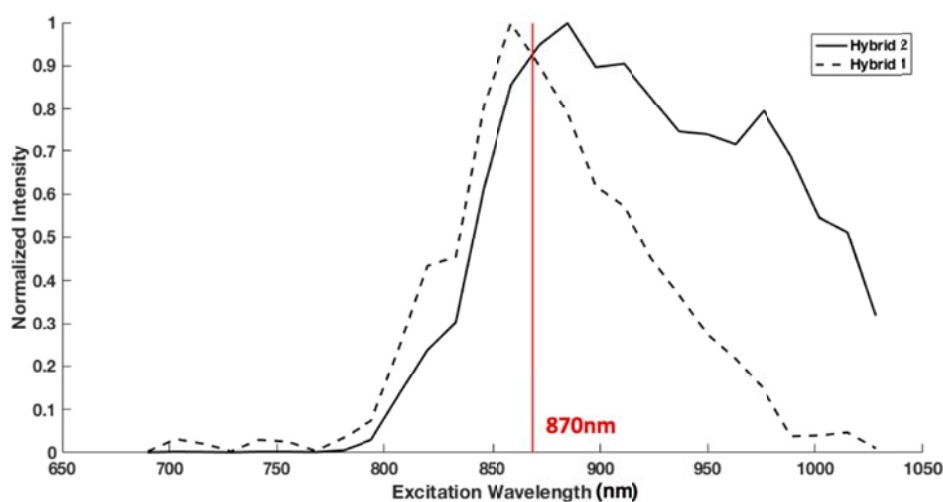


**Figure 3.** Different fluorescent emission with different excitation wavelength (690-1030nm) in hybrid NDD detector.

The spectral results are shown on the Figure 4. We compared the intensity level of the emitted spectra in the Fig.4a. The higher the grade is, the lower is the fluorescence signal. Healthy urothelium has the higher fluorescence intensity.

Then we were able to calculate the redox ratio for each tissue group. The results are presented in Fig.4.b.c. The redox ratio was significantly higher in the healthy urothelium compared with tumors samples ( $p < 0.001$ ). Moreover, it was able to discriminate low grade from high grade tumors. The low grade has a significantly higher redox ratio ( $p = 0.002$ ) than high grade tumor.

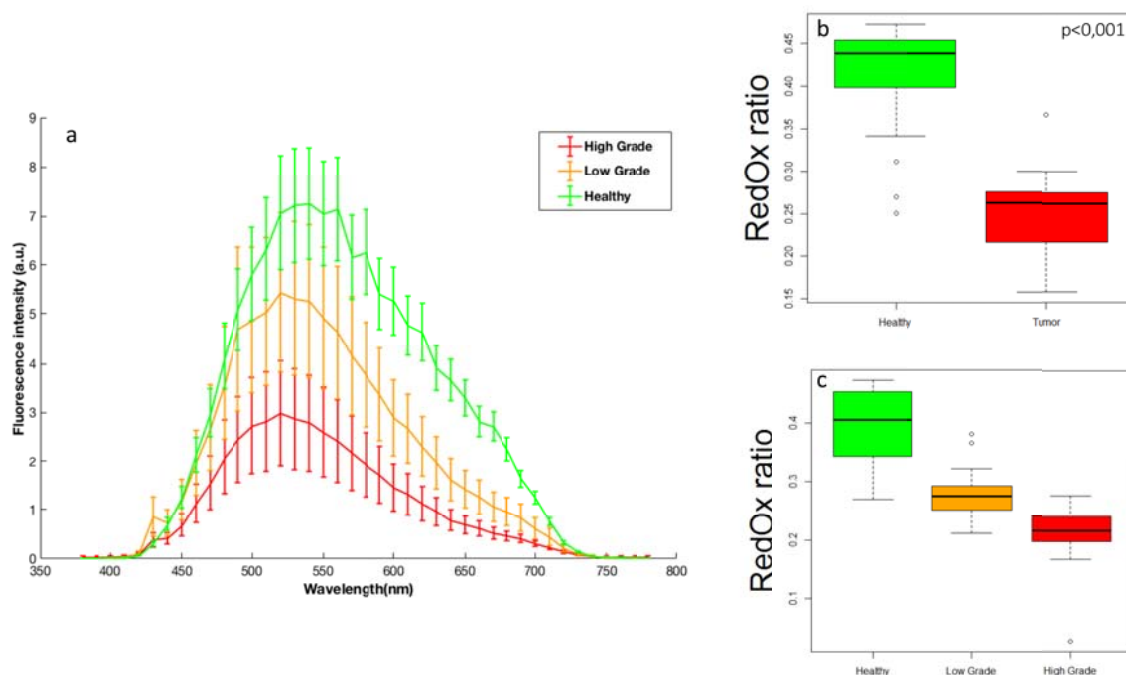


**Figure 4.** Spectral analysis of urothelial tissue at an excitation of 870 nm. (a) Comparison of the mean spectra in normal urothelium, low and high grade tumor (5 samples of each). (b) Comparison of the redox ratio in fifteen region of interest (ROI) in each type between healthy urothelium and tumors. (c) Comparison of redox ratio including low and high grade urothelial carcinoma.

To have a reliable answer and more discriminating indicator, the fluorescence lifetime was also measured. The different results are summarized in Figure 5. We were able to identify the cells structure in the FLIM images and to compare the different grades. This analysis also allowed us to discriminate the different origins. The average lifetime in low grade tumor appeared shorter on our images and in the histogram, Fig.5.a.b.c.

To have a numerical discriminating indicator, fluorescence decay was fitted by a bi-exponential fit in fifteen ROIs and the amplitude lifetime was extracted. Fig.5.d. presents the result, and shows significant differences between healthy, low grade and high grade urothelial carcinoma: healthy vs. low grade ( $p = 0.002$ ), healthy vs. high grade ( $p < 0.001$ ) and high grade vs. low grade ( $p < 0.001$ ). Tumor tissue have a different metabolic equilibrium than normal tissue, in which the co-enzyme NADH and FAD are implied. The variation in the fluorescence lifetime translate this different metabolic state.

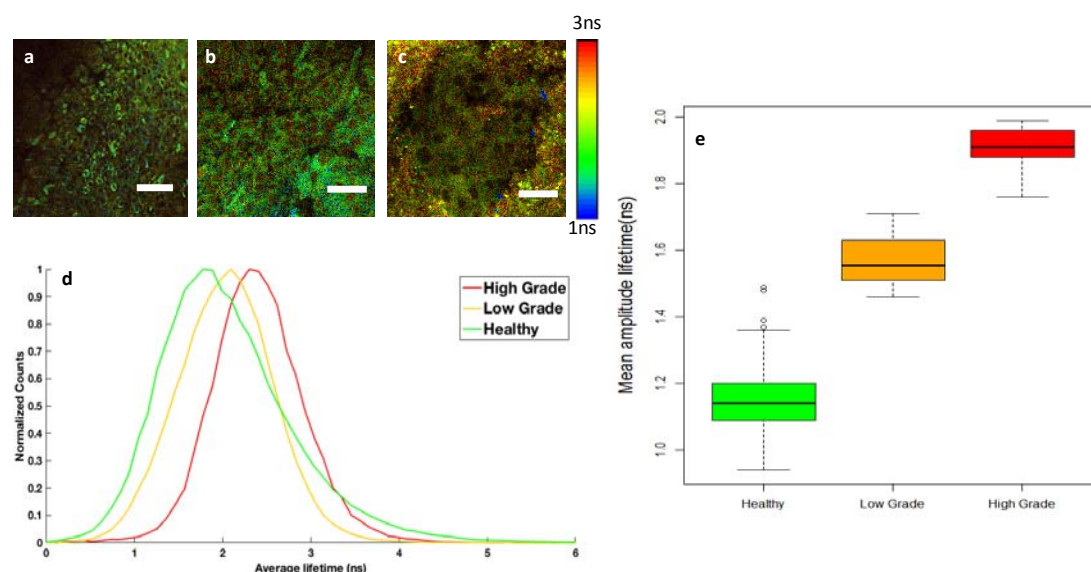


**Figure 5.** Fluorescence Lifetime analysis at 870nm excitation wavelength. FLIM images of (a) healthy, (b) low and (c) high grade tumor cells, (d) respective average lifetime histogram of each image. (e) Variation of mean amplitude lifetime between healthy urothelium, low grade and high grade tumor compared in fifteen ROIs in each type of tissue.

#### 4. Discussion and conclusion

The multimodal optical analysis of urothelial samples from bladder and urinary upper tract has proven its capacity to characterize the urothelium and discriminate healthy tissue, low grade and high grade tumor. This characterization was achieved by a qualitative and a quantitative analysis. These preliminary results are promising for the development of a peri-operative diagnostic tool.

Multiphoton microscopy is a rising technology in the field of tissue analysis. Its intrinsic characteristics make it an increasingly studied technique even in urology[25], [33]. Indeed, in urology, some studies have already shown a good correlation between multi-photon microscopy and histopathologic imaging. Yadav et al. have demonstrated the discrimination of periprostic neural tissue on a rat model with using 780 nm as excitation wavelength excitation[25]. For urothelial carcinoma, Jain et al.[33] have assessed the diagnostic potential of this technique in identifying and differentiating benign from malignant flat bladder lesion, especially carcinoma in situ (CIS). These studies have shown a good correlation between multi-photon microscopy and histopathology. However, none of them have performed a quantitative analysis such as spectral analysis or FLIM analysis. Multimodality as quantitative and qualitative analysis is important for reliable and precise

response. Moreover, Jain et al. have focused only on the capacity to detect CIS but have not sought to determine papillary tumors characteristics especially the grade. As PDD and NBI are performant tools for the CIS diagnosis, it is more interesting to develop a specific peri-operative tool able to help determine the histologic grade in order to improve oncologic management.

When multiphoton microscopy is used alone, it is still limited by the difficulty of easily recognizing abnormal aspects such as intranuclear modifications. In our study, multiphotonic imaging also lead us to recognize and discriminate structures as seen in histopathology. In particular, it was possible to discern healthy urothelium from low and high grade tumors. It is very interesting and promising that optical imaging could be used for live peri-operative histology. It offers high resolved, rapid images comparable to histological images. But because of the learning curve for the tissue recognition and potential intraoperative variability, imaging alone is not sufficient for a reproducible diagnostic tool. This is why, multimodality by adding quantitative analysis to qualitative makes major contribution to clinical applicability in endo-urology.

Our study has shown that fluorescent spectral analysis can discriminate among different types of urothelial tissue from healthy to high grade tumors. Likewise, the redox ratio and FLIM analysis were able to significantly distinguish tissues characteristics. To date, only one study has used the multimodality for urothelial evaluation. Cicchi et al. have assessed TPM for healthy bladder mucosa and CIS. Their results shown a potential difference between both groups even with the redox ratio analysis. But again, the limitation to the diagnosis of CIS is a limitation for a real applicability comparatively to our study which was focused on the grade. To evaluate the redox ratio, different formula are proposed in the literature but we decided to take the most used[21], [26], [34].

Discrimination was also obtained by using the FLIM analysis. The FLIM data are bi-exponential fitted, each component fitted will be associated to one of the form of FAD in tissue, either protein-bound or free. The average amplitude lifetime translates the distribution between free and bound FAD, having longer average lifetime In tumoral tissue means that the free FAD is in higher concentration. This change in the ratio of protein-bound FAD is a consequence of the impact of the Warburg effect. In tumor, an increased metabolizing of glucose to lactate by neoplastic tissue compared with healthy

tissue[35]. Indeed the major co-enzyme in this reaction are NADH and FAD. This is in correlation with previous results shown on healthy bladder mucosa compared to in situ carcinoma [33].

There are some limitations to discuss. First, we analyzed fixed samples. This could lead to some modifications of the fluorescence and the redox ratio analysis compared to an in-vivo analysis. Indeed, the NADH and FAD concentration decrease after the excision of the tissue and that could affect the performance of redox ratio analysis. Nevertheless, our analysis has been able to discriminate the different tissue as described in the previous literature for the redox ratio in healthy and tumoral tissues[21], [26], [34], [36]–[38]. This means that the redox ratio is also a promising tool for an in-vivo evaluation. The other limitation of our study is the low number of samples included. To confirm our results, we need to increase the number of samples and work on fresh biopsy analysis.

These preliminary results confirm the potential of multimodal optical analysis and represent the first step for the development of a laser fiber optical tool for peri-operative diagnosis. The possibility of discriminating the tumor's grade during the surgery is an essential tool for the oncologic management.



## Acknowledgements

This work is supported by PhysiCancer in Plan Cancer with “IMOP” grant, by CNRS with “Défi instrumental” grant, and the Institut National de Physique Nucléaire et de Physique des Particules (IN2P3). This work was done in the PIMPA Platform partly funded by the French program “Investissement d’Avenir” run by the “Agence Nationale pour la Recherche” (grant “Infrastructure d’avenir en Biologie Santé – ANR – 11-INBS-0006”). This work is supported by the French association of Urologist (AFU) with a research grant delivered to B.P. The authors declare no competing financial interests.

## References

- [1] R. L. Siegel, K. D. Miller, and A. Jemal, “Cancer Statistics, 2017,” *CA. Cancer J. Clin.*, vol. 67, no. 1, pp. 7–30, Jan. 2017.
- [2] M. Rouprêt *et al.*, “European Association of Urology Guidelines on Upper Urinary Tract Urothelial Cell Carcinoma: 2015 Update,” *Eur. Urol.*, vol. 68, no. 5, pp. 868–879, Nov. 2015.
- [3] M. Babjuk *et al.*, “EAU guidelines on non-muscle-invasive urothelial carcinoma of the bladder: update 2013,” *Eur. Urol.*, vol. 64, no. 4, pp. 639–653, Oct. 2013.
- [4] M. Brausi *et al.*, “Variability in the recurrence rate at first follow-up cystoscopy after TUR in stage Ta T1 transitional cell carcinoma of the bladder: a combined analysis of seven EORTC studies,” *Eur. Urol.*, vol. 41, no. 5, pp. 523–531, May 2002.
- [5] J.-N. Cornu *et al.*, “Oncologic control obtained after exclusive flexible ureteroscopic management of upper urinary tract urothelial cell carcinoma,” *World J. Urol.*, vol. 28, no. 2, pp. 151–156, Apr. 2010.
- [6] S. Daneshmand, M. L. Quek, and J. L. Huffman, “Endoscopic management of upper urinary tract transitional cell carcinoma: long-term experience,” *Cancer*, vol. 98, no. 1, pp. 55–60, Jul. 2003.
- [7] A. K. Smith *et al.*, “Inadequacy of biopsy for diagnosis of upper tract urothelial carcinoma: implications for conservative management,” *Urology*, vol. 78, no. 1, pp. 82–86, Jul. 2011.
- [8] F. X. Keeley, D. A. Kulp, M. Bibbo, P. A. McCue, and D. H. Bagley, “Diagnostic accuracy of ureteroscopic biopsy in upper tract transitional cell carcinoma,” *J. Urol.*, vol. 157, no. 1, pp. 33–37, Jan. 1997.
- [9] A. M. Batlle, “Porphyrins, porphyrias, cancer and photodynamic therapy--a model for carcinogenesis,” *J. Photochem. Photobiol. B*, vol. 20, no. 1, pp. 5–22, Sep. 1993.
- [10] K. Gono *et al.*, “Appearance of enhanced tissue features in narrow-band endoscopic imaging,” *J. Biomed. Opt.*, vol. 9, no. 3, pp. 568–577, Jun. 2004.

- [11] E. V. Zagaynova *et al.*, “Contrasting properties of gold nanoparticles for optical coherence tomography: phantom, in vivo studies and Monte Carlo simulation,” *Phys. Med. Biol.*, vol. 53, no. 18, pp. 4995–5009, Sep. 2008.
- [12] J.-L. Bonnal, A. Rock, A. Gagnat, S. Papadopoulos, B. Filoche, and B. Mauroy, “Confocal laser endomicroscopy of bladder tumors associated with photodynamic diagnosis: an ex vivo pilot study,” *Urology*, vol. 80, no. 5, pp. 1162.e1–5, Nov. 2012.
- [13] H. Hamzeh, C. Lefort, F. Pain, and D. Abi Haidar, “Optimization and characterization of nonlinear excitation and collection through a gradient-index lens for high-resolution nonlinear endomicroscopy,” *Opt. Lett.*, vol. 40, no. 5, p. 808, Mar. 2015.
- [14] A. Ibrahim, F. Poulon, R. Habert, C. Lefort, A. Kudlinski, and D. A. Haidar, “Characterization of fiber ultrashort pulse delivery for nonlinear endomicroscopy,” *Opt. Express*, vol. 24, no. 12, p. 12515, Jun. 2016.
- [15] G. Ducourthial *et al.*, “Development of a real-time flexible multiphoton microendoscope for label-free imaging in a live animal,” *Sci. Rep.*, vol. 5, no. 1, Nov. 2016.
- [16] C. Duan, Q. Tanguy, A. Pozzi, and H. Xie, “Optical coherence tomography endoscopic probe based on a tilted MEMS mirror,” *Biomed. Opt. Express*, vol. 7, no. 9, p. 3345, Sep. 2016.
- [17] M. Zanello *et al.*, “Multimodal optical analysis discriminates freshly extracted human sample of gliomas, metastases and meningiomas from their appropriate controls,” *Sci. Rep.*, vol. 7, p. 41724, Feb. 2017.
- [18] A. Ustione and D. W. Piston, “A simple introduction to multiphoton microscopy,” *J. Microsc.*, vol. 243, no. 3, pp. 221–226, Sep. 2011.
- [19] L. Marcu, “Fluorescence lifetime techniques in medical applications,” *Ann. Biomed. Eng.*, vol. 40, no. 2, pp. 304–331, Feb. 2012.
- [20] A. Ibrahim *et al.*, “Spectral and fluorescence lifetime endoscopic system using a double-clad photonic crystal fiber,” *Opt. Lett.*, vol. 41, no. 22, pp. 5214–5217, Nov. 2016.
- [21] S. Palmer, K. Litvinova, E. U. Rafailov, and G. Nabi, “Detection of urinary bladder cancer cells using redox ratio and double excitation wavelengths autofluorescence,” *Biomed. Opt. Express*, vol. 6, no. 3, pp. 977–986, Mar. 2015.
- [22] C. Schäfauer *et al.*, “Detection of bladder urothelial carcinoma using in vivo noncontact, ultraviolet excited autofluorescence measurements converted into simple color coded images: a feasibility study,” *J. Urol.*, vol. 190, no. 1, pp. 271–277, Jul. 2013.
- [23] M. E. Llewellyn, R. P. J. Barretto, S. L. Delp, and M. J. Schnitzer, “Minimally invasive high-speed imaging of sarcomere contractile dynamics in mice and humans,” *Nature*, vol. 454, no. 7205, pp. 784–788, Aug. 2008.
- [24] S. M. Zhuo, J. X. Chen, T. Luo, X. S. Jiang, and S. S. Xie, “Multiphoton microscopy of unstained bladder mucosa based on two-photon excited autofluorescence and second harmonic generation,” *Laser Phys. Lett.*, vol. 6, no. 1, pp. 80–83, Jan. 2009.
- [25] R. Yadav *et al.*, “Multiphoton Microscopy of Prostate and Periprostic Neural Tissue: A Promising Imaging Technique for Improving Nerve-Sparing Prostatectomy,” *J. Endourol.*, vol. 23, no. 5, pp. 861–867, May 2009.
- [26] R. Cicchi *et al.*, “Time- and Spectral-resolved two-photon imaging of healthy bladder mucosa and carcinoma in situ,” *Opt. Express*, vol. 18, no. 4, pp. 3840–3849, Feb. 2010.
- [27] P. A. Humphrey, H. Moch, A. L. Cubilla, T. M. Ulbright, and V. E. Reuter, “The 2016 WHO Classification of Tumours of the Urinary System and Male Genital Organs-Part B: Prostate and Bladder Tumours,” *Eur. Urol.*, vol. 70, no. 1, pp. 106–119, Jul. 2016.
- [28] D. A. Haidar, B. Leh, M. Zanello, and R. Siebert, “Spectral and lifetime domain measurements of rat brain tumors,” *Biomed. Opt. Express*, vol. 6, no. 4, pp. 1219–1233, Apr. 2015.
- [29] M. Zanello, A. Ibrahim, F. Poulon, P. Varlet, B. Devaux, and D. Abi Haidar, “Spectral

and Lifetime Measurements of the Endogenous Fluorescence Variation of Freshly Resected Human Samples over Time - Measuring Endogenous Fluorescence Changes at Different Moment after Tumor or Epileptic Cortex Excision:,” 2016, pp. 13–17.

[30] M. C. Skala *et al.*, “In vivo multiphoton microscopy of NADH and FAD redox states, fluorescence lifetimes, and cellular morphology in precancerous epithelia,” *Proc. Natl. Acad. Sci. U. S. A.*, vol. 104, no. 49, pp. 19494–19499, Dec. 2007.

[31] M. C. Skala *et al.*, “Multiphoton microscopy of endogenous fluorescence differentiates normal, precancerous, and cancerous squamous epithelial tissues,” *Cancer Res.*, vol. 65, no. 4, pp. 1180–1186, Feb. 2005.

[32] A. Varone *et al.*, “Endogenous two-photon fluorescence imaging elucidates metabolic changes related to enhanced glycolysis and glutamine consumption in precancerous epithelial tissues,” *Cancer Res.*, vol. 74, no. 11, pp. 3067–3075, Jun. 2014.

[33] M. Jain *et al.*, “Multiphoton microscopy: a potential intraoperative tool for the detection of carcinoma in situ in human bladder,” *Arch. Pathol. Lab. Med.*, vol. 139, no. 6, pp. 796–804, Jun. 2015.

[34] S. Palmer, K. Litvinova, A. Dunaev, J. Yubo, D. McGloin, and G. Nabi, “Optical redox ratio and endogenous porphyrins in the detection of urinary bladder cancer: A patient biopsy analysis,” *J. Biophotonics*, vol. 10, no. 8, pp. 1062–1073, Aug. 2017.

[35] O. Warburg, F. Wind, and E. Negelein, “The metabolism of tumors in the body,” *J. Gen. Physiol.*, vol. 8, no. 6, p. 519, 1927.

[36] W. R. Zipfel, R. M. Williams, R. Christie, A. Y. Nikitin, B. T. Hyman, and W. W. Webb, “Live tissue intrinsic emission microscopy using multiphoton-excited native fluorescence and second harmonic generation,” *Proc. Natl. Acad. Sci. U. S. A.*, vol. 100, no. 12, pp. 7075–7080, Jun. 2003.

[37] L. H. Laiho, S. Pelet, T. M. Hancewicz, P. D. Kaplan, and P. T. C. So, “Two-photon 3-D mapping of ex vivo human skin endogenous fluorescence species based on fluorescence emission spectra,” *J. Biomed. Opt.*, vol. 10, no. 2, p. 024016, Apr. 2005.

[38] K. Alhallak, L. G. Rebello, T. J. Muldoon, K. P. Quinn, and N. Rajaram, “Optical redox ratio identifies metastatic potential-dependent changes in breast cancer cell metabolism,” *Biomed. Opt. Express*, vol. 7, no. 11, pp. 4364–4374, Nov. 2016.

### Graphical Abstract

In urologic oncology, quality and rapidity of diagnosis is an influent element in the choice of

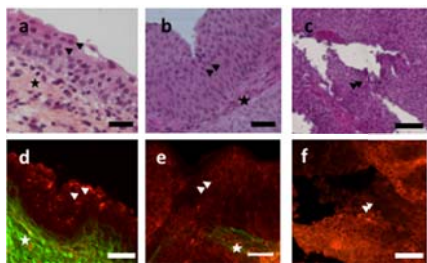
treatment. Intraoperative imaging techniques could help in real-time the surgeon in decision making.

This paper presents a new technology for intraoperative assessment of the nature of bladder tissue. A

multimodal tools with two-photon exciton and quantitative-qualitative detection. Histological

landmarks were found in two-photon images of biopsy and quantitative measurements gave

numerical indicators of malignancy.



**Titre :** Base de données sur le signal d'autofluorescence des tissus pour améliorer le diagnostic peropératoire des tumeurs cérébrales

**Mots clés :** Base de donnée, autofluorescence, tumeurs cérébrales, deux-photon, endomicroscopie

**Résumé :** Le premier traitement standard pour les tumeurs cérébrales est la résection chirurgicale. Dans cette procédure un enjeu important demeure, l'identification des berges tumorales pour assurer une résection totale et éviter le risque de récurrence pour le patient. A ce jour aucune technique d'imagerie peropératoire n'est capable de résoudre l'infiltration tumorale du tissu sain. La norme pour le diagnostic des berges tumorales est l'analyse histologique des biopsies. Une méthode *ex vivo* qui requiert un à plusieurs jours pour fournir un rapport pathologique final, un laps de temps qui peut s'avérer fatal pour le patient. La microscopie optique a récemment été développée vers une utilisation clinique peropératoire pour répondre à cet enjeu. Dans cette thèse, la technique de microscopie à deux-photons a été préférée pour essayer de répondre à cette problématique. Cette méthode donne accès à deux contrastes d'imagerie, la génération de seconde

harmonique et l'émission de fluorescence, qui peuvent être combinés à des mesures quantitatives, tel que la spectroscopie et le temps de vie de fluorescence. Combiner ces quatre modalités de détection donnera une information complète sur la structure et le métabolisme de la région observée. Pour soutenir le développement technique vers une sonde endomicroscopique visant une utilisation peropératoire, les données en résultants doivent être fiables, et se montrer d'un intérêt pour le chirurgien. Par conséquent, une base de données sur le signal d'autofluorescence des tissus a été construite et présentée dans ce manuscrit, avec des algorithmes capables de discriminer de façon fiable les régions tumorales des régions saines. Des algorithmes qui ont montré le potentiel d'être automatisé dans une configuration clinique, afin de fournir une réponse en temps-réel au chirurgien.

**Title :** Tissue database of autofluorescence response to improve intra-operative diagnosis of primitive brain tumors

**Keywords :** Database, autofluorescence, brain tumors, two-photon, endomicroscopy

**Abstract:** The first standard approach for brain tumor treatment is the surgical resection. In this protocol an important challenge remains, the identification of tumor margins to ensure a complete resection and avoid risk of tumor recurrence. Nowadays no intra-operative means of contrast are able to resolve infiltrated regions from healthy tissue. The standard for tumor margin diagnosis is the histological analysis of biopsies. An *ex vivo* method that requires one to several days to issue a final pathological reports, a time lapse that could be fatal to the patient. Optical microscopy has recently been developed towards an intra-operative clinical use to answer this challenge. In this work, the technique of two-photon microscopy, based on the autofluorescence of tissue, has been favored. This technique gives access to two imaging contrasts, fluorescence

imaging and second harmonic generation and emission of fluorescence, and can be combined to quantitative measurement, such as spectroscopy and fluorescence lifetime. The combination of these four modalities of detection will give a complete structural and metabolic information on the observed region. To support the technical development towards an endomicroscopic probe, the resulted data have to be reliable and proved to be of interest for the surgeon. Consequently, an extensive database of the autofluorescence response of brain tumor tissue has been constructed and presented in this manuscript, with algorithms able to discriminate with reliability tumoral from healthy regions. Algorithms that have shown potential to be automatized in a clinical setting, in order to give a real-time answer to the surgeons.